Lithospheric Controls on Arc Volcano Distributions

THESIS

submitted as a requirement for the degree of *Doctor of Philosophy*

HARISMA ANDIKAGUMI
Student ID. 000627145
Ustinov College

Supervisors:
Prof. Colin G. Macpherson
Prof. Kenneth J. W. McCaffrey

DEPARTMENT OF EARTH SCIENCES
DURHAM UNIVERSITY
UNITED KINGDOM
FEBRUARY 2020

this page is intentionally left blank

Lithospheric Controls on Arc Volcano Distributions

by Harisma Andikagumi

Abstract

Distributions of arc volcanoes represent complex processes taking place at many depths. It has been suggested that the alignment of volcanoes in an arc can be described by a small circle geometry on a sphere. However, this assumption neglects the arc-specific tectonic framework that could influence arc volcanism. Here we investigated the distribution of arc volcanoes in three study areas (i.e. Mariana, Java and Lesser Sunda, and Sumatra) and further 16 arcs in global scale study, using quantitative tools to establish the preferred alignment model. We demonstrate that volcanoes at an arc are preferably described by segmented great circles – linear alignments on the Earth's surface that we term 'arc-segments'. This distribution model is best explained by control from the upper plate stress regime where the arc-segments are associated with arc-normal tension located at the base of flexed lithosphere. Lithosphere flexure is the result of down-pulling near the edge of the overriding plate by slab motion because plate-coupling maintains contact between the upper and lower plates. At the location of maximum downward flexure of the overriding plate, a lithospheric weakness zone partitions stress into compression in the near-surface and tension at greater depth. We suggest this is the site where magma pathways through the upper plate are created and lead to construction of a volcanic arc. Oblique convergence can influence the arrangement of arc segments into an *en-echelon* pattern, in addition to the lithosphere flexure. Where arc segments overlap and/or have been rotated an extended weakness zone with greater lithosphere thinning allowed the generation of more melt which can accumulate in the crust. In the latter case, the enhanced magma supply has contributed to the formation of a large-scale caldera (e.g. Toba). At global scales, a segmented great circle distribution model is statistically preferred at 16 arcs. Multivariate statistics display the importance of upper plate thickness in subduction dynamics where it correlates with the distance from trench to arc-segment, slab dip at shallow depth, and the rms-misfit of great circle fitting. Thus, control from the overriding plate on arc volcanism is important and should be considered in future arc studies.

this page is intentionally left blank

Contents

Abstract . . . . . **iii**

Contents . . . . . **v**

List of Figures . . . . . **x**

List of Tables . . . . . **xiv**

Declaration . . . . . **xv**

Acknowledgements . . . . . **xvii**

1 Introduction **1**

1.1 Background 2

1.2 Objectives 4

1.3 Thesis Overview 4

2 Upper Plate Stress Controls the Distribution of Mariana Arc Volcanoes 6

Abstract 7

2.1 Introduction 7

2.2 Mariana Arc 9

2.3 Datasets 13

2.4 Methods 13

2.4.1 Geometric Fitting 15

2.4.1.1 Small Circle Fitting 15

2.4.1.2 Great Circle Fitting 15

2.4.1.3 Comparing Small and Great Circles 16

2.4.2 Surface Strain Observation 17

2.4.2.1 Lineament Mapping . . . 17
2.4.2.2 Volcano Ellipticity . . . 19
2.4.3 Model Evaluation . . . 19
2.4.3.1 Earthquake Focal Mechanisms . . . 19
2.4.3.2 Southern Mariana . . . 21
2.5 Results . . . 21
2.5.1 Geometric Fitting . . . 21
2.5.1.1 Small Circles . . . 21
2.5.1.2 Great Circles . . . 21
2.5.1.3 Comparing Small and Great Circles . . . 22
2.5.2 Surface Strain and Stress . . . 27
2.5.2.1 Backarc Structures . . . 27
2.5.2.2 Volcano Ellipticity . . . 27
2.6 Discussion . . . 30
2.6.1 Vertical Strain Partitioning . . . 34
2.6.2 Model Evaluation . . . 40
2.6.2.1 Earthquake Focal Mechanisms . . . 40
2.6.2.2 Southern Mariana . . . 44
2.7 Summary . . . 46

3 The Apparent Rotation of Java and Lesser Sunda Drives the Arc Deep Upper Plate Structures . . . 48

Abstract . . . 49
3.1 Introduction . . . 49
3.2 Sunda Arc . . . 51
3.3 Data and Methods . . . 52
3.4 Results . . . 54
3.4.1 Geometric Fitting . . . 54
3.4.2 Structural Synthesis . . . 55
3.5 Discussion . . . 58
3.5.1 Surface Strain and Oblique Convergence . . . 59

3.5.2 Deep Structures and Java LS Rotation 62
3.6 Conclusion 68

4 Arc Lithosphere Structure Influenced Caldera Formation at Toba, Sumatra 69
Abstract 70
4.1 Introduction 70
4.2 Sumatra 72
4.3 Data and Methods 72
4.4 Results 73
4.4.1 Geometric Fitting 73
4.4.2 Structural Lineaments 76
4.5 Discussion 76
4.5.1 Lithospheric Weakness Zone 76
4.5.2 Young Slab and Toba Caldera 81
4.6 Conclusion 86

5 The Role of Arc Lithosphere in the Segmentation of Volcanic Arcs . . 88
Abstract 89
5.1 Introduction 89
5.2 Data and Methodology 92
5.3 Results 97
5.3.1 Geometric Fitting 97
5.3.2 Relation with Subduction Dynamics 101
5.4 Discussion 105
5.4.1 Arc-segment Distance, Crustal Thickness, and Slab Dip 106
5.4.2 Crustal Thickness and Arc-segment Misfits 109
5.4.3 Depth to Slab and Descent Speed of Slab 111
5.4.4 Insignificant Variables 113
5.5 Conclusion 114

6 Summary and Conclusion 115

6.1 Observations . . . 116
6.2 Interpretations . . . 117
6.3 Applications . . . 120

Appendices . . . 122

A Map Lists . . . 122
A.1 Regional Geological Maps of Java LS . . . 123
A.2 Regional Geological Maps of Sumatra . . . 127
A.3 Volcano Geological Maps of Java LS . . . 130
A.4 Volcano Geological Maps of Sumatra . . . 131

B Global Volcano Locations Datasets . . . 133

C Spatial Analysis Methods . . . 148
C.1 Small Circles . . . 149
C.1.1 Simulated Annealing . . . 149
C.1.2 Script . . . 149
C.2 Great Circles . . . 152
C.2.1 Hough Transform . . . 152
C.2.2 Script . . . 153

D Geometric Fitting Results . . . 158
D.1 Small Circles . . . 159
D.2 Segmented Great Circles . . . 160
D.3 Segmented Small Circles . . . 166
D.4 Comparing Small and Great Circles . . . 169
D.5 Residual Analyses . . . 188
D.5.1 Mariana Arc . . . 188
D.5.2 Java and the Lesser Sunda . . . 191
D.5.3 Sumatra . . . 193

E Surface Strain Observations . . . 195
E.1 Ellipticity of Mariana Arc volcanoes . . . 196

E.2 Structural Lineaments of Java LS 199
E.3 Structural Lineaments of Sumatra 202

F Subduction Dynamic Variables 206

G Multivariate Statistics 216
G.1 Coefficient of Correlation 218
G.2 Scatter Plots 220

References 226

List of Figures

2.1 Distribution of Mariana arc volcanoes on a gnomonic projection 14

2.2 Use of residuals from fitting small and great circles to volcano distributions to determine true shape of arc-segments 18

2.3 Estimation of shallow crustal stresses from volcano ellipticity 20

2.4 Segmentation of Mariana Arc identified using the Hough Transform method 23

2.5 Residuals of small and great circle fitting plotted against distance along arc 26

2.6 Surface strain distribution of Mariana presented in gnomonic projection. . . 28

2.7 Rose diagram for each arc-segment comparing: arc-segment azimuth and surface strain orientations 29

2.8 Depth to slab under the individual volcanoes on B08 dataset 31

2.9 Trench-perpendicular stress regime in the shallow crust interpreted from volcano ellipticities, along with the backarc extension 35

2.10 Schematic illustration of the stress regime in the north and mid-north segments, central and mid-south segments, and south segment of the Mariana Arc 41

2.11 Earthquake focal mechanisms distribution in the Mariana 42

2.12 Individual earthquake focal mechanisms from the CMT catalogue projected on cross-sections of each segment with bathymetric profiles 43

2.13 Lineament map of the Southern Mariana area to the southwest of Tracey seamount 45

3.1 Geometric fitting to Java LS arc volcanoes 56

3.2 Surface strain synthesis of Java and Lesser Sunda 57

3.3 Orientations of structural lineaments in the west, central and east segments of Java and Lesser Sunda 58

3.4 Diagram of convergence obliquity along Sunda Trench 61
3.5 Model for the rotation of Java and Lesser Sunda 67

4.1 Geometric fitting on Sumatra arc volcanoes 75
4.2 Summary rose diagram comparing the orientation of great circle arc-segment and structural lineaments 77
4.3 The relative distance diagrams between the great circle segments and Sumatran Great Fault 78
4.4 Interpretation of Sumatra tectonics and magmatism 85
4.5 Schematic cross-sections of Sumatra 87

5.1 Global distribution of arc volcano locations 91
5.2 Schematic diagram of subduction dynamic variables 96
5.3 Geometric fitting of Kamchatka arc volcanoes 99
5.4 Circular charts showing relationship between subduction dynamic variables and great circle arc-segmentation from 16 arcs 103
5.5 Schematic illustration describing the relationship of upper plate thickness to arc-segment distance from trench, and also to segment rms-misfit 107
5.6 Schematic illustration describing the relationship between the slab dip and arc-segment distance from trench 108
5.7 Schematic illustration showing the correlation between the main variables . 109
5.8 Schematic diagram illustrating the depth to slab from the arc as a variable associated with the return point of mantle wedge corner flow 113

6.1 Schematic diagram of lithospheric flexure as the main control of arc volcano location 118
6.2 Types of arc-segment arrangements 119
6.3 Schematic diagram of the controls in locating the off-segment volcanoes . . 120

C.1 Great circle fitting procedure based on Hough Transform analysis 153

D.1 Geometric fitting of arc volcanoes in Kuriles 169
D.2 Geometric fitting of arc volcanoes in Kamchatka 170

D.3 Geometric fitting of arc volcanoes in North Japan . . . 171
D.4 Geometric fitting of arc volcanoes in Izu-Bonin . . . 172
D.5 Geometric fitting of arc volcanoes in Ryukyu . . . 173
D.6 Geometric fitting of arc volcanoes in Aleutians . . . 174
D.7 Geometric fitting of arc volcanoes in Alaska . . . 175
D.8 Geometric fitting of arc volcanoes in Central America . . . 176
D.9 Geometric fitting of arc volcanoes in Lesser Antilles . . . 177
D.10 Geometric fitting of arc volcanoes in Northern Andes . . . 178
D.11 Geometric fitting of arc volcanoes in Central Andes . . . 179
D.12 Geometric fitting of arc volcanoes in Southern Andes . . . 180
D.13 Geometric fitting of arc volcanoes in Scotia . . . 181
D.14 Geometric fitting of arc volcanoes in Kermadec-North Island . . . 182
D.15 Geometric fitting of arc volcanoes in Tonga . . . 183
D.16 Geometric fitting of arc volcanoes in Vanuatu . . . 184
D.17 Geometric fitting of arc volcanoes in Mariana . . . 185
D.18 Geometric fitting of arc volcanoes in Java and the Lesser Sunda Islands . . . 186
D.19 Geometric fitting of arc volcanoes in Sumatra . . . 187
D.20 Plots between arc volcano misfits against the distance of a single small circle in the Mariana . . . 188
D.21 Plots between arc volcano misfits against the distance of segmented great circles in the Mariana . . . 189
D.22 Plots between arc volcano misfits against the distance of segmented small circles in the Mariana . . . 190
D.23 Plots between arc volcano misfits against the distance of a single small circle in Java and the Lesser Sunda . . . 191
D.24 Plots between arc volcano misfits against the distance of segmented great circles in Java and the Lesser Sunda . . . 192
D.25 Plots between arc volcano misfits against the distance of segmented small circles in Java and the Lesser Sunda . . . 192
D.26 Plots between arc volcano misfits against the distance of a small circle in Sumatra . . . 193

D.27 Plots between arc volcano misfits against the distance of segmented great circles in Sumatra 194
D.28 Plots between arc volcano misfits against the distance of segmented small circles in Sumatra 194

E.1 Horizontal stress configuration that influences volcano morphology 196
E.2 Examples of the longest axis orientation of volcano ellipticity in Mariana Arc 197
E.3 Structural lineament orientations in the west segment of Java LS 199
E.4 Structural lineament orientations in the central segment of Java LS 200
E.5 Structural lineament orientations in the east segment of Java LS 201
E.6 Structural lineament orientations in the north segment of Sumatra 202
E.7 Structural lineament orientations in the mid-north segment of Sumatra . . . 203
E.8 Structural lineament orientations in the mid-south segment of Sumatra . . . 204
E.9 Structural lineament orientations in the south segment of Sumatra 205

G.1 Scatter plot of the arc-segment distance from trench (Dt) and other subduction dynamic variables 220
G.2 Scatter plot of the crustal thickness (Tc) and other subduction dynamic variables 221
G.3 Scatter plot of the depth to the slab beneath the arc (H) and other subduction dynamic variables 222
G.4 Scatter plot of the trench depth (Ht) and other subduction dynamic variables 223
G.5 Plot of the Upper Plate Nature (UPN) against other subduction dynamic variables 224
G.6 Plot of the Upper Plate Strain (UPS) against other subduction dynamic variables 225

List of Tables

2.1 Small circle properties and fitting results for each dataset 22

2.2 Mariana arc-segments, with volcanoes, properties and fitting results, for both great and small circles. 25

5.1 Abbreviation list of subduction dynamic variables 95

5.2 Corrected Akaike Information Criterion (AICc) of geometric fitting on arc volcanoes 100

5.3 Example of subduction dynamic variables 102

B.1 Locations of volcanoes in 19 arcs 134

D.1 Best-fit small circle parameters at each arc 159

D.2 Great circle fitting properties I 160

D.3 Great circle fitting properties II 163

D.4 Parameters of best-fit small circles at each arc-segment 166

E.1 Mariana arc volcano ellipticity observation result 198

F.1 Subduction dynamic variables I 207

F.2 Subduction dynamic variables II 210

F.3 Subduction dynamic variables III 213

G.1 Coefficient of correlation among subduction dynamic variables 218

G.2 P-value of subduction dynamic variables correlations 219

Declaration

The work in this thesis is based on the research carried out by the author, at the Department of Earth Sciences, Durham University. No part of this thesis has been submitted elsewhere for any other degree or qualification and it is all the author's work unless referenced to the contrary in the text.

this page is intentionally left blank

Acknowledgements

The journey of my doctoral study would have been impossible without the help and support of many people and their institutions. First and foremost, I want to thank Colin Macpherson and Kenneth McCaffrey, my supervisors throughout my study, who always supported me in many ways and let me learn new things so I could develop myself. My meetings with them were always insightful and fun! I couldn't imagine having better supervisors than them.

I would also thank Stefan Nielsen and David Pyle (Oxford) for their time examining my thesis and conducting my PhD viva. My viva was filled with exciting discussion because of them.

I am grateful for the funding provided by *Lembaga Pengelola Dana Pendidikan, Republik Indonesia* (Indonesian Endowment Fund for Education), grant number 20150922024459. They made it possible for me to come to Durham and have this experience as a postgraduate student.

I appreciate the support of the academic staffs at the Department of Earth Sciences in Durham, especially Richard Walters and Jeroen van Hunen who were happy to discuss my project with me so that I could improve my findings. I also thank Mark Allen, my main reviewer during my study and Claire Horwell for giving me the opportunity to get involved in a few volcano projects.

I would like to thank Kyle Bradley and Kerry Sieh at the Earth Observatory of Singapore, Nanyang Technological University, for the opportunity to get involved in MIRAGE and Palu projects during my internships. I also thank the Volcano group at EOS, especially Caroline Bouvet de la Moisonneuve and Christina Widiwijayanti, for fruitful discussions about volcanoes in Java and Sumatra. I would also thank Gina Sarkawi, a friend I met in EOS who made my stay in Singapore a lot more fun.

Thanks also go to the Department of Mining Engineering and the Department of Geology in Institut Teknologi Bandung (ITB), Indonesia, for their help during my fieldwork in Java, especially to Benyamin Sapiie, Ahmad Kamal Mubarok, Mohamad Nur Heriawan, Sudarto Notosiswoyo, and Syafrizal.

On a personal note, I would like to thank David Leslie Hughes, for his unconditional and limitless support throughout my ups and downs in the last four years.

I am grateful for the support of my Indonesian friends in Durham: Nur Dhani Hendranastiti, Fauziah Rizki Yuniarti, Dzulfian Syafrian, Fama Syafrian; they made me feel that home is not that far away. I would also thank my friends in the Gamelan Society in Durham: Meg Fenwick Pomfret, Ayu Rahayu, Paul Fletcher, and Simon Mills; for making Wednesday afternoon a nice break time between work; and to my Angklung Orchestra team who made it to perform outside Durham!

I would also thank my friends I met in Durham: Loraine Pastoriza, Sam Jackson, Nicholas Schliffke, Oliver Sanford, Nipada Santha, Zeyang Liu, Junjie Liu, Sarah Clancy, Miles Wilson, and Kate Hereema; for the friendship and support to each other to finish this phase of academic life in Durham.

I also need to thank my friends in Indonesia and many different parts of the world: Heru Fianisal, Dyah Firgiani, Zulfikar Muslim, Triana Rahajeng, Rizky Wirastomo, Nimas Gania Ayuningtyas, Resmita Kusprasetianty, Imam Fadli, Humaira Azachrania Jati, Sendy Dwiki, and Salmawati; for their constant support from wherever they are.

Lastly, to my family: *Ayah*, *Ibu*, and Ranggi Arohmansani, who let me chase my dream so far from home in the last five years.

Durham, February 2020

Harisma Andikagumi

"Climb every mountain, ford every stream,

follow every rainbow 'till you find your dream."

- The Sound of Music

This thesis is dedicated to

Ibu Sri and *Ibu Wildan*, my primary school teachers,

who made me feel safe,

Nindia Wiraning Puspita, my best friend

who told me that life is better with rainbows in it.

"For every action, there is an equal and opposite reaction."

- Newton's Third Law

this page is intentionally left blank

Chapter 1

Introduction

1.1 Background

Arc volcanism influences human life in many ways and scales. It provides natural resources, such as mineral deposits and geothermal energy, which are beneficial for human life. As an example, mineralisation of copper and gold deposits are known to be associated with arc volcanism (Mitchell & Bell, 1973; Carlile & Mitchell, 1994). Nevertheless, arc volcanism also causes natural hazards, specifically volcanic eruption, which could threaten the environments and the human population. Historical and geological records exhibit the impact of volcanic eruptions from local to a global scale. Locally, magma emplacement at the surface during eruption might cause death and injuries, mental health problems, damage to infrastructure and agriculture, and economic disruption (Blong, 1984). Globally, large-scale volcanic eruptions could cause climatic change and affect the environment where we live in (Oppenheimer, 2011). Recognised, large-scale volcanic eruptions, such as the 1815 eruption of Mt. Tambora and the ∼74ka eruption of Toba, have been shown to have caused climatic changes due to the amount of material ejected to the atmosphere (Oppenheimer, 2003; Williams, 2012). Therefore, understanding the processes involved in arc magmatism is key in managing the resources and mitigating the future risk from the volcanic hazard.

The distributions of arc volcanoes at the surface reflect complex magmatism processes at many depths within the subduction zone. Petrological observations have been used to suggest a critical depth beneath the arc, at about 110 km, where subducted slabs dehydrate (Tatsumi, 1986). At the critical depth, certain temperatures and pressures cause slab dehydration and fluid addition to the mantle, triggering partial melting and magma generation (Schmidt & Poli, 1998; Grove et al., 2009). Assuming the distribution of arc volcanoes in a single small circle model, England et al. (2004) proposed that the critical depth at each arc varies, ranging from 65 km to 130 km, depending on the descent speed of the slab (the product of convergence rate and slab dip). England & Katz (2010) used the correlation between the descent speed of the slab and the depth to slab beneath the arc as the foundation in modelling the thermal structure of the mantle wedge. They suggested the accumulation of anhydrous solidus in the mantle wedge causing thermal erosion and initiating magma pathway, hence controlling volcano locations.

However, England & Katz (2010) also acknowledged some arcs where the relationship between the two variables (depth to slab and descend speed of the slab) are different and some arcs where the depth to the slab has higher uncertainty than 15 km. The arcs which are the outliers to the correlation include Scotia, Java, Bali, Nicaragua, West Indies, and Vanuatu. Meanwhile, the arcs with high uncertainty of the slab depth are New Zealand, Mariana, Vanuatu, Nicaragua, and Scotia. Moreover, the assessment of individual volcanoes (Syracuse & Abers, 2006) found no correlation between the descent speed of the slab and the slab depth beneath the arc. Instead, Syracuse & Abers (2006) proposed that slab geometry and kinematics only affect the degree of melting in the mantle because the depth to the slab correlates with geochemical proxy. They also highlighted the possible control from the upper plate as significant changes of depth to the slab within an arc were observed, such as in Java and Central America. The slab depth in Java varies from 90 km to 150 km over less than 150 km distance along the arc, which was also confirmed by Pacey et al. (2013). Furthermore, Syracuse et al. (2010) used numerical modelling to demonstrate that slab dehydration can actually occur before the slab reaches the critical depth of 110 km beneath the arc. All in all, the small circle model of arc volcano distribution neglects any lateral variation within a single arc and focusses on the processes occurring in the mantle and the slab.

An interaction between upper plate deformation and distribution of arc volcanoes has been proposed, but the mechanism remains unclear. Previous studies have divided volcanoes within an arc into segments to distinguish the volcano morphology, recent deformation or processes from the slab surface (e.g. Carr et al., 1973; Stoiber & Carr, 1973) and magma transport in the mantle (Marsh, 1979). The distribution of volcanoes in Central America and the Lesser Antilles has been studied to understand the interaction between volcanism and upper plate deformation which is manifested in the spatial and temporal variation of magmatism within these arcs (e.g. Morgan et al., 2008; Bolge et al., 2009; Feuillet et al., 2010). Ranneft (1979) proposed that volcanoes in the island arcs are in approximately aligned along straight segments, instead of a curve of sinuous geometry. Pacey et al. (2013) identified linear segments (or "great circle" alignments) of arc volcanoes in the central Sunda Arc with an *en-echelon* pattern, suggesting some control from the stress regime of the upper plate. The linear segmentation in the central Sunda Arc

was identified using a mathematical method, the Hough Transform, as a more quantitative approach than the previous attempt (e.g. Marsh, 1979). The Hough Transform is an analytical method that was developed to extract the geometrical features of an image (Duda & Hart, 1972). This method has been applied in various field in Earth sciences, for instance, to identify the alignment of volcanic vents (e.g. Wadge & Cross, 1988) and to determine the orientation of anisotropy (e.g. Fernández-Álvarez et al., 2016).

1.2 Objectives

The purpose of this study of arc volcano distributions is:

- to develop objective and quantitative tools in analysing the spatial distribution of point-set type data that is applicable to volcanic centres,
- to determine the best-fit geometry to describe the distribution of arc volcanoes based on quantitative assessment and statistical tests,
- to understand the influence of subduction dynamics that control the alignment of arc volcanoes and their relationship with upper plate deformation,
- to propose the importance of lithosphere structure in arc volcanism, such as in the caldera-formation events, and
- to observe the global applicability of arc volcano spatial distribution analysis and identify which subduction dynamic variables may possibly control the location of arc volcanoes

1.3 Thesis Overview

The lithospheric controls on arc volcanoes are discussed in six chapters of this thesis. Following this introductory chapter, there are three chapters of case studies, a chapter of global application, and a summary chapter.

Chapter 2 discuss the distribution of arc volcanoes in the Mariana, which is built on the relatively young oceanic lithosphere and so the influence from pre-existing structures should be minimum. This chapter also explains the methods used in this study, which can

be divided into three main parts: geometric fitting, surface strain observations, and model evaluation. The analysis of Mariana Arc is intended to identify the main control on the alignment of arc volcanoes. Lithospheric stress controls on arc volcano distribution are summarised in a schematic model and then tested by evaluating the distribution of earthquake focal mechanisms and by assessing the structures of amagmatic areas in Southern Mariana.

Chapter 3 focus on the distribution of arc volcanoes in Java and the Lesser Sunda Islands. This chapter improves the spatial analysis of volcano distribution in the Sunda Arc over a previous study by Pacey et al. (2013). The schematic model of stress control on arc volcanoes from **Chapter 2** is applied in this chapter to build a comprehensive tectonic model of the Sunda Arc. This chapter also explores the arc-specific tectonic framework and history that might have produced the arc volcano distribution.

Chapter 4 considers the importance of arc lithosphere structure in the formation of a large-scale caldera. The previous discussions of such structures have focussed on magmatic or eruptive processes while tectonic control, such as arc structure, is rarely considered. The Toba supervolcano in Sumatra is an example of a large-scale caldera that has been attributed to high magma supply by previous studies. This chapter showcases the importance of the arc lithosphere role by highlighting the variation of the subducting slab, and the deformation processes along the Sumatran margin.

Chapter 5 applies the arc volcano alignment analysis from the preceding chapters into 16 other arcs around the world. This chapter demonstrates the applicability of the spatial analysis tool on a global scale. Subduction dynamic variables are compiled from various sources and with the location of arc volcanoes expressed by the distance from trench to the arc. Correlation between variables and their significance are then explored to determine the subduction dynamic processes that possibly control the location of arc volcanoes.

Chapter 6 summarises the discussion from the previous case studies and global scale synthesis. The conclusion is divided into three parts: observations, interpretations and applications.

Chapter 2

Upper Plate Stress Controls the Distribution of Mariana Arc Volcanoes

By the time of the final thesis submission, this chapter has been accepted as an article for publication by *Journal of Geophysical Research: Solid Earth*. Citing this chapter should follow the appropriate citation to the following article:

Andikagumi, H., Macpherson, C. G., & McCaffrey, K. J. W. (2020). Upper Plate Stress Controls the Distribution of Mariana Arc Volcanoes. *Journal of Geophysical Research: Solid Earth*. doi: 10.1029/2019JB017391

Abstract

We present a spatial analysis of volcano distribution and morphology in the young, intraoceanic Mariana Arc. Both the quality of fit to idealised models and the divergence from those ideals indicate that Mariana Arc volcanoes are arranged into five great circle segments, rather than a single small circle or multiple small circles. The alignment of magmatic centres suggests that magma transport is controlled by the stress regime in the deep crust and/or lithospheric mantle of the Philippine Sea Plate, into which the arc is emplaced, and that arc-normal tension is the dominant process operating in the deep lithosphere along the whole arc. Volcano morphologies indicate that the stress regime in the shallow crust varies between arc-normal tension and compression, which also implies that the stress field can vary with depth in the arc lithosphere. We show that this horizontal and vertical stress partitioning can be related to the changing dip of the subducting plate and the breadth of the zone where it is coupled with the overriding plate. The variation in stress regime is consistent with both the distribution of seismicity in the Philippine Sea Plate and with the structural fabrics of the non-volcanic part of the plate margin to the south. Our analysis suggests that the upper plate exerts the principal control on the distribution of volcanoes in the Mariana Arc. Where tension in the deeper parts of arc lithosphere is sufficiently concentrated then a distinct volcanic front is produced.

2.1 Introduction

Locations of volcanic edifices provide an opportunity to explore magma generation and transport beneath volcanic arcs (England & Katz, 2010). Processes occurring within the slab and mantle wedge, in particular through addition of fluid from the subducted slab to the wedge, make significant contributions to subduction zone magmas, therefore some relationship between the locations of arc volcanoes and subduction dynamics can be anticipated (Stoiber & Carr, 1973; Carr et al., 1973; Marsh, 1979; Gill, 2012; England et al., 2004; Tatsumi, 2005). England et al. (2004) approximated the distribution of arc volcanoes as small circles to define an average depth to slab (H) in each arc for comparison with other subduction dynamic parameters. This approach led them to propose that the locus of melting is related to the descent speed of slabs, from which it was inferred that

the thermal structure of the mantle wedge is an additional key factor in localising melting and, hence, volcano location (England et al., 2004; England & Katz, 2010). While the small circle approximation reveals correlated parameters for many arcs, the metamorphic reactions that release fluid from subducted slabs occur over a range of pressures and temperatures depending on the thermal and compositional profile of each slab (Schmidt & Poli, 1998; Grove et al., 2009). Thus, despite broadly similar H values within and between arcs (Jarrard, 1986; England & Katz, 2010; Wilson et al., 2014), with an average close to 105 km, it should be no surprise that there are wide variations, from about 60 to 200 km, in H within single subduction zones, often for volcanoes is close proximity (Syracuse & Abers, 2006; Pacey et al., 2013).

While mantle wedge hydration is clearly vital to the creation of arc volcano sources, an alternative view of volcano locations is that these are a function of structures or processes operating in the arc lithosphere, since the locations of volcanoes are the surface expression of magmatic pathways through the upper plate. The possibility that arc lithosphere might control arc volcano distribution was recognised from the early days of plate tectonics (Isacks et al., 1968) and substantial interplay of upper plate structural features with both spatial and temporal distributions of magmatism have been suggested in the Central American and Lesser Antilles margins (Burkart & Self, 1985; Weinberg, 1992; Feuillet et al., 2002; Morgan et al., 2008; Bolge et al., 2009; Feuillet et al., 2010). Pacey et al. (2013) demonstrated that volcanoes of the central Sunda Arc are aligned into a series of great circle segments, an arrangement that had previously been proposed to result from the locus of melt formation in many subduction systems (Marsh, 1979; Ranneft, 1979). In contrast to these previous studies however, Pacey et al. (2013) attributed this arrangement to control of magma transport by the arc lithosphere because, with the exception of ocean island chains, most examples of great circle features on the Earth's surface are accepted as consequences of lithospheric control. The most notable examples of this are the products of tension, as seen to control alignment of magmatism at oceanic spreading centres and continental rifts, or association with lithospheric-scale fault systems, such as transverse and major normal faults. Therefore, recognition of great circle alignment in volcanic arcs may provide a means to determine the stress regime affecting arc lithosphere (Pacey et al., 2013). However, the margins mentioned above are predominantly conti-

nental systems, where structures inherited over protracted geological histories may also influence magmatic pathways.

To explore the distribution of arc volcanoes in an intraoceanic system, this paper examines the Mariana Arc (**Figure 2.1**), which initiated approximately 5 million years ago as the latest of several arcs to form in response to subduction of the Pacific Plate beneath the eastern margin of the Philippine Sea Plate (Fryer, 1996). The Mariana Arc covers geologically young, extensional basement and structures associated with rifting of the Mariana Ridge from the Mariana West Ridge (Hussong & Uyeda, 1981; Bloomer et al., 1989; Yamazaki et al., 2003; Oakley et al., 2009). Its youth, intraoceanic setting and, relatively, simple geological history mean that this margin is less susceptible to the structural and rheological complexities that influence continental arcs (Fryer, 1996). Thus, the Mariana Arc is well suited to understand the effect of current tectonic development upon arc volcano distributions. We demonstrate that the arrangement of Mariana Arc volcanoes is best described by a pattern of great circle segments. This segmentation is consistent with tensional forces dominating strain at the base of the arc lithosphere, thus focussing magma towards the volcanic arc. Comparison of these alignments with volcano ellipticity and seafloor fabrics indicates that stress is vertically partitioned in the arc lithosphere and that the nature of this partitioning varies along the arc. We develop a model for these stress variations which is consistent with both earthquake focal mechanisms within the volcanic arc and the structural features of the non-volcanic continuation of the Mariana margin to the southwest.

2.2 Mariana Arc

The intraoceanic Mariana Arc (**Figure 2.1**) is at margin where subduction and volcanism have been ongoing since the Eocene (Hussong & Uyeda, 1981). Located at the eastern edge of Philippine Sea Plate, where the Pacific Plate is subducted westwards, the active Mariana Arc, which is dominated by basalt and basaltic andesite magmatism (Bloomer et al., 1989), has previously been described as comprising: the Northern Seamount Province from 21° to 24°N, the Central Island Province from 16° (Anatahan) to 21°N (Uracas), and the Southern Seamount Province from 13° to 16°N (Dixon & Stern, 1983). Designation

of boundaries between these provinces is arbitrary being based on volcano elevations with respect to sea level, which overlooks the presence of seamount volcanism within the Central Island Province. The whole arc, from Nikko in the north to Tracey in the south, comprises 60 groups of volcanic centres of which 26 are active. Twenty of the active centres are submarine (Baker et al., 2008). The active arc is located immediately to the west of Mariana Ridge which is 100 km wide in the south and peaks at 300 m above sea level in Guam, narrowing to 20 km width near Sarigan where its crest is 1100 m below sea level. This ridge forms a non-volcanic island chain from Guam in the south to Asuncion in the north then becomes indistinct, further north (**Figure 2.1**; Bloomer et al., 1989).

Hussong & Uyeda (1981) proposed that active edifices in the Mariana Arc are constructed on a basement of backarc crust or rifted, arc crust that subsided along steeply-dipping normal faults, to the west of the Mariana Ridge. Later, Bloomer et al. (1989) proposed that Mariana Arc edifices were aligned parallel to the West Mariana Ridge, Mariana Trough and the forearc, from which they suggested that normal faults channel magma on its route to constructing the edifices. Accordingly, Bloomer et al. (1989) concluded that Mariana Arc volcanism is controlled by the structural development of the upper plate. Moreover, Oakley et al. (2009) interpreted scarps in the backarc, observed on seismic reflection profiles, as normal faults that formed by backarc spreading with most of the faults facing towards the spreading axes. Thus, it is also important to understand development of the backarc in order to understand the volcanism in the active arc.

The spreading-related, active faulting in the Mariana backarc is different to that in most ocean basins (Fryer, 1996), especially at fast or superfast spreading ridges where active faulting is concentrated within a narrow zone near the spreading axis (M. H. Edwards et al., 1991; Fornari et al., 1998). In contrast, diffuse extension of the Mariana Trough occurs as widely distributed normal faulting across the backarc even though a spreading axis is present and active (Fryer, 1995). Martìnez et al. (1995) proposed that the diffuse deformation is caused by far-field strain as the upper plate deforms in response to subduction, and described three types of structural development in the northern Mariana Trough: (1) asymmetric rifting between 22°15′N and 24°N, (2) localised rifting where spreading axis start to separate from the active arc between ∼ 21°N and 22°15′N, and (3) concentrated rifting from 20°N to 21°N to where the spreading axis is separated from active arc and

forms deep grabens. This structural arrangement was later confirmed by identification of the rifting to spreading transition zone at about 22°N, through seafloor-spreading patterns in the bathymetry, magnetic field lineaments, and bulls-eye patterns in gravity data (Yamazaki et al., 2003). The same data also indicated diachronous initiation of spreading. Observations by Yamazaki et al. (2003) suggest that spreading between 19°N and 20°N started before 5 Ma then propagated to the north, which is compatible with the conclusion of Hussong & Uyeda (1981) who stated the spreading began after late Miocene.

Asymmetric spreading in the Mariana Trough has produced more backarc crust to the west of the spreading axis than to the east (Karig et al., 1978; Oakley et al., 2009). Yamazaki et al. (2003) suggested that this resulted from interaction of mantle upwelling beneath the active arc and the backarc spreading centre. Deschamps & Fujiwara (2003) proposed it could be caused by pre-existing magmatism in the east leading to asymmetry of crustal rheology, melting processes and stress regime conditions, by resistance of the Pacific Plate slab in the eastern margin to the northwestward relative motion of the Philippine Plate, or by rollback of the Pacific Plate causing migration of the trench towards the east and southeast (Faccenna et al., 2009; Boutelier & Cruden, 2013). Slab rollback plays a significant role in backarc basin formation by causing hinge retreat and creating extension in the backarc (Macpherson & Hall, 1999, 2002), hence rollback of the Pacific Plate caused trench retreat and began the opening of Mariana backarc basin (Faccenna et al., 2009).

The Mariana Trough spreading rate varies from north to the south. Based on modelling of magnetic anomalies and deep ocean drilling core analyses, the spreading half-rate to the west of the spreading centre has varied from 2 to 3 cm/year since late Miocene (Hussong & Uyeda, 1981; Yamazaki et al., 2003). GPS observations conducted from 1991 to 1999 used the stable Eurasia reference frame for GPS stations in the island arc to determine the present backarc spreading rate relative to Philippine Sea Plate. The backarc spreading rates are 15.9 ± 6.6 mm/year with an azimuth of $57.8° \pm 19.9°$ near Agrigan at the centre of the arc, with a maximum rate of 44.6 ± 2.7 mm/year directed towards $97.1° \pm 4.1°$ near Guam in the south (Kato et al., 2003). This study also showed lateral, N-S motion in the residual data which aligned with the model of spreading developing in the centre of the Trough propagating to the north and south (Martìnez et al., 1995; Oakley et al., 2009).

Motion of the subducting Pacific Plate relative to the Philippine Sea Plate varies from north to south along the trench (Argus et al., 2011; T. W. Becker et al., 2015). At about 23°N the rate of convergence is 34 mm/year with an azimuth of N290°E (Argus et al., 2011). Convergence gradually decreases to the south and the subduction direction rotates clockwise to 21 mm/year directed to N317°E at around 12°N (**Figure 2.1**). Thus, as the trench azimuth rotates so does convergence obliquity from highly oblique in the north to orthogonal at about 13°N then oblique in the opposite sense further south. Stern & Smoot (1998) noted that this obliquity variation along the arc is manifest as the prevalence of left-lateral, strike-slip faults in the forearc north of 18°N contrasting with forearc grabens in the southern forearc (**Figure 2.1**).

When averaged from 80 to 400 km depth the Pacific Plate has a steep dip of approximately 75° beneath the Philippine Sea Plate (England et al., 2004), with some variation along the arc. Syracuse & Abers (2006) showed that between 50 and 250 km depth the average dip decreases from 60° under Farallon de Pajaros (20.5°N) to 49° under the Esmeralda Bank (15°N). This is the same sense of variation as observed for depths greater than 125 km, where dips are 84° at 21°N compared to 73° at 12°N (Lallemand et al., 2005). However, at depths less than 125 km slab dips are steeper in the south, varying from 36° at about 21°N to 46° at 12°N (Fukao et al., 2001; Lallemand et al., 2005; Miller, Gorbatov, & Kennett, 2006; Miller, Kennett, & Toy, 2006). Variations in slab dip play no systematic role in variations in the depth from arc volcanoes to the slab, however. **Figure 2.1** shows that in the southernmost arc there is an almost 60 km variation in depth to slab between Tracey and Northwest Rota seamounts. There is negligible variation in slab dip, or convergence rate and vector, between these volcanoes which are separated by only 115 km.

Gvirtzman & Stern (2004) used the term "plate coupling", which is different to "seismic coupling", to refer to the contact between upper and lower plates in a subduction zone. The steepening slab dip in the south, possibly related to tearing of the subducting slab and asthenospheric upwelling under the upper plate (Gvirtzman & Stern, 2004; Miller, Gorbatov, & Kennett, 2006), also affects the zone in which such coupling occurs. The plate coupling zone is the horizontal breadth of this region of plate coupling at the surface, which they took to be represented by the distance from the trench to the front of

the Mariana Ridge. This zone narrows southward from 170 km at 17.5°N, in the centre of the arc, to 100 km at 11°N, in the south (Gvirtzman & Stern, 2004).

2.3 Datasets

We employed three compilations of volcano locations to allow direct comparison of previous approaches with the method applied here (**Figure 2.1**). Following England et al. (2004) the first dataset (GVP04), which largely equates to the sub-aerial Mariana Arc, takes the locations of 12 volcanoes from the Smithsonian Institute's Global Volcanism Program (2013) catalogue; from Esmeralda at the southern end to Farallon de Pajaros in the north. The second dataset (GVP04+SM) includes all submarine volcanoes between Esmeralda and Farallon de Pajaros, which increases the number of edifices to 21. The third dataset (B08) is taken from the study of Baker et al. (2008) on hydrothermal activity in the Mariana Arc. This includes 37 volcanoes from Nikko in the north to Tracey in the south, which geochemical studies suggest are all part of the volcanic arc (Pearce et al., 2005; Baker et al., 2008). The presence or absence of hydrothermal emissions (Baker et al., 2008) was used to constrain the locus of active volcanic craters. For centres lacking such emissions we used the least weathered crater morphologies to identify the most likely location of active or recent volcanism. The complete lists of volcanic centre location datasets are listed in **Appendix B**.

2.4 Methods

We applied quantitative and objective methods to investigate the distribution of Mariana Arc volcanoes. Small circles were fitted to each dataset (i.e. GVP04, GVP04+SM, B08) and the Hough Transform method was applied to identify potential great circle alignments in B08 (Pacey et al., 2013). To determine whether a segmented small circle model might be more appropriate, best fit small circle were also obtained for the segments identified using the Hough Transform approach. Candidate great circle segments were compared to the structural lineament trends in the backarc basement, and to the ellipticity of arc volcanoes (Nakamura, 1977). All results are integrated into a model that is evaluated against earthquake focal mechanisms and a structural understanding of the adjacent, amagmatic,

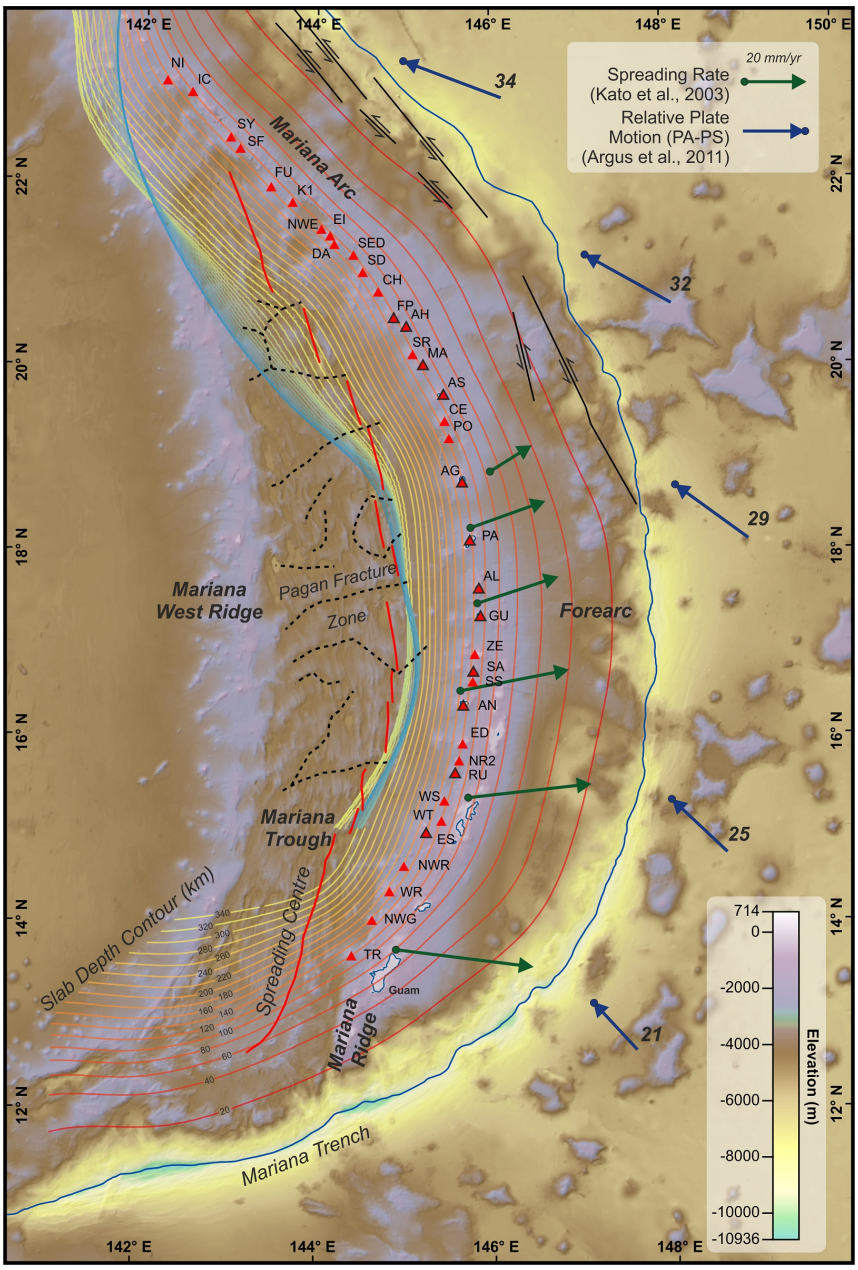

Figure 2.1. Distribution of Mariana arc volcanoes on a gnomonic projection with centre at 139.305°E, 17.333°N. Red triangles with black outline are subaerial volcanoes (Smithsonian's Institute Global Volcanism Program; our dataset GVP04), those with no outline are submarine (abbreviations in **Appendix B**). Subaerial and submarine volcanoes between Farallon de Pajaros (FP) and Esmeralda (ES) are included in the second dataset (GVP04+SM). All volcanoes from Nikko (NI) in the north to Tracey (TR) in the south comprise dataset B08 (Baker et al., 2008). Digital elevation model in 30-arc-second resolution (J. J. Becker et al., 2009) and additional 6-arc-second resolution (Lim et al., 2013) from NOAA. Black dashed lines are backarc fracture zones. Thick red lines are sites of backarc spreading (Yamazaki et al., 2003; Martinez & Taylor, 2003; Oakley et al., 2009). Black lines with arrows are sinistral strike-slip faults (adapted from Stern & Smoot, 1998). Thin red to blue solid lines are slab contours in km beneath surface, from SLAB2.0 (Hayes et al., 2018). Green arrows illustrate backarc spreading directions inferred from motion of islands (Kato et al., 2003) with length proportional to rate. Blue arrows are the relative plate motion of Pacific Plate (PA) to stable Philippine Sea Plate (PS) with length proportional to rate which is annotated in mm/year (Argus et al., 2011).

southernmost part of the plate margin. A more detailed explanation of the methods is presented in the **Appendix C**.

2.4.1 Geometric Fitting

2.4.1.1 Small Circle Fitting

The geometry of a small circle is defined by the coordinates of its centre (latitude and longitude) and its radius (r). The best fit small circles for the whole arc and for arc-segments were obtained by varying those parameters to minimise the standard root-mean-square misfit (rms-misfit) of the volcanoes, as expressed by the equation:

$$m = \sqrt{\frac{\sum_1^n {d_n}^2}{n}} \tag{2.1}$$

where d_n is the shortest (perpendicular) distance from each volcano to the small circle and n is the number of the volcanoes in the dataset. This equation weights each volcano in the calculation equally, in contrast to alternative approaches which more heavily weight those volcanoes lying close to the small circle (e.g. England et al., 2004).

2.4.1.2 Great Circle Fitting

To evaluate whether the Mariana Arc volcanoes are aligned as great circles, we used a Hough Transform approach (Duda & Hart, 1972; Crane & Ballard, 1981). This method has been used in earth sciences to detect aligned structures, including volcanic vents and monogenetic volcanoes (Wadge & Cross, 1988; Martìnez et al., 2000; von Veh & Németh, 2009; Cebriá et al., 2011; Fernández-Álvarez et al., 2016). Specific to arcs, Pacey et al. (2013) applied a Hough Transform approach to identify great circle segmentation in the central Sunda Arc. We have developed their method and applied this to determine potential alignment of Mariana Arc volcanoes. The quality of data fit to each potential great circle was, again, quantified by rms-misfit. Initially, the endpoints of each segment were fixed as the locations of the two volcanoes at its ends (Pacey et al., 2013). Then, linear transformations were applied iteratively to the length, centre point, and orientation of each potential alignment to minimise the misfit. Misfits for the overall arc were calculated for all possible segment combinations and weighted based on the number of volcanoes in each

arc-segment. The best-fit combination of great circle segments was then identified by minimising the total number of segments, where possible associating each volcano with one segment only, maximising the number of volcanoes on each segment, and minimising the overall misfit.

2.4.1.3 Comparing Small and Great Circles

We employed two approaches to compare the quality of fit of small and great circles. We used the Akaike Information Criterion to compare the segmented small circle and segmented great circle cases because, although the number of segments are similar in each, the numbers of adjusted parameters (i.e. degrees of freedom) differ. A small circle has three degree of freedom (radius, and central latitude and longitude) while a great circle has only two (central latitude and longitude). To allow direct comparison we adapted the least square fit case of the Akaike Information Criterion (AIC; Akaike, 1974) where the model estimator is the rms-misfit that we obtained from fitting the geometric models (Burnham & Anderson, 2004; Banks & Joyner, 2017). The AIC is expressed as:

$$AIC = n \log\left(\hat{\sigma}^2\right) + 2K \tag{2.2}$$

where n is the number of data points, K is the number of adjusted parameters, and $\hat{\sigma}^2$ is the estimator. Since we use the rms-misfit as model estimators,

$$\hat{\sigma}^2 = \frac{\sum {d_n}^2}{n} \tag{2.3}$$

where d_n is the residual or misfit from each volcano to its geometric model.

Given that the number of volcanoes in our datasets is small compared to the number of adjusted parameters in our geometric fitting, the AIC parameters should be corrected (AICc) to prevent bias from the model with more adjusted parameters (Hurvich, 1989; Akpa & Unuabonah, 2011). The AICc parameter formula is expressed as:

$$AIC_C = AIC + \frac{2K(K+1)}{n-K-1} \tag{2.4}$$

hence,

$$AIC_C = n \log\left(\hat{\sigma}^2\right) + 2K + \frac{2K(K+1)}{n-K-1} \tag{2.5}$$

Since any AIC parameter represents the amount of information lost in fitting any model, models with the lowest AICc values should be preferred (Akaike, 1974; Burnham & Anderson, 2004).

A segmented model, whether of small or great circles, will involve considerably more degrees of freedom than for a single small circle, therefore, it is questionable how appropriate the AICc is for comparing a single small circle with a segmented great circle model. Instead, we analysed the systematic changes in misfit (residuals) along the length of each segment with respect to ideal great and small circles. The principal behind this is outlined in **Figure 2.2**. Relative to a great circle datum, a chain of volcanoes that form a great circle on the surface of a sphere (**Figure 2.2a**) would have residuals (ΔGC) that produce a $y \approx 0$ regression line when plotted against distance along the segment (**Figure 2.2b**). Residuals for the same chain of volcanoes with respect to a small circle datum (ΔSC) would form a polynomial curve (**Figure 2.2c**). Conversely, if the volcanoes are actually distributed as a small circle (**Figure 2.2d**) then the systematics of residual plots would be reversed, i.e. ΔGC plotted against along-segment distance would generate a polynomial curve (**Figure 2.2e**) and a line of $y \approx 0$ would be produced for ΔSC (**Figure 2.2f**). The patterns predicted would be apparent regardless of whether a single small circle datum or segmented circle datums are used, although segmentation of either the dataset or the datums would lead to inflections or reversals of the residual variation along the length of the arc.

2.4.2 Surface Strain Observation

2.4.2.1 Lineament Mapping

Extensional faults are distributed widely across the backarc and not concentrated within a narrow zone near the spreading axis (Fryer, 1996). We mapped individual normal faults, with the assumption that they are still in an early stage of development and can be considered as isolated structures (Cowie et al., 2000). Faults were identified on the bathymetric surface as lineaments across which the seafloor depth changes significantly.

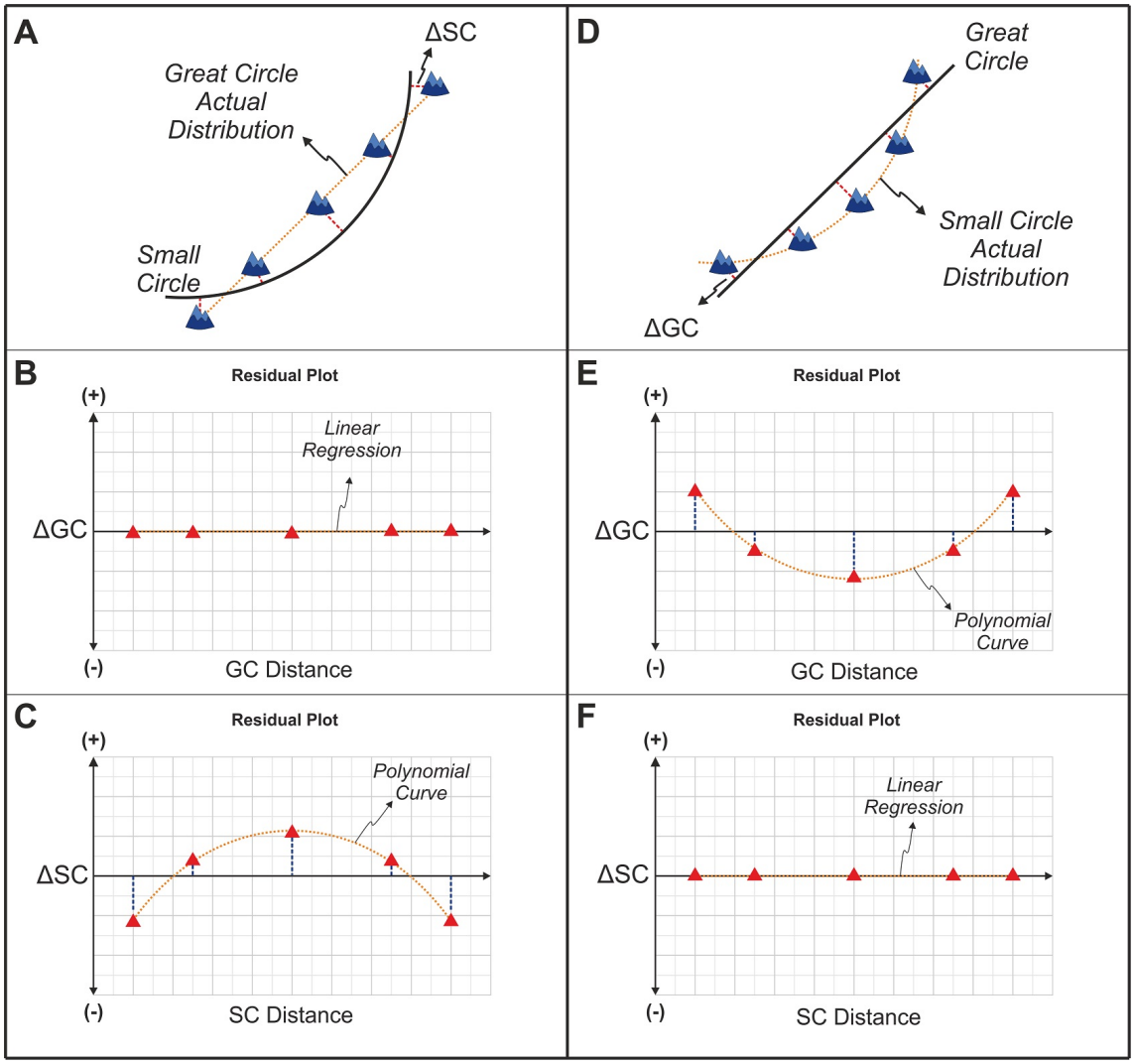

Figure 2.2. Use of residuals from fitting small and great circles to volcano distributions to determine true shape of arc-segments. For volcanoes in great circle alignment (**A**) the residuals to a great circle (ΔGC) yield a linear regression with $y \approx 0$ when plotted against distance along the segment (**B**), whereas the residuals for the best fit small circle (ΔSC) form a polynomial curve (**C**). The reverse is true for volcanoes distributed as a small circle (**D**) where ΔGC varies as a polynomial curve along the alignment (**E**), while ΔSC gives $y \approx 0$ (**F**).

Backarc faults were assigned to a particular arc-segment by projecting segment ends along the direction of backarc spreading (Kato et al., 2003).

2.4.2.2 Volcano Ellipticity

Nakamura (1977) proposed a method to approximate tectonic stress orientation from volcano morphologies by assuming that volcanos experiencing a uniform, horizontal stress regime would produce a radially symmetrical central conduit and dyke-swarm in the shallow crust (Muller & Pollard, 1977). Using the Nakamura & Uyeda (1980) principle, that the vertical stress (σ_v)around the volcanic arc always forms the intermediate principal stress (σ_2), the two-dimensional near-surface stress regime perpendicular to the trench can be determined for any deviation from the ideal symmetrical arrangement towards an elliptical form. For a two-dimensional cross-section perpendicular to the trench, trench-perpendicular compression would produce a maximum horizontal stress (σ_{Hmax}) parallel to the section. This, in turn, would produce volcanoes that are elongated perpendicular to the trend of the arc (**Figure 2.3A** and **B**). Conversely, trench-perpendicular tensional stress would lead to a minimum horizontal stress (σ_{Hmin}) perpendicular to the trench and cause volcanoes to be elongated parallel to the arc (**Figure 2.3C** and **D**).

As proxies of elongation of the magmatic systems, Mariana Arc volcano ellipticity was determined for craters (Marliyani, 2016) or, in their absence, the footprint of the edifice (Tibaldi, 1995; Bonini, 2012). For some edifices the proximity of other volcanoes obscures the edifice shape; in which case those volcanoes are not included in this analysis. Ellipticity was quantified by determining the azimuth and length of the longest and shortest axes, which are considered to approximate the orientation of horizontal maximum and minimum stresses (σ_{Hmax} and σ_{Hmin}), respectively. Examples of volcano ellipticity observations are presented in the **Appendix E**.

2.4.3 Model Evaluation

2.4.3.1 Earthquake Focal Mechanisms

Apperson (1991) employed earthquake focal mechanisms at shallow and intermediate depths in subduction zones to determine the seismic strain field of overriding plates. We

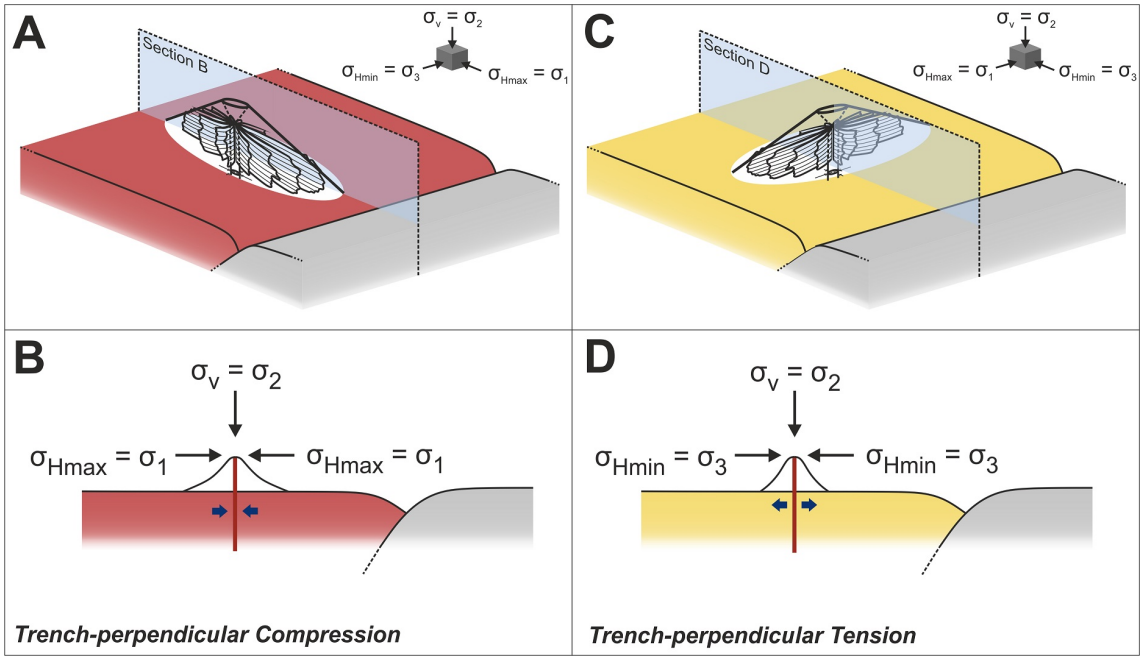

Figure 2.3. Estimation of shallow crustal stresses from volcano ellipticity (Nakamura & Uyeda, 1980; Marliyani, 2016). Vertical stress acts as the intermediate principal stress in the volcanic arc ($\sigma_v = \sigma_2$), implying that the minimum and maximum principal stress are horizontal ($\sigma_{Hmax} = \sigma_1$ and $\sigma_{Hmin} = \sigma_3$). (**A** and **B**) Compression perpendicular to the trench produces maximum horizontal stress normal to arc trend which is also the direction in which volcanoes are elongated. (**C** and **D**) Tension perpendicular to the trench leads to maximum horizontal stress that is parallel to the arc and volcanoes that are elongated along the trend of the arc.

applied the same method to focal mechanisms of earthquakes $Mw \geq 5.5$ from the Global CMT catalogue database (Dziewonski et al., 1981; Ekström et al., 2012) to evaluate the stress regime in the overriding plate. The analysis was carried out by projecting the individual focal mechanisms onto cross-sections located at the centre of each of the segments identified using the Hough Transform approach. Moment tensors were gathered in a swathe width equal to the corresponding linear segment. We focussed on depths from 0 to 30 km where the relevant focal mechanisms appear.

2.4.3.2 Southern Mariana

To further constrain the stress regime in the overriding plate we studied the seafloor structures of the non-volcanic, southwest continuation of the Mariana margin (Martinez et al., 2018). We extended the lineament map to the SSW of Tracey seamount into a part of the subduction system from 140°E to 146°E and from 11°N to 13°N that is referred to here as the Southern Mariana (Lim et al., 2013).

2.5 Results

2.5.1 Geometric Fitting

2.5.1.1 Small Circles

The best fit small circle for GVP04 has an rms-misfit of 2.5 km, essentially identical to the 2 km value reported by England et al. (2004). Dataset GVP04+SM, which shares geographical boundaries with GVP+04 but includes submarine volcanoes, yielded a small circle with a higher misfit of 3.9 km. Dataset B08, with geographical boundaries incorporating the whole Mariana Arc, gave the highest misfit of 8.4 km (**Table 2.1**). Thus, the effect of including all the edifices of dataset B08 is a small circle with significantly larger misfit to the Mariana Arc than previously recognised.

2.5.1.2 Great Circles

The Hough Transform method generated 12 potential great circle alignments within the Mariana Arc (**Figure 2.4A**). These were optimised and combined, as discussed in the

Table 2.1. Small circle properties and fitting results for each dataset

Dataset	**nV**	**Mrms** (km)	**Radius** (km)	**Centre Latitude** (°N)	**Centre Longitude** (°E)
GVP04	12	2.5	655.0	17.391	139.655
GVP04+SM	21	3.9	683.3	17.302	139.390
B08	37	8.4	688.7	17.333	139.305

Explanation: nV = number of volcanoes, Mrms = root-mean-square misfit

Methods section, to produce a refined pattern of five, best-fit, great circle segments (**Table 2.2** and **Figure 2.4B**): north segment (rms-misfit = 2.9 km), mid-north segment (rms-misfit = 3.2 km), central segment (rms-misfit = 2.7 km), mid-south segment (rms-misfit = 2.9 km), and south segment (rms-misfit = 0.7 km). The combined misfit values for all segments are 3.3 km before optimisation, and 2.7 km after optimisation.

2.5.1.3 Comparing Small and Great Circles

Once segments were identified from great circle fitting, their best-fit small circles were also found. Comparison of the great and small circles for each segment with the corrected Akaike Information Criterion (AICc) shows that segmented great circles are consistently better fitted to the arc than segmented small circles (**Table 2.2**). Treating the arc as a whole (**Appendix D**) the AICc value for a series of great circle segments is 60.6, which is lower, and statistically preferable, to the AICc value for a series of small circle segments (89.9). Although we prefer a different method to compare the segmented great circle model with a single small circle (next paragraph) the AICc also returns a more favourable value for segmented great circles than for a single small circle (75.2). Therefore, despite the differences in the degrees of freedom the Mariana Arc is better approximated as segments of great circles than segments of small circles.

Comparison of residual plots for fits to small circle (ΔSC) and great circle (ΔGC) datums also show indicate that a segmented great circle model is preferable to either a single or segmented small circle model (**Figure 2.5**). Residuals to the best fit, whole arc small circle for each dataset do not show systematic variation for the whole arc (**Figure 2.5A**). However, for shorter distance along the B08 dataset the small circle residuals show poly-

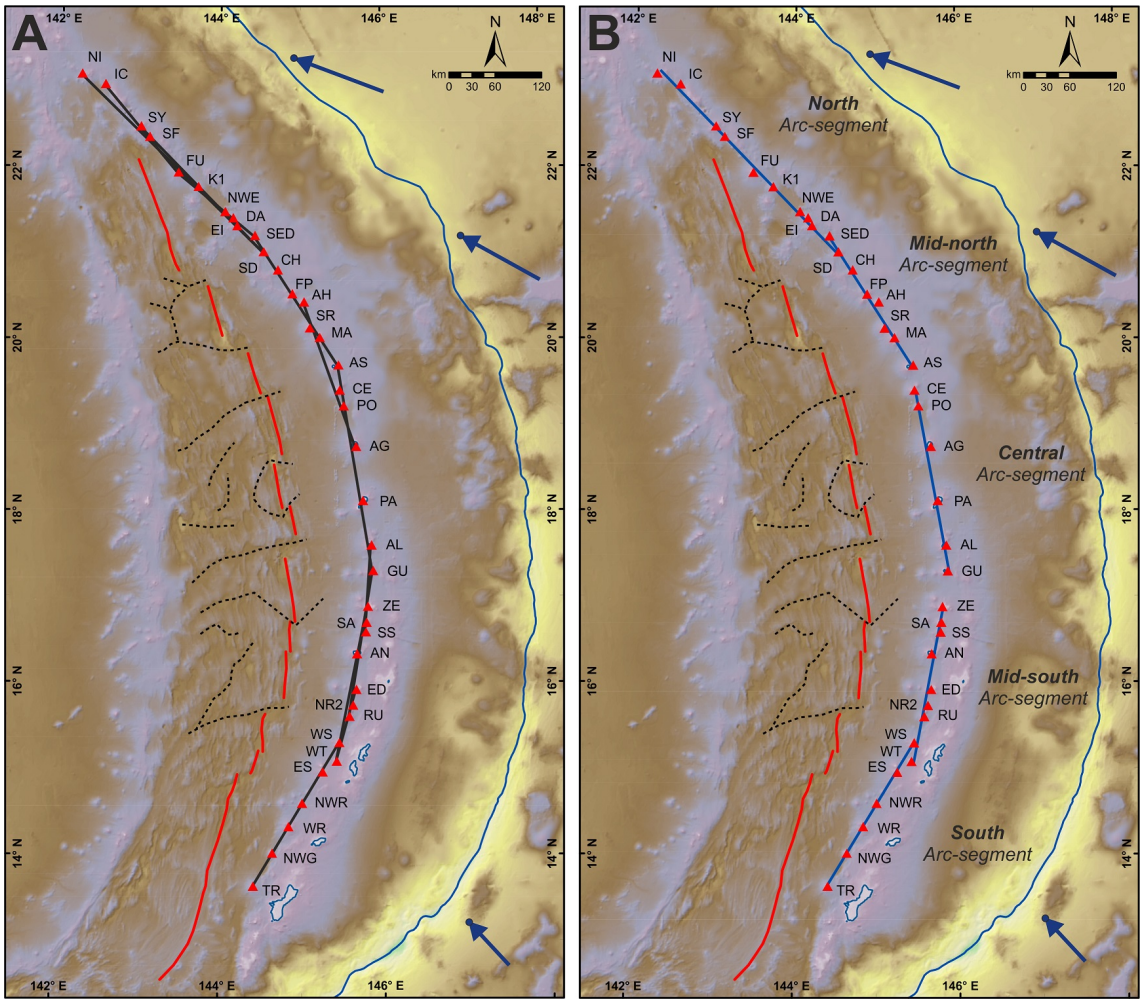

Figure 2.4. Segmentation of Mariana Arc identified using the Hough Transform method; (**A**) Black lines show 12 potential alignments identified using our Hough Transform approach. (**B**) Best-fit segment combination consists of five segments (blue lines) along the arc: north [10 volcanoes], mid-north [7], central [6], mid-south [8] and south [6]. Maps use gnomonic projection upon which great circles appear as straight lines. Blue arrows show motion of the Pacific Plate relative to the Philippine Sea Plate (Argus et al., 2011).

nomial deviation. This is most evident in the south from Tracey (TR) to West Saipan (WS), and the north, from Nikko (NI) to South Daikoku (SD). Inflections or reversals in the residual variation occur close to the ends of segment identified using the Hough Transform. **Figure 2.5C** displays ΔSC residuals for the five segments identified using the Hough Transform method relative to the best fit, whole arc small circle. The residuals vary systematically along the length of each segment as anticipated for a distribution of volcanoes as a great circle. None of the residual plots in **Figure 2.5C** yield ΔSC distributions that can be better described as a straight line than a polynomial curve. This is corroborated by using a great circle datum for each segment which produces straight lines that closely approach $y = 0$ (**Figure 2.5B**). This approach also replicates the result of the AICc approach by suggesting that Mariana Arc volcanoes are not arranged as multiple segments each constituting a different small circle (**Figure 2.5D**).

The analyses of distributions in this section lead us to reject the hypotheses that Mariana Arc volcanoes are distributed either as a single small circle arc or as segments made up of multiple small circles. In view of these observations, the simplest conclusion is that Mariana Arc volcanoes are distributed along five, great circle segments, which we shall refer to as arc-segments. Not only is this most consistent with the Mariana Arc data, it is also most consistent with the Java arc system where a similar quantitative approach has been applied (Pacey et al., 2013), and to less quantitative analysis of multiple arcs worldwide (Marsh, 1979; Ranneft, 1979).

Table 2.2. Mariana arc-segments, with volcanoes, properties and fitting results, for both great and small circles.

Segments	**North**	**Mid-north**	**Central**	**Mid-south**	**South**
Volcanoes	Nikko	SE Daikoku	Cheref	Zealandia	W Saipan
	Ichiyo	Chamoro	Poyo	Sarigan	Esmeralda
	Syoyo	Farallone de Pajaros	Agrigan	S Sarigan	NW Rota #3
	S Fukuyama	Ahyi	Pagan	Anatahan	W Rota
	Fukujin	Supply Reef	Alamagan	E Diamante	NW Guam
	Kasuga #1	Maug	Guguan	N Ruby 2	Tracey
	NW Eifuku	Asuncion		Ruby	
	Eifuku			W Tinian	
	Daikoku				
	S Daikoku				
n Volcano	10	7	6	8	6
Segmented Great Circle Properties					
Misfit (km)	3.00	3.17	3.92	4.14	0.78
Opt. Misfit (km)	2.92	3.16	2.69	2.91	0.67
Distance (km)	322	199	270	204	216
XA (°E)	142.287	144.419	145.492	145.819	145.450
YA (°N)	23.124	21.210	19.413	16.880	15.298
XB (°E)	144.518	145.450	145.450	145.454	144.405
YB (°N)	21.016	19.698	17.305	15.076	13.635
Azimuth	316	327	350	12	31
Segmented Small Circle Properties					
Misfit (km)	3.79	3.89	2.12	2.71	3.16
Radius (km)	1066	721	662	613	853
Centre Latitude (°N)	28.569	16.916	17.221	16.989	18.339
Centre Longitude (°E)	151.154	139.222	139.612	140.011	138.052
AICc at Each Arc-segment					
Small Circles	21.56	21.52	21.91	18.93	23.99
Great Circles	14.94	14.14	13.16	13.85	5.82

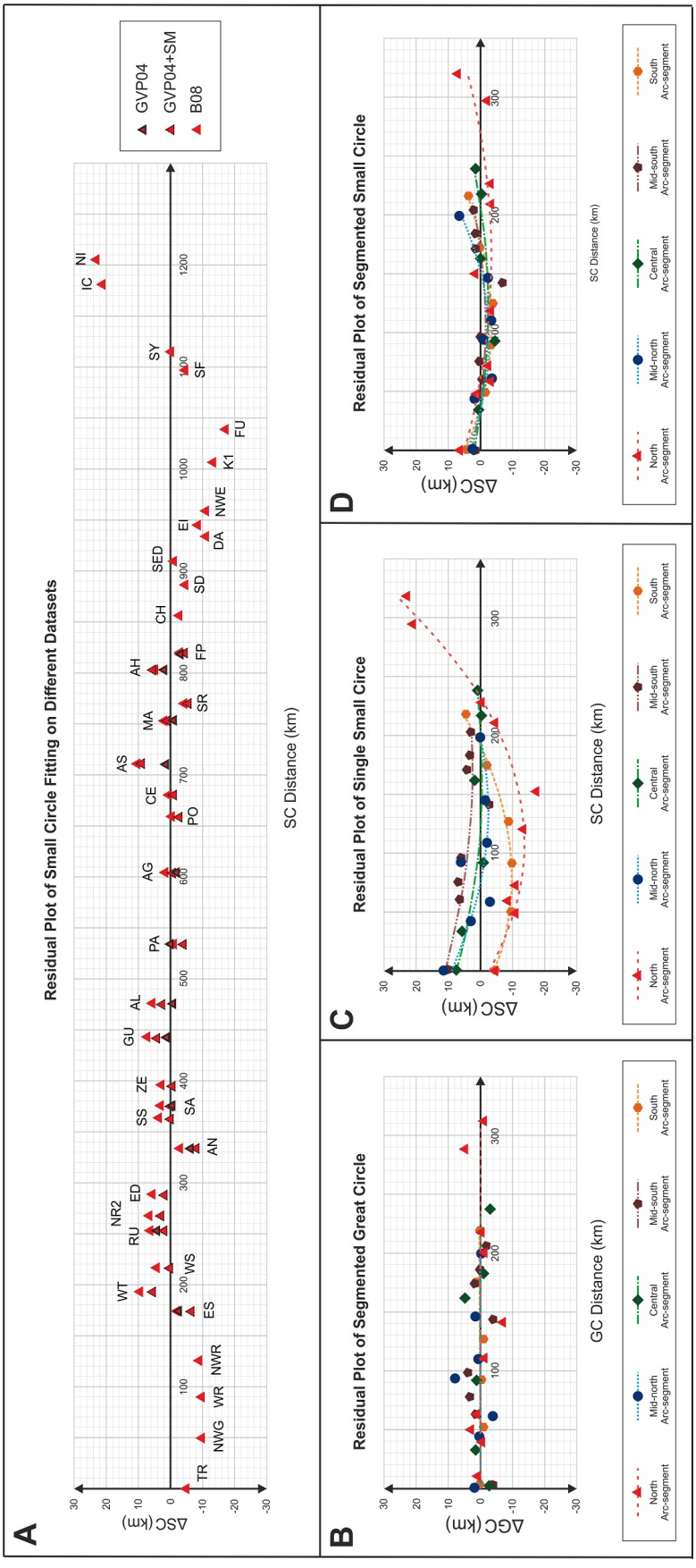

Figure 2.5. Residuals of small and great circle fitting plotted against distance along arc. (**A**) ΔSC of GVP04, GVP04+SM and B08 datasets against distance from Tracey (TR). Full abbreviation list in **Appendix B**. (**B**) ΔGC for Mariana Arc volcanoes from dataset B08 using the best fit great circle alignments as the datum (**Figure 2.2B**). All segments plot as lines approaching $y = 0$; (**C**) ΔSC for Mariana Arc volcanoes from dataset B08 using a single best fit small circle for the whole arc as the datum (**Figure 2.2C**; **Table 2.1**). (**D**) ΔSC for Mariana Arc volcanoes from dataset B08 using the best fit small circle to each segment as the datum. All of the ΔGC and ΔSC residual plots suggest that Mariana Arc volcanoes follow great circle alignment.

2.5.2 Surface Strain and Stress

2.5.2.1 Backarc Structures

Orientations of backarc faults associated with each arc-segment (**Figure 2.6A**) were compared to the backarc spreading direction, the segment azimuths, and the motion of the Pacific Plate relative to Philippine Sea Plate. Rose diagrams show that fault orientations are perpendicular to the backarc spreading direction (**Figure 2.7**). This is consistent with the interpretation of Oakley et al. (2009) that the faults are associated with spreading. The arc-segment azimuths are sub-parallel to the fault orientations. In the northern segment the azimuths are slightly counter clockwise of the faults and this offset gradually shifts to clockwise towards the south, but the deviation never exceeds 10°. In contrast, the subduction direction of the Pacific Plate does not show any systematic relationship to arc-segment azimuths.

2.5.2.2 Volcano Ellipticity

There are significant differences in the relationship between arc-segment azimuth and volcano ellipticity in the northern and southern segments (**Figure 2.6B** and **2.7**). Volcano ellipticities in the north arc-segment are elongated between N0°E and N80°E, the majority being strongly oblique to the segment azimuth (N316°E), the backarc faults, the convergence direction, and the trench. Similar, but stronger, relationships occur in the mid-north segment as the volcanoes are elongated between N40°E and N90°E while the segment trends towards N328°E. In contrast, the ellipticities of south arc-segment volcanoes are mostly elongated between N330°E and N20°E and, apart from West Saipan (WS), sub-parallel to the segment azimuth, which is oriented N31°E. Between these segments, the central and mid-south segments trend towards N350°E and N11°E, respectively. Volcano ellipticities in these two segments vary between perpendicular to and parallel to the segment orientations, ranging from N340°E to N70°E on the central segment and from N45°E to N150°E in the mid-south segment.

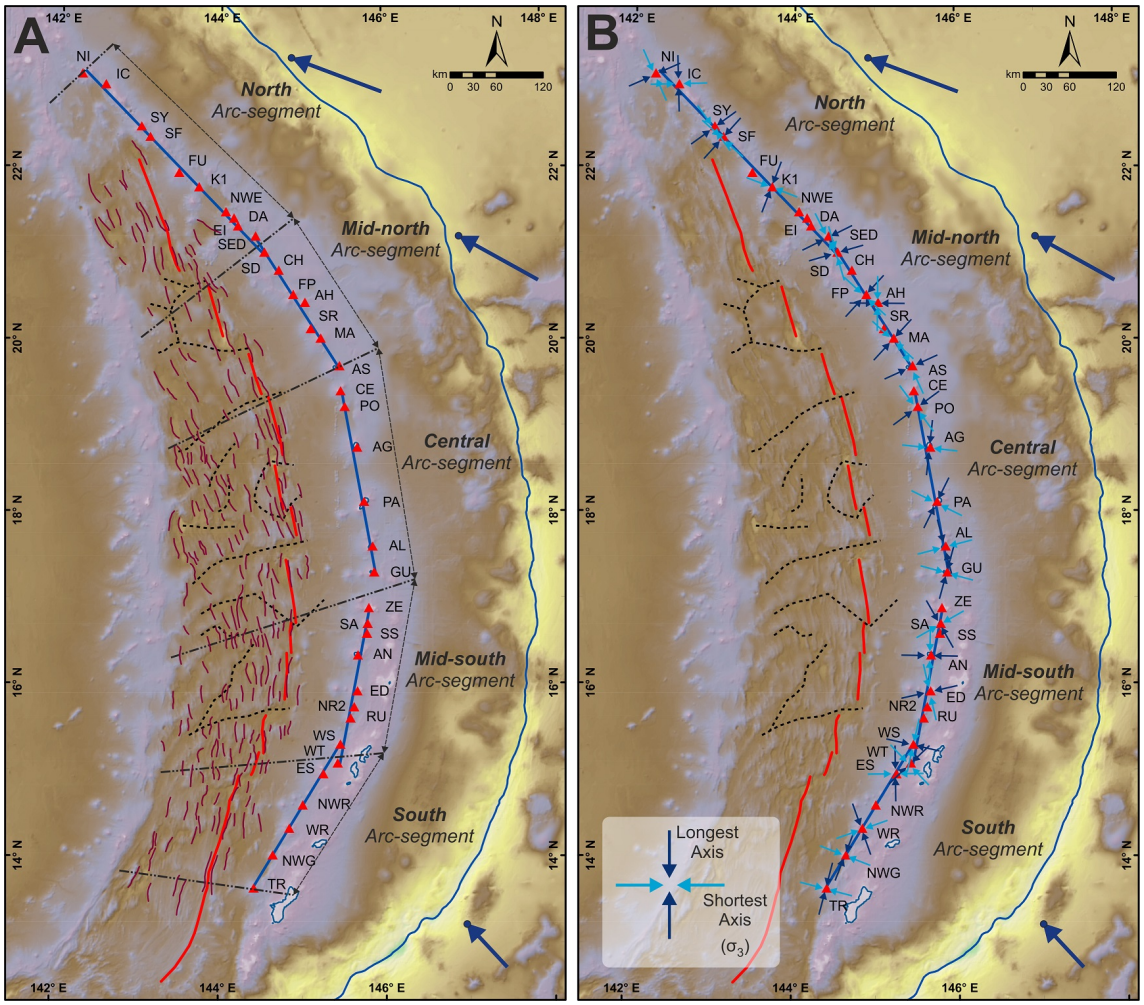

Figure 2.6. Surface strain distribution of Mariana presented in gnomonic projection. (**A**) Faults in the backarc (dark red) compared to the orientation of arc-segments (thick, blue lines). Dashed-dot lines are the boundaries used to attribute faults to particular arc-segments. (**B**) Volcano ellipticity showing long (dark blue) and short axis (light blue) directions. The latter is inferred to approximate the horizontal minimum principal stress (σ_3) direction.

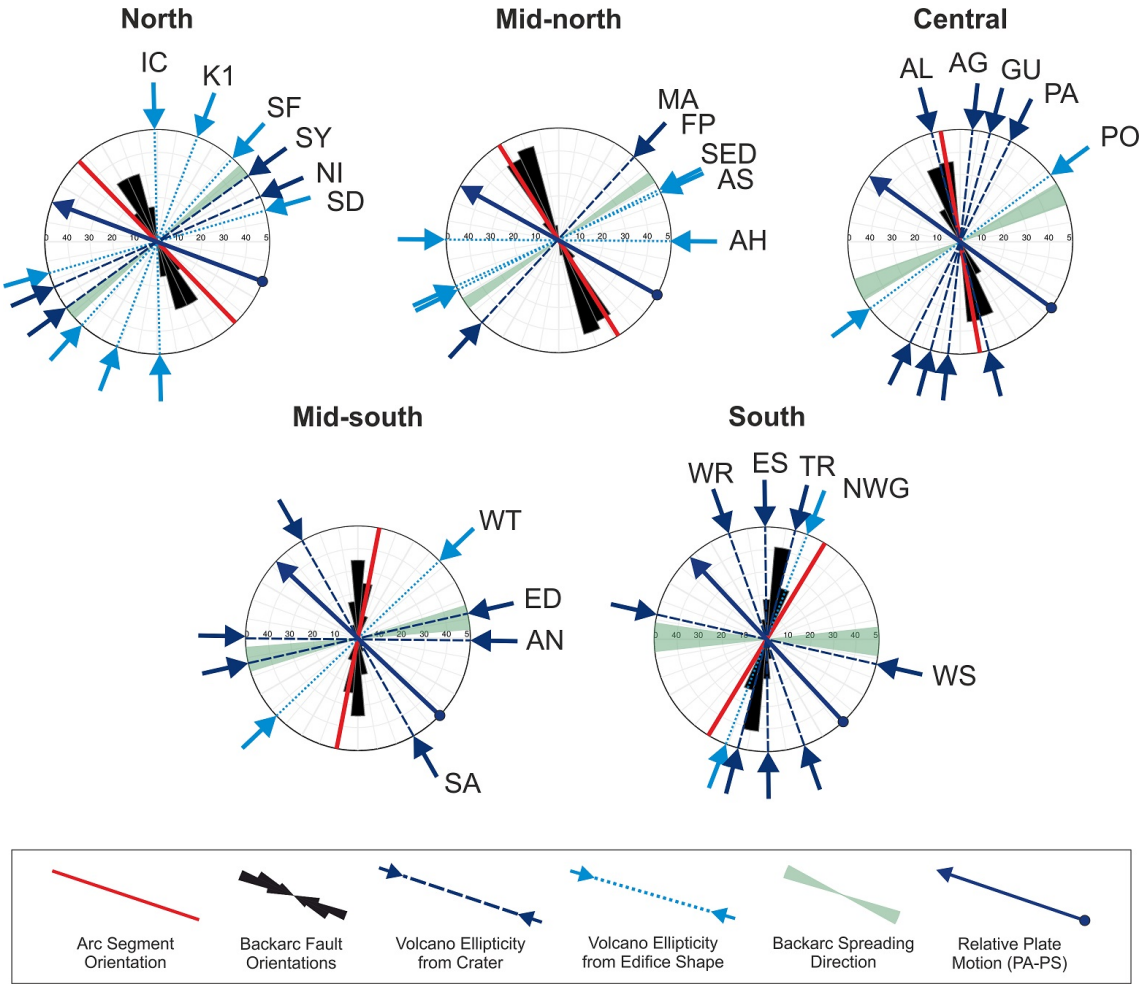

Figure 2.7. Rose diagram for each arc-segment comparing: arc-segment azimuth (red), backarc spreading direction (light green; Kato et al., 2003), long axis of volcano craters (dark blue) or edifices (light blue), backarc fault orientation (black), and relative plate motion of PA to PS plate (dark blue arrow; Argus et al., 2011). Initials are volcanoes where ellipticity was determined (abbreviations in **Appendix B**).

2.6 Discussion

A relationship between averaged depths of subducted slabs beneath volcanoes (H) and descent speeds of slabs in some arcs has been used to infer a geodynamic significance for H (England et al., 2004; Syracuse & Abers, 2006). But several arcs, including Scotia, Java, Bali, Nicaragua, the Lesser Antilles, and Vanuatu, do not fit the global trend while other individual arcs show large fluctuations in H over distances where neither descent speed nor slab dip can vary (Syracuse & Abers, 2006). For example, in the central Sunda arc values of H change by more than 100 km, over horizontal separations of less than 150 km (Pacey et al., 2013). We have shown that Mariana is another example of this variation, since H for active arc volcanoes, determined from the SLAB2 model (Hayes et al., 2018), ranges from 110 to 180 km across the arc. This entire range is apparent over short distances in the south, from Tracey to Esmerelda, where there can be no change in slab descent speed (**Figure 2.1** and **Figure 2.8**). Furthermore, L. T. White et al. (2019) have suggested that earthquakes in the mantle wedge behind the Mariana Arc may reflect significant transport of slab derived fluid across a much greater breadth of the subduction margin than a simple, vertical conduit directly beneath the volcanic arc. This conclusion is consistent with modelling of fluid flow within the mantle wedge (Wilson et al., 2014). Both these approaches further illustrate that caution should be applied in relating H to the processes that localise volcanic and magmatic centres in arcs.

Several early studies of arcs which proposed that volcanoes form "linear" - in fact great circle – segments attributed segmentation to processes in the mantle wedge or to structures and processes at the slab surface (Carr et al., 1973; Stoiber & Carr, 1973; Marsh, 1979), or were equivocal as to the causes of such distribution (e.g. Ranneft, 1979; J. M. Hughes et al., 1980). Pacey et al. (2013) documented great circle alignments of volcanoes in the central and eastern Sunda Arc but concluded that both the alignment and its segmentation into an *en-echelon* arrangement resulted from magma transport being focussed by the arc lithosphere. Close study of the Central American and Lesser Antilles systems has also demonstrated links between arc-segmentation and structural development in the upper plate (Burkart & Self, 1985; Feuillet et al., 2002; Morgan et al., 2008; Bolge et al., 2009).

We propose that the great circle segmentation of the Mariana Arc reflects focussing

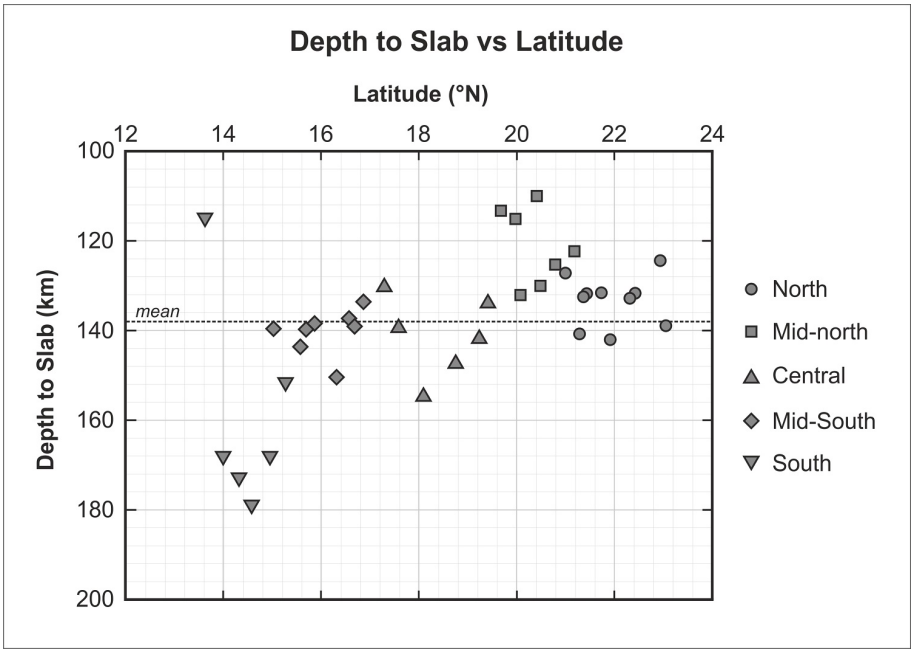

Figure 2.8. Depth to slab under the individual volcanoes on B08 dataset, extracted from SLAB2 model (Hayes et al., 2018)

of magma in the deep crust and/or lithospheric mantle of the upper plate, as has been suggested for the central Sunda Arc. Pacey et al. (2013) inferred that great circle segmentation in central Sunda occurred due to magma exploiting stress-related, upper plate weaknesses and identified three principal mechanisms that might contribute to this: arc-normal tension; oblique tectonics; or upper plate flexure. In the remainder of this section, we evaluate these and potential alternative mechanisms in the Mariana Arc.

Alignment of contemporaneous volcanic, magmatic, and tectonic features in ocean ridge and rift settings is widely accepted to reflect magma channelling by the plates through which magma is transported (e.g. Crane & Ballard, 1981; Searle, 1992; Mazzarini, 2007; Rooney et al., 2011). Tension in the arc lithosphere might result from rollback of the subducting slab (Macpherson & Hall, 1999, 2002) and links between extension and volcanic productivity have been recognised in many arcs (Smellie, 1995; Acocella & Funiciello, 2010). The similarity of Mariana's arc-segment orientations to tension indicators in the immediate backarc (**Figure 2.7**) provides another indication that arc-normal tensional stress in the upper plate contributes to alignment of arc volcanoes. While tension, alone, would be consistent with the similar sense of deep and shallow lithospheric strain that we have determined from volcano alignment and volcano morphology, respectively, in

the southern Mariana Arc, it cannot explain why the volcanoes of the north and mid-north segments have ellipticities consistent with arc-normal compression (**Figure 2.7**). Therefore, tension across the whole depth of the upper plate is unlikely to be the sole, or principal, cause of segmentation.

The influence of oblique convergence upon subduction magmatism may differ from arc to arc and both transtension or transpression can focus magma flow within convergent margins (Tikoff & Teyssier, 1992; K. J. W. McCaffrey, 1992; McNulty et al., 1998). Arc-parallel faulting has been inferred to focus volcanic centres in the Lesser Antilles (Feuillet et al., 2002) and Central America (Bolge et al., 2009). Unlike the case in central Sunda, however, the Mariana arc-segments do not show the consistent *en-echelon* stepovers, that led Pacey et al. (2013) to consider a role for oblique tectonics. Furthermore, the presence of arc segmentation is independent of changes in both the presence of strike-slip faulting in the Mariana forearc, and the overall convergence vector. Strike slip faults, oriented at about N314°E, cut the Mariana forearc north of 18°N where convergence becomes highly oblique (Stern & Smoot, 1998) but are absent further south (**Figure 2.1**), yet segmentation of the arc persists there. Indeed, the great circle segmentation persists along the entire length of the Mariana Arc as convergence varies from highly oblique in the north to entirely orthogonal at the latitude of the southernmost stratovolcanoes. Further south, convergence is again oblique but in a reversed sense, yet there is no strongly developed chain of arc volcanoes here (see below). Thus, we conclude that oblique convergence does not play a strong role in producing segmentation of volcanism in the Mariana Arc, although it may influence the extent of individual segments.

Downward flexure can produce compression in the shallow parts of a plate with simultaneous tension at greater depth (Hieronymus & Bercovici, 2000). Indeed, during the earliest days of plate tectonics arc-parallel tension at the base of arc lithosphere was considered as a dynamic response to flexure (Isacks et al., 1968). Husson (2006) modelled the development of negative dynamic topography in upper plates of subduction zones due to the presence of the dense, subjacent slab. In the Mariana margin this effect was predicted to produce maximum downward displacement of the Earth's surface in a broad, arc-parallel band between the Mariana Ridge and the backarc ridge axis (Husson, 2006), close to the location of the active arc. More generally, Hassani et al. (1997) demonstrated

the development of lithosphere flexure at convergent margins due to the downward force from the slab as the hydrostatic suction maintained the coupling surface between the slab and upper plate. Crameri et al. (2017) showed that vertical deflection of the upper plate due to downgoing slab could occur up to thousand kilometres from the trench, however the wavelength of the flexure would depend on the upper plate's resistance to deformation based on its thickness and rheology (e.g Meyer & Schellart, 2013; Sharples et al., 2014). In any case, horizontal tension at the base of upper plate would still occur regardless of the flexure wavelength as long as the coupling surface maintained the plate-to-plate contact and resistance (Hassani et al., 1997). In older arcs, flexure of the upper plate may be augmented by the load imposed by the arc but this is unlikely to be a major effect in younger arcs such as Mariana (Waltham et al., 2008). In addition, Bonnardot et al. (2008) also predicted the possible contribution from mantle corner flow in enhancing the arc-normal tension at the base of flexed upper plate. Thus, they key feature to induce downward flexure of the upper plate is the operation of subduction and, therefore, we consider this to be the most viable mechanism for producing arc-normal tension in the deeper parts of the upper plate along the length of the margin.

Other processes that may generate upper plate stress can also be evaluated at the Mariana margin. Lateral forces due to topographic or tectonic features may contribute to upper plate stress. For example, the topographic high of the Mariana Ridge (Bloomer et al., 1989) may exert tensional stress due to higher vertical loading or gravitational effects (Artyushkov, 1973; P. Bird, 1991; Bada et al., 2001). However, the form of the Mariana Ridge changes substantially along its length from around 100 km wide near Tracey seamount in the south, where it emerges as the island of Guam, to approximately 20 km width near Guguan, north of which it is not evident (**Figure 2.1**; Stern & Smoot, 1998). The presence of arc-segmentation is not correlated with the presence or absence of the Mariana Ridge, or any other, topographic feature. Thus, we conclude that topographic effects have a negligible influence upon the development of segmentation in the Mariana Arc but are limited, perhaps, to the near surface stress regime.

To the west of the arc, backarc extension across a broad part of the Mariana Trough is suggested by the widespread distribution of normal faults (Fryer, 1995; Martìnez et al., 1995; Fryer, 1996). A small ridge push effect from the spreading centre, potentially close

to zero due to the subdued topography in the backarc, may contribute to stress on the arc, however, a tensional stress regime induced as a passive response to the far-field rollback is likely to be dominant (Macpherson & Hall, 2002; Deschamps & Fujiwara, 2003; Nakakuki & Mura, 2013). Nonetheless, Mariana shares a great circle segmentation pattern with other arcs that lack backarc basins, including Sunda and Central America (Marsh, 1979; Pacey et al., 2013), suggesting that backarc spreading it not a primary control upon the development of arc-segmentation.

Consideration of all the factors above leads us to infer that arc-segmentation results from arc-normal tension in the deeper parts of the arc lithosphere, which is produced by tension and/or flexure of the plate upon which the Mariana Arc is constructed. This contrasts with a more complex variation of stress in the shallow upper plate, as indicated by volcano ellipticity (**Figure 2.6** and **2.7**) and mapped out in **Figure 2.9** (Nakamura & Uyeda, 1980; Apperson, 1991; Oakley et al., 2009). In the north and mid-north arc-segments, volcanoes are generally elongated sub-normal to arc-segment azimuths (**Figure 2.7**), suggesting that horizontal maximum stress is perpendicular to the segments and that trench-perpendicular compression affects the shallow crust of the northern segment. While this is consistent with the general expectation of plate margin compression (**Figure 2.3**; Nakamura & Uyeda, 1980), it appears to contradict our interpretation of arc normal tension in the deep arc lithosphere. This contradiction would be resolved if the plate is flexing downward (Hassani et al., 1997; Hieronymus & Bercovici, 2001). In the south segment the volcano ellipticities suggest that horizontal maximum stress in the shallow arc crust is parallel to the arc-segments (**Figure 2.7**), conforming to the conclusion reached for the deep crust but contrasting with the expectations from Nakamura & Uyeda (1980). In the central and mid-south segments, the orientation of the major axis of ellipticity is more variable suggesting a transition between trench-perpendicular compression and trench-perpendicular tension in the shallow crust.

2.6.1 Vertical Strain Partitioning

The apparent contradiction of inferred deep and shallow stress regimes in the lithosphere of the north and mid-north, and to a lesser extent in the central and mid-south, segments can be resolved by considering a model of vertical stress partitioning in the overriding

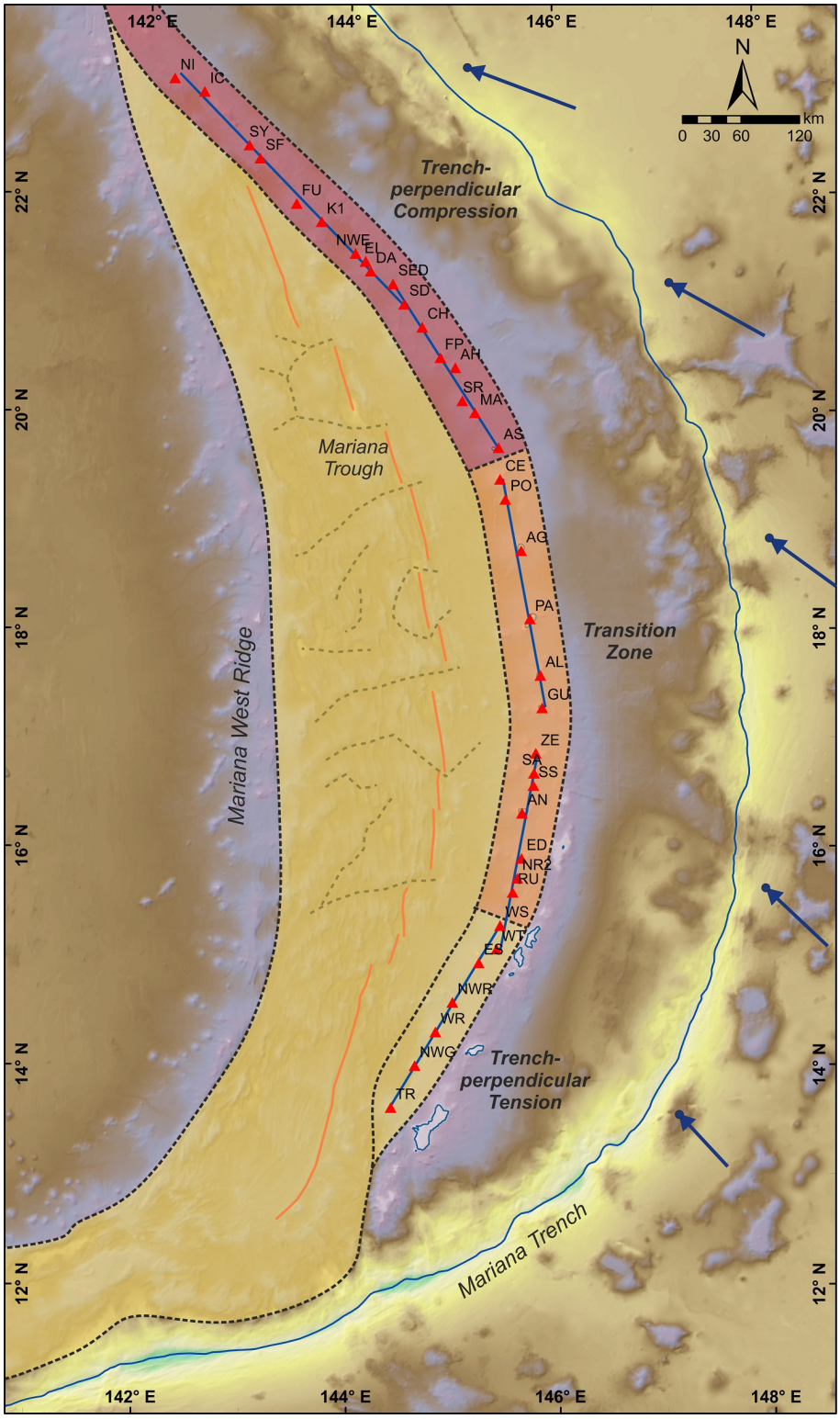

Figure 2.9. Trench-perpendicular stress regime in the shallow crust interpreted from volcano ellipticities, along with the backarc extension. Trench-perpendicular compression is marked by red shading, trench-perpendicular tension by yellow shading and transition zone by orange shading. Map is a gnomonic projection. Blue arrows show the PA-PS relative motion.

plate. The gradual increase in vertical stress (σ_v), due to lithostatic pressure and rheological stratification, is recognised as an important control upon stress geometry and can potentially cause different stress regimes in the shallow and deep crust (McGarr & Gay, 1978; Hasegawa et al., 1985; Ranalli & Murphy, 1987; Petrini & Podladchikov, 2000). This increase in vertical stress means that the stress orientations approximated from volcano ellipticity should strictly be applied to the shallow lithosphere only and may not be the same as those in the deeper crust. In the shallow crust of an active arc, vertical stress acts as the intermediate principal stress ($\sigma_v = \sigma_2$). However increasing vertical stress, due to lithostatic stress, in the deeper crust might modify the principal stress geometry such that the vertical stress becomes the maximum principal stress ($\sigma_v = \sigma_1$). Brace & Kohlstedt (1980) explained the mechanism of stress regime changes at depth using the limit of lithospheric strength, which is defined as the maximum difference between horizontal stress and vertical stress ($\sigma_H - \sigma_v$). With a thermal gradient of 15°C/km, in a crustal column with hydrostatic pore pressure, $\sigma_H - \sigma_v$ would reach a maximum value at about 15 km for a quartz rheology or 30 km for an olivine rheology, with shallower depths predicted for their dry equivalents. At deeper levels $\sigma_H - \sigma_v$ would decrease gradually towards zero stress at 25 km for the quartz rheology and 50 km for olivine. This change with depth provides a mechanism that could produce different stress regimes at different depths, even in the absence of forces external to the crustal volume. Therefore, it seems possible there is a mechanism that allows vertical partitioning of the stress regime in the upper plate, as most evident in the northern segments of the Mariana Arc. Furthermore, the relationships between shallow and deep stress appears to vary along the arc; they are aligned in the south but contradictory in the north. Thus, the stress regime must also be responding to changes along the length of the plate margin.

To further investigate vertical and horizontal stress partitioning in the Mariana margin we investigated how the contrasting stress patterns vary with respect to along-arc changes in subduction dynamic parameters. The dip (δ) of the Pacific Plate beneath the Mariana Arc varies from south to north. Earthquake data show that the general dip of the subducting plate is less steep in the south (Syracuse & Abers, 2006) but at depths less than 125 km the slab dip (δ_{sh}) is actually steeper in the south (Fukao et al., 2001; Lallemand et al., 2005). In assessing plate coupling between the two plates, Gvirtzman & Stern (2004)

focussed on the shallow slab dip because this covers, and extends beyond, the depth range within which the Philippine Plate and Pacific Plate are in contact. The average crustal thickness within the volcanic arc ranges from 14.5 to 20 km (Zellmer, 2008; G. R. Hughes & Mahood, 2011) and the average plate thickness is about 50 km (Gvirtzman & Stern, 2004). Therefore, δ_{sh} is likely to be a more important influence than δ upon the stress regime of the overriding plate compared.

Gvirtzman & Stern (2004) estimated the extent of plate-to-plate coupling in the Mariana margin by measuring the horizontal, perpendicular distance from the trench to Mariana Ridge. The breadth of this plate-to-plate coupling zone is about 170 km in the vicinity of our central arc-segment and narrows southward to 100km where we identify the south arc-segment. Applying the Gvirtzman & Stern (2004) treatment to the margin at our north arc-segment suggests a coupling distance of up to 190 km. Assuming the thickness of the forearc is constant along the length of the arc and that coupling distances are defined in the horizontal plane, then the contact surface between the plates is approximated by the coupling distance divided by the cosine of the slab dip. Using these assumptions suggests that the contact surface between the plates would be wider in the north and narrower in the south.

Descent of the slab produces frictional resistance along the contact with the overriding plate. The down-going slab movement itself is induced by a slab pull force (F_{sp}; Carlson et al., 1983). Gvirtzman & Stern (2004) proposed that the frictional resistance between the two plates and the downward movement of the subducting slab act to pull-down the overriding plate. Since variations in this pull-down force (F_{pd}) are likely to be generated by changes in the surface resistance between the two plates, then F_{pd} would be proportional to the breadth of the contact surface. Therefore, F_{pd} would be stronger in the Mariana north arc-segment and weaker in the south arc-segment.

Variation of δ_{sh} from north to south could also contribute further to modify the stress regime variation in the Mariana Arc. As the subducting slab descends below the overriding plate, a horizontal slab push (F_{up}) force is exerted upon the upper plate (Heuret & Lallemand, 2005). Since velocity and force are proportional, F_{up} will be proportional to the subducting velocity of the down-going slab (v_{slab}) and the cosine of the shallow slab dip. Assuming that v_{slab}, normal to the trench, does not vary significantly along

the length of the arc, F_{up} would be controlled by δ_{sh} and, so, the shallow slab dip in the north would generate stronger F_{up} than the steeper dip in the south. Therefore, stronger compression would be exerted in the northern arc than towards the south.

Variation in the pull-down force may contribute to stronger upper plate flexure in the north compared to the south. In the north, vertical stress partitioning is most distinct where it may be enhanced by the strong compression from F_{up}. Meanwhile, in the south, vertical stress partitioning is less obvious as the segment experiences stronger trench-perpendicular tension due to the seaward trench rollback and weaker F_{up}. However, tension of deeper arc lithosphere occurs in all segments and is responsible for generating magma pathways in the deep crust of the Mariana Arc, which are manifest as arc-segments.

Three-dimensional mechanical modelling of the strain mechanisms proposed above is beyond the scope of this study, but we can make a very simplified estimate of the possible magnitude of the operating stresses by assuming that the thickness of the upper plate (z) is a constant 50 km along the margin, comprising 20 km crust and 30 km lithospheric mantle (Gvirtzman & Stern, 2004). Then, the average shear stress (τ) operating along the plate interface is estimated as the product of the friction coefficient (μ), gravitational acceleration (g), density (ρ), and upper plate thickness ($\tau = \mu.g.\rho.z$). For this purpose, we assumed a typical friction coefficients (μ) for plate-to-plate coupling of 0.032 ± 0.006 for crust with a density of $2800\,\mathrm{kg/m^3}$, and 0.019 ± 0.004 for lithospheric mantle with density of $3300\,\mathrm{kg/m^3}$ (Lamb, 2006). This results in an estimated shear stress along the plate interface of approximately 36 MPa. Although this is towards the upper end of estimates made for other subduction zones (e.g. Lamb, 2006; Duarte et al., 2015; Holt et al., 2015) it is not unreasonable in view of the limited constraints on real friction coefficients and on the thickness of lithosphere and crust. As the shear operates along the coupling surface, the horizontal and vertical stresses can be estimated as vector components of the mean value. The horizontal stress component, associated with F_{up}, is the product of $\tau \times \cos\delta_{sh}$. Therefore, based on variation of δ_{sh} along the margin, the horizontal stress is estimated to be about 29 MPa in the north and 25 MPa in the south. This is a small variation but one that is consistent with the changing forces we have proposed along the plate margin. The non-lithostatic component of vertical stress, arising from F_{pd}, is $\tau \times \sin\delta_{sh}$ leading to estimates of 21 MPa in the north and 25 MPa in the south. This decreases in vertical

stress from north to south contrasts with the suggestion above but is, again, small and would be eliminated or even reversed if, for example, the arc lithosphere in the south were slightly thinner than and/or had proportionately more crust than lithosphere in the north. In general, basal traction exerted upon the lithosphere by the asthenosphere is thought to affect plates at a regional rather than at a local scale (Naliboff et al., 2009), therefore we do not expect plate scale forces of the sort described by Forte et al. (2010) and Ghosh et al. (2013) to be relevant to subduction zones. However, the more intensely focussed flow of mantle generated by a subducting slab does have the potential to induce stress in the overriding plate (Hassani et al., 1997; Bonnardot et al., 2008). Quantification of such stress is highly dependent upon assumptions about the rheological properties of the two plates and the mantle wedge, but estimates are of comparable magnitude to those we have determined for the shear stress at the plate interface (Bonnardot et al., 2008).

Figure 2.10 is a schematic illustration of how we interpret the stress regime of the overriding plate responds to changing dynamic parameters in the Mariana subduction system. The overall distribution of stress is similar to that envisaged due to plate flexure (Hieronymus & Bercovici, 2000). In the northern part of the arc the near-surface crust is dominated by trench-perpendicular compression that must give way to tension downwards and to extension towards the backarc (**Figure 2.10A**). We envisage this being accommodated in a transition zone, which may have an intermediate stress state or may be composed of smaller domains of contrasting stress. In the southern arc (**Figure 2.10C**) the trench-normal tensional regime is expressed as spreading in the backarc and tensional magma transport throughout most depths beneath the arc. The Mariana Ridge may represent compression of the upper plate with some component of bending at these latitudes, and there may also be some compression in the very shallow depths due to a volcano loading effect (Waltham et al., 2008). In the central parts of the arc the transition between tension and compression extends closer to the surface than in the north (**Figure 2.10B**). Like the north, the deeper crust beneath the central arc is under tension with the exact form of the volcano depending on the balance of tension and compression over the shallow depth range, where a loading effect may also come into play (**Figure 2.10B**). This geometry maintains a tensional regime at depth under all parts of the active arc allowing magma to ascend into the arc lithosphere where decreasing pressure and/or differentiation

may aid further buoyant rise towards the surface regardless of the stress in the shallower crust.

2.6.2 Model Evaluation

Two independent sets of observations can be used to test our interpretation of stress distribution in Mariana Arc lithosphere. The first uses earthquake focal mechanism as a direct measure of strain in the arc. The second uses the structures present in the southward, non-volcanic continuation of the upper plate to explore the stresses that might be generated by subduction.

2.6.2.1 Earthquake Focal Mechanisms

Figure 2.12 shows trench-perpendicular cross-sections for each of the five arc-segments. Focal mechanisms of individual earthquakes are plotted on the sections, together with elevation profiles and our interpretation of stress regime boundaries from **Figure 2.10**. **Figure 2.12C** also shows the Moho profile of the central Mariana Arc from Takahashi et al. (2007). The location of these cross-sections on the map view is in the **Figure 2.11**.

Most available focal mechanisms are concentrated at shallow and intermediate depths, from 10-22 km. In the north and mid-north segments, compressional focal mechanisms are located in the forearc and extensional focal mechanisms occur in the backarc. Compressional mechanisms also occur near the trench, showing compressional stress fields both at the toe of the overriding plate and in the slab. In the south segment, extensional mechanisms are distributed widely from the backarc to the forearc and compressional mechanisms are concentrated at the tip of the overriding plate. Between forearc and backarc compressional and extensional focal mechanisms are co-located in the south segment and the arc lies within such a zone at the surface of the central and mid-south segments.

Seismic events are rare in the deep crust/shallow mantle zone beneath arcs. However, extensional events have been recorded at about 10 to 20 km depth beneath the north and mid-north arc-segments (**Figure 2.12A** and **B**). In our model, this coincides with the deep expression of the great circle alignments which define the arc-segments that we infer to be the main supply routes for arc magma. Of the remaining events beneath the arc, most have an oblique sense but often with a strong normal component (**Figure 2.12C** and

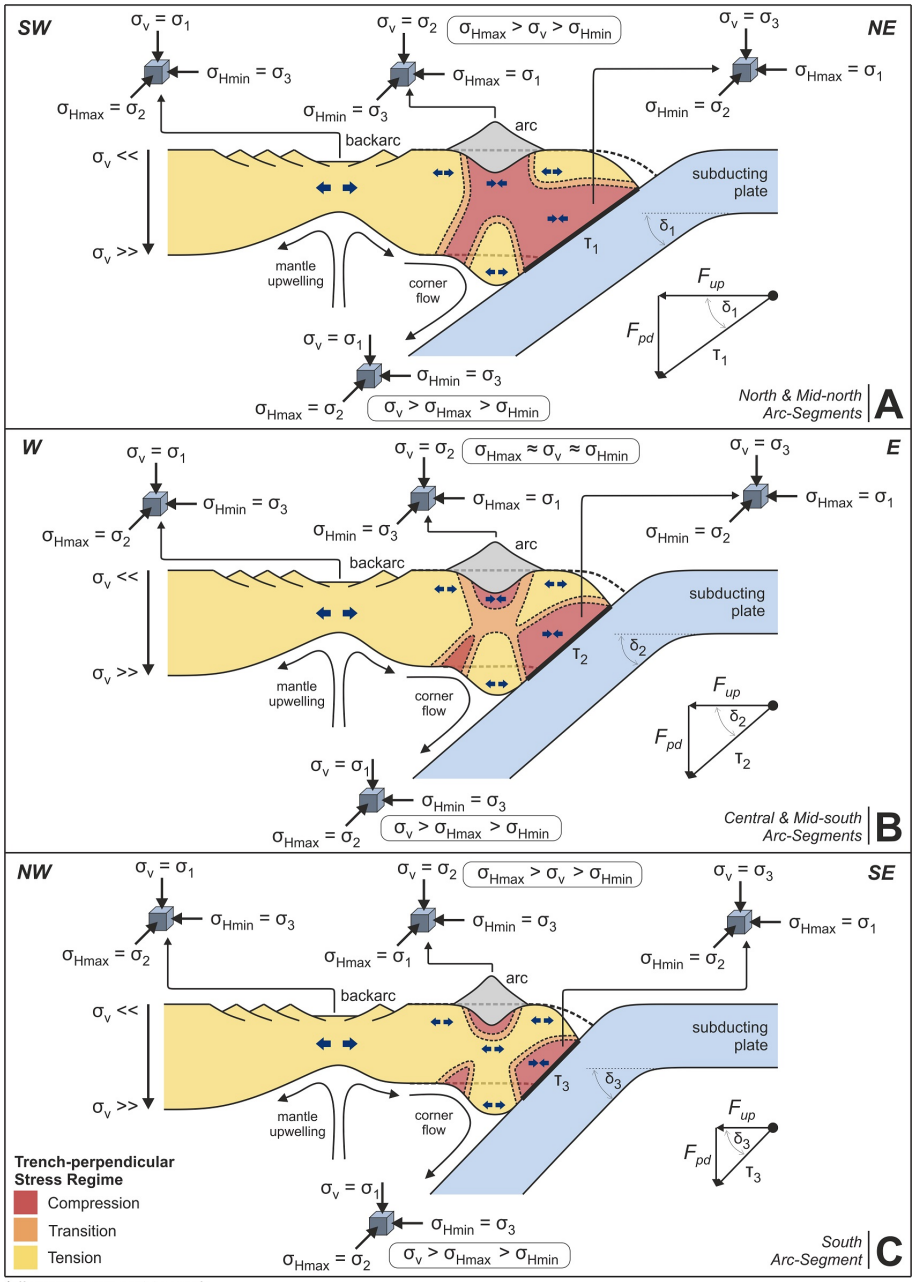

Figure 2.10. Schematic illustration of the stress regime in the (**A**) north and mid-north segments, (**B**) central and mid-south segments, and (**C**) south segment of the Mariana Arc, showing volumes dominated by trench-perpendicular compression (red), trench-perpendicular tension (yellow), and the transition zone between these (orange). The pull-down force (F_{pd}) on the overriding plate is controlled by plate coupling and shallow slab dip (δ_{sh}) where slab dip in the north is shallower than in the south ($\delta_1 < \delta_2 < \delta_3$). Slab dip also controls the force to the upper plate (F_{up}) from the motion of the subducting slab. Plate flexure acts to cause tension in the deeper crust of the upper plate and focus magma flow into arc-segments. There may also be a trench-perpendicular compression effect from volcano loading. The transition between the trench-perpendicular compression and tension may exist as subdomains of each type of stress or a gradual transition from compression to tension with depth. Dashed lines at the arc and inner trench wall show the upper and lower surfaces of the arc lithosphere before, or with less extreme, application of the subduction related forces.

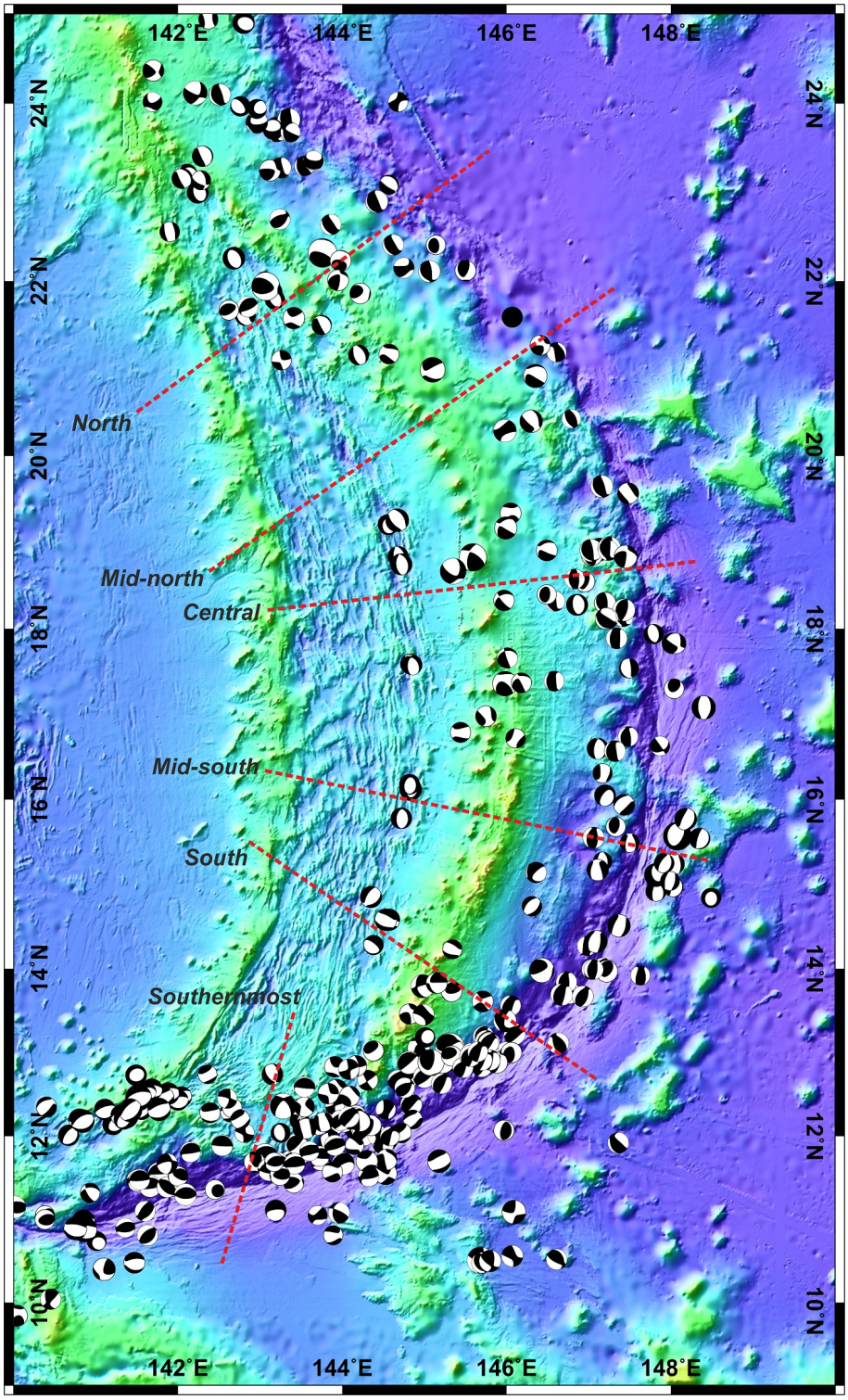

Figure 2.11. Earthquake focal mechanisms distribution in the Mariana (Ekström et al., 2012). Red dashed lines are the location of cross-sections on **Figure 2.12**. The map is generated using GMT package (Wessel & Smith, 1998).

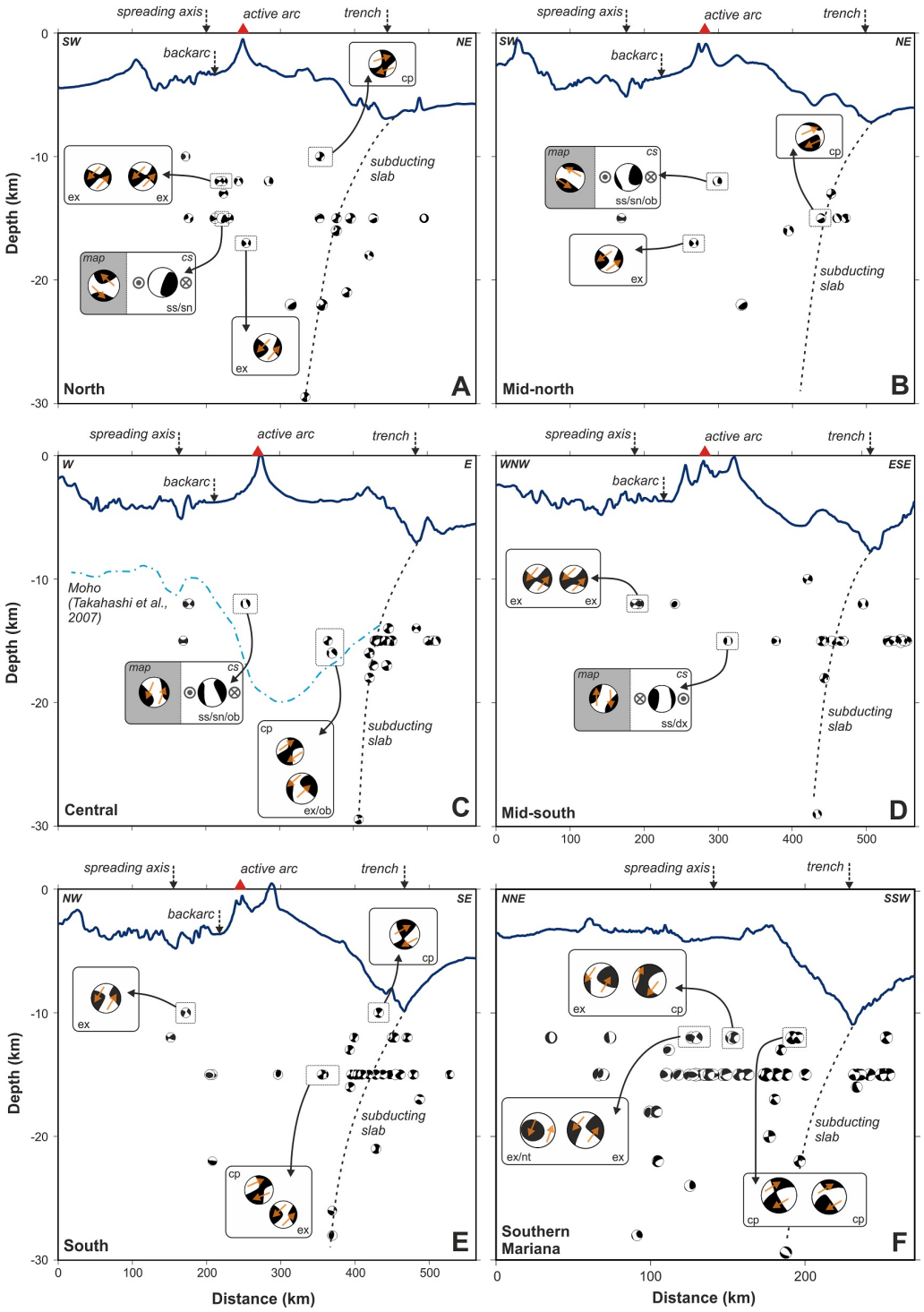

Figure 2.12. Individual earthquake focal mechanisms from the CMT catalogue (Dziewonski et al., 1981; Ekström et al., 2012) projected on cross-sections of each segment (adapted from Apperson (1991)) with bathymetric profiles. Moho depth details are only available in the central segment (Takahashi et al., 2007). Section were plotted with GMT software (Wessel & Smith, 1998). Orange arrows describe the interpreted relative motion on the fault plane. Inset with grey background on sections (**A**) to (**D**) show the focal mechanisms in map view (map) and cross-section (cs) to illustrate the strike-slip mechanisms. Abbreviations on insets describe the deformation type: ex – extension, cp – compression, ss – strike slip, sn – sinistral, dx – dextral, ob – oblique, nt – (strike) normal to trench.

D). The rarity of seismic events probably results from the rheology of the crust, its water content, and/or temperatures at that depth (Wortel, 1982; Meissner & Strehlau, 1982; Maggi et al., 2000), but could also be due to uncertainty in determining source locations of shallow to intermediate earthquakes (Ekström et al., 2012). In addition, dykes that intruding the deeper crust would be involve tensile failure and, so, probably be aseismic (Grandin et al., 2011). Despite the low number of observations, these focal mechanisms plots describe a strain pattern in the overriding plate that is consistent with our proposed model of stress regime fluctuation in the Mariana Arc lithosphere (**Figure 2.10**).

Combining our result with the findings of Apperson (1991) implies that our approach should reveal upper plate tension in other subduction zones. This is because Apperson (1991) concluded that sub-horizontal, arc-normal tension was the principal stress regime in the overriding plates of most subduction zones, including Mariana. If we are correct to infer that the segmentation pattern of the Mariana Arc is controlled by variation in forces generated by the plate margin, then we predict that segmentation of other volcanic arcs will reflect changes in the forces generated at each margin.

2.6.2.2 Southern Mariana

Lineament analysis of the Southern Mariana area reveals short wavelength features in the bathymetry that are interpreted as normal faults (red lines on **Figure 2.13**) produced by extension perpendicular to the lineament orientations. South of the West Mariana Ridge the principal lineaments are oriented NE-SW at 140°E and ENE-WSW at 141°E, which is generally parallel to the trench and indicates NNW-SSE directed extension (σ_3). There are also a few lineaments near the trench that are oriented NNE-SSW, cross-cutting the major lineaments. The main lineament orientation remains ENE-WSW near 142°E then deflects to NE-SW at about 143°E, which we infer means σ_3 in a NW-SE direction. The lineament orientation becomes parallel to the main NNE-SSW spreading axis near 144°E, consistent with σ_3 oriented WNW-ESE.

Our study is consistent with the findings of Martìnez et al. (2000) and Martinez et al. (2018) who showed that lineaments display contrasting orientation on either side of the spreading axis at its southern end. From the spreading axis to the West Mariana Ridge, as described above, most lineaments are parallel to spreading axis orientations

while from the spreading axis to the Mariana Ridge lineaments are normal to the spreading axis and the trench (oriented in ENE-WSW and ESE-WNW directions). Ishihara et al. (2001) recognised these shorter lineaments at about 144°E as showing minor extension in a NNE-SSW direction and GPS measurements also show a residual azimuth in N209°E direction near Guam (Kato et al., 2003). The trench-parallel lineaments formed during crustal accretion as a response to trench rollback in a southward direction such that these lineaments conform to the spreading direction and trench axis. Meanwhile, the trench-normal lineaments propagated to accommodate the increase of Mariana trench curvature (Martìnez et al., 2000; Martinez et al., 2018), and thus appear as secondary structures on the surface. These variations of lineament orientation are part of diffuse extension as a result of weakening of the upper plate due to extensive hydration from the slab during early development of the subduction zone (Martinez et al., 2018). The diffuse extension in the Southern Mariana area developed rapidly and restricted the development of large, central arc-type volcanoes south of Tracey seamount (Stern et al., 2013).

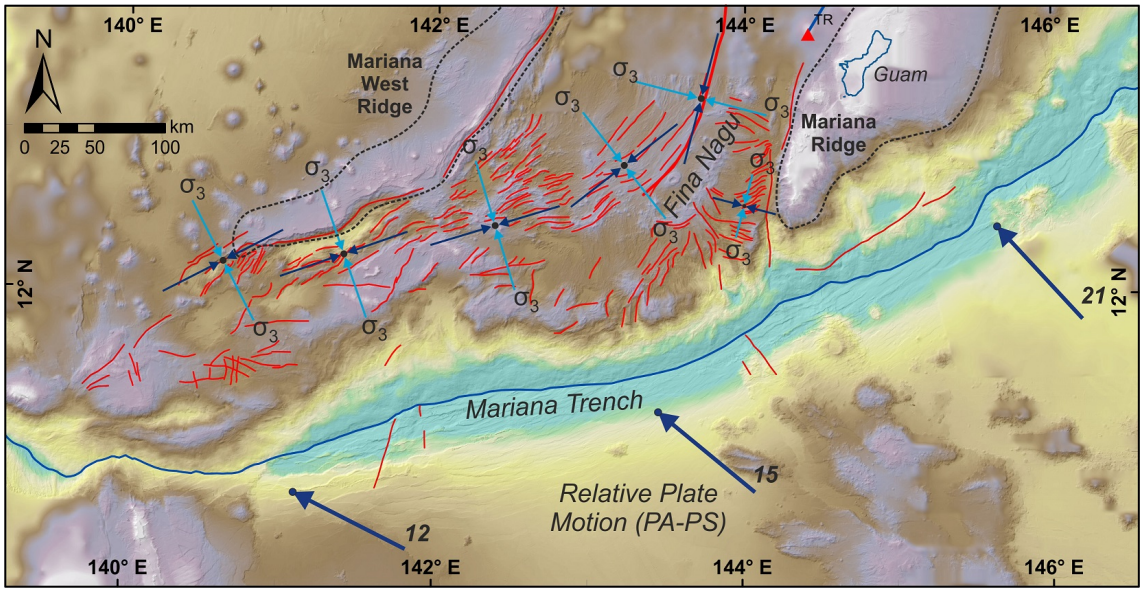

Figure 2.13. Lineament map of the Southern Mariana area to the southwest of Tracey seamount. Light blue arrows indicate the minimum horizontal stress (σ_{Hmin}) as the minimum principal stress (σ_3) direction identified from the mapped lineament while dark blue indicate the maximum horizontal stress (σ_{Hmax}) as the intermediate principal stress (σ_2) direction. Principal lineament orientations imply that extension occurs normal to the trench with secondary extension parallel to the trench to accommodate the strong curvature of the margin (Martinez et al., 2018).

Our lineament mapping in Southern Mariana (11°N-13°N) shows σ_3 mainly perpendicular to the trench, despite the relatively oblique convergence (**Figure 2.13**). This is

particularly evident between 140°N and 143.5°E consistent with our conclusion of trench-perpendicular tension in the adjacent (south) Mariana arc-segment (**Figure 2.7** and **2.9**). A strong tensional regime is also consistent with the deep crustal tension implied from the volcano alignment of the south arc-segment. Therefore, we infer that the trench-perpendicular tensional stress in the south arc-segment formed in a similar stress regime to structural lineaments of the Southern Mariana seafloor and was mainly caused by roll-back of the subducting Pacific Plate. Martinez et al. (2018) have suggested that the absence of discrete central arc volcanoes here is due to the more diffuse focus of deep arc stress. This contrasts with the concentration of stress in the deep arc lithosphere between 13.5° and 23°N, which produces a more distinct arc front. Brounce et al. (2016) and Martinez et al. (2018) have postulated that the Fina Nagu volcanic complex, immediately west of the southern tip of the Mariana Ridge (**Figure 2.13**), may have been generated by the same mechanisms as arc volcanoes but that its elongate, multi-vent form may be due to focussing of magma by lithosphere deformation. Interestingly, the NE-SW arrangement of cones and vents of the Fina Nagu volcanic complex shows a similar degree of alignment to that of stratovolcanoes into arc-segments that we have identified throughout the rest of the Mariana arc, albeit over a shorter distance, and is co-linear with the principal lineaments immediately to its southwest (**Figure 2.13**).

The tensional stress regime across Southern Mariana and the compressional stress regime at the plate margin can also be observed in the earthquake focal mechanisms. **Figure 2.12F** shows similar features to the south arc-segment, where extensional focal mechanisms are widely distributed in the overriding plate while compressional mechanisms are concentrated at its trenchward tip. Strike-slip mechanisms are not observed from the spreading axis to the upper plate toe. This suggests that the stress regime depicted in our model is applicable to both the volcanic arc-segments and the non-volcanic region to the south west along the same plate margin.

2.7 Summary

Spatial analyses indicate that Mariana Arc volcanoes are distributed as a series of five great circle segments with lengths of 190 to 320 km. Two approaches demonstrate that

the volcano locations are more consistent with great circle segments than any combination of small circles. First, the corrected Akaike Information Criterion (AICc) values indicate that the great circle pattern (AICc = 60.6) is more consistent with volcano locations than either a series of small circles fit to multiple segments (AICc = 89.9) or a single small circle (AICc = 75.2). Second, deviation of volcano locations from best fit small and great circles show systematic variations consistent with the Mariana Arc volcanoes describing a segmented great circle distribution (**Figure 2.5**).

The subduction direction and obliquity of convergence have no systematic relationship to the segmentation pattern. Arc-segment azimuths are parallel to the orientations of faults in their adjacent backarc and, so, to tension in the backarc. We infer that the arc-segments are caused by tensional stress present in the deep arc lithosphere. This creates pathways that magma can exploit, leading to the alignment of magmatic pathways and the volcanic edifices that are their surface expression. Therefore, each arc-segment represents a volume with relatively consistent tensional stress in the deep upper plate.

Elongation of volcanoes and/or their craters shows that the stress regime in the shallow crust of the north and mid-north arc-segments is dominated by trench-perpendicular compression. We infer vertical and horizontal partitioning of stress in the arc lithosphere to explain both the apparent contradiction between indicators of deep (volcano alignment) and shallow (volcano elongation) stress, and the change of shallow crustal stress orientation along the arc from north to south. Vertical and horizontal stress partitioning are a product of variations in dynamic subduction forces resulting from the coupling zone between the Pacific and Philippine plates being wider in the north, where the slab dip is shallower, and narrower in the south. These differences reflect a stronger pull-down force on the overriding plate and stronger, trench-perpendicular compressional force in the shallow parts of the upper plate in the north and mid-north compared to the south segment. The pull-down force contributes to flexure of the overriding plate which produces tension in the lower crust beneath the arc (**Figure 2.10**). In the south, rollback of the Pacific Plate means that tension is prevalent throughout the full depth of the upper plate in the arc.

Chapter 3

The Apparent Rotation of Java and Lesser Sunda Drives the Arc Deep Upper Plate Structures

Abstract

The alignment of arc volcanoes in great circle pattern represent the control from lithosphere flexure of the overriding plate in magma transport. Here we reassess the distribution of arc volcanoes and the upper plate deformation to build a comprehensive tectonic model for Java and Lesser Sunda. Volcano distribution was evaluated using a quantitative geometric fitting method based on the Hough Transform. Upper plate deformation is constrained by structural lineament mapping and existing geological mapping. Based on spatial analyses, we demonstrate the great circle alignments of arc volcanoes define three arc-segments (i.e. west, central, and east) with stepovers in West and East Java. We demonstrate that convergence between Indo-Australian plate and Sunda block with a minor oblique component influences the formation of the arc-segment stepovers. We suggest that counter-clockwise motion of the forearc caused by evolution of the Sunda trench produced sinistral shear along the central and east arc-segments during rotation of Java and Lesser Sunda. This rotation has been occurring since subduction started with rotational pole located in the central arc-segment. The effect of counter-clockwise forearc lateral motion caused transpressional and transtensional deformation at the surface and at the base of flexed lithosphere respectively. This vertically partitioned deformation regime facilitated the arc segments to act as magma pathways and produce the observed great circle alignments.

3.1 Introduction

Arc volcano distribution is commonly assumed to follow a small circle trace on the Earth's surface from which England et al. (2004) have estimated the depth to the underlying slab that reflects a critical depth where magma is generated in the mantle wedge (e.g. Gill, 2012; Jarrard, 1986; Tatsumi, 1986). At the critical depth, magma is generated at certain pressures and temperatures that allow the dehydration of the slab and cause partial melting in the mantle wedge (Schmidt & Poli, 1998; Grove et al., 2009; Wilson et al., 2014). England et al. (2004) proposed that the depth to slab varies systematically from arc to arc and controlled by the descent speed of the slab. England & Katz (2010) suggested that the descent speed of the slab controls the thermal wedge structure that locates the

anhydrous solidus thus establishing a magma pathway to the base of the upper plate. However, England & Katz (2010) also recognised several arcs which behave differently to the general trend they proposed between the depth to the slab and the descent speed of the slab. The central Sunda arc, extending from Java to the Lesser Sunda Islands (Java LS), is one such outliers to the general trend. Syracuse & Abers (2006) highlighted a large variation in the depth to the slab under the arc volcanoes over 100 km along the Java LS margin, even though the slab dip (Hayes et al., 2018) and the convergence rate (Argus et al., 2011) not changing significantly over these distances. This discrepancy allows us to investigate other possible controls that determine the arc volcano distribution in Java LS besides the processes occurring in the mantle.

Ranneft (1979) proposed that arc volcanoes aligned in approximately linear segments (map representation of great circles on a sphere representing the Earth) whose boundaries are defined by specific structures controlled by tectonics. In this scenario, volcano locations at the surface represent magma pathways in the subsurface and so could indicate the control from certain processes in the upper plate (Carr et al., 1973; Stoiber & Carr, 1973; Marsh, 1979). Pacey et al. (2013) identified four linear arc-segments, in an *en-echelon* pattern from the western tip of Java to central Flores which suggested an influence from the upper plate. Andikagumi et al. (2020) attributed the alignment of arc volcanoes into a segmented great circle distribution to arc-normal tension located at the base of the upper plate. The arc-normal tension induced at great depth while compression in the near-surface are the result of vertical stress regime partitioning by lithosphere flexure (Hieronymus & Bercovici, 2000). Lithosphere flexure is generated as the hydrostatic pressure maintains the contact between upper and lower plates while slab motion pulled-down the overriding plate (Hassani et al., 1997). Therefore, the alignment of arc volcanoes should reflect the upper plate stress regime that should be accounted for in tectonic models of subduction margins.

In this paper, we explore the interplay between the surface structures and the upper plate deformation to develop a comprehensive tectonic model of Java LS on the basis of arc volcano distributions. We improved the geometric fitting tools and incorporate the previous study by Pacey et al. (2013). We provide objective evidence that the volcanoes in Java LS are indeed distributed in linear arc-segments. We show that the tectonic controls

at the boundary between the subducting Indo-Australian Plate and the Eurasian Plate have increased the subduction margin curvature and gradually rotate Java LS in anti-clockwise sense. This rotation of Java LS allowed minor eastward subduction obliquity to develop and form the stepover geometry of the present volcano distribution. Minor eastward motion in Java LS also manifested in the near-surface as faults with sinistral motions, in contrast to Sumatra where highly oblique motion established the Sumatran Great Fault with dextral displacement.

3.2 Sunda Arc

The Sunda volcanic arc extends from the north-western tip of Sumatra, through Java to the east end of the Lesser Sunda Islands in Flores. The active arc is the product of subduction of the Indo-Australian Plate under the Sunda block of Eurasian Plate (P. Bird, 2003; Simons et al., 2007). Subduction at this plate margin has been going on since 45 Ma with significant reorganisation at 25 Ma when the formation of the Lesser Sunda Islands due to subduction beneath it were initiated, and at 5 Ma when Australian continent start to collide at the east end (Hall, 2002; Hall et al., 2008; Hall & Smyth, 2008; Hall, 2012). The convergence rate and direction slightly varies from 54 ± 0.4 mm/year towards N$9.5° \pm 0.5°$E at the north end of Sumatra to 61.8 ± 0.4 mm/year towards N$15.6 \pm 0.6°$E near the Sunda Strait and 70.3 ± 0.6 mm/year towards N$14.2° \pm 0.6°$E near Bali and Lombok (DeMets et al., 2010; Argus et al., 2011). The high obliquity between the convergence direction and plate margin orientation in Sumatra produces partitioned dextral transpressional strain, whereas in Java, the deformation regime reflects nearly orthogonal or tends to be sinistral oblique subduction (McCaffrey, 1996b). The average slab dip along the arc is relatively consistent at about 49° (Syracuse & Abers, 2006). At depths less than 125 km the slab dip is also consistent along the arc at approximately 28°, but at greater depths varies from 40° in the northern Sumatra to 63° near the Sunda Strait, and 68° near Bali and Lombok (Widiyantoro & van der Hilst, 1996; Lallemand et al., 2005).

This study focusses on the current arc volcanism in Java and Lesser Sunda which initiated in the Pliocene (Hamilton, 1988) and developed throughout the Quaternary (Soeria-Atmadja et al., 1994). Quaternary volcanoes produce island arc basaltic andesite

to andesite type lavas (Whitford, 1975). Highly potassic lavas are produced by volcanoes located in northern Java, such as Muria, Lasem, Lurus, Ringgit, and Baluran (**Figure 3.1**; Leterrier et al., 1990; C. Edwards et al., 1991, 1994). The basement of Java LS consisted of the Borneo-West Java continental block in the west and East Java-West Sulawesi continental block in the east, which unified in the Cretaceous then covered by volcanoclastic and marine deposits in Early Cenozoic (Hall, 2012). Arc volcanism occurred from Eocene to Late Miocene which volcanic rock thrusted northward in between Early Miocene and Pliocene and displaced to the south of the current arc location (Clements et al., 2009).

The surface structures in Java LS is dominated by compressional structures (Malod et al., 1995; Simandjuntak & Barber, 1996) with possible minor strike-slip faults manifested (**Figure 3.2**; McCaffrey, 1996b). The Baribis Fault in West Java and the Kendeng Thrust zone in East Java are both contractional structures and trend WNW-ESE with slip rates perpendicular to strike of 2.3 and 5.6 mm/year respectively (Abidin et al., 2009; Koulali et al., 2017). The Cimandiri Fault in west Java stretches NE-SW and continues out to sea, acting as a conjugate to the dextral Sumatran strike-slip fault (Malod et al., 1995). Slip mechanisms of the Cimandiri Fault has been dominated by reverse motion and sinistral slip (Dardji et al., 1994; Marliyani et al., 2016) of between 2-5 mm/year (Safitri et al., 2018; Griffin et al., 2019). Adjacent to the Cimandiri Fault, the Lembang Fault stretches E-W with a sinistral displacement of $2.0-3.5$ mm/year slip rate (Meilano et al., 2012; Afnimar et al., 2015; Daryono et al., 2019). In central Java, to the south of Merapi volcano, the Opak Fault extends NNE-SSW and displays sinistral strike-slip (Tsuji et al., 2009; Abidin et al., 2009), although the slip rate is poorly constrained. Extensional structures in Java, include the Pasuruan Fault in East Java that extends 13 km in an E-W direction and also splays NW-SE (Marliyani et al., 2019).

3.3 Data and Methods

Volcano locations in Java LS were compiled from on the regional geological maps published by the Geological Research and Development Centre of Indonesia, the volcano geological maps and volcano activity reports from the Centre for Volcanology and Geological Hazard Mitigation of Indonesia, a digital elevation model from SRTM with 1-arc second resolution

(Farr et al., 2007), the Smithsonian Institution's Global Volcanism Program (2013), and aerial imagery from Google Earth. The dataset contains 45 arc volcanic centres from Krakatau in the west to Nangi in the east Lombok (**Figure 3.1**). Highly potassic volcanoes in the backarc are not included in this study because of their distinct age and intra-plate magmatic origin (Leterrier et al., 1990; C. Edwards et al., 1991, 1994; Pacey et al., 2013). The full list of volcano locations, abbreviations, and source maps used in this study are provided in the **Appendix B**. The eastern limit of volcanoes investigated here does not extend as far as Pacey et al. (2013) because the development of the Flores back thrust and the subduction of Australian continent (Hall, 2012) may influence volcanism further to the east.

A detailed explanation and discussion of the methods used in this study can be found in (Andikagumi et al., 2020). Briefly, we undertook geometric fitting to volcano distributions and surface strain observations to observe the upper plate deformation. Geometric fitting involved comparing small circle distributions and possible great circle alignments identified using Hough Transform. Following previous attempt by Pacey et al. (2013), several volcanoes are classified as off-segment volcanoes because of their large distances from the arc-segment trends (**Figure 3.1**). Three volcano distribution models were explored; a single small circle, segmented small circles, and segmented great circles. Based on their geometry, a small circle and a great circle have different degrees of freedom during the geometric fitting. The radius of a great circle is fixed while the radius of small circles vary, as do their central latitudes and longitudes. Hence, a great circle only has two degrees of freedom while a small circle has three. The corrected Akaike Information Criterion parameter (AICc) was used to pick the preferred model between segmented small circles and segmented great circles. The AICc was not used to explore the single small circle distribution because of the considerably smaller degree of freedom compared to the other two models. Comparison between a single small circle and segmented great circles is based on residual analysis (Andikagumi et al., 2020). Residual analysis plots the volcano misfits to small circle (ΔSC) and great circle (ΔGC) datums against distance along those datums. If volcanoes are actually distributed in a great circle then ΔSC will show a polynomial regression deviation from datum while ΔGC will forms a linear regression approximating $y = 0$ (Andikagumi et al., 2020).

Surface strain was observed from lineament mapping on the SRTM digital elevation model (Farr et al., 2007). The structural lineament types (e.g. thrust, strike-slip faults, normal faults, fold axes, unit boundaries) were interpreted by compiling the data from 58 regional geological maps of Indonesia (Supporting Information). The orientations of each type of structural lineament were then compared with the alignment of volcanoes.

3.4 Results

3.4.1 Geometric Fitting

The quantitative comparison in this study refines previous attempts to quantify volcano distributions (e.g. England et al., 2004; Pacey et al., 2013). We refined the procedure for fitting great circles to Java LS volcanoes of Pacey et al. (2013) by first, quantifying the goodness-of-fit using the root-mean-square misfit. Based on Hough Transform results, we identified three alignments of arc volcanoes in great circle distributions: West, Central and East arc-segments. The root-mean-square volcano misfits from great circle trend (ΔGC) for West, Central, and East arc-segments are 6.2 km, 5.0 km, and 7.8 km, respectively, with the average misfit is 6.5 km. Meanwhile, the best-fit single small circle for the volcano locations, excluding the off-segment volcanoes, has a misfit of 17.5 km (ΔSC). **Figure 3.1** compares the possible distributions where the ΔGC is generally 11 km less than the ΔSC.

Next, we also evaluated the possibility that each segment is, itself, a small circle, and addressed the different degrees of freedom between the possible geometries. To account for the different degrees of freedom, the AICc is used to indicate the preferred segmented distribution model (Andikagumi et al., 2020). The AICc for the segmented great circle model is 76.7 and for segmented small circle model is 88.5. Given that the AICc represents the amount of information loss then the lower value is preferred (Akaike, 1974; Andikagumi et al., 2020; Burnham & Anderson, 2004) and so the segmented great circle distribution model is a better approximation of the arc than the segmented small circle model.

To compare the segmented great circle and single small circle models, the residual variation for each arc-segment were examined (**Figure D.23** to **D.25** in **Appendix D**). The trend of ΔGC against distance along the great circle segments form horizontal lines with $y \approx 0$. In contrast, the trends of ΔSC for a single small circle model, show polyno-

mial curves. In addition, corroborating our conclusion from AICc evaluation, ΔSC plots of segmented small circles also form polynomial curves. These observations follow the expected behaviour of volcanoes distributed in a great circle pattern (Andikagumi et al., 2020). Therefore, the residual analysis supports and validates the results that Sunda LS arc volcanoes are distributed in segments that each follow a great circle.

3.4.2 Structural Synthesis

The structural lineaments mapped in Java LS are WNW-ESE to E-W trending with small number aligned in NE-SW and NNW-SSE (**Figure 3.2A** and **3.3**; **Appendix E**). Java LS can be divided into three structural orientation areas corresponding to the arc-segments identified by the alignment study: west, central and east segments. In the west, most structural lineaments are associated with the Cimandiri, Baribis and Lembang fault zones. Thrust faults oriented NE-SW are related to the Cimandiri Fault while ESE-WNW oriented thrusting is associated with the Baribis fault zone. Fold axes and formation boundaries are also oriented ESE-WNW. Strike-slip faults trend mostly N-S while normal faults are more dispersed along NNW-SSE, ESE-WNW, and NNE-SSW orientations. In the central and east segments, thrust faults, fold axes, and formation boundaries are elongated along E-W and ESE-WNW directions. Thrusts and folds in the central and east segments mostly developed as part of the Kendeng thrust zone in the backarc. Strike-slip faults are minor, trending N-S, NE-SW, and NW-SE. Normal faults mostly occur in the forearc, striking in NNW-SSW, ESE-WNW, and NE-SW directions. A synthesis of the structural framework of Java LS is shown in **Figure 3.2B** where major fault zones are annotated.

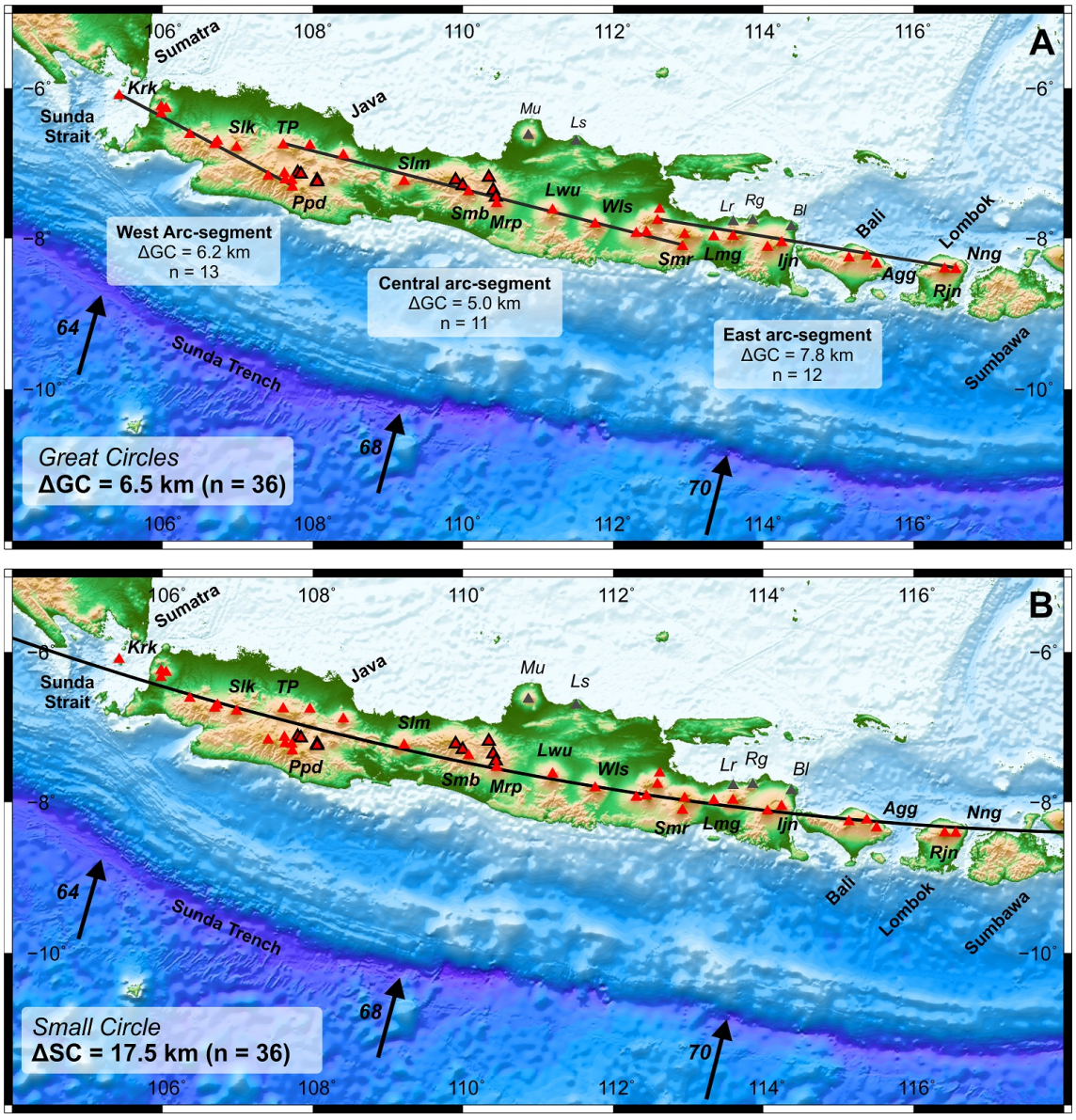

Figure 3.1. Geometric fitting to Java LS arc volcanoes. Volcano locations are marked by triangles: red – arc volcano that associated with segmentation; black-outlined – arc volcanoes classified as off-segment volcanoes; dark grey– highly potassic volcanoes, not included in this study (Pacey et al., 2013); Major volcanoes are annotated (abbreviation list in **Appendix B**); (**A**) Great circle segmentations identified by Hough Transform, marked by black solid lines, consisting of West, Central, and East arc-segments; (**B**) Best fit small circle to arc (n=36, excluding the off-segment volcanoes), marked with black line. Black arrows are the motion of the Indo-Australian Plate relative to the stable Sunda block annotated with velocity in mm/year (Argus et al., 2011).

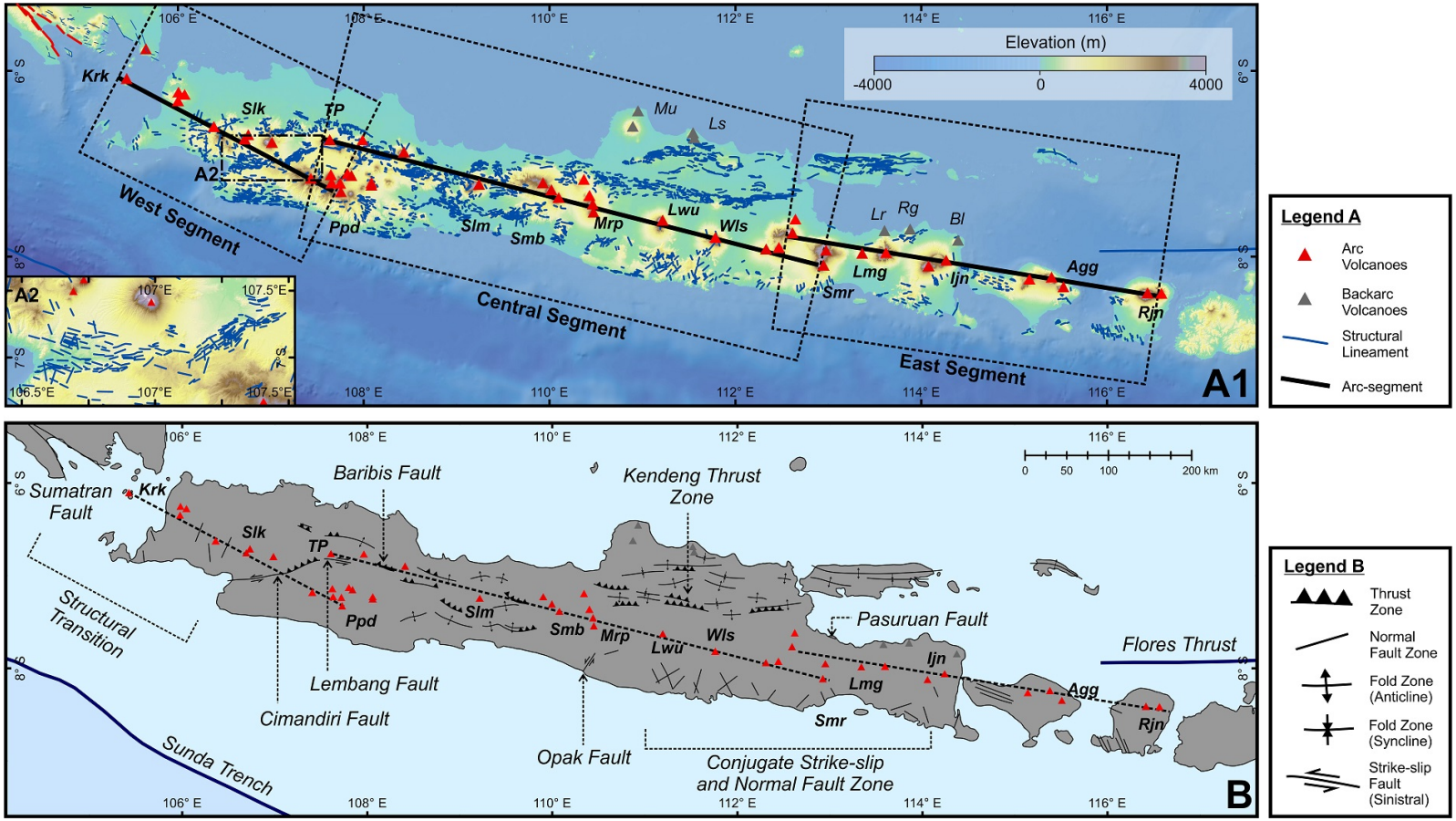

Figure 3.2. Surface strain synthesis of Java and Lesser Sunda. (**A**) Lineament mapping on SRTM 30-m resolution digital elevation model (Farr et al., 2007). Blue lines are mapped lineaments with the structural type identified using the Systematic Geological Maps of Indonesia at 1:100,000 and 1:250,000 scales (after Geological Agency of Indonesia, lists in **Appendix A**). Inset A2 shows details of lineament mapping around Cimandiri Fault zone; (**B**) Summary of major structure exposed at surface in Java and Lesser Sunda. Compressional structures (thrust and fold zones) are widely distributed to the north of the volcanic arc. Faults with sinistral strike-slip motion (Lembang and Cimandiri faults) are located in western Java. Normal fault zones developed approximately normal to the trench and are distributed mainly to the south of volcanic arc in eastern Java and Lombok.

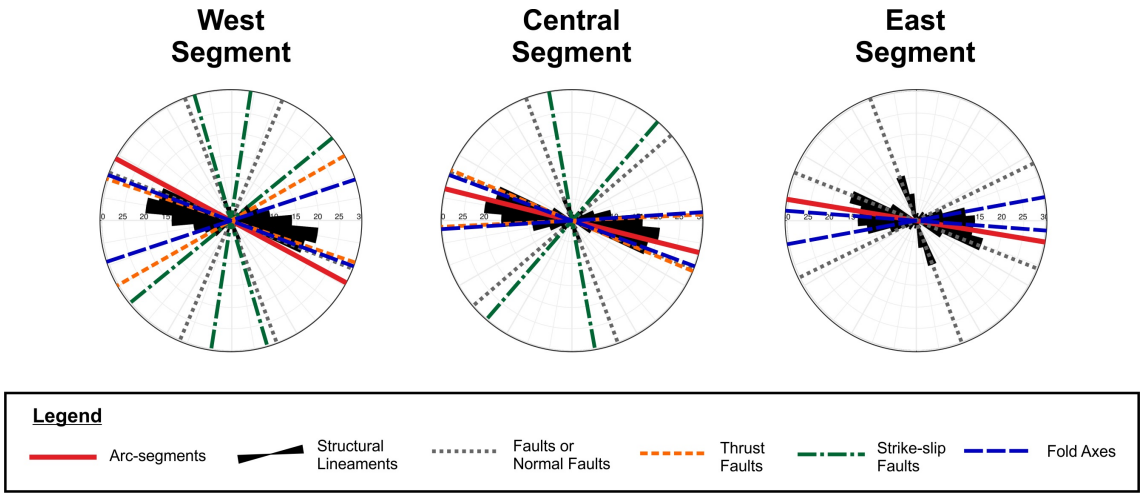

Figure 3.3. Orientations of structural lineaments in the west, central and east segments. The general direction of each structural types are shown (see Legend)

3.5 Discussion

The results from this study reinforces, using AICc parameters and residual analyses, the Pacey et al. (2013) finding that arc volcanoes in Java LS are distributed in great circle segments in an *en-echelon* pattern. Pacey et al. (2013) considered several mechanisms that could have formed the stepover geometry of the arc volcano segments, including arc lithosphere flexure, extensional relay structures, and oblique tectonics. Our recent study of the Mariana Arc concluded that the main cause of the arc volcano alignments is the arc-normal tension in the deeper parts of the flexed upper plate (Andikagumi et al., 2020). The downward lithospheric flexure is the product of subduction dynamics where the resistance on the plate-to-plate contact pulls down and deflects the upper plate (Hassani et al., 1997). The upper plate bending model is appropriate along the Mariana margin as the main cause of volcano alignments regardless of variations in the surface stress regime (Andikagumi et al., 2020). Downward lithosphere flexure allows vertical stress partitioning where compression dominates the near-surface stress regime while there is tension towards the base of the upper plate (Hieronymus & Bercovici, 1999). This linear alignment of arc volcanoes in Mariana Arc also occurs despite variations in the obliquity of convergence, from nearly orthogonal in the south to highly oblique in the north (Stern & Smoot, 1998).

However, the alignments of arc volcanoes in Java LS developed a stepover geometry

between arc-segments, which is a different arrangement to that at Mariana. Stepover geometry is a common structural arrangement in strike-slip tectonics (e.g. Christie-Blick & Biddle, 1985; Cunningham & Mann, 2007; Woodcock & Fischer, 1986), indicating the possible influence from trench-parallel strain rate along Java LS margin. McCaffrey (1996a,b) proposed varying trench-parallel strain rate along the Sunda margin, from Sumatra to Java and Lesser Sunda, based on changing obliquity of convergence. Here we evaluate the variation of oblique convergence to understand the upper plate deformation and proposed the tectonic model of Java LS that influence the structures both in the surface and in the greater depth.

3.5.1 Surface Strain and Oblique Convergence

To understand the influence of convergence obliquity upon upper plate deformation, we compare the occurrence of the strike-slip faults in Java LS and the obliquity variation along the Sunda margin. Variation in convergence obliquity (θ) along Sunda Arc is calculated from the motion direction of Indo-Australian Plate relative to the stable Sunda block (DeMets et al., 2010; Argus et al., 2011) and the geometry of Sunda trench (**Figure 3.4**; adapted from McCaffrey, 1996a). The Sumatran margin is included in this analysis to illustrate a highly oblique convergent margin with a corresponding major strike-slip fault at the surface. In **Figure 3.4**, positive values indicate the westward or clockwise motion of the forearc relative to the Sunda block while a negative value represents eastward or counter-clockwise motion of the forearc; hence, $\theta = 0$ indicates orthogonal convergence. Convergence obliquity is very high in Sumatra (θ generally from $+20°$ to $+60°$) causing the forearc to move clockwise relative to Sunda block and producing the dextral Sumatran Great Fault (SGF; Barber et al., 2005; Sieh & Natawidjaja, 2000).

In Java LS, the convergence obliquity ranges from $+20°$ to $-20°$, changing from positive to negative values at about 108.5°E. This obliquity along Java LS margin is small compared to Sumatra, hence strike-slip faults have not formed as a major structure in the same way. Nonetheless, we observe two substantial obliquity deviations along the Java LS margin at 105°E and 110°E that are co-located with Cimandiri Fault and Opak Fault zones, respectively. These peaks indicate higher trench-parallel strain rate due to stronger convergence obliquity that are possibly manifest as upper-crustal scale faults in

the surface, the Cimandiri and Opak faults. Since most of the Java LS margin has negative obliquity values, the forearc is moving counter-clockwise relative to Sunda block leading to sinistral slip at both faults. The obliquity convergence decreases and fluctuates to the east of 110°E, possibly because of the irregular trench axis from 110°E to 115°E (**Figure 3.1**). This irregularity may be affected by the presence of more buoyant lithosphere entering the trench (i.e. Roo Rise) that is more resistant to subduction (Jacob et al., 2014).

There are three region along Sunda margin where the convergence obliquity has close proximity to zero or orthogonal system, based on the span of data points from the average graph, at (1) 103.25° – 104.5°E, (2) 107.75° – 109.25°E, and (3) 111° – 115.5°E (**Figure 3.4**). However, the surrounding area around Region (1) and (3) are dominantly in a similar convergence obliquity type, which are positive and negative, respectively. Meanwhile, region (2) demonstrates a substantial change between positive and negative obliquity values, at about 108.5° ± 0.7°E, indicating the location of obliquity transition zone. Nonetheless, the structural transition zone between the dextral SGF and the sinistral Cimandiri Fault developed further to the west than the location of $\theta = 0$. The structural transition zone (**Figure 3.2B**) is expressed as the juxtaposition between SGF and Cimandiri fault where the lateral slip changes from dextral to sinistral at around 105°E (Huchon & Le Pichon, 1984; Susilohadi et al., 2009). The structural transition zone plays a major role in the opening of the Sunda Strait by the propagation of normal faults, forming a submarine graben geometry which ends at the west tip of Cimandiri fault (Schlüter et al., 2008). The separation between structural transition zone (105°E) and the obliquity transition zone (108.5°E) could possibly be influenced by the pre-existing structures around the area. Hamilton (1979) suggested a boundary line of the Cretaceous continental crust margin that cut through west Java in NE-SW direction and parallels with Cimandiri Fault. This boundary persisted in the Oligocene, in turn, possibly affected the initiation of Cimandiri Fault in Late Oligocene (Susilohadi et al., 2005), hence the juxtaposition of the SGF and Cimandiri Fault located further west than the obliquity transition zone. Therefore, we conclude that minor convergence obliquity (+20° to −20°) is a component of the upper plate deformation and manifest as surface structures that exhibit strike-slip motion where there are excursions of convergence obliquity.

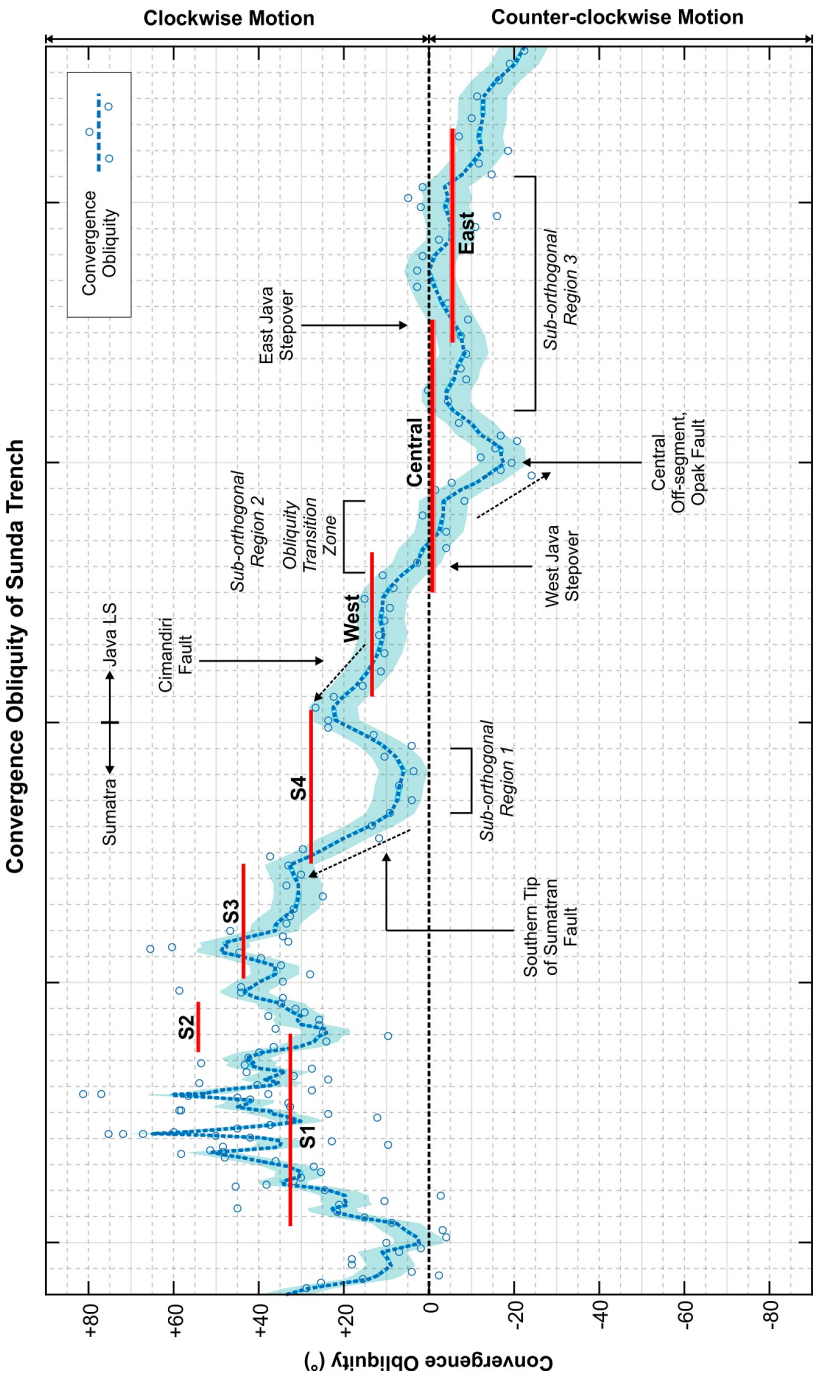

Figure 3.4. Diagram of convergence obliquity along the Sunda Trench. The blue-dashed line is the filtered graph of convergence obliquity data (blue circles) using the moving average method. Blue shading indicates the average deviation based on the span of data points. Positive obliquity ($\theta > 0$) indicates clockwise forearc motion relative to the Sunda block while negative obliquity ($\theta < 0$) denotes counter-clockwise motion of the forearc. Two excursions along Java are co-located (at about 105°E) with the sinistral strike-slip Cimandiri Fault and (at about 110°E) the central off-segment volcano complex, and location of Opak Fault. High obliquity in Sumatra is manifested as the SGF. Red lines are location of arc-segments in Java LS (west, central, and east) and Sumatra (S1-4).

3.5.2 Deep Structures and Java LS Rotation

The influence from minor oblique convergence to the deep structures of Java LS is explored by observing the arrangement of arc volcanoes alignments as it reflects the structures in the great depth that channel magma transport. The discussion above shows that the convergence obliquity, although minor, has influenced Java LS surface structures where strike-slip faults established in compressional dominated structural development, then transpressional regime. Downward lithosphere flexure produces a stress regime with compression near the surface and extension at the base of the upper plate (Hieronymus & Bercovici, 1999). As the surface structures demonstrate the manifestation of the oblique convergence, the structures at the greater depth are also expected to exhibit a similar effect. Shear stress due to trench-parallel motion, resulting from oblique convergence, would extent as deep as the coupling between the upper and lower plates persisted (R. McCaffrey, 1992), albeit the deformation will be transtensional at the base of the flexed upper plate.

Comparing the orientation of arc volcano alignments and the relative plate motion resulted in an average oblique convergence at each arc-segment: $+13° \pm 0.8°$ for the west, $-1° \pm 1.8°$ for the central, and $-6° \pm 1.5°$ for the east (**Figure 3.4**). The plots in **Figure 3.4** also displays that the stepover between the west and central arc-segment is co-located with the obliquity transition zone. It indicates that the forearc moves counter-clockwise relative to the Sunda block on the east arc-segment and most of the central arc-segments, with a sinistral motion. Meanwhile, the forearc on the west arc-segment is expected to move clockwise and generate dextral movement. However, the structural inheritance from the Cretaceous margin possibly affects the development of structure in the surface (see above). Hence, the Cimandiri Fault, cuts through the west arc-segment, has sinistral motion following the majority of Java's counter-clockwise forearc motion. Nevertheless, the stepover between the west and central arc-segments suggests that this coincides with where the trench-parallel motion changes from clockwise (west of 107.5°E) to counter-clockwise (east of 108.1°E). This would generate extension, parallel to the trench, at the west stepover between 107.5°E and 108.1°E turning it into a releasing bend or pull-apart like structure as the manifestation of transtensional stress regime (Cunningham & Mann,

2007).

Trench-parallel extension in the deep upper plate may channel more magma migration leading to the off-segment volcanoes. These off-segment volcanoes were formed within the stepovers of the west and central arc-segments, which are Kamojang, Guntur, Talagabodas and Galunggung. Pacey et al. (2013) also pointed out the existence of the off-segment volcanoes in central Java, as well as in west Java, which was possibly controlled by the cross-arc lithospheric scale structure. Furthermore, in **Figure 3.4**, the degree of convergence obliquity increases drastically from $-3°$ at 109.3°E to $-18°$ at 110°E which infer faster trench-parallel motion to the east of this range. This faster motion would also cause tension, parallel to the trench, and generate extensional structure normal to the trench and arc (R. McCaffrey, 1992) which may influence the location of off-segment volcanoes in the central arc-segment, such as the Dieng volcanic complex, Sunduro, Ungaran, Telomoyo and Merbabu. For these reasons, we propose that the variations of oblique convergence along Sunda margin affect the upper plate deformation, both at the surface and at great depths.

Variation of convergence obliquity is controlled by the trench geometry and the subduction direction (McCaffrey, 1996a). The trench margin itself has been evolving since subduction initiation at 45 Ma since when the subduction direction has been relatively constant (Hall, 2012). During subduction initiation, the Sunda trench margin, from Sumatra to Java, was less arcuate and oriented generally NNW-SSE, until the collision of India and Australia at each end of Sunda block (Hall, 2012; Pubellier & Morley, 2014). The evolution of the Sunda trench can be explained by this variation of the nature of the lower plate. To east and west, the Indo-Australian plate consisted of continental lithosphere (i.e. Indian and Australian continents) which oceanic lithosphere between. For a uniform subducting plate, the trench margin would advance (i.e. migrate towards the upper plate) when convergence rate is higher than subduction rate, while the trench retreats towards the subducting plate when the convergence rate is less than the subduction rate (Royden, 1993; Macpherson & Hall, 1999). Continental collision would lower subduction rate and cause the trench margin to advance (Magni et al., 2012). Given the continental-oceanic-continental arrangement of the Indo-Australian margin, the trench migration along the Sunda margin would vary along its length. This would cause the margin to advance at

each end, where the Indian and Australian continental blocks collided, and to retreat where the oceanic plate subducted along the Sumatra and Java LS margin (e.g. Magni et al., 2014). In turn, this variation would have caused the margin to have greater curvature.

During trench migration, Java LS would appear to have experienced an apparent rotation in counter-clockwise manner. Ninkovich (1976) inferred a 20° clockwise rotation of Sumatra with the rotation pole area located at the Sunda Strait, assuming the stable Java LS. However, the motion of the Indo-Australian Plate relative to the Sunda block is higher towards Australia rather than India, 70 mm/year around the east of Java and 54 mm/year around the north of Sumatra (Argus et al., 2011). This is caused by the limited motion of India due to Himalayan resistance while Australia moves faster towards the north (Cloetingh & Wortel, 1986; Delescluse & Chamot-Rooke, 2007). Hence, it seems likely that rotation should affect the Java LS margin more than the Sumatran margin.

To locate the pole of Java LS apparent rotation, we explored the surface and deep deformation of the upper plate. At the surface, the eastern Java LS region features more compressional structures which accommodate a higher shortening rate. GPS observations and tectonic block motion modelling show stronger convergent motion of Java forearc relative to Sunda block in the east of Java LS compared to the west (Koulali et al., 2017). Stronger convergence in the east is manifested in intense folding and thrusting in the Kendeng Thrust zone which decreases towards the Baribis fault zone (Abidin et al., 2009; Koulali et al., 2017). Further to the east, the Flores thrust develops with higher shortening in the east than the west and start to close the Lombok and Bali basins (McCaffrey & Nabelek, 1987; Widiyantoro & Fauzi, 2005). We infer that the development of Flores thrust is associated with the collision of Australian continent. This collision increased trench curvature and generated higher compressional deformation, then the back thrust formed to accommodate high shortening. In the forearc, the increasing curvature of the plate margin could generate normal faulting to accommodate extension parallel to trench (Martinez et al., 2018). As the trench margin curvature increased, the trench-parallel extension also became stronger. This trench-parallel extension, in addition to trench-normal compression, would propagate normal faults sub-normal to the trench or in conjugate geometry. This could explain the occurrence of normal faults, generally perpendicular to trench, in the south part of Java and Lombok (**Figure 3.2**).

As the conjugate faults are oblique to the trench, trench-parallel extension would cause slip in both dextral and sinistral senses at each fault plane (**Figure 3.5**), depending on how oblique these structures are to the trench (e.g. Harding, 1974; Waldron, 2005). To the west of Java LS, extensional structures are presents as the graben, parallel to the trench, in Sunda Strait. Western Java also features sinistral strike strike-slip structures in addition to less profound compressional deformation compared to the east. The changes of upper plate deformation in the surface infer the possibility of a pole of rotation located around the central of Java LS, where compression and extension are balanced. At greater depth, the obliquities of arc-segments to the relative plate motions are also consistent with increasingly sinistral motion towards the east (**Figure 3.4**). Meanwhile, the west arc-segment is consistent with dextral motion. Therefore, the deep structures also support the location of the apparent rotational pole around the centre of Java LS where the lateral motion is in balance between sinistral and dextral.

Despite the fact that the subduction of Sunda block began 45 million years ago (Hall, 2012), the current arc is relatively recent, and demonstrably younger than the Tertiary volcanic products in south Java (Soeria-Atmadja et al., 1994; Clements et al., 2009). Approximating from the plate reconstruction of Hall (2012), the total rotation of Java LS in the last 45 Ma has been about 22 degrees. Assuming the NNE motion of the Indo-Australian Plate relative to the Sunda block did not change substantially in the last 45 Ma and that the trench margin was less arcuate and oriented NNW-SSE, the entire margin along Sumatra and Java LS should have experience oblique deformation, with clockwise forearc motion or dextral displacement, initially. In contrast, present observations indicate sinistral displacement of the forearc in the central and east arc-segments, with the maximum convergence obliquity of about $-6^\circ \pm 1.5^\circ$ (**Figure 3.4**). The apparent rotation of Java LS during trench migration implies that the oblique convergence to the east of the rotation pole also progressed from dextral to normal and then sinistral, while dextral motion continued to the west of pole of rotation. Since the east arc-segment exhibit the stronger contrast to the most of Sunda margin, we suggest the development of the stepover geometry structures only occurred in about the last $6^\circ \pm 1.5^\circ$ rotation of the whole 22° rotation of Java LS as the subduction progress from orthogonal to slightly oblique. In the last $6^\circ \pm 1.5^\circ$ rotation, the lateral motion parallel to the trench has been progressing and

causing the forearc motion of Java LS, in addition to the lithosphere flexure which partition the compression near the surface and extension at the greater depth. As the result, the present day structures in the surface exhibit the transpression deformation while the deep upper plate structures display the transtensional structures. **Figure 3.5** illustrates the deep structures and volcanic development and the surface structures in Java LS. We propose that the apparent rotation of Java LS enabled the minor oblique convergence and sinistral trench-parallel lateral motion that influenced the lithosphere flexure and volcano distributions.

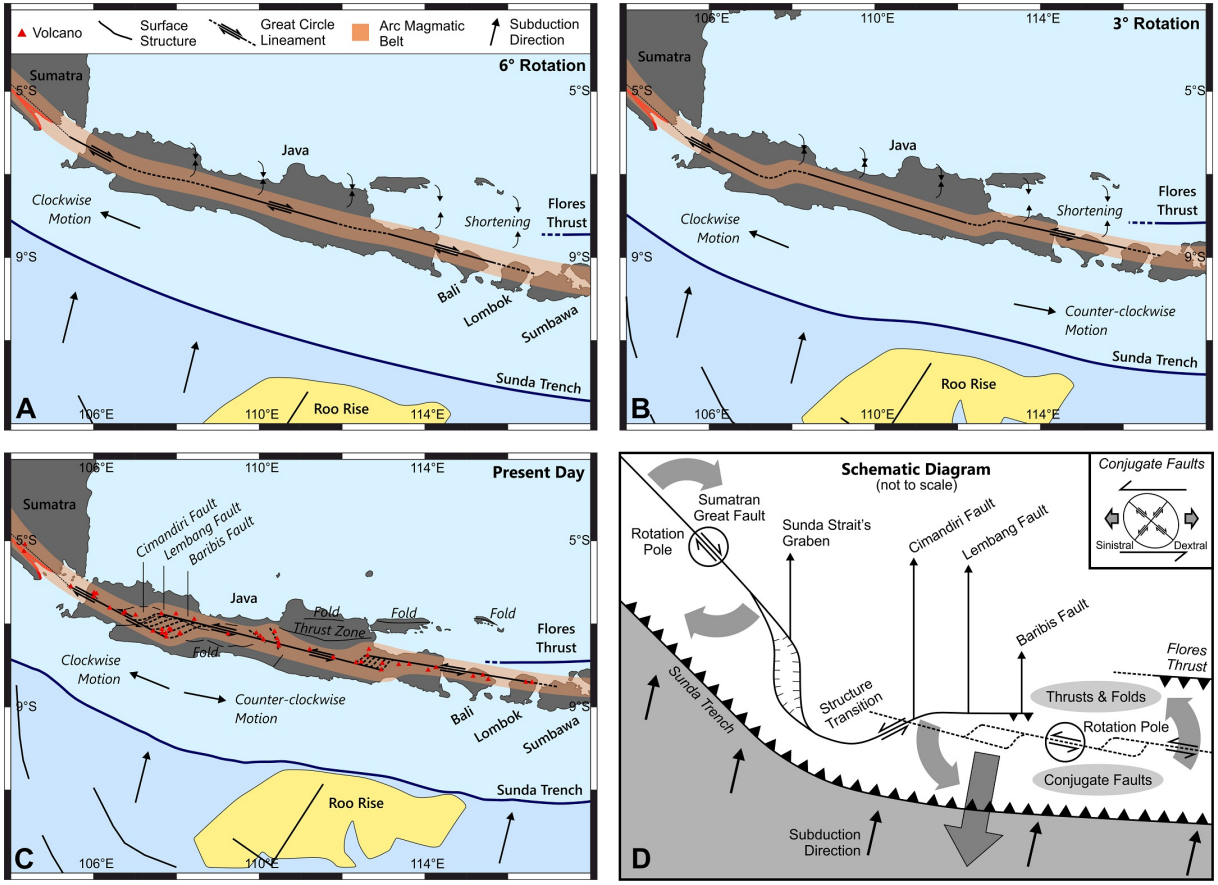

Figure 3.5. Model for the rotation of Java and Lesser Sunda from (**A**) 6° rotation, (**B**) 3° rotation to (**C**) the present day, and (**D**) the schematic diagram of the rotation mechanism. Rotation of Java LS is associated with increasing curvature of the Sunda Trench due to Indo-Australian Plate subduction. The current distribution of volcanoes was formed during the last $6° \pm 1.5°$ rotation. Higher compression rates occurs further east near Lombok and Sumbawa where the Flores Thrust developed to accommodate the increasing shortening and rotation. Minor strike-slip motion at the base of the lithosphere is sinistral from Lombok west to the rotation pole in central Java, then becomes dextral towards Sumatra. These minor strike-slip motions generated a releasing bend like geometry at the stepovers of arc-segments in the east and west of Java and allow more volcanoes to form at the these location on the surface. Normal faults in the south occur to accommodate trench-parallel extension due to the increasing curvature.

3.6 Conclusion

An objective quantitative comparison corroborate that arc volcanoes in Java LS are distributed in three great circle segments with en-echelon pattern and stepovers located in the west and east Java (108.5°E and 112.5°E). This distribution is controlled by a minor oblique convergence along Java LS, of about $+20°$ to $-20°$ in average, inferred from the relative plate motion between Indo-Australian plate and the Sunda block to Sunda trench geometry. Counter-clockwise forearc motion of Java LS is the result of an apparent rotation during increasing curvature of Sunda trench. The trench evolved into a sharper curvature geometry as India and Australia collided at each end of Sunda block since 45 Ma. The rotation pole is located around the central Java LS where compression in the east and extension in the west are at balance as are the dextral and sinistral displacements along the arc-segments. However, the rotation that affects Java LS and the current volcanism only occurs in the last $6° \pm 1.5°$ degrees rotation, of an approximate 22 degrees total rotation of Java LS since 45 Ma.

Chapter 4

Arc Lithosphere Structure Influenced Caldera Formation at Toba, Sumatra

Abstract

The relative importance of structural control on caldera-forming eruptions, versus eruptive or magmatic processes, remains unclear. In arc settings, it is widely accepted that a magma source in the mantle wedge is required to generate the thermal and mechanical conditions to develop caldera-forming events. Toba, in Sumatra, is one example where the formation of a large-scale caldera has been linked to a voluminous magma supply. However, recent investigation shows that the feeder system accumulated magma not only beneath Toba but also hundreds of kilometres south of the caldera; yet, the large-scale caldera only formed in a specific region. We used spatial analysis to explore the location of Toba in the context of an observed alignment of Sumatran vents into great circle segments with stepover geometry. The alignments of arc volcanoes reflect focussing of magma pathways controlled by arc-normal tension at the base of the deforming lithosphere. We propose that Toba, located at an arc-segment stepover, formed in a zone of weak, extended arc lithosphere with enhanced extension and thinning of the arc lithosphere. The extended weakness zone developed due to northeastward migration of the more northerly arc-segment. This occurred because of substantial changes in the age, for about 50 Ma, and the buoyancy of the subducting oceanic plate. The thinning in arc lithosphere may also increase the amount of upwelling, and therefore the amount of crustal melting. We conclude that the latest caldera-forming event at Toba was driven by both a voluminous magma supply and by the arc lithosphere structure.

4.1 Introduction

Large scale caldera-forming eruptions are dangerous geological hazards that could affect the environment and threaten human life. Investigations into the controls on caldera formation are generally focussed on eruptive or magmatic mechanisms, while the control from plate tectonics in a broader context remains unclear (de Silva, 2008). It is widely accepted that formations of large calderas require significant mafic magma flux from the mantle to feed the magmatic system in order to produce large silicic volcanic events (de Silva & Gosnold, 2007). Silicic magma could be originated from magmatic differentiation of basaltic magma, or from crustal partial melting (Rapp & Watson, 1995; Sisson et al.,

2005), or from both sources simultaneously (e.g. Annen et al., 2006). Large scale crustal melting due to basaltic magma input occurs when high thermal energy ($\geq 900°C$) reached (Leeman et al., 2008). Consequently, large-scale crustal melting would contribute to a formation of large scale magma chamber, especially when melting occurs rapidly within hundreds of thousands of year's period (e.g. Michaut & Jaupart, 2006; Gelman et al., 2013). Nevertheless, these processes neglect any control from arc lithosphere structures, hence our understanding of the role of the upper plate in arc volcanism and caldera formation is limited.

The Toba caldera in northern Sumatra, Indonesia, is an example of a large scale silicic caldera volcano that has been suggested to relate with a voluminous magma supply. Toba is the world's largest Quaternary caldera, which formed during the latest eruption ~74k years ago, with prior caldera-forming events at ~840ka and ~501ka (Chesner, 2012). The latest eruption ejected amount 100 times more sulphur than the 1991 Mt. Pinatubo eruption and caused climatic changes, and possibly, human population decline (Williams, 2012). The subduction of the fluid-rich Investigator Fracture Zone (IFZ) was suggested as the main control in generating voluminous volatile-rich basic magma supply (at least 50,000 km^3) and then inducing the latest caldera-forming eruption (Koulakov et al., 2016). Seismic tomography by Stankiewicz et al. (2010) identified a low seismic velocity area, interpreted as zones of magma storage, in a complex geometry with at least two sub-chambers. Koulakov et al. (2016) also imaged the feeder system beneath Toba with two other accumulations of magma located about 50 and 100 km away to the south of the caldera. However, the caldera formation only took place specifically at Toba rather than occurring in the other sites where the magma supplies are also high.

The alignments of arc volcanoes, such as in Sunda, Mariana, and Central American arcs, demonstrate the interaction between tectonics and magma transport through arc lithosphere in controlling volcano distribution (e.g. Andikagumi et al., 2020; Ranneft, 1979; Morgan et al., 2008; Pacey et al., 2013). We analyse volcano distribution in Sumatra by applying the Hough Transform method to understand the relationship of Toba to other volcanoes in an arc. We compare the alignment of volcanoes as the representation of arc lithosphere structures to the structural lineaments mapped at the surface in order to comprehend the tectonic development which affecting Toba and the surrounding area.

We conclude that the segmented magma pathway at Toba points to a unique structural control the formation of large-scale caldera which focuses high magma supply from the mantle.

4.2 Sumatra

The island of Sumatra (**Figure 4.1**), west Indonesian, is the home of numerous basaltic-to-andesitic arc volcanoes of the Sunda Arc. Volcanism has been going on since at least 45 Ma as the Indo-Australian plate was subducted northward beneath the Sunda block, part of the Eurasia plate (Hall, 2012). The convergence rate and direction of the subducting plate vary slightly along the Sumatran margin from 54 ± 0.4 mm/year towards N9.5° ± 0.5°E in the north to 61.8 ± 0.4 mm/year towards N15.6° ± 0.6°E near the Sunda Strait (Argus et al., 2011). The subducting slab geometry is relatively constant, with a narrow range in average slab dip from $46° - 50°$ (Syracuse & Abers, 2006). Highly oblique convergence between the Indo-Australian Plate and Sumatra has produced strain partitioning where subduction is followed by the propagation of a major dextral strike-slip fault, known as the Sumatran Great Fault (SGF), in the upper plate (McCaffrey, 1996b; McCaffrey et al., 2000). Many arc volcanoes are co-located with the SGF (**Figure 4.1**), but their influence upon the geometry of the fault is not clear (Sieh & Natawidjaja, 2000). A recent investigation by Bradley et al. (2017) suggested a relatively uniform slip along the SGF of about $14 - 15$ mm/year, controlled by the mechanical property variation, i.e. the slip rates, of the diffuse boundary between Indian and Australian plates. The diffuse boundary of Indo-Australian plate consisted of several fracture zones, including the Investigator Fracture Zone (IFZ), and a fossil spreading centre which varies the age of oceanic lithosphere along the Sunda Trench (Jacob et al., 2014).

4.3 Data and Methods

Our dataset of volcano locations in Sumatra from the Smithsonian Institution's Global Volcanism Program (2013) was updated with local data and geomorphological observations compiled from regional geological maps published by the Indonesian Geological Research and Development Centre, and volcano geological maps and activity reports from the In-

donesian Volcanology and Geological Hazard Mitigation Centre. Volcano morphology was also observed on an SRTM digital elevation model with 1-arc second resolution (Farr et al., 2007) and satellite imagery from Google Earth. The dataset comprises 39 volcanoes from Pulau We in the north to Krakatau in the south end (**Figure 4.1**). The list of volcano locations and the maps used in the data compilation are provided in **Appendix B**.

The data analyses and methodologies used in this study are geometrical fitting and surface strain observation. Detailed methods are explained in Andikagumi et al. (2020) and references therein. Geometric fitting aimed to resolve whether Sumatran arc volcano distribution is best approximated as a single small circle, segmented great circles, or segmented small circles. The great circle alignments of Sumatran arc volcanoes were identified using Hough Transform analysis (Pacey et al., 2013). After the fitting, any volcanoes which located far away from the great circle trend, about 30 km or more, are excluded and classified as off-segment volcanoes. The preferred model was chosen based on the variations in residuals (root-mean-square misfits) from fitted great circle (ΔGC) and small circle (ΔSC) pattern and also using a statistical test, the corrected Akaike Information Criterion (AICc; Andikagumi et al., 2020). To corroborate the preferred distribution model, both residuals (ΔSC and ΔGC) were then compared on the plot against the distance along the small and great circles. The residual regression that forms a linear line with the function $y = 0$, or approximating, indicate the preferred fitting model. For a more robust conclusion, statistical and residual analysis were also applied to segmented small circle model for comparison and allowing the possibility of such distribution model. Surface strain observations mapped structural lineaments on the digital elevation model to understand the structural pattern in Sumatra, focusing especially on the geometry of the SGF, and its relation to the arc volcanism. The nature of the structural lineaments was confirmed based on the regional geological map of Indonesia.

4.4 Results

4.4.1 Geometric Fitting

Based on Hough Transform analysis, we recognised four segments of arc volcanoes aligned as great circles in Sumatra: north (n = 9 volcanoes, rms-misfit = 12.4 km), mid-north (n =

5, rms-misfit = 4.4 km), mid-south (n = 11, rms-misfit = 10.5 km) and south (n = 12, rms-misfit = 5.8 km). We define these as arc-segments (**Figure 4.1**). Two volcanoes (Isauisau and Lumut-Balai) are classified as off-segment volcanoes due to their distance from the alignment, up to 30 km away, while 37 volcanoes are associated with the arc-segments. A stepover geometry is recognised between the north and mid-north arc-segments with an orientation change from N313°E for the north arc-segment to N335°E for the mid-north arc-segment. This stepover coincides with the location of the Toba caldera (**Figure 4.1D**). Details of the great circle arc-segment properties are in the **Appendix D**.

The overall misfit for the segmented great circle distribution model (ΔGC) is 9.1 km. This is smaller than the small circle misfit (ΔSC = 28.0 km) (**Figure 4.1**). However, the degrees of freedom associated with small and great circles are different, so such direct comparison of rms-values is not sufficiently robust. Therefore, we used the AICc parameter which takes into account the number of adjusted parameters and the number of the data in the comparison (Andikagumi et al., 2020). The AICc represents the amount of information lost from a model and lower values indicate a suitable model (Akaike, 1974; Burnham & Anderson, 2004). The AICc parameter for the great circle segments is 92.27, while for a single and segmented small circle fittings are 113.83 and 109.04, respectively. The distribution model of Sumatran arc volcanoes in a series of great circle segments which has the lowest AICc value is preferred, compared to a single or multiple small circle models.

The misfit from each volcano along the distance of the distribution model was plotted to identify the residual characteristic and corroborate the result from statistical analysis. The ΔSC plots form unsystematic distribution along the small circle distance while the ΔGC plots form linear regression line approximating $y = 0$. For a comparison, residuals of the segmented small circles produce polynomial trend line along the small circle distance. Figures of the residual plots are available in **Appendix D**. The linear trends of ΔGC with $y \approx 0$ indicate that the distribution of arc volcano is indeed in the great circle pattern. Based on the residual analysis, the distributions of volcanoes in Sumatra are better fitted with a series of great circles.

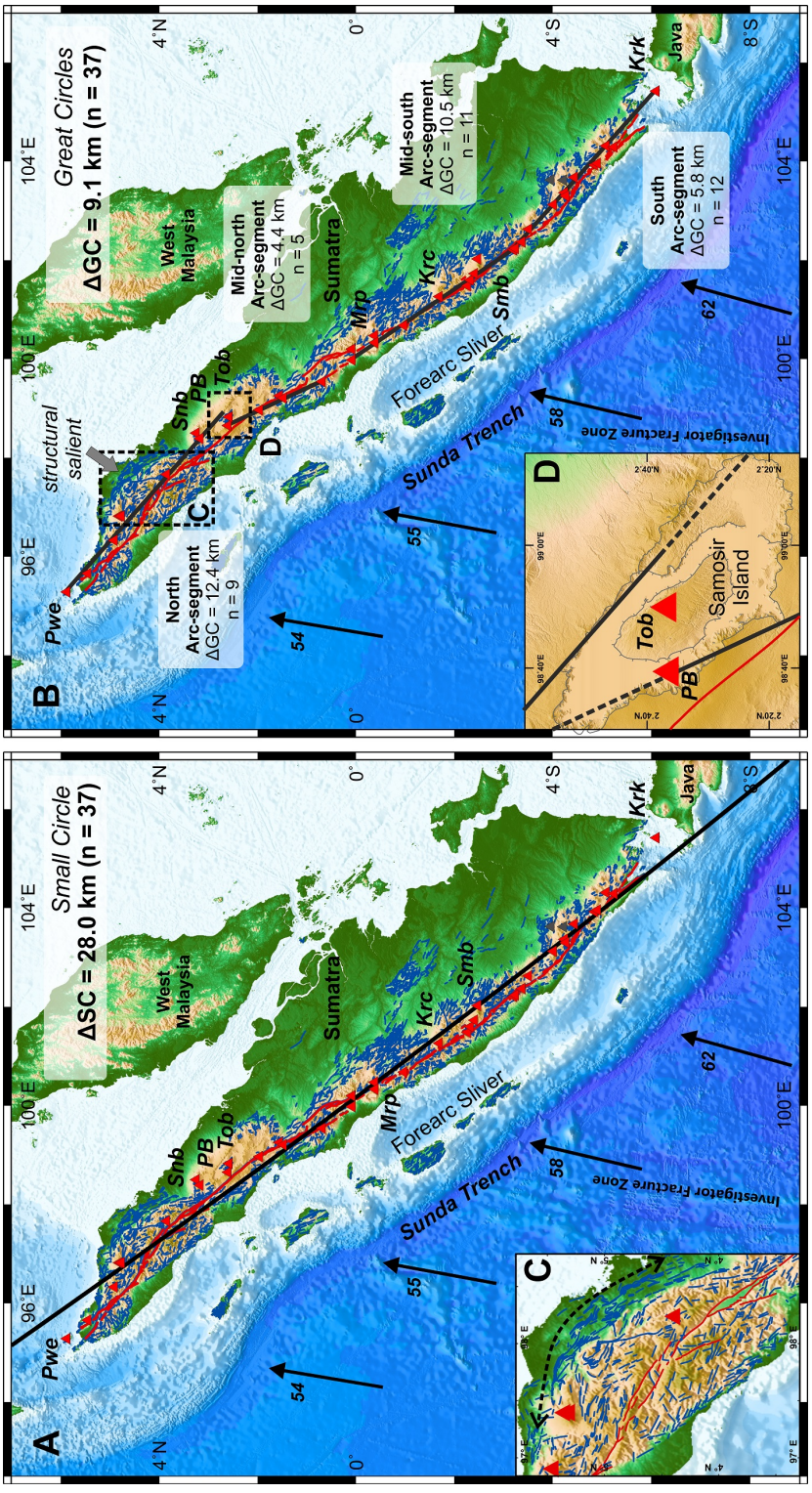

Figure 4.1. Geometric fitting on Sumatra arc volcanoes. Arc volcanoes included in the dataset (n=39) are denoted by triangles: red – volcanoes that are associated with great circle arc-segments after Hough Transform analysis (n=37); grey – off-segment volcanoes that are excluded after Hough Transform analysis (n=2). Major volcanoes annotated are: Pulau We (Pwe), Sinabung (Snb), Pusuk Bukit (PB), Toba (Tob), Merapi (Mrp), Kerinci (Krc), Sumbing (Smb), and Krakatau (Krk); (**A**) Best fit small circle is plotted with black line; (**B**) Four great circle arc-segments generated from Hough Transform analysis: north, mid-north, mid-south and south; (**C**) Structural salient in northern Sumatra; Dashed arrow marks the changes of general structural orientation; (**D**) Toba caldera and the orientation of arc-segment; Black arrows are the relative plate motion of Indo-Australian plate to stable Sunda block (Argus et al., 2011) with rate in mm/year. Red lines are the mapped Sumatra Great Fault (SGF). Blue lines are mapped structural lineaments on the SRTM elevation model with 1 arc-second resolution. The area where structural salient identified is marked with a grey arrow.

4.4.2 Structural Lineaments

Structural lineaments are divided into four groups: north, mid-north, mid-south, and south; based on the closest arc-segment from their location. The orientations of structural lineaments are presented in rose diagrams (**Figure 4.2** with detailed diagrams in **Appendix E**). There are two main trends of lineament orientations observed in all of the arc-segments: Group I oriented NNW-SSE (N325°E – N355°E) and Group II WNW-ESE (N275°E – N305°E). The SGF (blue shaded region), the arc-segment (red line), and the trench margin (black dashed line) are generally sub-parallel within $5° - 15°$ deviation from the general trend and lie between the Group I and II orientations. Measuring the root-mean-square average distance of the SGF to the arc-segments (ΔGC_F), the SGF generally is located within close proximity (4.4 to 11.3 km) to the arc-segment (**Figure 4.3**). Significantly wider ΔGC_F is observed in the north with a mean distance of 24.1 km. Compressional structure (thrust and folds) orientations split into Group I and II trends with different proportion around each arc-segment. Compressional structures are more commonly oriented along Group II near the south arc-segment, but the relative frequency of Group I increases in the mid-south and mid-north arc-segments. Around the north arc-segment, compressional structures are distributed evenly in both Group I and II orientations. Meanwhile, extensional structures are parallel to both in Group I and II orientations throughout the island.

4.5 Discussion

4.5.1 Lithospheric Weakness Zone

The alignment of Sumatran volcanoes in great circle segments provides further evidence for upper plate structures in controlling arc volcano locations, as demonstrated by the previous studies in Mariana and Java arcs (Andikagumi et al., 2020; Pacey et al., 2013). The Mariana study concluded that the great circle segment that represents tension in the deeper upper plate, probably due to downward lithospheric flexure. Hassani et al. (1997) explained that lithosphere flexure is generated because the overriding plate is deflected by the slab whiles the contact between both plates is maintained by hydrostatic suction.

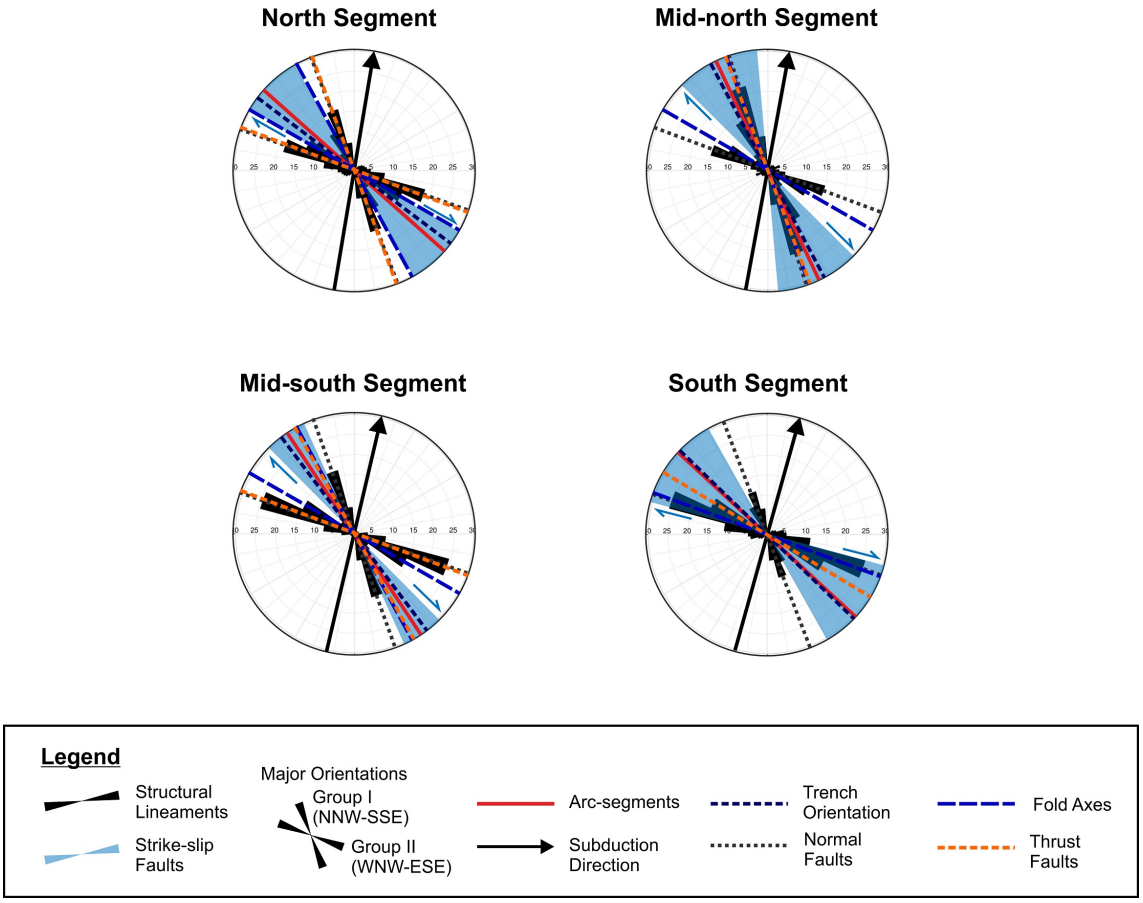

Figure 4.2. Summary rose diagram comparing the orientation of great circle arc-segment (red line), SGF orientation (blue shaded region with dextral kinematic arrows) and AU-SU relative plate motion (black arrows), general structural lineament orientation (black shaded data), Sunda trench margin orientation (short-dashed blue lines), folds (long-dashed blue lines), thrust (dashed orange lines), normal faults (dotted grey lines)

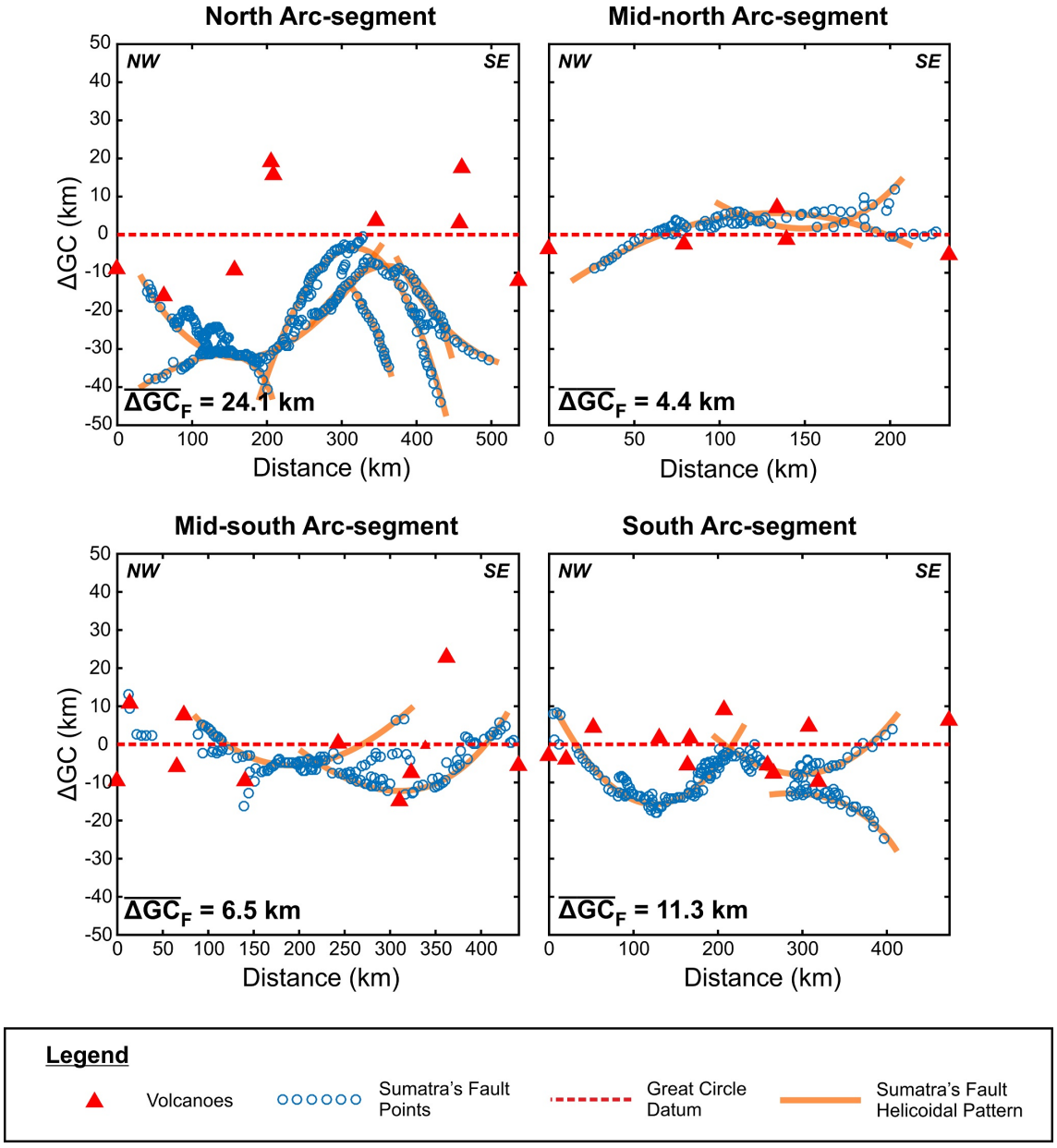

Figure 4.3. The relative distance diagrams between the great circle segments and SGF (ΔGC_F). Red triangles mark the misfit of each volcano the best fit great circle (dashed red lines). Blue circles are the SGF distance points from the great circle lineament. ΔGC_F is the root-mean-square average of the fault distance from the great circle arc-segment.

Hieronymus & Bercovici (2000) showed that downward lithospheric flexure partitions the stress regime vertically such that the most deflected volume experiences compression occurs at shallow depth with extension towards the base of the plate. Tension in the deep upper plate initiates vertical planar pathways that enable magma to migrate to the surface. This lithosphere flexure is possibly located at the end of the forearc down-pulled zone (Gvirtzman & Stern, 2004). Such flexure would concentrate lithospheric weakness into a narrow zone parallel to the trench margin as permanent deformation occurred within the plate bending, both at the surface and the base of the plate (Turcotte et al., 1978; Bodine & Watts, 1979). Vertical stress partitioning, with compression in the shallow part of the upper plate, is supported by the observation of sill complexes beneath Toba caldera at a depth less than 30 km (Jaxybulatov et al., 2014). In the compressional system, vertical stress acts as the least principal stress ($\sigma_v = \sigma_3$), allowing horizontal planar discontinuity to initiate and allow sill emplacements (Walker, 2016; Walker et al., 2017). Meanwhile, in the deep upper plate, vertical stress is high due to lithostatic stress, and so may become the maximum principal stress ($\sigma_v = \sigma_1$), hence the least principal stress ($\sigma_{Hmin} = \sigma_3$) is horizontal this would favour tension and vertically oriented, planar magma conduits (i.e. dykes).

The relationship between the arc volcanism and the SGF is debatable, but we propose that both features are developed within the lithospheric weakness zone due to lithosphere flexure. Acocella et al. (2018) claimed that the relationship is limited as there is only a weak correlation observed between fault slip rate and volcanic productivity. Sieh & Natawidjaja (2000) also suggested that the co-location of the arc volcanoes and the SGF may be a coincidence and the geometry of SGF is not affected by the volcanism, with tectonics, perhaps in a minor extent, controlling only a few of the young volcanoes. Nonetheless, our study can explain the close proximity of both the arc-segments and the SGF as different manifestations of a deep lithospheric control within the same narrow zone parallel to the trench margin. Strike-slip fault orientations of the SGF are parallel to the orientation of volcano great circle segments and the geometry of trench margin, also reflecting the potential colocation between those features within the lithospheric weakness zone. Muraoka et al. (2010) identified a systematic location of geothermal system in Sumatra where the occurrences of the system are concentrated along the SGF, especially within the pull-

apart basin between fault segments. In more detail, structural and tomographic studies in Tarutung and Sarulla geothermal fields, in northern Sumatra, shows that the magmatism interacted with the SGF where the fault zone acted as the hydrothermal fluid pathway (Hickman et al., 2004; Muksin et al., 2013).

The existence of lithospheric weakness zone would enhance the localisation of the trench-parallel shear strain and the manifestation of the strike-slip faults at the surface (McCaffrey et al., 2000). Meanwhile, the alignment of arc volcanoes at the surface is the manifestation of the arc-normal tension at the base of lithospheric flexure; hence the fault processes at the shallow depth may not be expected to influence the volcano location directly. In contrast to the assessment by Sieh & Natawidjaja (2000) on individual volcano location to the SGF, we compare the distance of SGF to volcano location mapped in our arc-segments to represent the structure at greater depth. Assuming both SGF and arc-segment developed within the lithospheric weakness zone, the average distance between both structures could indicate the width of the weakness zone. The rms-average distance between the SGF and arc-segments (ΔGC_F) ranges from 4.4 to 11.3 km and is significantly wider in the north at 24.1 km (**Figure 4.3**). This width of the weakness zone agrees with the maximum width of the zone at 25 km proposed by McCaffrey et al. (2000) which enhance the propagation of strike-slip fault. We also identified the shape of SGF segments in polynomial curves when plotted against the arc-segment distance (**Figure 4.3**). These curves are possibly the traces of shear faults in helicoidal geometry from the early development of strike-slip fault (e.g. Naylor et al., 1986; Richard et al., 1995; Xiao et al., 2017), indicating the possibility that SGF is actually relatively young. Therefore, we suggest that the slab pulled-down bent the upper plate and formed the lithospheric weakness zone where arc volcanoes and SGF co-located but no direct correlation expected from both of them. However, further analysis of the plate bending wavelength should also consider the plate thickness (Walcott, 1970) and rheology, especially the rigidity (Burov, 2011).

Toba is located at the stepover between the north and mid-north arc-segments where the proximity and overlap of the two arc-segments would extend the width of the deep lithosphere weakness zone. Extension of lithospheric weakness zone should be manifest structurally at Toba. The arc-segments would act as the boundary and control the general orientation of faults parallel to the weakness at the base of the upper plate. In the

caldera-forming eruption, the final shape of the caldera may be controlled by the pre-existing structures, such as regional faults (Cole et al., 2005). Gregg et al. (2012) also demonstrated that a large-scale caldera-formation requires fault propagation, induced by magma chamber overpressure, with orientations determined by the host rock strength. In **Figure 4.1D**, the orientation of north arc-segment is parallel to the northeast wall of the Toba caldera and mid-north arc-segment parallel to the west caldera wall. Therefore, the alignment between the arc-segment orientations and the northeast and southwest caldera margins is perhaps not a coincidence; in this interpretation, the caldera walls reflect the lithospheric scale weakness in great depth. Moreover, extension of the weakness zone should have generated strain oriented normal to the segment in the stepover area. Normal faults structures within Samosir Island within Toba caldera (**Figure 4.1D**) are compatible with this model as they mostly strike in NW-SE (Aldiss & Ghazali, 1984), which is parallel to the arc-segments and also the northeast and west caldera walls. Samosir formed due to a continuous magma influx prior to and after the latest caldera-forming eruption then caused the resurgence of the collapsed structure (Chesner & Rose, 1991). Accordingly, the NW-SE structures possibly initiated before the latest caldera-forming activity at Toba and were then reactivated during the resurgence (Chesner & Rose, 1991). The orientations of these contradict the pull-apart geometry model, suggested by Bellier & Sébrier (1994), which require high angle structures to the main stepover or the SGF (e.g. Christie-Blick & Biddle, 1985).

4.5.2 Young Slab and Toba Caldera

The Sunda trench west of northern Sumatra is indented (from 1°S to 2°N) indicating possible variation in the properties of the subducting slab, including age, thickness, buoyancy, and half-spreading rate. Jacob et al. (2014) determined ages along the N-S fracture zones at the ocean lithosphere between the Indian and Australian continents and identified a fossil spreading axis ridge formed at 34.7 Ma while the age of the flank, mostly already subducted under Sunda block, could reach 84 Ma. Changes in the age of oceanic lithosphere are usually associated with different thickness and buoyancy. Younger lithosphere would be thinner and more buoyant, so it would resist the subduction, while thicker and denser older lithosphere easier to subduct (R. S. White et al., 1992; Stern, 2002). Moreover, the

half-spreading rates possibly control the surface roughness of the slab which contributes to the subduction resistance (R. T. Bird & Pockalny, 1994). Slow spreading rate generates a smoother surface of the slab, hence it subducts easily, while faster spreading causes the opposite (Corbi et al., 2011; Tan et al., 2012). Müller et al. (2008) data display that the age and half-spreading rate of the oceanic lithosphere of Indo-Australian plate are also proportional to each other, hence the fast half-spreading rate might support the buoyancy in resisting the subduction. The younger part of the slab extends from 92°E to 98°E, or from 1°S to 2°N in latitudinal range, and so is likely to have been more resistant to subduction. This portion of the lithosphere, young with slow half-spreading rate, indented the trench within this margin range. Therefore, the variations in several slab properties possibly affect the trench margin geometry due to their resistance to subduction.

Since the trench margin near Toba is indented by the younger slab, we propose that the trench evolution in this range of the margin is associated with the development of the stepover geometry. Since subduction is directed towards NNE, the north arc-segment would have experienced the strongest lateral push due to the indented margin as the arc migrate northward. As the variation of slab age is observed laterally along the trench margin (**Figure 4.4**), this variation is also expected with the depth along the plate-to-plate coupling between the upper and lower plate (**Figure 4.5**). Hence, age and buoyancy variation with depth along the plate coupling would cause variation in the subduction rate, as slab pull force depends on the age of the lithosphere (Lallemand et al., 2005). At the greater depth, the oceanic lithosphere is older and less buoyant so slab pull and subduction rate are higher while it's younger near the surface. The difference in the subduction rate would extend the lateral distance of plate coupling from the trench or widening the down-pulled zone, therefore the arc-segment at the end of down-pulled zone migrate northward into the Eurasian Plate. Meanwhile, the SGF continued to develop at the surface, closer to the trench than arc-segment, because it initiated possibly before the trench evolved, therefore the distance between the north arc-segment to the SGF became wider (**Figure 4.3**). Furthermore, slab age changes are more significant near the IFZ (at 98°E), younger to west of IFZ and significantly older to the east of IFZ. Stronger lateral push at the west of IFZ would cause the north arc-segment to rotate counter-clockwise and the mid-north segment to rotate clockwise (**Figure 4.4**). The transition between the

north and the mid-north arc-segment develop the stepover geometry where Toba is now located. This would localise and extend the weakness zone between the two arc-segments and cause thinning of the arc lithosphere (**Figure 4.5**).

Trench margin indention would also affect the surface structures to form a salient geometry (Marshak, 2004). The predominant orientation of compressional structures changes gradually from around the south arc-segment (Group II orientation) to mid-north arc-segment (Group I orientation). These changes follow the trench margin orientation for each arc-segment and can be explained by convergence exerted normal to the trench. However, around the north arc-segment, the compressional structures are split between Group I and II (**Figure 4.2**). These patterns reflect the structural salient where thrust-and-fold orientations change along the segment, as also observed in map-view (shown in **Figure 4.1B** and **C**). The variations of slab age along the trench margin support the indenter-controlled salient model mechanism where more buoyant lithosphere advances the trench margin farther than the other parts (Macedo & Marshak, 1999). However, because the arc-segment remain in a straight alignment, possibly related to the slab age and buoyancy variation along the plate coupling. In the greater depth where slab is easier to subduct, the plate-to-plate contact is possibly less detached while the shallow crust is more detached, so the indenter affects the shallow deformation more than in great depth. There are also other factors that might influence the upper plate deformation, such as geothermal gradient and rheological stratification where the shallow depth is more brittle while the greater depth is more ductile (Ranalli & Murphy, 1987). Therefore, the structural salient only occurs in the surface, while in the greater depth arc-segment structures remain in a relatively straight alignment.

The north arc-segment migration and the thinning of arc lithosphere at Toba would imply to the amount of partial melting in the crust. Increased thinning in the lithosphere would trigger more melting in the mantle as it enhances mantle upwelling, heat energy accumulation, and can also accommodate more magma from the mantle (Latin & White, 1990). Mantle upwelling at extended lithosphere causes underplating which, in turn, enhances the lithospheric thinning due to the weaker rheology of the underplated material than the mantle (Yamasaki & Gernigon, 2009). High thermal energy would cause partial melting in the crust (Leeman et al., 2008) and supply more mafic magma to the system in

Toba as (Budd et al., 2017). Hence, we propose that lithospheric thinning and voluminous melt generation at Toba (Koulakov et al., 2016) are two processes that feed each other that were initiated by the migration of north arc-segment.

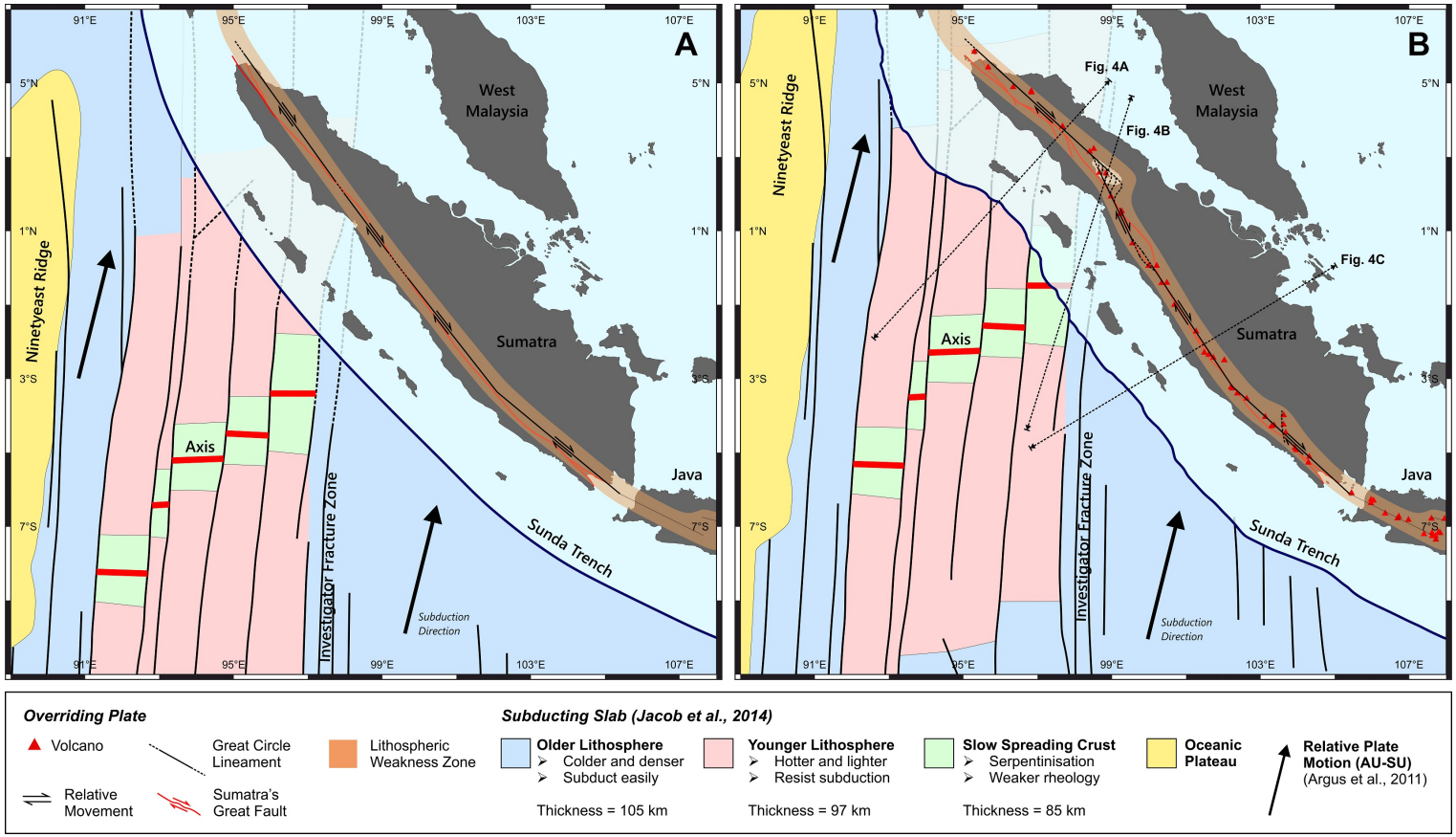

Figure 4.4. Interpretation of Sumatra tectonics and magmatism; (**A**) before subduction of the fossil spreading axis and (**B**) at the present day. The younger oceanic lithosphere (green and pink shades) between the Indian and Australian continents is more resistive to subduction than the older lithosphere (darker blue). Therefore, resistance differential to subduction modified the trench geometry pushing the northern part of the upper plate with stronger lateral push-force. This also rotated the north arc-segment counter-clockwise and extended the upper plate weakness zone around Toba. This arc-segment migration allowed thinning in the lithosphere generating more magma from the mantle and upper plate. Orange shades indicate the lithospheric weakness zone of approximately 25 km width where volcanoes and Sumatran Great Fault are located. Dashed lines mark the location of the schematic cross-section in **Figure 4.5**.

4.6 Conclusion

The distributions of Sumatran volcanoes in great circle segments reflect the structural control of the upper plate on the arc volcanism processes. Great circle alignments reflect arc-normal tension at the base of the flexed lithosphere. Plate bending defines the lithospheric weakness zone where the arc volcanism and the SGF developed. Toba is located at the stepover between the north and mid-north segments of Sumatran arc volcanoes. The stepover extended the area of lithospheric weakness zone and caused enhanced thinning in the upper plate due to the north arc-segment migration northeastward. The stepover was formed due to trench margin indentation when the young and buoyant slab offshore northern Sumatra resisted the subduction. Thinning in the lithosphere also enhanced the amount of melting in the crust in addition to high magma supply from the mantle wedge. Therefore, we propose that the caldera-forming eruption of Toba is triggered by both the voluminous amount of magma supply and the specific location that structurally allowed the formation of the extended lithospheric weakness zone.

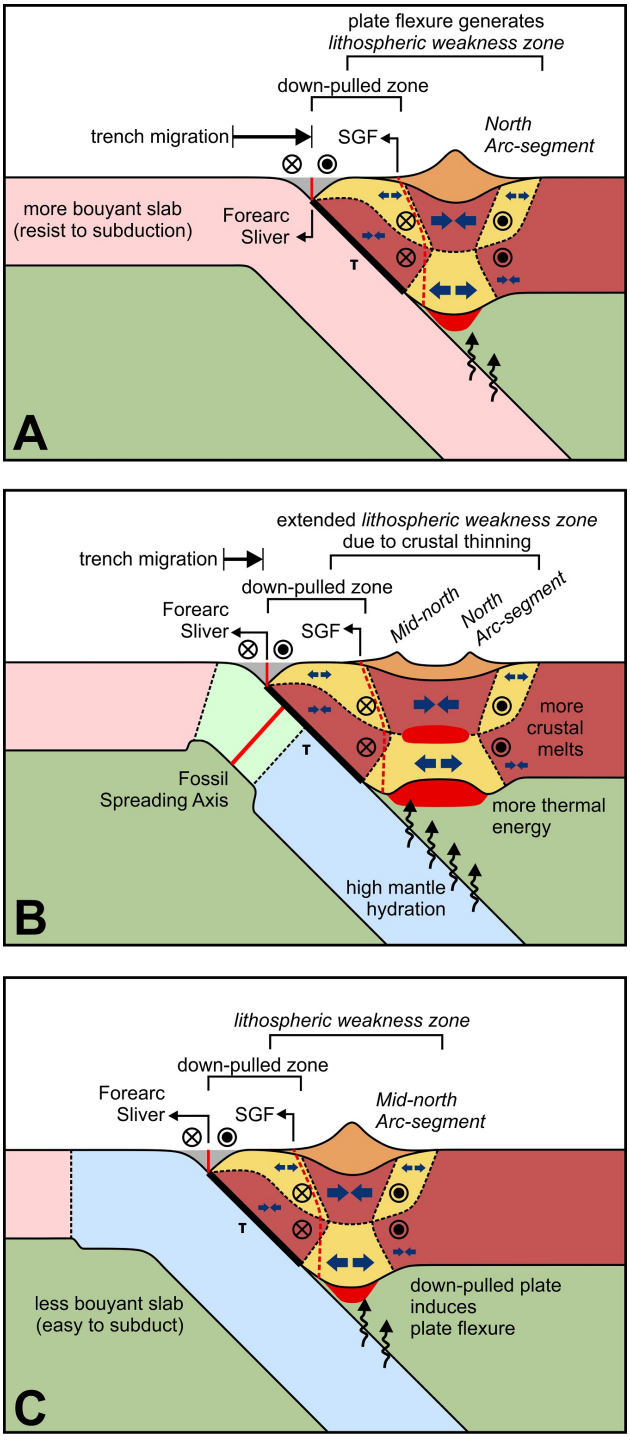

Figure 4.5. Schematic cross-sections of Sumatra (see **Figure 4.4** for location); (**A** and **C**) Through most of the arc a weakness zone occurs due to lithosphere flexure in response to the down-pulled upper plate. This zone concentrates development of the volcanic arc and Sumatran Great Fault. (**B**) Crustal thinning in Toba occurs as the result of the arc-segment migration as younger oceanic lithosphere subducted and the lithospheric weakness zone widens. Thinning allows more melting in the mantle and in the crust. The extra heat supplied to the crust allows greater crust melting encouraging formation of extensive silicic magmatism and caldera-forming supereruption. **Cross-section A** and **B** illustrate the trench migration, compared to cross-section **C** as the result of slab age and buoyancy.

Chapter 5

The Role of Arc Lithosphere in the Segmentation of Volcanic Arcs

Abstract

The locations of arc volcanoes are usually viewed as being situated above the locus of melting in the mantle which itself is interpreted as a function of slab dehydration at some critical depth. This critical depth was inferred as the depth from arc to slab while assuming that arc volcanoes are distributed as small circles on the Earth's surface. However, this approach does not account for how the upper plate may influence arc volcano locations. Instead, we fit great circles on arc volcano distribution and suggest the distance from trench to arc-segment as an important variable to address arc volcano location. Using statistical quantification by Hough Transform analysis of 19 arcs we show that volcanoes in most arcs are distributed as segments of great circles, rather than single or multiple small circles. We compare subduction dynamic variables with properties of these segments to determine which factors most probably control arc-segment location. The arc-segment distance from trench is correlated with the crustal thickness ($R = 0.57$) and the shallow slab dip ($R = -0.74$), while the latter two also correlated ($R = -0.76$) with each other. The great circle alignments reflect the arc-normal tension at the base of upper plate as the result of stress regime partitioning by lithosphere flexure. At subduction margin, plate flexure occurs at the end of down-pulled zone where the breadth of such zone is defined by the coupling between upper and lower plates. Thicker crust and shallower slab dip both lead to wider plate coupling zones that locate lithosphere flexure and arcs farther from the trench. Therefore, we propose that the thickness of the upper plate and slab dip in shallow depth control the location of arc volcano segments relatively to the trench.

5.1 Introduction

Arc magmatism in subduction zones reflects processes at various depths from the surface to the mantle wedge and the slab. Studies of the controlling variables that determine the location of arc volcanoes have been focusing on processes occurring in the mantle wedge. The depth to the slab under the arc, H, has been proposed as the key indicator to where an arc would be located on the basis that it denotes a critical phase where fluid addition from the slab would trigger melting in the mantle (e.g. Gill, 2012; Jarrard, 1986; Tatsumi, 2005). England et al. (2004) showed that the average H for arcs varied from 65 km to 130

km and was inversely proportional to the descent speed of the slab, $Vdes$. The correlation of H and $Vdes$ underlined their model in which changes in the mantle wedge thermal structures would concentrate and channel melts to form magma pathway at the base of the upper plate (England & Katz, 2010; Perrin et al., 2018). Other alternatives focussed on the location where slab dehydration occurring in which the descent speed of the slab is also suggested to control the process (e.g. Schmidt & Poli, 1998; Grove et al., 2009).

However, the relationship between H and $Vdes$ was established by assuming that arc volcanoes are aligned in a small circle patterns (e.g. Tovish & Schubert, 1978; England et al., 2004). The small circle assumption neglects any possible controlling variables from the upper plate and generalises any lateral variation along an arc. Pacey et al. (2013) recognised great circle or linear segmentation of arc volcanoes in Sunda Arc based on a quantitative approach and suggested that the segmentation is related to upper plate stress. Furthermore, Andikagumi et al. (2020) has demonstrated that the distributions of arc volcanoes are also better approximated as a series of great circles rather than single or multiple small circles. They also proposed that the alignment of volcanoes in great circle segments is associated with arc-normal tension located at the base of the upper plate which creates a magma pathway. This tensional stress regime is due to lithosphere flexure created by the downward-pull force exerted by slab motion on the overriding plate.

Moreover, Syracuse & Abers (2006) observed no correlation between H and $Vdes$ when assessing the subduction dynamic variables at individual volcanoes or the average values for each arc. The same study also showed the wide range of H values within an arc, such as a 70 km range of H along Java and Central America, while convergence rate does not change significantly along the arc. Some arcs also have high uncertainty when determining H; such as in New Zealand, Mariana, Vanuatu, Nicaragua and Scotia (England & Katz, 2010). Subsequently, Syracuse et al. (2010) showed that some of the slab dehydration reaction that control melting in the mantle actually occur before the slab reaches the depth under the arc, H. For these reasons, H is not a straight-forward variable in defining the location of a volcanic arc. Instead, the distance from trench to arc (Dt), also used by Perrin et al. (2018) in their thermal modelling study, is a more direct parameter to denote the arc location.

In this study, we apply geometric fitting to the distribution of Holocene volcanoes in 19

arcs around the world (**Figure 5.1**). Some arcs are not included due to the complexity of the subduction processes and their tectonics such as Philippine island arc, Halmahera and Sangihe arc, Banda arc, and Solomon arc (e.g. Yang et al., 1996; Hall, 2000; Spakman & Hall, 2010; Holm et al., 2016). Here we show that distributions of arc volcanoes are better fitted with great circles, rather than single or multiple small circles, based on quantitative and statistical approaches. This finding implies that the stress regime of the upper plate controls magma transport through the lithosphere and the location of volcanoes at the surface. We also compile estimates of dynamic variables from recent studies on subduction systems and compare with the best geometrical attributes from our analysis of arc volcano distributions. This study focuses on the location of the arc-segment, expressed by Dt, and the controlling variables that determine where the lithospheric flexure occurs in the upper plate. We suggest that upper plate thickness and the dip of the slab at depths less than 125 km are the main dynamic variables in controlling the location of volcanic arc.

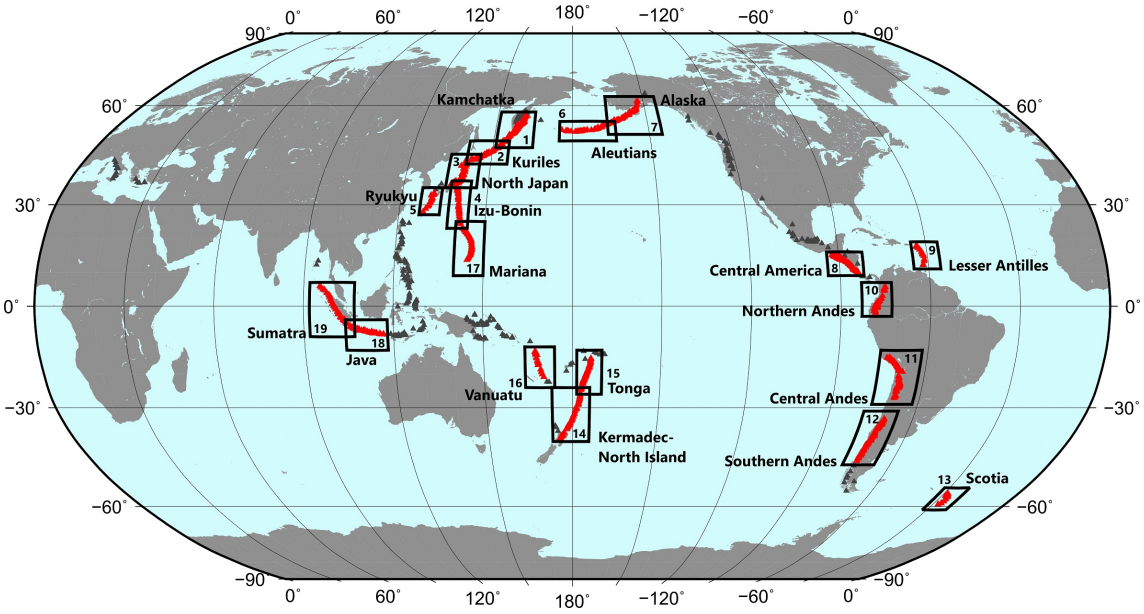

Figure 5.1. Global distribution of arc volcano locations (triangle markers), compiled from the Smithsonian Institution's Global Volcanism Program (2013), global study by Syracuse & Abers (2006) and Lallemand et al. (2005), regional scale study in Java (Pacey et al., 2013) and Mariana (Andikagumi et al., 2020). Arcs that are included in the study marked with rectangles and arc volcanoes with red triangles:[1] Kamchatka, [2] Kuriles, [3] North Japan, [4] Izu-Bonin, [5] Ryukyu, [6] Aleutians, [7] Alaska, [8] Central America, [9] Lesser Antilles, [10] Northern Andes, [11] Central Andes, [12] Southern Andes, [13] Scotia, [14] Kermadec-North Island, [15] Tonga, [16] Vanuatu, [17] Mariana, [18] Java and Lesser Sunda, [19] Sumatra.

5.2 Data and Methodology

Arc volcano location datasets were compiled from the Smithsonian Institution's Global Volcanism Program (2013), previous global scale arc volcano studies (e.g. Syracuse & Abers, 2006; Lallemand et al., 2005), and regional scale studies such as in the Mariana (Andikagumi et al., 2020) and the central Sunda Arc (Pacey et al., 2013). Datasets were also verified by examining individual volcano morphology on Google Earth aerial imagery. In total, the datasets comprise 773 volcanoes in 19 arcs (**Figure 5.1**; **Appendix B**). In this study, some volcanoes in these 19 arcs were excluded due to their complex setting. For instance, we exclude volcanoes in northern part of Izu-Bonin arc as they are located around the triple junction plate boundary (trench-trench-trench) and may be influenced by more than one slab.

The spatial distributions of arc volcanoes were then analysed to determine the best-fit geometry by comparing their goodness-of-fit. Andikagumi et al. (2020) has demonstrated that Mariana Arc volcanoes are better fitted with great circles rather than a single or segmented small circle. Here we fit geometries using the same method we employed in the Mariana Arc (Andikagumi et al., 2020). First, we used the Hough Transform, a mathematical feature-extraction method, to identify the alignment and segmentation of arc volcanoes in each arc. Volcanoes which lie more than 30 km from any great circle trend are classified as off-segment and excluded in further analysis (marked in the **Appendix B**). Pacey et al. (2013) showed that such volcanoes in Java and the Lesser Sunda have distinctive, non-subduction sources or associated with major upper plate structures. Next, for comparison purpose we applied small circle fitting to the volcano dataset; both at each arc as a whole and for the segments identified with the Hough Transform. The rms-misfit of volcanoes to the great circle trend (ΔGC) then compared to the rms-misfit from the small circle (ΔSC) as the first basis in establishing the preferred geometry. Andikagumi et al. (2020) used two approaches in determining which of segmented great circles, a single small circle, or segmented small circles provide the best fit to an arc: the corrected Akaike Information Criterion (AICc) and residual analysis. They also show that the outcomes from AICc method are similar to those from residual analysis. Since AICc is a statistical method and better in handling large numbers of model comparisons, we only use AICc

here in determining the preferred volcano distributions. The AICc parameter takes into account the volcano misfits, the number of volcanoes, and the degree of freedom in each model. The AICc value represents the information lost in geometry fitting, hence a lower AICc value indicates the preferred model.

Subduction dynamic variables were gathered from various sources of global scale studies and averaged at each arc-segment. The full list of the subduction dynamic variables and the abbreviation used in this study are listed in **Table 5.1** and illustrated in **Figure 5.2**. Slab dip (δ) data were based on contours of Wadati-Benioff zones from earthquakes hypocentres and averaged within the 50-250 km depth range (Syracuse & Abers, 2006). Lallemand et al. (2005) separated the slab dip into a shallow dip for depth less than 125 km (δs), and a deep slab dip for portions deeper than 125 km (δd). They also describe the slab geometry using slab length (L), estimated from the slab dip and maximum depth (670 km). We determine depth to slab under the arc (H) from the SLAB2 model (Hayes et al., 2018), which images the slab in three-dimensional geometry from extensive seismicity data. Subduction rate ($Vtot$) and direction was calculated using the MORVEL tool (Argus et al., 2011) with no-net-rotation reference frame and the subducting slab was set to move relative to the fixed overriding plate. Slab properties near the trench, the slab age (Age) and the half-spreading rate of the slab formation (Vhs), were obtained from Müller et al. (2008) based on magnetic anomalies and the global set of finite rotations. For the upper plate properties, the classification of upper plate nature (UPN), as continental or oceanic, and upper plate strain (UPS), from active extension (E3) to active compression (C3), were taken from Lallemand et al. (2005). We also included other variables that have been investigated in previous studies such as trench sediment thickness (Ts; Heuret et al., 2012), thermal parameter (ϕ; Kirby et al., 1996) and slab-pull force (Fsp; Carlson et al., 1983).

Some subduction dynamic variables are derived from other variables. Total convergence rate ($Vtot$) and slab dip (δ) are the main variables used to calculate other types of slab velocity. Orthogonal speed ($Vort$) is derived from the total convergence rate ($Vtot$) and obliquity angle (Ao). $Vdes$ is calculated from $Vort$ using the average dip from 50 to 250 km (δ). Lateral speed of the slab ($Vlat$) is calculated from $Vort$ and the shallow slab dip (δs) as the upper plate thickness is generally less than 125 km. $Vdes$ contributes to

the value of the thermal parameter (ϕ) as well as the age of the slab. Slab-pull force (Fsp) is dependent on the age and length (L) of the slab. Relative trench depth ($Htrel$) is the sum of average elevation (He) and trench depth (Ht).

We use crustal thickness as a proxy for upper plate thickness because of higher uncertainty and on-going researches in establishing global lithospheric thickness model (e.g. Conrad & Lithgow-Bertelloni, 2006; Pasyanos, 2010). The most current global lithospheric thickness model (i.e. LITHO1.0) was introduced by Pasyanos et al. (2014) based on surface wave inversion and included the crustal thicknesses from CRUST1.0 by Laske et al. (2013) as one of the components for estimating the lithosphere thickness. Therefore, the trend of upper plate thickness at a subduction zone margin is expected to align with the trend acquired from crustal thickness model (Turner et al., 2016). Crustal thickness (Tc) data was extracted from CRUST1.0 model (Laske et al., 2013), a development from the previous model CRUST5.1 by Mooney et al. (1998). This crustal thickness model is mainly based on the compiled seismic refraction surveys and studies of global ice and sediment thickness.

Table 5.1. Abbreviation list of subduction dynamic variables

Category	Abbr.	Variables	Unit	Function
Segment related	nV	Number of volcanoes	-	-
	$Lseg$	Segment length	km	-
	$S.Az.$	Orientation of arc-segment (clockwise from North)	°	
	$Mrms$	Root-mean-square misfit	km	-
Trench related	Dt	Distance from trench to segment	km	-
	$T.Az.$	General orientation of trench	°	-
	At	Angle between arc-segment and trench	°	
	Ts	Sediment thickness at trench	km	-
	Ht	Trench depth	m	-
	$Htrel$	Relative trench depth, measured from He	m	$He + Ht$
Slab related	δ	Average slab dip (50-250 km depth)	°	-
	δs	Shallow slab dip (less than 125 km)	°	-
	δd	Deep slab dip (depper than 125 km, up to 670 km depth)	°	-
	Ao	Obliquity angle between the subduction direction and trench-normal orientation	°	-
	$Vtot$	Convergence rate	mm/year	-
	$Vort$	Trench-normal convergence rate	mm/year	$Vtot \times \cos Ao$
	$Vdes$	Descent rate of the slab	mm/year	$Vort \times \sin \delta$
	$Vlat$	Lateral rate of the slab	mm/year	$Vort \times \cos \delta$
	H	Depth to the slab under the arc	km	-
	Vhs	Half-spreading rate of the slab formation near the trench	mm/year	-
	Age	Age of the slab near the trench	Ma	-
	Fsp	Slab pull	(10^{12} N/m)	$K \times \Delta\rho \times L \times \sqrt{\delta}$
	ϕ	Thermal parameter	km	$Age \times Vdes$
	L	Slab length	km	$125/\sin\delta_s + (Dmax - 125)/\sin\delta_d$
Upper Plate related	Tc	Crustal thickness	km	-
	He	Average elevation of the arc segment	m	-
	UPN	Upper plate nature, continental (C) or oceanic (O)	-	-
	UPS	Upper plate strain, from active extension (E3) to active compression (C3)	-	-

Explanation: $\Delta\rho$ = mean density difference between the slab and the surrounding asthenosphere, constant, 80 km/m^3,
K = constant, 4.2 times gravitational acceleration (9.81 m/s^2), Dmax = maximum slab depth (670 km)

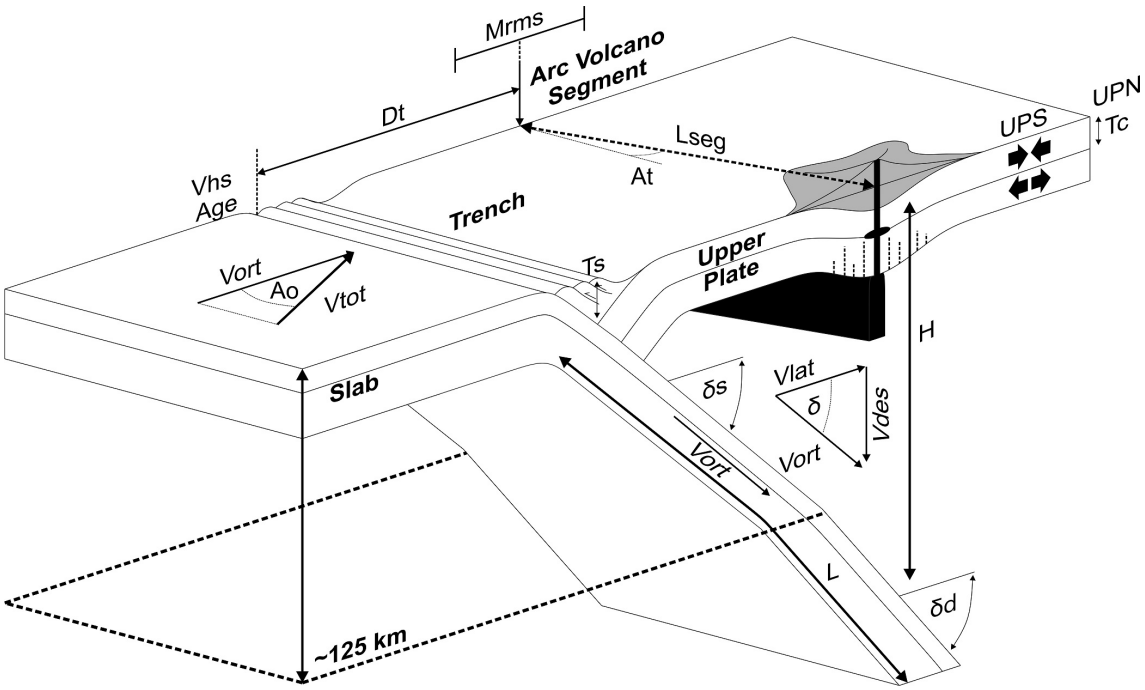

Figure 5.2. Schematic diagram of subduction dynamic variables. Variables are classified into arc-segment related, slab-related, upper plate-related and trench-related variables. Slab dip variables have three categories: average (δ), shallow (δs, less than 125 km) and deep (δd, deeper than 125 km). Convergence rates, $Vtot$, are calculated using NNR-MORVEL by Argus et al. (2011) where the upper plate is fixed and subducting slab moves. Orthogonal speed, $Vort$, is the trench-normal convergence rate, calculated from $Vtot \times Ao$, the obliquity angle. Descent rates ($Vdes$) and lateral rates ($Vlat$) are calculated from $Vort$ and δ. Full abbreviation list in **Table 5.1**. Diagram is not to scale.

We determined correlations between the subduction dynamic variables and arc distribution properties from the geometric fitting to investigate the possible factors that control the arc location. Correlations of the variables were divided into three categories. Correlations based on numerical values were calculated using standard Pearson correlation coefficient (R), ranging from -1 to 1, together with their significance (p-value). Correlations for non-numerical values, mainly for UPN and UPS, were judged by visual inspection on the scatter plots. Finally, strong correlations or trends are expected between variables and its derivatives, such as the convergence rate ($Vtot$) and its derivatives (i.e. $Vort$, $Vdes$, $Vlat$), because the derivative variables are the product of the main variables calculated using a certain function (**Table 5.1**).

5.3 Results

5.3.1 Geometric Fitting

Based on Hough Transform analysis, great circle arc-segments were identified in each arc. The number of segments varies but each arc has at least two great circle segments (Ryukyu and Scotia), while the maximum is five segments (Kuriles, Central America, Tonga, and Mariana). Misfits for the great circle patterns (ΔGC) vary from 2.7 km (Mariana) to 14.5 km (Central Andes) with an average value of 7.0 km (**Table D.2** and **D.3**). These misfits are substantially lower than those for small circles. The rms-misfit of the best-fit small circle (ΔSC) range from 3.9 km (Lesser Antilles) to 28.0 km (Sumatra) with the average being 13.1 km (**Table D.1**). The radii of the best fit small circles range from 281 km (Scotia) to 8,403 km (Sumatra), which almost approaches the radius of a great circle. **Figure 5.3** demonstrates a comparison of great circle and small circle distribution models for the Kamchatka Arc. Comparison of the rms-misfit values of volcano distribution fitting shows that great circle patterns are preferred as ΔGC values are generally 0.6 to 18.9 km less than the ΔSC, except in Scotia arc where ΔSC is 3.6 km less than ΔGC.

The number of degree of freedom between great and small circles are different, hence we use AICc parameter to allow direct comparison between these distribution models. For an even more robust comparison, we also compare the AICc values for a single small circle fit, a series of great circle segments, and a series of small circle segments. Small circles were fitted to each segment identified as potential great circle segment using the Hough Transform analysis (**Table D.4**). The purpose of this comparison is to evaluate the possibility of volcano distribution in multiple small circles within the arc as an alternative model to a series of great circles.

Table 5.2 provides the AICc parameters calculated for each distribution model at each arc. The AICc parameters of the great circle model are the lower than single or multiple small circle models in 16 arcs. Since AICc represents the goodness-of-fit from each distribution model, volcanoes in these 16 arcs are better described as a series of great circle segments. Three arcs, the Lesser Antilles, Scotia, and Vanuatu, have the lowest AICc value for a single small circle model. The AICc values favour the single small circle model in these arcs because of the high ratio between adjusted parameters

(k) and the number of volcanoes (nV) in most segments. Moreover, fewer submarine volcanoes have been identified or even explored for, in these island arcs. A detailed study of submarine volcano locations can make a substantial difference to the preferred distribution model as demonstrated for the Mariana Arc (Andikagumi et al., 2020). Exploration of submarine volcanoes in these arcs, such as in Lesser Antilles has been going on and show the control on the upper plate deformation to the volcanism (Feuillet et al., 2002). Because of the uncertainty in the number of volcanoes within these arcs, we exclude them from the multivariate analysis. The remaining 16 arcs cover 16,500 km or about 91% of the total length of the 19 arcs included in this study. In addition, one of the segments in North Japan Arc is also excluded in the multivariate statistics as it is terminated at its southern end by trench-trench-trench subduction zone and so is probably influenced by two slabs. Therefore, based on the constant lower Mrms and lower AICc values, we infer that volcanoes in the 16 arcs are aligned in segmented great circle distributions.

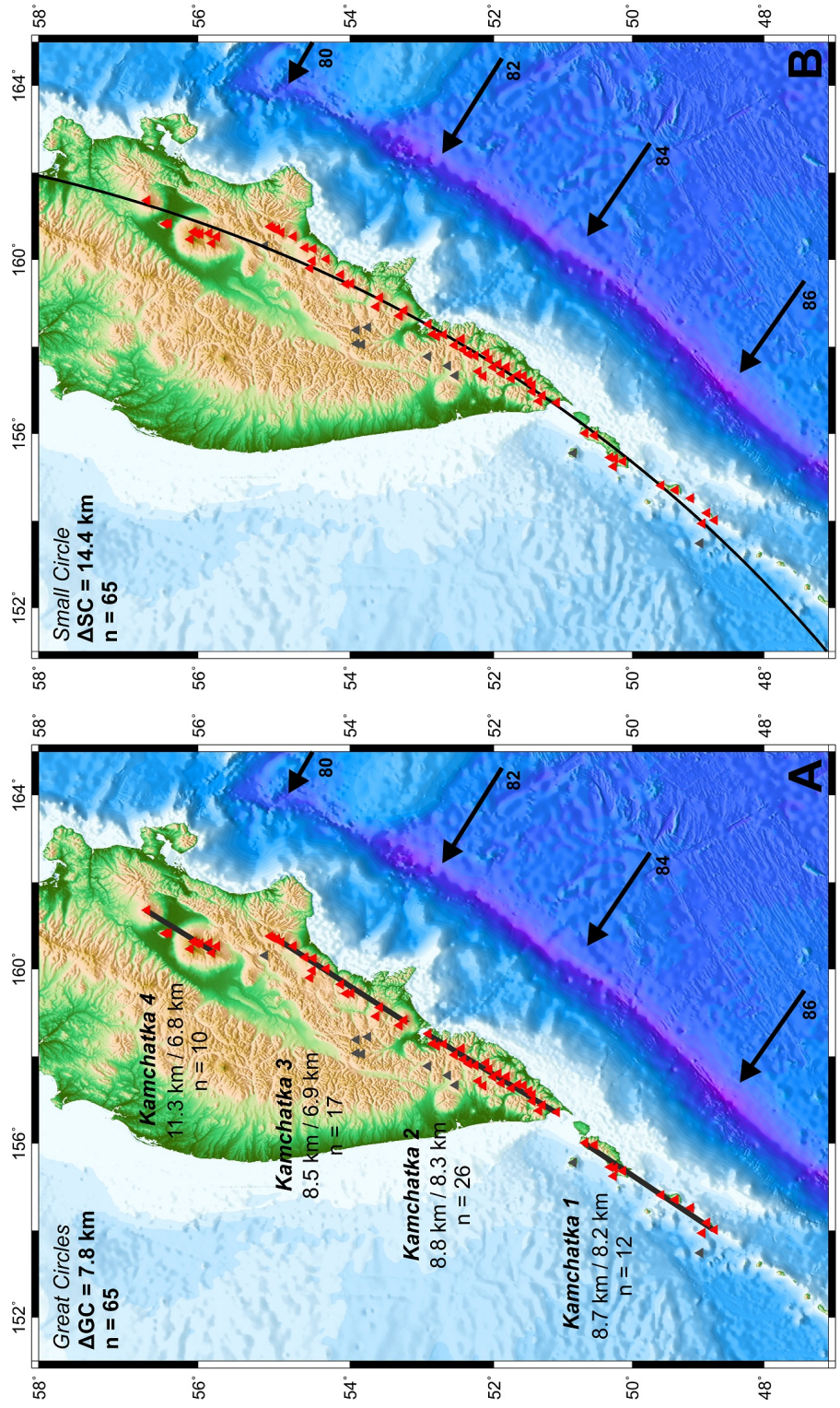

Figure 5.3. Geometric fitting of Kamchatka arc volcanoes. (**A**) Great circle segments identified from Hough Transform analysis. (**B**) Best fit small circle for the volcanoes associated with great circle segmentations (n = 65, solid line). Red triangles are volcanoes associated with great circle segments while the grey triangles are classified as off-segment volcanoes due to the distance from the trend of great circle alignments (30 km). ΔSC and ΔGC are the root-mean-square misfit of the volcanoes from the small and great circles Black arrows indicating the subduction direction of Pacific Plate to Eurasia Plate, calculated from Argus et al. (2011). Geometric fittings for the other 18 arcs are presented in the **Appendix D**, **Figure D.1-D.19**.

Table 5.2. Corrected Akaike Information Criterion (AICc) of geometric fitting on arc volcanoes

No.	Arc Name	nV	Single Small Circle				Segmented Great Circles				Segmented Small Circles			
			k	RSS	AIC	AICc	k	RSS	AIC	AICc	k	RSS	AIC	AICc
1	Kamchatka	65	3	207.62	156.62	157.02	8	60.19	131.67	***134.24***	12	65.27	141.95	147.95
2	Kuriles	39	3	82.94	80.83	81.52	10	18.25	69.19	***77.05***	15	17.57	78.54	99.41
3	North Japan	30	3	501.40	87.01	87.93	6	116.72	74.01	***77.67***	9	120.74	80.46	89.46
4	Izu-Bonin	24	3	24.88	39.50	40.70	4	18.47	38.40	***40.50***	6	70.89	56.41	61.36
5	Ryukyu	15	3	42.94	30.49	32.68	4	22.24	28.21	***32.21***	6	30.88	34.34	44.84
6	Aleutians	37	3	95.78	79.31	80.03	8	35.65	73.43	***78.57***	12	41.28	83.78	96.78
7	Alaska	43	3	255.09	109.49	110.10	8	42.26	85.91	***90.15***	12	36.61	91.24	101.64
8	Central America	66	3	204.81	158.55	158.94	10	43.00	127.81	***131.81***	15	46.79	140.23	149.83
9	Lesser Antilles	17	3	14.99	25.99	***27.84***	6	9.68	28.76	37.16	9	7.06	32.43	58.14
10	Northern Andes	25	3	275.44	67.00	68.14	8	31.80	53.56	***62.56***	12	37.19	63.26	89.26
11	Central Andes	57	3	682.41	167.54	167.99	8	210.17	148.39	***151.39***	12	183.89	153.08	160.17
12	Southern Andes	49	3	113.60	106.71	107.25	6	79.39	105.09	***107.09***	9	101.19	116.25	120.87
13	Scotia	8	3	38.99	18.73	***24.73***	4	97.78	23.92	37.26	6	6.62	18.57	102.57
14	Kermadec-North I.	40	3	47.65	73.12	73.79	6	24.32	67.44	***69.99***	9	66.57	90.93	96.93
15	Tonga	43	3	150.09	99.58	100.20	10	33.08	85.34	***92.21***	15	35.47	96.64	114.42
16	Vanuatu	16	3	218.81	43.44	***45.44***	6	108.32	44.56	53.89	9	67.56	47.27	77.27
17	Mariana	37	3	71.05	74.51	75.24	10	7.33	52.02	***60.48***	15	10.05	67.08	89.94
18	Java	36	3	306.26	95.50	96.25	6	42.92	70.77	***73.67***	9	58.32	81.57	88.49
19	Sumatra	37	3	784.63	113.10	113.83	8	83.64	87.13	***92.27***	12	88.52	96.04	109.04

Explanation: nV = number of volcanoes, k = number of adjustable parameters, RSS = residual sum of squares,
AIC = Akaika Information Criterion, AICc = corrected Akaike Information Criterion

5.3.2 Relation with Subduction Dynamics

The relationships between our arc volcano great circle segments and subduction dynamic variables, such as convergence rate ($Vtot$) and slab dip (δ), were explored. The correlation analyses includes the following great circle arc-segment properties: arc-segment distance from trench (Dt), segment length ($Lseg$), rms-misfit ($Mrms$), and angle to trench (At). **Table 5.3** provides the example dataset used in the multivariate correlation analysis, while the full table are presented in **Table F.1** to **F.3** in **Appendix F**. Correlation among 26 variables related to the arc-segment properties and subduction dynamic parameters are displayed in the circular graphs on **Figure 5.4**. **Figure 5.4A** shows the expected correlation between variables which are derived from another variables (**Table 5.1**), such as $Vtot$, $Vort$, $Vdes$, and $Vlat$. Since these variables were derived from other variables (mentioned above), such correlation are will not be discussed further.

Table 5.3. Example of subduction dynamic variables. Full tables are presented in Supporting Information

Arc-segment	**nV**	**Lseg** (km)	**Mrsm** (km)	**Dt** (km)	δ (°)	δs (°)	δd (°)	**H** (km)	**Vtot** (mm/yr)	**Age** (Ma)	**Tc** (km)	**He** (km)
01 Kamchatka 1	12	258	8.3	198	50	36	50	81	86	108	26	18
02 Kuriles 2	8	125	2.4	200	47	32	46	89	89	117	22	125
03 North Japan 3	10	330	6.6	298	29	21	27	96	92	131	31	220
04 Izu-Bonin 1	9	407	3.9	202	49	30	56	100	46	136	16	-930
05 Ryukyu 2	9	334	5.8	228	57	26	64	116	69	34	33	304
06 Aleutians 1	5	92	0.9	185	46	32	-	83	69	56	28	184
07 Alaska 2	16	206	7.7	315	43	22	44	75	60	44	33	729
08 Central America 3	8	127	1.1	174	61	32	66	127	74	24	28	227
09 Lesser Antilles 1*	4	198	2.2	444	41	34	55	79	20	92	20	-950
10 Northern Andes 2	4	188	2.0	297	37	26	45	147	60	12	44	3251
11 Central Andes 3	20	367	12.2	325	28	18	45	108	73	50	62	3958
12 Southern Andes 1	17	409	9.6	261	28	22	35	106	74	35	49	2607
13 Scotia 2*	4	192	13.9	152	61	51	78	114	76	32	7	-1302
14 Kermadec-North Island 1	15	508	5.8	226	52	-	-	87	45	121	24	944
15 Tonga 2	15	253	8.0	195	51	39	56	80	74	95	10	-1399
16 Vanuatu 3*	5	127	16.4	178	69	52	82	162	95	-	10	-895
17 Mariana 4	7	199	3.2	201	61	36	84	122	32	145	7	-1855
18 Java LS 1	13	288	6.2	252	49	27	70	81	64	102	31	694
19 Sumatra 2	5	235	4.4	277	46	28	40	109	55	44	33	1035

Explanation: nV = number of volcanoes, $Lseg$ = segment length, $Mrms$ = root-mean-square misfit, Dt = arc-segment distance from trench, δ = average slab dip, δs = shallow slab dip (less than 125 km), δs = deep slab dip (deeper than 125 km), H = depth to the slab beneath the arc, $Vtot$ = convergence rate, age = slab age, Tc = crustal thickness, He = average elevation

* = Segments are not included in the multivariate statistics (see main text)

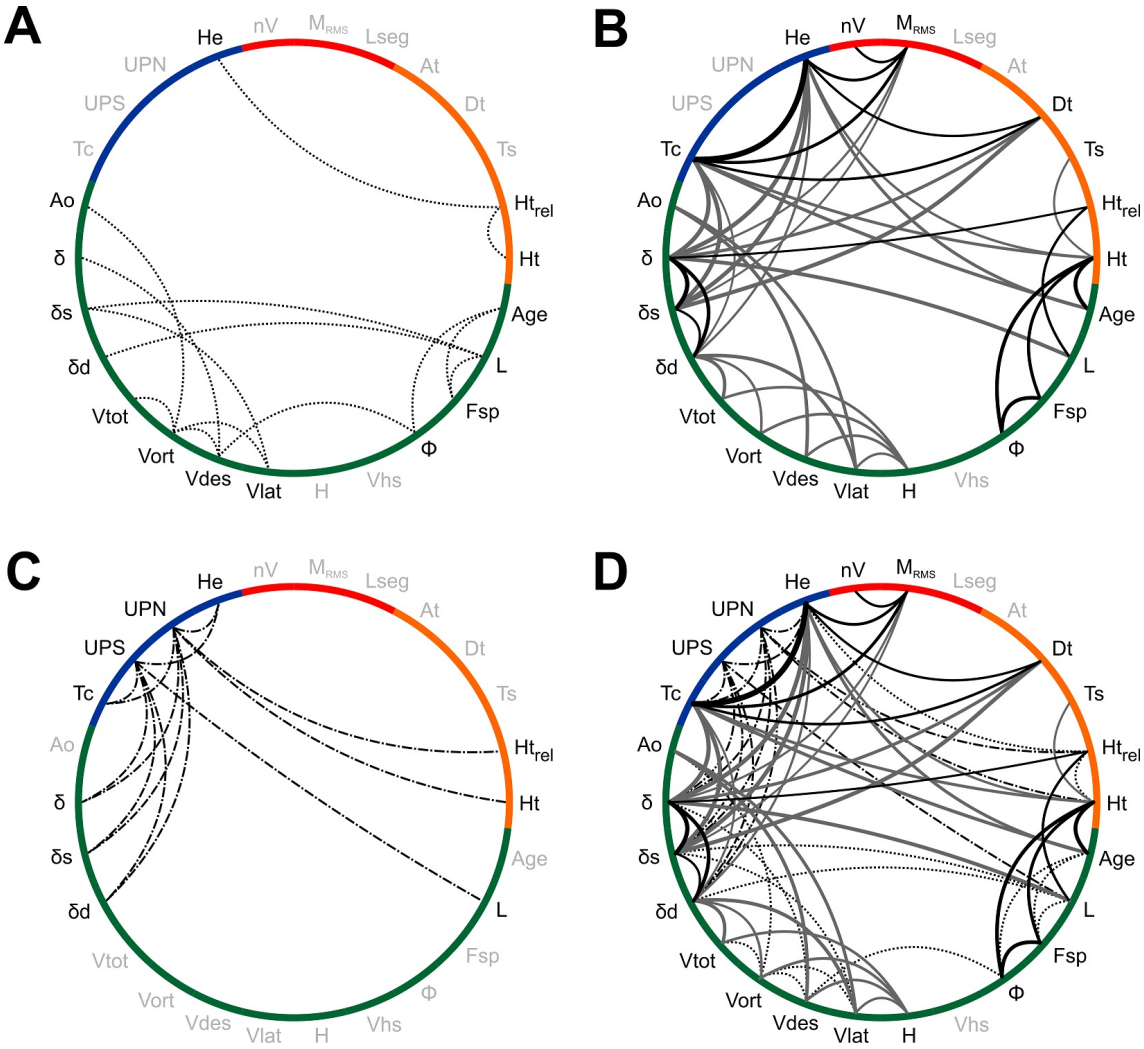

Figure 5.4. Circular charts showing relationship between subduction dynamic variables and great circle arc-segmentation from 16 arcs. (**A**) Circular graph demonstrating the variables that are related as a function of other variables. (**B**) Cross-correlation of numeric variables. Black lines indicate proportional correlation ($R \geq 0.5$) and grey lines for inversely proportional correlation ($R \leq -0.5$). Line thickness indicates the strength of the correlation. (**C**) Non-numerical trend observed from scatter plot. (**D**) Compilation of the function, numeric cross-correlation and non-numeric trends diagrams. Full table of coefficient of correlation between numeric variables and their p-values are presented in **Table G.1** and **G.2** in the **Appendix G**.

Based on the coefficient of correlation (**Figure 5.4B**), the parameters which are mostly correlated to other variables are the arc-segment distance from trench (Dt), crustal thickness (Tc), slab dip (δ, δs, δd), volcano rms-misfit ($Mrms$), average elevation (He), and trench depth (Ht). The arc-segment distance from trench correlates with the thickness of the upper plate ($R = 0.57$, $p \approx 0.00$), the average elevation along the segment ($R = 0.54$, $p \approx 0.00$), the average slab dip ($R = -0.64$, $p \approx 0.00$) and the shallow slab dip ($R = -0.74$, $p \approx 0.00$). The crustal thickness and the average elevation have the strongest

correlation between each other ($R = 0.94$, $p \approx 0.00$) and mostly correlates with the same other variables. The crustal thickness is proportional to the volcano rms-misfit ($R = 0.63$, $p \approx 0.00$) and inversely proportional with the trench depth ($R = -0.61$, $p \approx 0.00$), average dip ($R = -0.77$, $p \approx 0.00$), shallow dip ($R = -0.76$, $p \approx 0.00$), deep dip ($R = -0.50$, $p \approx 0.00$), and slab age ($R = -0.66$, $p \approx 0.00$). The volcano rms-misfit at each segment also relates to the number of volcanoes at each segment ($R = 0.55$, $p \approx 0.00$), slab dip ($R = -0.52$, $p \approx 0.00$) and shallow slab dip ($R = -0.50$, $p \approx 0.00$). We also observe the correlation of other subduction dynamic parameters such as between the depth to the slab with the descent speed of the slab ($R = -0.58$, $p \approx 0.00$). The trench depth is correlated with sediment thickness ($R = -0.51$, $p \approx 0.00$), slab age ($R = 0.73$, $p \approx 0.00$), slab pull ($R = 0.64$, $p \approx 0.00$), and thermal parameter ($R = 0.70$, $p \approx 0.00$). Nonetheless, some variables have no correlation at all which are the half-spreading rate of the slab, length of the arc-segment and the angle between the arc-segment and the trench.

Trends for non-numeric variables shown are summarised on (**Figure 5.4C**) and presented in detail in the **Appendix G**, **Figure G.5** and **G.6**. Slab dip tends to be shallower under continental upper plates than oceanic upper plate. The upper plate nature (UPN) also shows a consistent trend with the crustal thickness where oceanic upper plates has the crustal thickness ranging from 7 to 15.9 km while continental from 18 to 62 km. Furthermore, the upper plate strain (UPS) also exhibits a possible trend with slab dip where shallow slab dip is associated with the upper plates that display compressional structure at the surface. Meanwhile, the upper plate with backarc spreading is usually associated with steeper slab dip. Upper plates with active compression also tend to be associated with thicker arc crust while active extension is found with thinner arc crust. The slab length also has a possible trend with the UPS where longer slab length correlates with compressional upper plate. The trends observed in this study regarding the UPN and UPS and the other subduction dynamic parameters are similar to what have been discussed by Lallemand et al. (2005), thus it demonstrate the plausibility of our dataset compilation. The plausibility of our dataset are also supported by the correlations shown by trench depth (Ht and $Htrel$) and other variables, which are similar to what have been demonstrated in previous studies (Vlaar & Wortel, 1976; Hilde & Uyeda, 1983; Jarrard, 1986; Zhong & Gurnis, 1992; Gurnis et al., 719-727; Simpson, 2010). Nevertheless, since such

correlations are not directly related to the arc-segment, these variables are not discussed further.

5.4 Discussion

Great circle segments better describe the alignment of volcanoes in 16 arc systems compared a single or segmented small circles. The volcano misfit from great circle distribution pattern (ΔGC) is consistently less than the misfit of a single small circle (ΔSC). The AICc parameter corroborated the segmented great circle distribution model for arc volcanoes. Andikagumi et al. (2020) proposed that alignment of volcanoes in great circle segments reflects arc-normal tension in the deep upper plate, probably due to lithospheric flexure. Their study of the Mariana Arc showed the consistent association of volcano alignment with arc-normal tension at the base of flexed upper plate, even though there is a marked variation in the near surface stress regime and the degree of oblique convergence along the arc. Changes in stress regime, from compression near the surface to tension at greater depth, can be accommodated by vertical and lateral stress partitioning during lithospheric flexure (e.g. Hieronymus & Bercovici, 2000). Stress partitioning in the upper plate also supports the observations of Acocella & Funiciello (2010) that arc volcanoes occur in a variety of near-surface stress regimes.

Downward displacement of a dense, subjacent slab in subduction systems causes dynamic topography in the upper plate (Husson, 2006). Flexure of the arc lithosphere can accommodate the downward displacement as the hydrostatic suction maintains contact, due to their resistance, between the upper and lower plate (Hassani et al., 1997, **Figure 5.5**). Gvirtzman & Stern (2004) described the breadth of this contact between upper and lower plate as the plate coupling zone or the down-pulled zone. Moreover, Bonnardot et al. (2008) suggest that the arc-normal tension at the base of the flexed lithosphere could also be enhanced by corner flow in mantle wedge. Motion of this corner flow depends on the mantle wedge viscosity, with low mantle viscosity allowing higher motion, hence stronger arc-normal tension (Bonnardot et al., 2008). The lower mantle wedge viscosity itself, compared to the surrounding asthenosphere, depends on the amount of hydration from the slab (Billen & Gurnis, 2001; Nakao et al., 2016), which is controlled by various

subduction dynamic variables such as convergence rate and slab dip (e.g. Tatsumi, 2005; Grove et al., 2009).

Correlations among subduction dynamic variables (**Figure 5.4**) display possible complex relationship which could influence each other. Here we discuss the possible mechanisms that established the correlation among the subduction dynamic variables in this study. Our discussion are limited to the variables that are related to arc segmentation, i.e. the distance from trench to arc-segment (Dt) and the volcano misfits ($Mrms$). Dt shows correlations with the crustal thickness (Tc) and slab dip (δ), while $Mrms$ also correlates with Tc and the number of volcanoes in each arc-segment (nV). We also discuss the correlation between the depth from arc to slab (H) and the descent speed of the slab ($Vdes$) as our result exhibits a similar trend with the previous study by England et al. (2004). We evaluate the correlation between H and $Vdes$ in relation to the segmented great circle model of arc volcano alignments.

5.4.1 Arc-segment Distance, Crustal Thickness, and Slab Dip

The distance from arc-segment to trench (Dt) correlates with crustal thickness and slab dip, especially at less than 125 km depth (**Figure 5.5**). If great circle segmentation of volcanoes does reflect arc-normal tension and lithosphere flexure then location where segments develop should be related to the upper plate deformation. The study of subduction dynamic control on topography by Crameri et al. (2017) shows vertical deflection or flexure of the upper plate could occur up to 1,000 km from the trench into the back arc. The extent and the amplitude of the deflection depend on the strength of the upper plate and the rheology of the mantle wedge compared to its surrounding. The strength of the upper plate is more likely controlled by the thickness than their crustal nature, i.e. oceanic or continental (Meyer & Schellart, 2013). While the rheology of continental crust is, in fact, generally weaker than oceanic crust (Brace & Kohlstedt, 1980; Kohlstedt et al., 1995), continental lithosphere is substantially thicker than oceanic lithosphere (e.g. Pasyanos et al., 2014) hence we could assume that this difference in crustal rheology is negligible. A thicker upper plate will be stronger and, so, harder to deform (Meyer & Schellart, 2013). Therefore, the location of arc-segment is likely to be located farther from the trench when the crust is thicker. Crameri et al. (2017) also explained the high topographic expression

around the active arc, despite the overall downward deflection, that should occur because of the compressional tectonic stress that build the topography. Karig (1971) also highlighted the addition of magmatic products in high topographic expression at the active arc. Moreover, Hassani et al. (1997) implied that lithosphere flexure which induced the arc-normal tension at the base of upper plate, occurs at the end of the plate-coupling between the upper and the lower plates. The plate-coupling and its strength are suggested to depend on to the upper plate thickness (Sharples et al., 2014). A thicker upper plate would lead to a wider plate-to-plate contact and, hence, the centre of lithosphere flexure would be located farther from the trench (**Figure 5.5**). The magnitude of Dt is also similar to the width of the down-pulled zone, defined by Gvirtzman & Stern (2004), where the plate-to-plate contact controls the length of this zone and bounded by the trench and volcanic arc.

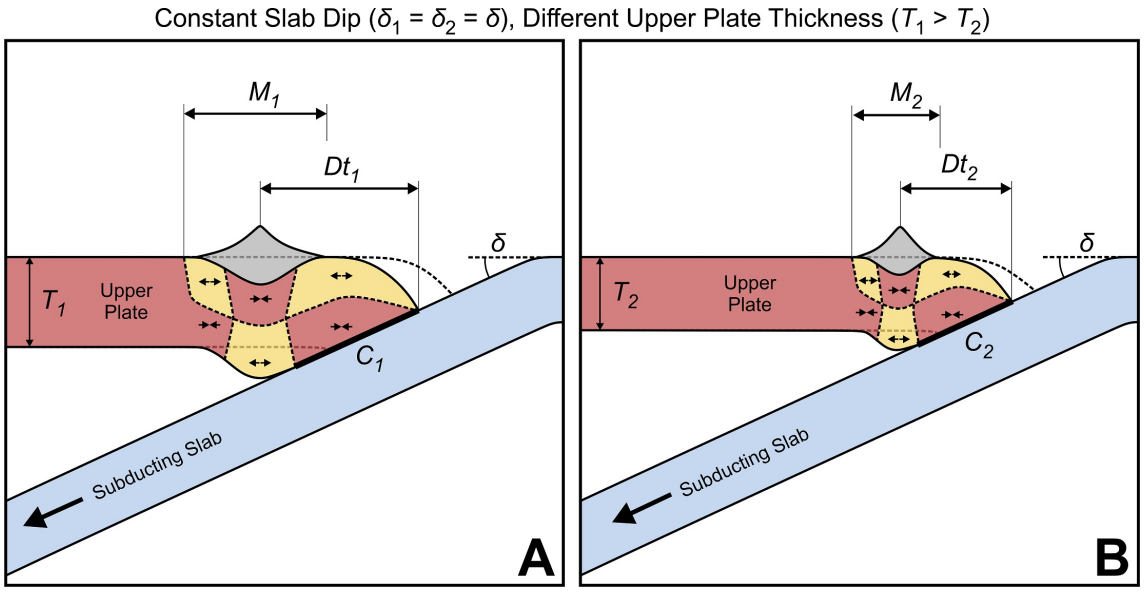

Figure 5.5. Schematic illustration describing the relationship of upper plate thickness (T) to arc-segment distance from trench (Dt), and also to segment rms-misfit ($Mrms$). At constant slab dip (δ), a thicker upper plate ($T_1 > T_2$) tends to locate the arc-segment farther from the trench ($Dt_1 > Dt_2$), possibly because of the greater breadth of plate-to-plate coupling between the overriding plate and the slab ($C_1 > C_2$). Thicker upper plates also tends to show higher rms-misfit ($M_1 > M_2$), possibly because a thicker upper plate would be resistive to downward deformation and so develop wider horizontal deformation.

The location of maximum vertical deflection, or lithospheric flexure, takes place is also affected by the slab dip (Crameri et al., 2017). Slab dip is one of the main controls in locating where the slab reaches a critical depth, causing substantial slab dehydration (e.g. Tatsumi, 2005; Grove et al., 2009; Perrin et al., 2018). Fluid addition to the mantle

wedge reduces the mantle wedge viscosity compared to the adjacent asthenosphere (Billen & Gurnis, 2001; Nakao et al., 2016). The less viscous mantle drives stronger tension at the base of the upper plate flexure because low viscosity allows higher rates of convective mantle flow (Bonnardot et al., 2008). This corner flow enhances the deflection or the deformation of the upper plate (**Figure 5.6**). Therefore, the correlation of arc-segment distance from trench and the slab dip is expected (Perrin et al., 2018). Moreover, at a constant upper plate thickness, a steeper slab dip would imply a shorter plate-to-plate contact and vice versa. As the result, a steeper slab would produce maximum lithosphere flexure closer to the trench than a slab with shallower dip (**Figure 5.6**).

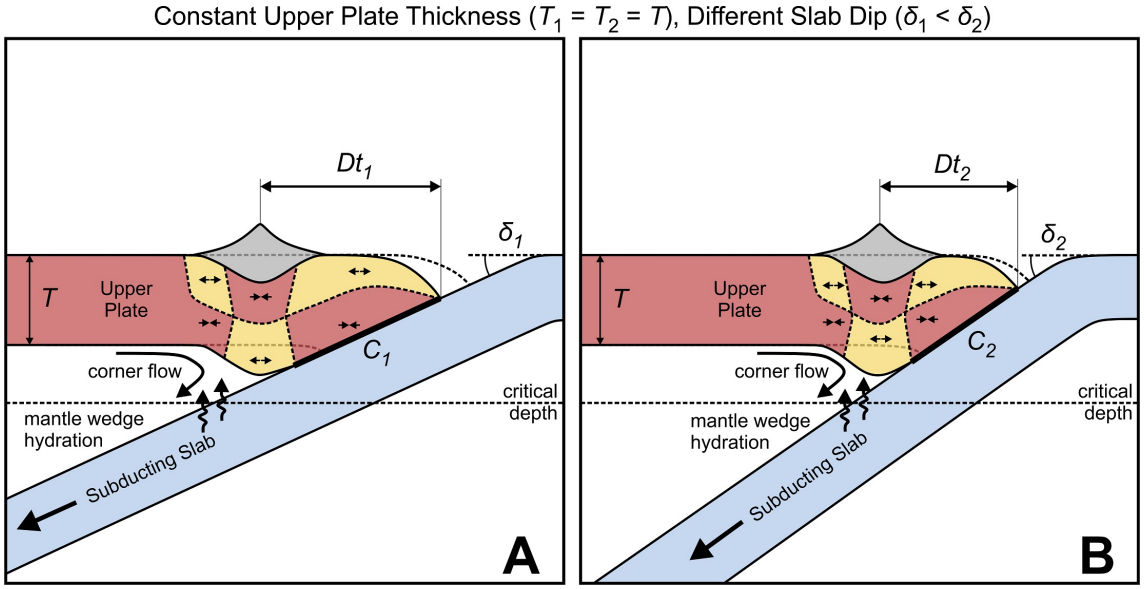

Figure 5.6. Schematic illustration describing the relationship between the slab dip (δ) and arc-segment distance from trench (Dt). At a constant upper plate thickness (T), the steeper dip ($\delta_2 > \delta_1$) produces an arc closer to the trench ($Dt_2 < Dt_1$). This may be a simple geometric control where steep slab dips caused narrower plate-to-plate coupling zones ($C_2 < C_1$), although the steep slab dip also locates mantle wedge hydration reaction closer to the trench.

Both the crustal thickness and slab dip correlate with Dt, as well as correlating with each other (**Figure 5.7**). An inverse proportional relationship between the upper plate thickness and slab dip has been observed in several studies (e.g. Roda et al., 2011; Sharples et al., 2014; Scott, 2019). The decrease of slab dip could be affected by different components such as slab buoyancy, stiffness, suction force, or far-field stress (Capitanio & Morra, 2012). The suction force in the mantle wedge plays an important role in the interaction of upper plate thickness and slab dip, especially in the subduction zones where a flat slab has formed (Tovish et al., 1978; Manea et al., 2012; O'Driscoll et al., 2012). Rodríguez-

González et al. (2012) proposed that the thermal structure of the overriding plate is more important than the slab in controlling the suction force and the slab dip. A colder upper plate, associated with older, denser, or thicker upper plate, maintains a more viscous mantle wedge at its base which, in turn, increases the hydrodynamic suction between the slab and overriding plate leading to a shallower slab dip. An additional mechanism that might influence the correlation between Tc and δs is that thicker crust in the upper plate provides a longer contact between the two plates and that shear along the contact reduces the plate bending effect from the slab pull (Conrad et al., 2004). In any case, since the thickness of the crust is generally less than 65 km, crustal thickness might be expected to correlate with the average or the shallow slab dip and be less likely to correlate with deep slab dip.

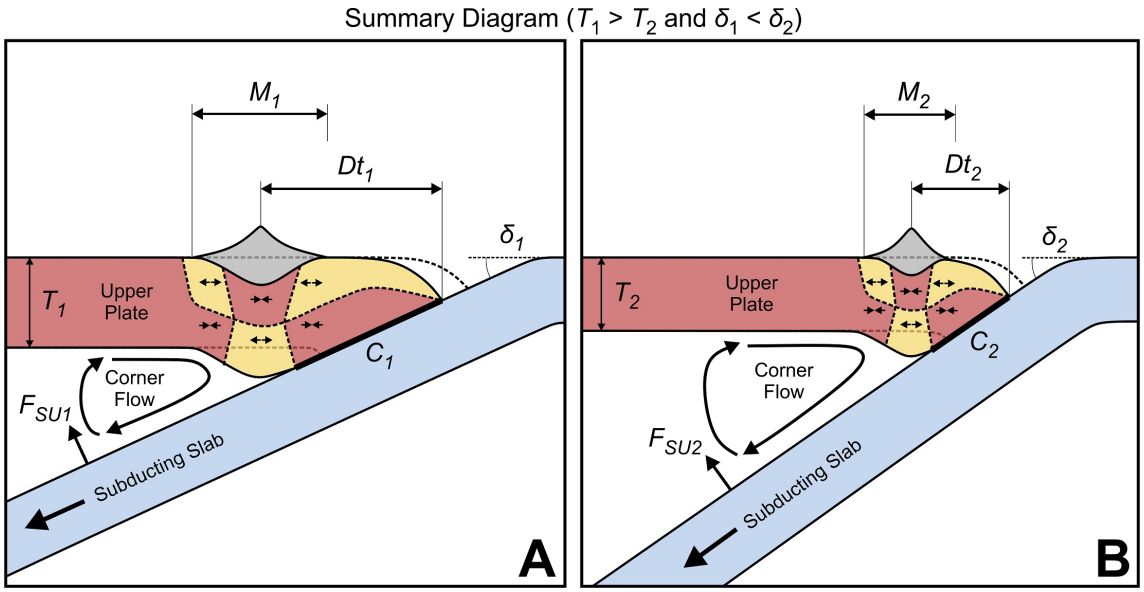

Figure 5.7. Schematic illustration showing the correlation between the main variables: arc-segment distance (Dt), thickness of the upper plate (T), slab dip (δ), and rms-misfit (M). Thickness of the upper plate is considered to be the main variable that controls the location of the arc-segment. Thicker upper plate ($T_1 > T_2$) could cause stronger corner flow and induce stronger suction force ($F_{SU1} > F_{SU2}$) which result in shallower slab dip ($\delta 1 < \delta_2$). A combination of thicker upper plate and shallower slab dip would locate the arc-segment farther from trench ($Dt_1 > Dt_2$) with higher rms-misfit ($M_1 > M_2$).

5.4.2 Crustal Thickness and Arc-segment Misfits

A positive correlation exists between crustal thickness and volcano misfit along each segment; arc-segments in thicker crust tend to have higher misfit (**Figure 5.5**). This correlation might be explained by considering the stress regime distribution in the lithosphere

where volcanic arc develops more closely. During lithospheric flexure, stress partitioning occurs, both vertically and horizontally, within the deflected plate (e.g. Andikagumi et al., 2020; Hieronymus & Bercovici, 1999). The plate bending region can be divided into two zones: the margin zone where the plate starts to deflect and the inner zone where the plate is fully displaced for downward flexure (Turcotte et al., 1978; Bodine & Watts, 1979). Arc-normal tensional stress is concentrated near the surface in the margin zone while compression occurs at the base of the plate. Simultaneously, in the inner zone, arc-normal tension occurs at the base of the plate and compression is present near the surface (**Figure 5.5** to **5.7**). The tensional region at the base of the inner zone is where vertical magma pathways from mantle wedge to upper plate are most likely to form (Andikagumi et al., 2020; Pacey et al., 2013). Thus, lithosphere flexure localises tensional stress to form a weakness zone where arc magmatism is focused.

If we assume that the width of the magmatic segment in the upper plate as measured by $Mrms$ is a proxy for the wavelength of lithosphere flexure, then we could evaluate the role of a thicker upper plate in causing higher $Mrms$. The wavelength of plate flexure is a function of the flexural rigidity which is dependent on plate thickness, mechanical properties (i.e. Young modulus, and Poisson's ratio; Walcott, 1970), rheology, and temperature (Kusznir & Karner, 1985). Consequently, assuming the mechanical properties along an arc margin does not vary significantly (e.g. Zandt & Ammon, 1995) for the similar lithosphere types, the principal control on the wavelength of flexure would be the thickness of upper plate. Meyer & Schellart (2013) also suggest that the thickness is more prominent variable in controlling the upper plate deformation, compared to other variables such as temperature, density or viscousity. Therefore, we suggest that lithosphere flexure in thicker plates generates bending with longer wavelength while thinner plates would experience shorter wavelength. Higher volcano misfit of arc-segments in the thicker crust is possibly caused by the wider extent of lithosphere flexure allowing magma transport across a broader wavelength of flexural deformation.

$Mrms$ also correlates with the number of volcanoes (nV) in each arc-segment. While the correlation is relatively weak, the association of arc-segments with more volcanoes having higher rms-mifit is expected. Higher $Mrms$ reflects greater breadth of the weakness zone due to lithosphere flexure as argued above, which implies wider lateral extent for

the arc-normal tension at the base of upper plate to allow magma to migrate to the surface. Furthermore, some arcs such as in the Northern and Central Andes, Central America, and Sumatra display highly variable $Mrms$ between their segments where crustal thicknesses vary little (**Figure G.2** in **Appendix G**). Pacey et al. (2013) suggested that the existence of lithospheric scale structures possibly produce some volcanoes away from the main trend. Other aspects such as arc migration, pre-existing structures, and arc-specific subduction history may also influence the location of some volcanoes away from the main trend (e.g. O'Driscoll et al., 2012). This could also be the reason why there is no correlation observed between arc-segment length ($Lseg$) and the number of volcanoes (nV), and why the volcano spacing in arcs appear to be randomly distributed (de Bremond d'Ars et al., 1995).

5.4.3 Depth to Slab and Descent Speed of Slab

The correlation between the depth from the arc to the slab (H) and the descent speed of the slab ($Vdes$) has been explored before by England et al. (2004) with the assumption that volcanoes in each arc form a single small circle and using an average value of H for that small circle. England & Katz (2010) then used the correlation obtained in this way as the basis for developing a thermal model of the mantle wedge that generates arc volcanoes above the anhydrous solidus. However, Syracuse & Abers (2006) observed no correlation of H and $Vdes$ when H was determined at each volcano because of the high variability of slab depth along each arc. Pacey et al. (2013) and study in Mariana arc (Andikagumi et al., 2020) have also draw attention to substantial variation of H within individual arcs and questioned whether average values have real significance in constraining volcano locations. Moreover, Syracuse et al. (2010) also summarised the diverse evidence that slab dehydration commences before the slab reaches the depth of H under many arc volcanoes. Experimental observation also suggest continuous slab dehydration process rather than a single pulse, which imply that models of arc volcano location based on the H values would be incompatible (Schmidt & Poli, 1998). This conclusion of slab dehydration between the trench and arc is corroborated by the observation of seismic evidence in Sumatra (Koulakov et al., 2016) and Ryukyu (Saita et al., 2015).

Nonetheless, we still observe a correlation between H and $Vdes$ (**Figure 5.4**). We

find H to be inversely proportional to total, orthogonal, and descent speed of the slab ($Vtot$, $Vort$ and $Vdes$), but not related directly to slab dip (δ, δs, δd). However, by definition (**Table 5.1**), slab dip influences the descent speed of the slab (**Figure 5.4A**). This study where volcano distribution is fitted using great circle segments has demonstrated the control from the upper plate and the slab upon the location of arc-segments (Dt, Tc, and δ). However, the location of arc-segment relative to the trench (Dt) show no correlation with H. We also observe no significant correlation between Tc and H, which contradicts the suggestion of Perrin et al. (2018) who used age of the overriding plate to estimate Tc and only include oceanic upper plate in their study. Even though Dt and H are not directly correlated, Dt shows a positive correlation with the horizontal component of H ($H/\tan\delta$; $R = 0.57$, $p \approx 0$; **Figure G.1** in **Appendix G**). Schmidt & Poli (1998) pointed out that H is more associated with the location where maximum mantle wedge temperature (1300°C; or 1250° − 1275°C on England & Katz (2010)) reached and convective flow returns or changes direction (**Figure 5.8**). The location where corner flow returns is also similar to where anhydrous solidus accumulated (England & Katz, 2010) and marks where the mantle wedge will be partially molten closest point to the trench. This location is located under the arc because penetration of corner flow any closer to the trench is limited by coupling between the upper and lower plates. Consequently, the correlation between Dt and $H/\tan\delta$ is not surprising. The occurrence of corner flow is important in maintaining the mantle wedge temperature structure and thus sustaining arc magmatism (Schmidt & Poli, 1998) and also enhancing the arc-normal tension at the base of the upper plate (Bonnardot et al., 2008). Correlation between $Vdes$ and H is limited to explain the processes in the mantle wedge, such as dehydration and magmatism, but not magma transport in the upper plate and the location of arc volcanoes in the surface. Here we propose that the correlation between H and $Vdes$ is important, to the extent of explaining the source of magmatism and corner flow in the mantle wedge. Arc-segment location (Dt) is mainly controlled by the plate-to-plate coupling (mainly affected by Tc and δs) where arc-normal tension at the base of flexed lithosphere channel magma through the plate (**Figure 5.8**).

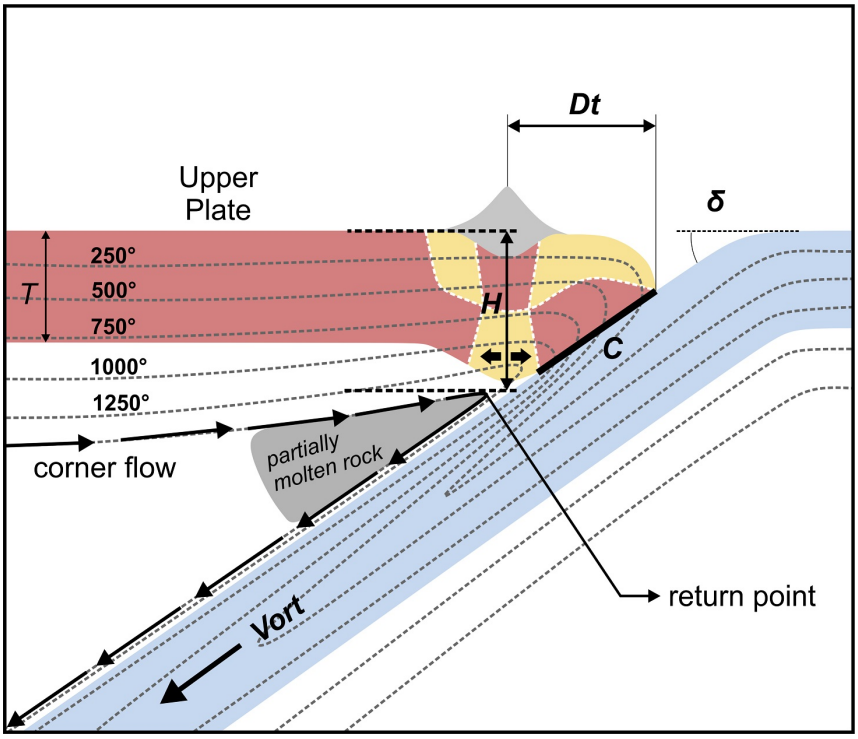

Figure 5.8. Schematic diagram illustrating the depth to slab from the arc (H) as a variable associated with the return point of mantle wedge corner flow. H correlates with the descent speed of the slab ($Vdes$, derived from $Vort \sin \delta$). $Vdes$ affects the thermal structure of the mantle wedge, lowering the viscosity which allows corner flow and thus focussing the production of partial melts.

5.4.4 Insignificant Variables

Arc-segment properties show no correlation with some subduction dynamic variables, such as the arc-segment length, angle between the arc-segment and the trench, and the slab half-spreading rate. Although these variables show no relationship at a global scale, they might affect the distribution of volcanoes on a more regional or local scale. The orientation of an arc-segment is strongly proportional to the trench margin orientation ($R = 0.91$, $p \approx 0.00$) which means the changes in trench margin geometry would strongly affect the arc-segment orientation. The trench margin, in turn, is likely to be controlled by slab properties. Some slab characteristics that might modify the margin are slab age (e.g. Jacob et al., 2014), which correlates with the half-spreading rate (Müller et al., 2008), subduction of pre-existing oceanic plateaux (O'Driscoll et al., 2012), and slab roll-back (Schepers et al., 2017). Therefore, regional studies of the distribution of volcanoes should also be conducted to understand the specific tectonic controls within particular arcs, as undertaken at the Mariana (Andikagumi et al., 2020) and Java (Pacey et al., 2013) margins.

5.5 Conclusion

This global study of arc volcano locations finds the AICc parameters of segmented great circle distribution to be lower than those of single or segmented small circles. The great circle volcano alignment represents arc-normal tension at the base of the upper plate that is induced by the lithospheric flexure. Lithospheric flexure varies the stress regime such that in the inner deflection zone arc-normal compression can be present at the surface while arc-normal tension controls the base. The opposite arrangement operates in the margin zone of the deflection.

The location of any particular arc-segment is affected by various subduction dynamic variables. The arc-segment distance from trench (Dt) is controlled by the crustal thickness and the slab dip, especially the slab at less than 125 km. Both these properties influence of the contact between the upper and lower plates exerts a downward force on the overriding plate and generate the flexure. The upper plate thickness also affects the slab dip such that thicker upper plates are usually observed with shallower slab dip. A thicker upper plate may increases the suction force affecting the slab, and may also lead to a wider zone of upper plate flexure, hence the volcano misfit along each segment is higher.

Correlation between depth to the slab under the arc and the descent speed of the slab influences the processes in the mantle wedge where slab dehydration add fluid and lowers the mantle wedge viscosity. However, we propose that the main control of arc-segment location is the upper plate thickness and shallow slab dip, based on the correlation between Dt, Tc and δs. Therefore, the alignments of arc volcanoes into great circle segments demonstrates the location of volcanic arcs is dictated by the response of the upper plate to subduction dynamic parameters.

Chapter 6

Summary and Conclusion

6.1 Observations

Spatial distributions of arc volcanoes demonstrate the influence from the upper plate deformation and regional tectonics. New tools for analysing the alignment of arc volcanoes has been developed based on quantitative methods and applied in this study. Alignment analyses of arc volcano distributions in regional scale, i.e. at the Mariana, Java and the Lesser Sunda Islands, and Sumatra, show that arc volcanoes are better described by segmented great circles, rather than a single or segmented small circle. Alignment of arc volcanoes in segmented great circles, referred to as 'arc-segment', indicate the possible control from the stresses operating in the upper plate. Alignment analysis of arc volcanoes in a global study displays a consistent outcome with the regional scale case studies that arc volcano distributions are better fitted with segmented great circles. The alignment of arc volcanoes in great circle distributions are observed in 16 arcs around the world, covering the length of 16,500 km of subduction margin.

The rms-misfit of volcanoes from the geometric pattern being tested, or the residuals, is a key parameter in quantifying and determining the best-fit geometry between small circles and great circles. There are two misfit-based comparison methods used in this study to determine the preferred model which are residual analyses and Akaike Information Criterion (AIC). The residual analysis involves plotting the rms-misfit of arc volcanoes against the alignment distance. The trend lines on the plot of great circle residuals (ΔGC) against the distance should form a straight-line approaching $y = 0$ when volcanoes are actually distributed in a great circle pattern. Meanwhile, in the same case, the residual of the best-fit small circle (ΔSC) would form a polynomial curve when plotted against their distance. The residual analyses of three regional case studies, i.e. Mariana, Java and Lesser Sunda, and Sumatra, demonstrate consistent results where ΔGC plots of the total 12 arc-segments generate linear $y \approx 0$ trend lines. These results suggest that arc volcanoes are preferentially distributed in great circle alignment pattern.

To ensure comparability in the statistics associated with the alignment analysis, the difference between the degrees of freedom for a small and great circle need to be accounted for. The difference arises because of the fixed radius of great circle geometry. Then, great circle geometry has only two freely-adjusted parameters which are the line's central latitude

and longitude. In contrast, a small circle has three degrees of freedom which are its radius, as well as its centre's longitude and latitude. A Corrected Akaike Information Criterion (AICc) was the statistical test indicator adopted to determine the preferred distribution geometry because it takes into account the different degree of freedom for each line fitting. The AICc values for the great circle arc-segments are the lowest in the three regional case studies, as well as the other 13 arcs around the world. It corroborates the result from the residual analysis that arc volcanoes are better fitted with segmented great circles.

6.2 Interpretations

The study in the Mariana Arc suggests the main control of arc volcanoes alignments in segmented great circles is lithosphere flexure. The flexed lithosphere is caused by the down-pulled force, induced by the subducting slab motion, where the resistance along the plate-to-plate contact drags down the upper plate. Downward lithosphere flexure allows stress regime partitioning both laterally and vertically. Deflected lithosphere generates permanent deformation near the surface and at the base of the plate within the plate bending, hence forms two zones of stress partitioning which are the margin zone and the inner zone. At the margin where the plate starts to deflect, arc-normal tension is dominant near the surface while compression occurs near the base. The plate is fully pulled down in the inner zone such that there is compression near the surface and tension at the base of the plate. Tension, normal to the arc within the inner zone is proposed to be the cause of the alignment of arc volcanoes as it initiates the magma pathways at the base of the upper plate. Moreover, the study of Sumatran volcanoes and faults indicates that the downward deflected plate is a lithospheric weak zone. This zone enhances and narrows down the fault propagation and the alignment of arc volcanoes to a narrow zone of a few kilometres width. Observations of the location of arc volcanoes in a global scale suggest that the location of the weakness zone, deducted as the distance from trench to arc-segment, is affected by the crustal thickness and slab dip. The thicker the crust and the shallower the slab mean the farther the arc from the trench.

Based on the regional case studies, there are two types of arc-segment arrangement identified. First, the most common arc-segment arrangement is the "series" type. This

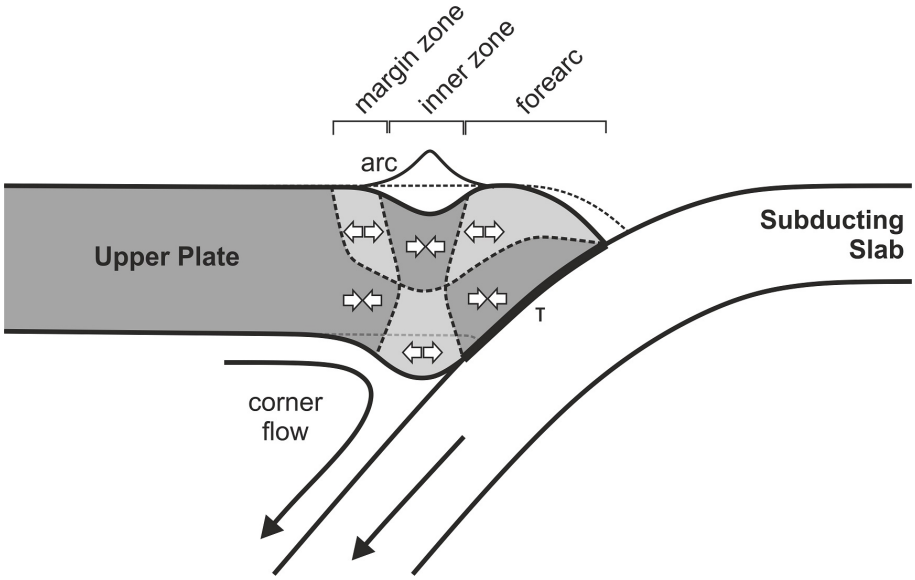

Figure 6.1. Schematic diagram of lithospheric flexure as the main control of arc volcano location.

type is identified in Mariana Arc and the south of Sumatra, also at other arcs in the global study such as Izu-Bonin, Ryukyu, Aleutians, and Kermadec-North Island. Changes of the arc segment orientation are usually small and remain parallel with the trench margin. This type, perhaps, indicating gradual changes of stress orientation following the geometry of trench margin. The second arc-segment arrangement is the "stepover" type, which occurs at Java LS and northern Sumatra, as well as at the other arcs such as in Central America, Central Andes and Vanuatu. This type marks lateral variation along the subduction margin which could include a variation of the strain rate or slab properties. The regional arc volcanoes studies display two types of stepover arc-segment arrangement which are "Java" and "Toba" types. Java type stepover is identified by a relatively minor oblique convergence. Also, the changes of arc-segment orientation are small, less than 15° in the case of West and East Java. Minor convergence obliquity affects the arc-segment by generating lateral forearc motion or relative tension, parallel to the trench. Trench-parallel tension would generate structures with high angle orientation (or sub-normal) to the arc-segment within the stepover, forming a releasing bend or pull-apart geometry. Next, Toba type stepover indicates laterally indented trench margin and high changes of arc-segment orientation, about 22° in Toba, following the changes of trench geometry. The stepover formed because of trench migration due to slab property variations, i.e. slab age and buoyancy in Toba case. It generated structures with small-angle orientation or

approximately parallel to the arc-segment orientation. Both types of stepover geometry are associated with extension or thinning in the lithosphere that affects the volcanism. In Java LS, the stepover is related to the development of off-segment volcanoes within the stepover. Meanwhile, in Toba, the stepover triggered lithosphere thinning that induced a higher amount of melting in the mantle and more magma accumulation. Voluminous melt in the mantle would cause higher geothermal gradient to which produce enough heat energy to lead to crustal melting and large-scale eruption.

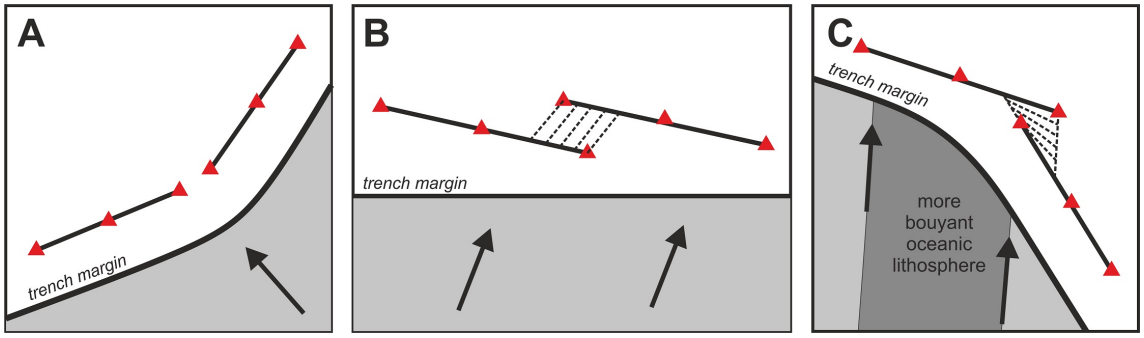

Figure 6.2. Types of arc-segment arrangements: (**A**) "series" type, (**B**) "Java" type, and (**C**) "Toba" type.

Some volcanoes are classified as off-segment volcanoes due to their distance from the main great circle alignments. In the regional case studies, off-segment volcanoes were identified in Java LS and Sumatra, while globally they also occur in several arcs such as Kamchatka, North Japan, Central America and Central Andes. Based on the regional study, especially in Java LS, there are two mechanisms that possibly locate the off-segment volcanoes. The first mechanism is an extension, parallel to the trench, due to changes of forearc motion. In Java LS, the forearc motion changes from clockwise to counter-clockwise relative to the Sunda block. Changes of motion caused an extension that propagated lithospheric structures with sub-normal or high angle orientation to the arc-segment. In Java LS, the forearc motion changes are located at stepover geometry in West Java, hence off-segment volcanoes occur within the stepover. The second mechanism is the changes of lateral strain rate along the trench margin, identified by a peak or excursion in the convergence obliquity plot against the distance. Increasing strain rate along the margin, especially in short distance, could generate apparent extension and propagate structures with a high angle to the trench.

In conclusion, the alignment of arc volcanoes is controlled by the lithosphere flexure

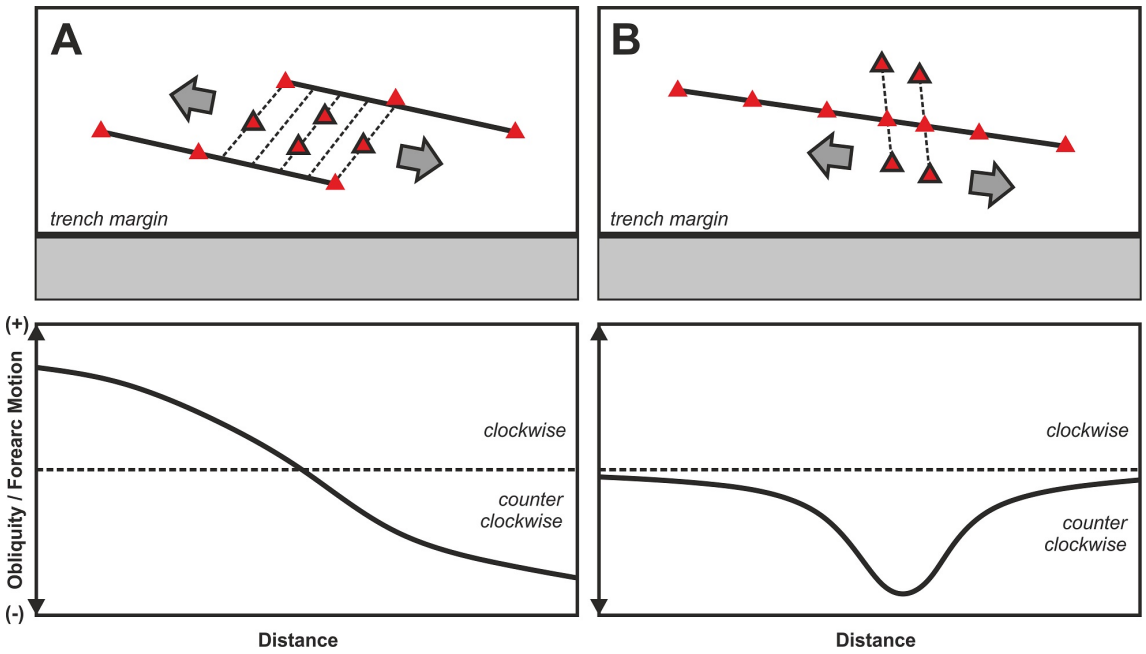

Figure 6.3. Schematic diagram of the controls in locating the off-segment volcanoes. (**A**) trench-parallel extension due to changes of forearc motion and (**B**) trench-parallel extension to increasing strain rate along the margin.

that concentrates arc-normal tension as the base of the upper plate. The specific regional tectonics influence the arrangement of arc-segments and manifested as the volcano distribution on the surface. Therefore, identifying the regional tectonic control to the upper plate deformation and the association to arc volcano distribution are important in understanding the magma transport in the subsurface. This understanding would lead us to better knowledge in mitigating the future risk from volcanic-related hazards.

6.3 Applications

The global study of arc volcano distribution has demonstrated the applicability of spatial analyses in different arc settings around the world. Nevertheless, the case studies in Mariana and Indonesia show the substantial influence of specific, local tectonic factors upon arc volcanism. Thus, specific studies at different arcs around the world should be conducted. The methods used in this study, such as spatial volcano distribution analyses and surface strain observation, can be applied in other arc settings. The preliminary study in the global scale identifies some interesting arcs for case studies in the future, such as at Central America, Central Andes and Vanuatu. Prior work in Central America has

shown the possible interplay between the upper plate structures and volcano distribution (Burkart & Self, 1985; Morgan et al., 2008; Bolge et al., 2009). The Central Andean Arc also has a stepover geometry within which off-segment volcanoes occur, showing a complex case in addition to the long history of subduction (Schepers et al., 2017; Scott et al., 2018) and the curve-shaped trench. Stepover between arc-segments is also observed at the New Hebrides arc, in Vanuatu, which has complex tectonics with the plate rotation (e.g. Christova & Scholz, 2003; Richards et al., 2011).

The spatial distribution tools can also be applied in different kind of geological features in a point-set data format other than volcanic centres. The point set data format is a type of data that require the location information in two-dimensional coordinate, such as latitude and longitude. Shallow earthquake epicentres are one of the examples of the point-set data type. Recognising the alignment of earthquake epicentres and their aftershocks can be used to infer the structural geometry where the earthquake generated (e.g. Kagan & Knopoff, 1980) or the segmentation of the structures (e.g. Magistrale & Sanders, 1996; Yue et al., 2012). Meanwhile, analysing earthquake hypocentres where depth variations could be significant, perhaps, will need further development of fitting tools or finding an appropriate coordinate projection system/method.

Beyond the Earth, the spatial distribution analyses can be applied in planetary science. Volcanic centres have been identified at different scale and regions on Mars. Pavonis Mons (Bleacher et al., 2009) and Alba Patera (Ivanov & Head, 2006) are local edifices while Syria Planum (Richardson et al., 2013) shows a regional field of volcanoes, potentially linked to local tectonism. Volcanic centres on Venus have also been identified (e.g. Head et al., 1992; Schaber et al., 1992) and provide an opportunity to explore their spatial distribution as an indicator of any stress control upon planetary volcanism (Grosfils & Head, 1994). Therefore, spatial analysis tools developed in this study open opportunities in various future research topics and areas, on Earth and beyond.

Appendix A

Map Lists

A.1 Regional Geological Maps of Java LS

1. Abidin, H. Z. & Sutrisno. (1992). *Geological Map of The Pamanukan Quadrangle, Jawa* (1209-6, scale 1:100,000). Bandung: Geological Research and Development Centre.

2. Achdan, A. & Sudana, D. (1992). *Geologic Map of the Indramayu Quadrangle, Jawa* (1309-4, scale 1:100,000). Bandung: Geological Research and Development Centre

3. Achdan, A. & Sudana, D. (1992). *Geological Map of The Karawang Quadrangle, Jawa* (1209-5 & 1210-2, scale 1:100,000). Bandung: Geological Research and Development Centre.

4. Achdan, A., & Bachri, S. (1993) *Geologic Map of the Blambangan Quadrangle, East Java* (1707-1 & 1707-2, scale 1:100,000). Bandung: Geological Research and Development Centre.

5. Agustiyanto, D. A., & Santosa, S. (1993). *Geological Map of the Situbondo Quadrangle, Jawa* (1708-1, scale 1:100,000). Bandung: Geological Research and Development Centre.

6. Alzwar, M., Akbar, N. & Bachri, S. (1992). *Geological Map of The Garut & Pameungpeuk Quadrangle, Jawa* (1208-6 & 1208-3, scale 1:100,000). Bandung: Geological Research and Development Centre.

7. Asikin, S., Handoyo, A., Busono, H., & Gafoer, S. (1992). *Geologic Map of the Kebumen Quadrangle, Jawa* (1401-1, scale 1:100,000). Bandung: Geological Research and Development Centre.

8. Asikin, S., Handoyo, A., Prastistho, B., & Gafoer, S. (1992). *Geologic Map of Banyumas Quadrangle, Jawa* (1308-3, scale 1:100,000). Bandung: Geological Research and Development Centre.

9. Atmawinata, S. & Abidin, H. Z. (1991). *Geological Map of the Ujung Kulon Quadrangle, West Java* (1109-1, scale 1: 100,000). Bandung: Geological Research and Development Centre.

10. Azis, S., Sutrisno, Noya, Y., & Brata, K. (1992). *Geological Map of Tanjungbumi & Pamekasan, Jawa* (1609-2 & 1608-5, scale 1:100,000). Bandung: Geological Research and Development Centre.

11. Aziz, S., Hardjoprawiro, S., & Mangga, S. A. (1993) *Geological Map of the Bawean and Masalembo Quadrangle, Jawa* (1610-1, 1710-1 & 1710-4, scale 1:100,000). Bandung: Geological Research and Development Centre.

12. Budhitrisna, T. (1986). *Geologic Map of the Tasikmalaya Quadrangle, West Java* (1308-4, scale 1:100,000). Bandung: Geological Research and Development Centre.

13. Condon, W.H., Pardyanto, L., Ketner, K. B., Amin, T. C., Gafoer, S., & Samodra, H. (1996). *Geological Map of the Banjarnegara and Pekalongan Sheet, Jawa* (1408-4 & 1409-1, scale 1:100,000). Bandung: Geological Research and Development Centre.

14. Datun, M., Sukandarrumidi, Hermanto, B., & Suwarna, N. (1996). *Geological Map of the Ngawi Quadrangle, Jawa* (1508-4, scale 1:100,000). Bandung: Geological Research and Development Centre.

15. Djuri, M., Samodra, H., Amin, T.C., & Gafoer, S. (1996). *Geological Map of the Purwokerto and Tegal Quadrangles, Jawa* (1309-3 & 1309-6, scale 1:100,000). Bandung: Geological Research and Development Centre.

16. Djuri. (1973). *Geologic Map of the Ardjawinangun Quadrangle, Java* (10/XIII-D, scale 1:100,000). Bandung: Geological Survey of Indonesia.

17. Effendi, A. C., Kusnama & Hermanto, B. (1998). *Geological Map of The Bogor Quadrangle, Jawa* (1209-1, scale 1:100,000). Bandung: Geological Research and Development Centre.

18. Hartono & Suharsono. (1997). *Geological Map of the Tuban Quadrangle, Jawa* (1509-3, scale 1:100,000). Bandung: Geological Research and Development Centre.

19. Hartono, U., Baharuddin & Brata, K. (1992). *Geological Map of the Madiun Quadrangle, Jawa* (1508-2, scale 1:100,000). Bandung: Geological Research and Development Centre.

20. Kadar, D., & Sudijono. (1993). *Geological Map of the Rembang Quadrangle, Jawa* (1509-1 & 1501-4, scale 1:100,000). Bandung: Geological Research and Development Centre.

21. Kastowo. (1975). *Geologic Map of the Majenang Quadrangle, Java* (10/ XIV-B, scale 1:100,000). Bandung: Geological Survey of Indonesia.

22. Koesmono, M., Kusnama & Suwarna, N. (1996). *Geological Map of The Sindangbarang & Bandarwaru Quadrangles, Jawa* (1208-5 & 1208-2, scale 1:100,000). Bandung: Geological Research and Development Centre.

23. Mangga, S. A., Atmawinata, S., Hermanto, B., Setyogroho, B., & Amin, T. C. (1994). *Geological Map of the Lombok Sheet, West Nusatenggara* (1807, scale 1:250,000). Bandung: Geological Research and Development Centre.

24. Noya, Y., Suwarti, Suharsono, & Sarmili, L. (1992). *Geological Map of the Mojokerto Quadrangle, Jawa* (1508-6, scale 1:100,000). Bandung: Geological Research and Development Centre.

25. Pendowo, B., & Samodra, H. (1997). *Geological Map of the Besuki Quadrangle, Jawa* (1608-3, scale 1:100,000). Bandung: Geological Research and Development Centre.

26. Pringgoprawiro, H., & Sukido. (1992). *Geologic Map of the Bojonegoro Quadrangle, East Jawa* (1508-5, scale 1:100,000). Bandung: Geological Research and Development Centre.

27. Purbo-Hadiwidjojo, M. M., Samodra, H., & Amin, T. C. (1998). *Geological Map of the Bali Sheet, Nusatenggara* (1707 & 1807, scale 1:250,000). Bandung: Geological Research and Development Centre.

28. Rahardjo, W., Sukandarrumidi, & Rosidi, H. M. D., (1995). *Geological Map of the Yogyakarta Sheet, Jawa* (1408-2 & 1407-5, scale 1:100,000). Bandung: Geological Research and Development Centre.

29. Rusmana, E., Suwitodirdjo, K., & Suharsono. (1991). *Geological Map of Serang Quadrangle, Jawa* (1109-6 & 1110-3, scale 1:100,000). Bandung: Geological Research and Development Centre.

30. Samodra, H., Gafoer, S., & Tjokrosapoetro, S. (1992). *Geological Map of the Pacitan Quadrangle, Jawa* (1507-4, scale 1:100,000). Bandung: Geological Research and Development Centre.

31. Samodra, H., Suharsono, Gafoer, S., & Suwarti, S. (1992). *Geological Map of the Tulungagung Quadrangle, Jawa* (1057-5, scale 1:100,000). Bandung: Geological Research and Development Centre.

32. Sampurno & Samodra, H. (1997). *Geological Map of the Ponorogo Quadrangle, Jawa* (1508-1, scale 1:100,000). Bandung: Geological Research and Development Centre.

33. Santosa, S. (1991). *Geological Map of the Anyer Quadrangle, West Java* (1109-5 & 1110-2, scale 1: 100,000). Bandung: Geological Research and Development Centre.

34. Santosa, S., & Atmawinata, S. (1992). *Geological Map of the Kediri Quadrangle, Jawa* (1508-3, scale 1:100,000). Bandung: Geological Research and Development Centre.

35. Santosa, S., & Suwarti, T. (1992). *Geological Map of the Malang Quadrangle, Jawa* (1608-1, scale 1:100,000). Bandung: Geological Research and Development Centre.

36. Sapei, T., Suganda, H., Astadiredja, K. A. S., & Suharsono. (1992). *Geological Map of the Jember Quadrangle, Jawa* (1607-6, scale 1:100,000). Bandung: Geological Research and Development Centre.

37. Sidarto, Suwarti, T., & Sudana, D. (1993). *Geological Map of the Banyuwangi Quadrangle, Jawa* (1707-4, scale 1:100,000). Bandung: Geological Research and Development Centre.

38. Silitonga, P. H. (1973). *Geologic Map of The Bandung Quadrangle, Java* (9/XIII-F, scale 1:100,000). Bandung: Geological Survey of Indonesia.

39. Silitonga, P. H., Masria, M., & Suwarna, N. (1996). *Geological Map of the Cirebon Quadrangle* (1309-2 & 1309-5, scale 1:100,000). Bandung: Geological Research and Development Centre.

40. Simandjuntak, T. O., & Surono. (1992). *Geologic Map of Pangandaran Quadrangle, Jawa* (1308-2, scale 1:100,000). Bandung: Geological Research and Development Centre.

41. Sitomorang, R. L., Agustianto, D. A., & Suparman, M. (1992). *Geological Map of the Waru – Sumenep Quadrangle, Jawa* (1609-3 & 1608-6, scale 1:100,000). Bandung: Geological Research and Development Centre.

42. Situmorang, R. L., Smit, R., & van Vessem, E. J. (1992). *Geologic Map of the Jatirogo Quadrangle, Java* (1509-2, scale 1:100,000). Bandung: Geological Research and Development Centre.

43. Sjarifudin, M. Z., & Hamidi, S. (1992). *Geological Map of the Blitar Quadrangle, Jawa* (1507-6, scale 1:100,000). Bandung: Geological Research and Development Centre.

44. Sudana, D. & Santosa, S. (1992). *Geological Map of the Cikarang Quadrangle, West Java* (1109-2, scale 1: 100,000). Bandung: Geological Research and Development Centre.

45. Sudjatmiko (1972). *Geologic Map of The Cianjur Quadrangle, Jawa* (9/XIII-E, scale 1:100,000). Bandung: Geological Research and Development Centre.

46. Suharsono & Suwarti, T. (1992). *Geological Map of the Probolinggo Quadrangle, Jawa* (1608-2, scale 1:100,000). Bandung: Geological Research and Development Centre.

47. Sujanto, Hadisantono, R., Kusnama, Chaniago, R., & Baharuddin, R. (1992). *Geologic Map of the Turen Quadrangle, Jawa* (1607-4, scale 1:100,000). Bandung: Geological Research and Development Centre.

48. Sujatmiko & Santosa, S. (1992). *Geological Map of The Leuwidamar Quadrangle, Jawa* (1109-3, scale 1:100,000). Bandung: Geological Research and Development Centre.

49. Sukamto, R. A. B. (1975). *Geological Map of The Jampang & Balekembang Quadrangles, Java* (9/XIV-A & 8/XIV-C, scale 1:100,000). Bandung: Geological Survey of Indonesia.

50. Sukardi & Budhitrisna, T. (1992). *Geological Map of the Salatiga Quadrangle, Jawa* (1408-6, scale 1:100,000). Bandung: Geological Research and Development Centre.

51. Supandjono, J. B., Hasan, K., Panggabean, H., Satria, D., & Sukardi. (1992). *Geological Map of the Surabaya & Sapulu Quadrangle, Jawa* (1608-4 & 1609-1, scale 1:100,000). Bandung: Geological Research and Development Centre.

52. Supriatna, S., Sarmili, L., Sudana, D., & Koswara, A. (1992). *Geological Map of the Karangnunggal Quadrangle, Jawa* (1308-1, scale 1:100,000). Bandung: Geological Research and Development Centre.

53. Surono, Toha, B., & Sudarno, I. (1992). *Geological Map of the Surakarta – Giritontro Quadrangles, Jawa* (1408-3 & 1407-6, scale 1:100,000). Bandung: Geological Research and Development Centre.

54. Sutisna, K., Samodra, H., & Koswara, A. (1993). *Geological Map of the Kangean and Sapudi Quadrangle, Jawa* (1708-4, 1709-3, 1808-4, 1809-1 & 1708-5, scale 1:100,000). Bandung: Geological Research and Development Centre.

55. Suwarti, T., & Suharsono. (1992). *Geological Map of the Lumajang Quadrangle, Jawa* (1607-5, scale 1:100,000). Bandung: Geological Research and Development Centre.

56. Suwarti, T., & Wikarno, R. (1992). *Geological Map of the Kudus Quadrangle, Jawa* (1409-3, scale 1:100,000). Bandung: Geological Research and Development Centre.

57. Thaden, R. E., Sumadirdja, H., & Richards, P. W. (1975). *Geologic Map of the Magelang and Semarang Quadrangles, Java* (11/XIV-B & 11/XIII-E, scale 1:100,000). Bandung: Geological Survey of Indonesia.

58. Turkandi, T., et al. (1992). *Geological Map of Jakarta & Kepulauan Seribu Quadrangles, Jawa* (1209-4 & 1210-1, scale 1:100,000). Bandung: Geological Research and Development Centre

A.2 Regional Geological Maps of Sumatra

1. Aldiss, D. T., Whandoyo, R., Ghazali, S. A., & Kusyono. (1983). *Geologic Map of the Sidikalang and (Part of) Sinabang Quadrangles, Sumatra* (0518 & 0618, scale 1:250,000). Bandung: Geological Research and Development Centre.

2. Amin, T. C., Kusnama, Rustandi, E., & Gafoer, S. (1993). *Geological Map of the Manna and Enggano Sheet, Sumatera* (0911 & 0910, scale 1:250,000). Bandung: Geological Research and Development Centre.

3. Amin, T. C., Sidarto, Santosa, S., & Gunawan, W. (1993). *Geological Map of the Kotaagung Quadrangle, Sumatera* (1010, scale 1:250,000). Bandung: Geological Research and Development Centre.

4. Aspden, J. A., Kartawa, W., Aldis, D. T., Djunuddin, A., & Diatma, D. (1982). *Geologic Map of the Padangsidempuan and Sibolga Quadrangles, Sumatra* (0617 & 0717, scale 1:250,000). Bandung: Geological Research and Development Centre.

5. Baharuddin & Sidarto. (1995). *Geological Map of the Belitung Sheet, Sumatera* (1212, 1213, 1312 & 1313, scale 1:250,000). Bandung: Geological Research and Development Centre.

6. Bennett, J. D., Bridge, D. McC., Cameron, N. R., Djunuddin, A., Ghazali, S. A., Jeffery, D. H., et al. (1981). *Geologic Map of the Bandaaceh Quadrangle, Sumatra* (0421 & 0521, scale 1:250,000). Bandung: Geological Research and Development Centre.

7. Bennett, J. D., Bridge, D. McC., Cameron, N. R., Djunuddin, A., Ghazali, S. A., Jeffery, D. H., et al. (1981). *Geologic Map of the Calang Quadrangle, Sumatra* (0420, scale 1:250,000). Bandung: Geological Research and Development Centre.

8. Budhitrisna, T., Mangga, S. A. (1990). *Geological Map of the Pagai and Sipora Quadrangle, Sumatra* (0712, 0713, 0812 & 0813, scale 1:250,000). Bandung: Geological Research and Development Centre.

9. Burhan, G., Gunawan, W., & Noya, Y. (1993). *Geological Map of the Menggala Quadrangle, Sumatra* (1111, scale 1:250,000). Bandung: Geological Research and Development Centre.

10. Cameron, N. R., Aspden, J. A, Miswar & Syah, H. H. (1981) *Geologic Map of the Tebingtinggi Quadrangle, Sumatra* (0719, scale 1:250,000). Bandung: Geological Research and Development Centre.

11. Cameron, N. R., Aspden, J. A., Bridge, D. McC., Djunuddin, S. A., Ghazali, H., Harahap, H., et al. (1982). *Geologic Map of the Medan Quadrangle, Sumatra* (0619, scale 1:250,000). Bandung: Geological Research and Development Centre.

12. Cameron, N. R., Bennett, J. D., Bridge, D. McC., Clarke, M. C. G., Djunuddin, A., Ghazali, S. A., et al. (1983). *Geologic Map of the Takengon Quadrangle, Sumatra* (0520, scale 1:250,000). Bandung: Geological Research and Development Centre.

13. Cameron, N. R., Bennett, J. D., Bridge, D. McC., Djunuddin, A., Ghazali, S. A., Harahap, H., et al. (1982). *Geologic Map of the Tapaktuan Quadrangle, Sumatra* (0519, scale 1:250,000). Bandung: Geological Research and Development Centre.

14. Cameron, N. R., Djunuddin, A., Ghazali, S. A., Harahap, H., Keats, W., Kartawa, W., et al., (1981). *Geologic Map of the Langsa Quadrangle, Sumatra* (0620, scale 1:250,000). Bandung: Geological Research and Development Centre.

15. Cameron, N. R., Ghazali S. A., & Thompson, S. J. (1982). *Geologic Map of the Bengkalis Quadrangle, Sumatra* (0917, scale 1:250,000). Bandung: Geological Research and Development Centre.

16. Cameron, N. R., Ghazali, S.A., & Thompson, S. J. (1982). *Geologic Map of the Siaksriindrapura and Tg. Pinang Quadrangles, Sumatra* (0916 & 1016, scale 1:250,000). Bandung: Geological Research and Development Centre.

17. Cameron, N. R., Kartawa, W., & Thompson, S. J. (1982). *Geologic Map of the Dumai and Bagansiapiapi Quadrangles, Sumatra* (0817 & 0818, scale 1:250,000). Bandung: Geological Research and Development Centre.

18. Clarke, M. C. G., Ghazali, S. A., Harahap, H., Kusyono, & Stephenson, B. (1982). *Geologic Map of the Pematangsiantar Quadrangle, Sumatra* (0718, scale 1:250,000). Bandung: Geological Research and Development Centre.

19. Clarke, M. C. G., Kartawa, W., Djunuddin, A., Suganda, E., & Bagdja, M. (1982). *Geologic Map of the Pekanbaru Quadrangle, Sumatra* (0816, scale 1:250,000). Bandung: Geological Research and Development Centre.

20. Djamal, B., Gunawan, W., Simandjuntak, T. O., & Ratman, N. (1994). *Geological Map of the Nias Sheet, Sumatera* (0517, 0617, 0516 & 0616, scale 1:250,000). Bandung: Geological Research and Development Centre.

21. Endharto, M., & Sukido. (1994). *Geological Map of the Sinabang Sheet, Sumatera* (0418 & 0518, scale 1:250,000). Bandung: Geological Research and Development Centre.

22. Gafoer, S., Amin, T. C., & Pardede, R. (1992). *Geological Map of the Bengkulu Quadrangle, Sumatra* (0912, scale 1:250,000). Bandung: Geological Research and Development Centre.

23. Gafoer, S., Amin, T. C., & Pardede, R. (1993). *Geological Map of the Baturaja Quadrangle, Sumatera* (1011, scale 1:250,000). Bandung: Geological Research and Development Centre.

24. Gafoer, S., Burhan, G., & Purnomo, J. (1995). *Geologic Map of the Palembang Quadrangle, South Sumatra* (2^{nd} edition, 1013, scale 1:250,000). Bandung: Geological Research and Development Centre.

25. Gafoer, S., Cobrie, T., & Purnomo, J. (1986). *Geologic Map of the Lahat Quagrangle, South Sumatra* (1012, scale 1:250,000). Bandung: Geological Research and Development Centre.

26. Kastowo, Leo, G. W., Gafoer, S., & Amin, T. C. (1996). *Geological Map of the Padang Quadrangle, Sumatera* (0715, scale 1:250,000). Bandung: Geological Research and Development Centre.

27. Keats, W., Cameron, N. R., Djunuddin, A., Ghazali, S. A., Harahap, H., Kartawa, W., et al. (1981). *Geologic Map of the Lhoksemawe Quadrangle, Sumatra* (0521 & 0621, scale 1:250,000). Bandung: Geological Research and Development Centre.

28. Kusnama, Pardede, R., Mangga, S. A., & Sidarto. (1992). *Geological Map of the Sungaipenuh and Ketaun Quadrangle, Sumatra* (0813 & 0812, scale 1:250,000). Bandung: Geological Research and Development Centre.

29. Kusnama, Sutisna, K., Amin, T.C., Koesoemadinata, S., Sukardi, & Hermanto, B. (1994). *Geological Map of theTanjung Pinang Sheet, Sumatera* (1016 & 1017, scale 1:250,000). Bandung: Geological Research and Development Centre.

30. Mangga, S. A., & Djamal, B. (1994). *Geological Map of the North Bangka, Sumatera* (1113 & 1114, scale 1:250,000). Bandung: Geological Research and Development Centre.

31. Mangga, S. A., Amirudin, Suwarti, T., Gafoer, S., & Sidarto. (1993). *Geological Map of the Tanjung Karang Quadrangle, Sumatera* (1110, scale 1:250,000). Bandung: Geological Research and Development Centre.

32. Mangga, S. A., Burhan, G., Sukardi, & Suryanila, E. (1994). *Geological Map of the Siberut Sheet, Sumatera* (0614, 0615 & 0714, scale 1:250,000). Bandung: Geological Research and Development Centre.

33. Mangga, S. A., Santosa, S., & Hermanto, B. (1993). *Geological Map of Jambi Quadragle, Sumatera* (1014, scale 1:250,000). Bandung: Geological Research and Development Centre.

34. Mangga, S. A., Sukardi, & Sidarto. (1993). *Geological Map of the Tulung Selapan Quadrangle, Sumatera* (1112, scale 1:250,000). Bandung: Geological Research and Development Centre.

35. Margono, U., Supandjono, R. J. B., & Partoyo, E. (1995). *Geological Map of the South Bangka Sheet, Sumatera* (1112, 1113 & 1213, scale 1:250,000). Bandung: Geological Research and Development Centre.

36. Rock, N. S., Aldiss, D. T., Aspden, J. A., Clarke, M. C. G., Djunuddin, A., Kartawa, W., et al. (1983). *Geologic Map of the Lubuksikaping Quadrangle, Sumatra* (0716, scale 1:250,000). Bandung: Geological Research and Development Centre.

37. Rosidi, H. M. D., Tjokrosapoetro, S., Pendowo, B., Gafoer, S., & Suharsono. (1996). *Geological Map of the Painan and Northeastern Part of the Muarasiberut Quadrangle, Sumatera* (0814 & 0714, scale 1:250,000). Bandung: Geological Research and Development Centre.

38. Silitonga, P. H., & Kastowo. (1995). *Geological Map of the Solok Quadrangle, Sumatera* (2^{nd} edition, 0815, scale 1:250,000). Bandung: Geological Research and Development Centre.

39. Simandjuntak, T. O., Budhitrisna, T., Surono, Gafoer, S., & Amin, T. C. (1994). *Geological Map of the Muarabungo Quadrangle, Sumatera* (0914, scale 1:250,000). Bandung: Geological Research and Development Centre.

40. Sutisna, K., Burhan, G., & Hermanto, B. (1994). *Geological Map of the Dabo Quadrangle, Sumatera* (1015, scale 1:250,000). Bandung: Geological Research and Development Centre.

41. Suwarna, N., Budhitrisna, T., Santosa, S., & Mangga S. A. (1994). *Geological Map of Rengat Quadrangle, Sumatera* (0915, scale 1:250,000). Bandung: Geological Research and Development Centre.

42. Suwarna, N., Suharsono, Gafoer, S., Amin, T.C., Kusnama, & Hermanto, B. (1992). *Geological Map of the Sarolangun Quadrangle, Sumatra* (0913, scale 1:250,000). Bandung: Geological Research and Development Centre.

A.3 Volcano Geological Maps of Java LS

1. Abdurachman, K., Suganda, O. K., Hendrasto, M. & Irianto. (n/a). *Geologic Map of Lawu Volcano, Central and East Java* (scale 1:50,000). Bandung: Volcanological Survey of Indonesia.

2. Asmoro, P., Wachyudin, D., & Mulyadi, E. (1989). *Geological Map of Papandayan Volcano, Garut, West Java* (scale 1:25,000). Bandung: Volcanological Survey of Indonesia.

3. Bronto, S., Zaenuddin, A, & Erfan, R. D. (1985). *Geologic Map of Arjuno – Welirang Volcanoes, East Java* (scale 1:70,000). Bandung: Volcanological Survey of Indonesia.

4. Effendi, A. C., Bronto, S., & Sukhyar, R. (1986). *Geological Map of Anak Krakatau Volcano, Lampung Province* (scale 1:25,000). Bandung: Center of Volcanology and Geological Hazard Mitigation.

5. Nasution, A., Haerani, N., Mulyadi, D., & Hendrasto, M. (2004). *Geological Map of Agung Volcano, Bali* (scale 1:50,000). Bandung: Directorate of Volcanology and Geological Hazard Mitigation.

6. Sitorus, K., Erfan, R. D. Bacharudin, R., & Mulayana, A. R. (1994). *Geological Map of Sumbing Volcano, Central Java* (scale 1:50,000). Bandung: Volcanological Survey of Indonesia.

7. Situmorang, T., & Hadisantono, R. D. (1992). *Geologic Map of Gede Volcano, Cianjur, West Java* (scale 1:50,000). Bandung: Volcanological Survey of Indonesia.

8. Situmorang, T., Hadisantono, R. D., & Asmoro, P. (1995). *Geologic Map of Cereme Volcano, West Jawa* (scale 1:50,000). Bandung: Volcanological Survey of Indonesia.

9. Soetoyo & Hadisantono, R. D. (1992). *Geologic Map of Tangkubanparahu Volcano, Sunda Complex Volcano, West Java* (scale 1:50,000). Bandung: Volcanological Survey of Indonesia

10. Sujanto, Syarifuddin, M. Z., & Sitorus, K. (1988). *Geological Map of the Ijen Caldera Complex, East Java* (scale 1:50,000). Bandung: Volcanological Survey of Indonesia.

11. Sukhyar, R., Sumartadipura, N. S., & Effendi, W. (1986). *Geologic Map of Dieng Volcano Complex, Central Java* (scale 1:50,000). Bandung: Volcanological Survey of Indonesia.

12. Sukhyar, R., Sumartadipura, N. S., & Erfan, R. D. (1992). *Geologic Map of Sundoro Volcano, Central Java* (1:50,000). Bandung: Volcanological Survey of Indonesia.

13. Surmayadi, M., Kartadinata, M. N., Budianto, A., & Sasongko, Y. (1998). *Geological Map of Guntur Volcano, West Java* (scale 1:25,000). Bandung: Volcanological Survey of Indonesia.

14. Sutawidjaja, I. S., Aswin, D., & Sitorus, K. (1985). *Geologic Map of Slamet Volcano, Central Java* (scale 1:50,000). Bandung: Volcanological Survey of Indonesia.

15. Sutawidjaja, I. S., Changiago, R., & Kamal, S. (1992). *Geologic Map of Batur Caldera, Bali, Indonesia* (scale 1:50,000). Bandung: Volcanological Survey of Indonesia.

16. Sutawidjaja, I. S., Suparman & Sitorus, K. (1996). *Geological Map of Raung Volcano, East Java* (scale 1:100,000). Bandung: Volcanological Survey of Indonesia.

17. Sutawidjaya, I. S., Wahyudin, D., & Kusdinar, E. (1996). *Geological Map of Semeru Volcano, East Java* (scale 1:50,000). Bandung: Volcanological Survey of Indonesia.

18. Wirakusumah, A. D., Juwarna, H., & Loebis, H. (1989). *Geological Map of Merapi Volcano, Yogyakarta Special & Central Java Province* (scale 1:50,000). Bandung: Center of Volcanology and Geological Hazard Mitigation.

19. Zaennudin, A., Dana, I. N., & Wahyudin, D. (1992). *Geologic Map of Kelut Volcano, East Java* (scale 1:50,000). Bandung: Volcanological Survey of Indonesia.

20. Zaennudin, A., Hadisantono, R. D., Erfan, R. D., & Mulyanam A. R. (1994). *Geological Map of Bromo – Tengger Volcano, East Jawa* (scale 1:50,000). Bandung: Volcanological Survey of Indonesia.

21. Zaenudin, A., Sutawidjaja, I. S., & Aswin, D. (1993). *Geological Map of Salak Volcano, West Java* (1:50,000). Bandung: Volcanological Survey of Indonesia.

A.4 Volcano Geological Maps of Sumatra

1. Effendi, A. C., Bronto, S., & Sukhyar, R. (1986). *Geological Map of Anak Krakatau Volcano, Lampung Province* (1110, scale 1:25,000). Bandung: Center for Volcanology and Geological Hazard Mitigation.

2. Kartadinata, M. N., Wahyudin, D., Taufiqurrahman, R. (2009). *Geological Map of Sibayak Volcano, North Sumatra* Province (0619, scale 1:50,000). Bandung: Center for Volcanology and Geological Hazard Mitigation.

3. Kusnadi, I., Solihin, A., & Irawan, W. (2015). *Geological Map of Marapi Volcano, West Sumatra* (0715 & 0815, scale 1:50,000). Bandung: Center for Volcanology and Geological Hazard Mitigation.

4. Munandar, A., Budianto, A., Irawan, W., Zainuddin & Nursusanto, I. (2000). *Geological Map of the Talang Volcano, West Sumatra* (1323, scale 1:50,000). Bandung: Center for Volcanology and Geological Hazard Mitigation.

5. Nasution, A., Santoso, M. S., Chaniago, R., & Mulyadi, D. (2005). *Geological Map of Kerinci Volcano, West Sumatra and Jambi* (1421, scale 1:50,000). Bandung: Center for Volcanology and Geological Hazard Mitigation.

6. Prambada, O., Zaenuddin, A., Iryanto, Santosa, I., Nakada N., & Yoshimoto, M. (2011). *Geological Map of Sinabung Volcano, North Sumatera Province* (0619, scale 1:25,000). Bandung: Center for Volcanology and Geological Hazard Mitigation.

7. Primulayana, S., Sutawidjaja, I. S., Prambada, O., Iryanto, & Zaenuddin, A. (2011). *Geological Map of the Sibual Buali Volcano, North Sumatera* (0717, scale 1:25,000). Bandung: Center for Volcanology and Geological Hazard Mitigation.

Appendix B

Global Volcano Locations Datasets

Table B.1. Locations of volcanoes in 19 arcs

No.	Volcano Name	Longitude	Latitude	No.	Volcano Name	Longitude	Latitude
1. Kamchatka							
1	Shiveluch	161.359	56.652	39	Mutnovsky	158.178	52.458
2	Karchinsky	160.825	56.425	40	Tolmacev Dol[*]	157.563	52.647
3	Zarechny	160.830	56.380	41	Opala[*]	157.338	52.543
4	Ushkovsky	160.470	56.100	42	Visokiy	157.931	52.432
5	Klyuchevskoy	160.641	56.057	43	Asacha	157.830	52.355
6	Kamen	160.595	56.019	44	Golaya	157.792	52.262
7	Bezymianny	160.595	55.972	45	Otdelniy	157.434	52.221
8	Zimina	160.605	55.861	46	Piratkovsky	157.851	52.110
9	Tolbachik	160.377	55.820	47	Khodutka	157.707	52.066
10	Udina	160.527	55.759	48	Olkoviy	157.530	52.011
11	Kizimen[*]	160.320	55.131	49	Ostanet	157.323	52.148
12	Vysoky	160.761	55.061	50	Zheltiy	157.607	51.936
13	Komarov	160.726	55.032	51	Ozernoy	157.385	51.893
14	Gamchen	160.702	54.973	52	Ksudach	157.535	51.818
15	Schmidt	160.627	54.914	53	Balenkaya	157.266	51.750
16	Kronotsky	160.533	54.753	54	Kell	157.358	51.658
17	Krasheninikov	160.275	54.596	55	Zheltovsky	157.328	51.577
18	Kikhpinych	160.252	54.488	56	Ilyinksky	157.202	51.498
19	Uzon	159.970	54.500	57	Kurile Lake	157.120	51.450
20	Taunshits	159.804	54.531	58	Diky Greben	156.975	51.452
21	Bolshoi Semiachik	160.015	54.313	59	Koshelev	156.753	51.356
22	Maly Semiachik	159.655	54.118	60	Kambalny	156.879	51.304
23	Karymsky	159.442	54.047	61	Mashkovtsev	156.720	51.100
24	Akademia Nauk	159.450	53.980	62	Alaid[*]	155.557	50.858
25	Zhupanovsky	159.125	53.588	63	Ebeko	156.014	50.686
26	Dzenzursky	158.920	53.640	64	Vernadskii	155.964	50.549
27	Zavaritsky[*]	158.384	53.907	65	Chikurachki	155.460	50.321
28	Bakening[*]	158.072	53.907	66	Lomonosov	155.434	50.252
29	Kostakan[*]	158.055	53.833	67	Fuss Peak	155.248	50.270
30	Veer[*]	158.448	53.752	68	Karpinsky	155.368	50.130

(cont.)

No.	Volcano Name	Longitude	Latitude	No.	Volcano Name	Longitude	Latitude
31	Koryaksky	158.712	53.321	69	Nemo Peak	154.814	49.564
32	Avachinsky	158.833	53.256	70	Tao-Rusyr Caldera	154.708	49.352
33	Unnamed 1	158.520	52.920	71	Harimkotan	154.520	49.118
34	Unnamed 2	158.289	52.860	72	Ekarma	153.940	48.946
35	Barakhatnaya Sopka	158.240	52.802	73	Sinarka	154.182	48.874
36	Vilyuchick	158.281	52.705	74	Kontumintar	154.016	48.758
37	Bolshe Banaya[*]	157.776	52.926	75	Chirinkotan[*]	153.484	48.977
38	Gorely	158.035	52.555				
2. Kuriles							
1	Raikoke[*]	153.248	48.294	24	Chirip	147.921	45.337
2	Sarychev Peak[*]	153.198	48.091	25	Baransky	148.015	45.103
3	Rasshua	153.022	47.756	26	Tebenkov	147.917	45.028
4	Srednii	152.920	47.600	27	Etorofu-Yakeyama	147.871	45.012
5	Ushishur	152.814	47.513	28	Bogatyr	147.344	44.839
6	Ketoi	152.479	47.343	29	Atsonopuri	147.128	44.807
7	Urataman	152.247	47.121	30	Lvinaya Past	146.994	44.608
8	Prevo Peak	152.115	47.011	31	Berutarube	146.928	44.479
9	Zavaritzki Caldera	151.950	46.925	32	Tiatia	146.251	44.354
10	Milne	151.786	46.815	33	Smirnov	146.139	44.454
11	Goriaschaia Sopka	151.751	46.832	34	Mendeleev	145.733	43.978
12	Chirpoi	150.866	46.522	35	Golovnin	145.505	43.844
13	Gora Desantnaya	150.369	46.192	36	Shiretoko-Iwo-Zan	145.163	44.130
14	Antipin	150.230	46.150	37	Rausu	145.122	44.076
15	Kolokol	150.065	46.061	38	Tenchozan	145.086	44.044
16	Petr Shmidt Ridge	150.053	45.953	39	Shari	144.722	43.762
17	Tri Sestry	149.925	45.910	40	Mashu	144.555	43.567
18	Rudakov	149.823	45.872	41	Kutcharo	144.438	43.611
19	Ivao	149.672	45.755	42	Akan	144.006	43.385
20	Demon	148.852	45.506	43	Daisetsu[*]	142.855	43.663
21	Medvezhia	148.811	45.382	44	Nipesotsu-Maruyama[*]	143.031	43.455
22	Rucharuyama	148.344	45.243	45	Shirakibetsu[*]	143.092	43.315
23	Tsirk	148.580	45.400	46	Tokachi[*]	142.682	43.421

(cont.)

No.	Volcano Name	Longitude	Latitude	No.	Volcano Name	Longitude	Latitude
3. North Japan							
1	Shikotsu	141.377	42.691	23	Adatara	140.283	37.627
2	Kuttara	141.180	42.500	24	Bandaisan	140.079	37.608
3	Toya[*]	140.833	42.543	25	Numazawa[*]	139.579	37.450
4	Yotei[*]	140.806	42.827	26	Nasu	139.963	37.125
5	Niseko[*]	140.636	42.884	27	Takahara	139.777	36.900
6	Komagatake[*]	140.686	42.066	28	Omanago	139.508	36.795
7	Essan	141.165	41.806	29	Nantai	139.491	36.767
8	Oshima-Oshima[*]	139.353	41.513	30	Nikko-Shiranesan	139.376	36.798
9	Osoremaya	141.120	41.279	31	Hiuchigatake	139.286	36.953
10	Hakkoda	140.878	40.658	32	Akagi	139.177	36.540
11	Iwaki[*]	140.303	40.656	33	Haruna	138.878	36.476
12	Towada	140.920	40.470	34	Kusatsu	138.536	36.643
13	Akita-Yakeyama	140.759	39.966	35	Shiga	138.514	36.690
14	Hachimantai	140.857	39.955	36	Niigata-Yakeyama[*]	138.035	36.921
15	Iwate	141.003	39.851	37	Myoko[*]	138.112	36.892
16	Akita-Komaga-Take	140.792	39.752	38	Asama	138.520	36.407
17	Chokai[*]	140.049	39.099	39	Tateshina	138.294	36.103
18	Kurikomayama	140.779	38.967	40	Tateyama[*]	137.605	36.554
19	Hijiori	140.180	38.600	41	Yakedake	137.587	36.228
20	Narugo	140.725	38.734	42	Norikuradake	137.548	36.107
21	Zao	140.450	38.136	43	Ontakesan	137.478	35.894
22	Azuma	140.261	37.722	44	Hakusan[*]	136.771	36.155
4. Izu-Bonin							
1	Fuji[**]	138.730	35.363	17	Sofugan	140.357	29.808
2	Hakoneyama[**]	139.022	35.243	18	Nichiyo	140.329	29.480
3	Izu-Tobu[**]	139.095	34.904	19	Getsuyo	140.466	29.311
4	Izu-Oshima[**]	139.395	34.726	20	Kayo	140.538	29.064
5	Toshima[**]	139.279	34.521	21	Suiyo	140.643	28.572
6	Niijima[**]	139.264	34.398	22	Mokuyo	140.567	28.316
7	Kozushima[**]	139.152	34.218	23	Doyo	140.801	27.679

(cont.)

No.	Volcano Name	Longitude	Latitude	No.	Volcano Name	Longitude	Latitude
8	Miyakejima	139.526	34.086	24	Kinyo	140.804	28.082
9	Kurose Hole	139.680	33.399	25	Nishinoshima	140.879	27.243
10	Mikurajima	139.601	33.869	26	Kaikata	140.930	26.667
11	Hachijojima	139.765	33.139	27	Kaitoku	141.102	26.122
12	Aogashima	139.910	32.470	28	Kita-Iwojima	141.265	25.446
13	Kita-Bayonnaise	139.844	32.108	29	Iwojima	141.379	24.780
14	Bayonnaise Rocks	139.986	31.894	30	Kita-Fukutokutai	141.419	24.414
15	Sumisujima	140.044	31.444	31	Fukutoku-Oka-no-Ba	141.480	24.285
16	Izu-Torishima	140.305	30.482				
5. Ryukyu							
1	Tsurumi	131.392	33.282	9	Kikai	130.308	30.792
2	Kuju	131.246	33.085	10	Kuchinoerabujima	130.216	30.446
3	Aso	131.085	32.885	11	Kuchinoshima	129.926	29.968
4	Unzen[*]	130.298	32.761	12	Nakanoshima	129.859	29.859
5	Kirishimayama	130.862	31.938	13	Suwanosejima	129.715	29.642
6	Sumiyoshi-ike	130.592	31.771	14	Akusekijima	129.593	29.466
7	Sakurajima	130.658	31.579	15	Yokoatejima	128.996	28.799
8	Ibusuki	130.569	31.219	16	Iwotorishima	128.228	27.869
6. Aleutians							
1	Buldir	175.908	52.346	20	Amukta	-171.255	52.495
2	Kiska	177.605	52.105	21	Chugalak	-171.141	52.574
3	Segula	178.136	52.015	22	Yunaska W	-170.778	52.609
4	Davidof	178.330	51.970	23	Yunaska E	-170.635	52.640
5	Little Sitkin	178.541	51.949	24	Herbert	-170.117	52.750
6	Semisopochnoi	179.586	51.936	25	Carlisle	-170.059	52.892
7	Galeroi	-178.795	51.789	26	Cleveland	-169.946	52.822
8	Tanaga	-178.143	51.884	27	Tana	-169.792	52.841
9	Takawangha	-178.006	51.872	28	Kagami	-169.720	52.973
10	Bobrof	-177.443	51.907	29	Uliaga	-169.763	53.065
11	Kanaga	-177.164	51.924	30	Vsevidof	-168.687	53.127
12	Moffett	-176.739	51.935	31	Recheschnoi	-168.571	53.153
13	Adagdak	-176.586	51.990	32	Okmok	-168.130	53.429

(cont.)

No.	Volcano Name	Longitude	Latitude	No.	Volcano Name	Longitude	Latitude
14	Great Sitkin	-176.132	52.078	33	Bogoslof[*]	-168.039	53.933
15	Kasatochi	-175.512	52.174	34	Makushin	-166.928	53.887
16	Koniuji	-175.132	52.222	35	Table Top	-166.681	53.969
17	Atka	-174.141	52.330	36	Wide Bay	-166.618	53.964
18	Korovin	-174.159	52.379	37	Akutan	-165.975	54.146
19	Seguam	-172.513	52.313	38	Gilbert	-165.660	54.252
7. Alaska							
1	Westdahl	-164.650	54.517	23	Kialagvik	-156.745	57.202
2	Fisher	-164.365	54.668	24	Ugashik-Peulik	-156.379	57.746
3	Shishaldin	-163.970	54.756	25	Ukinrek	-156.514	57.834
4	Isanotski	-163.730	54.767	26	Unnamed	-155.411	57.870
5	Round Top	-163.594	54.802	27	Martin	-155.356	58.169
6	Frosty	-162.836	55.067	28	Mageik	-155.247	58.196
7	Dutton	-162.275	55.185	29	Trident	-155.102	58.234
8	Emmons Lake	-162.076	55.341	30	Novarupta	-155.159	58.265
9	Pavlof	-161.894	55.417	31	Griggs	-155.106	58.351
10	Pavlof Sister	-161.854	55.457	32	Katmai	-154.978	58.262
11	Amak[*]	-163.147	55.418	33	Snowy	-154.686	58.333
12	Dana	-161.213	55.629	34	Denison	-154.451	58.417
13	Stepovak Bay 1	-160.098	55.869	35	Steller	-154.395	58.431
14	Stepovak Bay 2	-160.041	55.913	36	Kukak	-154.357	58.453
15	Stepovak Bay 3	-160.000	55.933	37	Kaguyak	-154.068	58.606
16	Stepovak Bay 4	-159.956	55.952	38	Fourpeaked	-153.673	58.770
17	Kupreanof	-159.792	56.014	39	Douglas	-153.541	58.854
18	Vemiaminof	-159.390	56.195	40	Augustine	-153.432	59.361
19	Black Peak	-158.788	56.557	41	Iliamna	-153.089	60.032
20	Aniakchak	-158.151	56.885	42	Redoubt	-152.763	60.491
21	Yantarini	-157.191	57.017	43	Spurr	-152.250	61.301
22	Chiginakagak	-156.987	57.133	44	Hayes	-152.411	61.641
8. Central America							
1	Takana	-92.109	15.132	39	Taburete	-88.533	13.439
2	Tajumulco	-91.904	15.043	40	Tecapa	-88.494	13.492

(cont.)

No.	Volcano Name	Longitude	Latitude	No.	Volcano Name	Longitude	Latitude
3	Chicabal	-91.656	14.787	41	Usulutan	-88.469	13.419
4	Santiaguito	-91.568	14.738	42	El Tigre	-88.430	13.470
5	Santa Maria	-91.553	14.755	43	Chinameca	-88.319	13.477
6	Almolonga	-91.519	14.799	44	San Miguel	-88.271	13.432
7	San Pedro	-91.267	14.657	45	Laguna Aramuaca	-88.105	13.430
8	Toliman	-91.186	14.621	46	Conchagua	-87.845	13.275
9	Atitlan	-91.188	14.583	47	Conchaguita	-87.768	13.231
10	Acatenango	-90.876	14.501	48	Isla El Tigre	-87.639	13.273
11	Fuego	-90.881	14.474	49	Isla Zacate Grande	-87.626	13.333
12	Agua	-90.742	14.466	50	Cosiguina	-87.567	12.982
13	Pacaya	-90.602	14.382	51	San Cristobal	-87.002	12.704
14	Tecuamburro	-90.400	14.153	52	Telica	-86.842	12.605
15	Cuilapa-Barbarena	-90.400	14.330	53	Rota	-86.750	12.550
16	Jumaytepeque	-90.271	14.339	54	Cerro Negro	-86.702	12.508
17	Moruta	-90.095	14.027	55	Las Pillas	-86.688	12.497
18	Flores[*]	-89.995	14.307	56	El Hoyo	-86.668	12.488
19	Tahual[*]	-89.901	14.437	57	Momotombo	-86.539	12.424
20	Cerro Santiago[*]	-89.870	14.339	58	Apoyeque	-86.341	12.244
21	Suchitan[*]	-89.775	14.398	59	Nejapa-Milaflores	-86.321	12.120
22	Ixtepeque[*]	-89.683	14.425	60	Masaya	-86.168	11.984
23	Ipala[*]	-89.640	14.556	61	Granada	-85.980	11.920
24	Chiquimula[*]	-89.547	14.830	62	Mombacho	-85.975	11.830
25	Quezaltepeque[*]	-89.426	14.585	63	Zepatera	-85.818	11.732
26	San Diego[*]	-89.480	14.273	64	Concepcion	-85.622	11.538
27	Chingo	-89.727	14.117	65	Maderas	-85.512	11.445
28	Cerro Singuil	-89.631	14.054	66	Orosi	-85.472	10.979
29	Apaneca Range	-89.787	13.891	67	Rincon de la Vieja	-85.337	10.831
30	Santa Ana	-89.629	13.849	68	Miravalles	-85.151	10.747
31	Izalco	-89.632	13.814	69	Tenorio	-85.012	10.671
32	Coatepeque Caldera	-89.550	13.870	70	Arenal	-84.703	10.463
33	San Salvador	-89.286	13.737	71	Platanar	-84.366	10.299
34	Cerro Cinotepeque	-89.245	14.008	72	Poas	-84.231	10.198

(cont.)

No.	Volcano Name	Longitude	Latitude	No.	Volcano Name	Longitude	Latitude
35	Guazapa	-89.114	13.902	73	Barva	-84.106	10.134
36	Ilopango	-89.053	13.672	74	Irazu	-83.846	9.981
37	San Vicente	-88.839	13.597	75	Turialba	-83.763	10.020
38	Apastapeque	-88.770	13.720				
9. Lesser Antilles							
1	Saba	-63.239	17.634	10	Morne Trois Pitons	-61.325	15.370
2	Northern Centres	-62.997	17.508	11	Morne Watt	-61.296	15.318
3	The Quill	-62.963	17.477	12	Morne Plat Pays	-61.347	15.250
4	Liamuiga	-62.810	17.370	13	Pelee	-61.167	14.810
5	Nevis	-62.582	17.156	14	Qualibou	-61.047	13.838
6	Soufriere Hills	-62.176	16.711	15	Soufriere St Vincent	-61.183	13.335
7	Soufriere Guadaloupe	-61.664	16.043	16	Kick 'em Jenny	-61.631	12.299
8	Morne aux Diables	-61.432	15.615	17	St Catherine	-61.675	12.162
9	Morne Diablotins	-61.398	15.504				
10. Northern Andes							
1	San Diego	-74.961	5.650	19	Quicocha	-78.364	0.308
2	Cerro Bravo	-75.292	5.091	20	Imbabura	-78.180	0.258
3	Romeral	-75.365	5.212	21	Soche[*]	-77.577	0.552
4	Ruiz	-75.319	4.892	22	Reventador[*]	-77.658	-0.081
5	Santa Isabel	-75.367	4.818	23	Cayambe[*]	-77.989	0.025
6	Nevada del Quindo	-75.389	4.715	24	Mojanda	-78.275	0.123
7	Nevada del Tolima	-75.330	4.658	25	Pulagua	-78.465	0.035
8	Machin	-75.390	4.487	26	Guagua Pichinca	-78.613	-0.170
9	Nevado del Huila	-76.026	2.932	27	Atacazo	-78.623	-0.356
10	Purace	-76.396	2.314	28	Chacana[*]	-78.252	-0.369
11	Sotara	-76.590	2.106	29	Sumaco[*]	-77.627	-0.540
12	Dona Juana	-76.936	1.500	30	Antisana[*]	-78.139	-0.481
13	Galeras	-77.359	1.221	31	Cotopaxi[*]	-78.437	-0.684
14	Azufral	-77.719	1.086	32	Illiniza	-78.716	-0.662
15	Cumbal	-77.885	0.956	33	Quilotoa	-78.904	-0.860
16	Cerro Negro	-77.934	0.819	34	Tungurahua[*]	-78.447	-1.469
17	Chachimbiro	-78.290	0.469	35	Chimborazo[*]	-78.817	-1.469

(cont.)

No.	Volcano Name	Longitude	Latitude	No.	Volcano Name	Longitude	Latitude
18	Cotacachi	-78.346	0.367	36	Sangay[*]	-78.341	-2.005
11. Central Andes							
1	Sara Sara	-73.446	-15.329	32	Seiracabur	-67.891	-22.719
2	Nevados Firura	-72.640	-15.237	33	Licancabur	-67.884	-22.834
3	Coropuna	-72.657	-15.520	34	Guayaques	-67.575	-22.893
4	Andahua-Orcumpampa	-72.339	-15.426	35	Purico Complex	-67.746	-22.993
5	Huambo	-72.133	-15.837	36	Colachi	-67.646	-23.241
6	Sabancaya	-71.856	-15.788	37	Aramachi	-67.620	-23.293
7	Cerro Nicholson	-71.754	-16.262	38	Lascar	-67.732	-23.363
8	Nevado Chachani	-71.528	-16.192	39	Cerro Overo	-67.662	-23.517
9	El Misti	-71.406	-16.299	40	Chiliques	-67.702	-23.579
10	Ubinas	-70.898	-16.346	41	Cordon de Puntas Negras	-67.540	-23.743
11	Huaynaputina	-70.854	-16.614	42	Caichinque	-67.739	-23.949
12	Ticsani	-70.604	-16.766	43	Miniques	-67.758	-23.819
13	Tutupaca	-70.359	-17.027	44	Cerro Tujle[*]	-67.952	-23.835
14	Yucamane	-70.199	-17.183	45	Tilocalar[*]	-68.129	-23.978
15	Nevados Casiri	-69.814	-17.470	46	El Negrillar	-68.250	-24.180
16	Tacora	-69.772	-17.721	47	La Negrillar	-68.589	-24.318
17	Tapaca	-69.508	-18.097	48	Pular[*]	-68.056	-24.191
18	Parinacota	-69.143	-18.164	49	Aracar[*]	-67.791	-24.288
19	Guallatiri	-69.092	-18.420	50	Socompa	-68.247	-24.396
20	Tambo Quemado	-68.757	-18.626	51	Llullaillaco	-68.537	-24.720
21	Isluga	-68.835	-19.156	52	Escorial	-68.366	-25.081
22	Tata Sabaya	-68.523	-19.136	53	Lastarria	-68.504	-25.168
23	Laguna Jaya Khota[*]	-67.432	-19.464	54	Cordon del Azufre	-68.524	-25.335
24	Irruputuncu	-68.558	-20.734	55	Cerro Bayo Gorbea	-68.589	-25.413
25	Olca Paruma	-68.480	-20.944	56	Sierra Nevada	-68.578	-26.481
26	Ollague	-68.182	-21.305	57	El Condor	-68.361	-26.632
27	San Pedro	-68.407	-21.884	58	Peinado	-68.115	-26.621
28	Cerro del Azufre	-68.240	-21.785	59	False Azufre	-68.363	-26.806
29	Cerro Toconce	-68.079	-22.188	60	Nevados Ojos del Salado	-68.543	-27.109
30	Cerros de Tocorpuri	-67.891	-22.442	61	El Solo	-68.713	-27.105

(cont.)

No.	Volcano Name	Longitude	Latitude	No.	Volcano Name	Longitude	Latitude
31	Putana	-67.854	-22.557	62	Tipas	-68.559	-27.195
12. Southern Andes							
1	Tupungatito	-69.797	-33.425	31	Caburgua-Holloemolle	-71.826	-39.201
2	San Jose	-69.901	-33.785	32	Villarica	-71.940	-39.420
3	Maipo	-69.834	-34.165	33	Quetrupillan	-71.717	-39.499
4	Palomo	-70.297	-34.611	34	Lanin[*]	-71.503	-39.637
5	Caldera del Ateul	-70.003	-34.594	35	Huanquihue[*]	-71.580	-39.887
6	Tinguiririca	-70.354	-34.817	36	Mocho-Choshuenco	-72.028	-39.930
7	Sordo Lucas	-70.455	-34.992	37	Carran-Los Venados	-72.059	-40.361
8	Infiernillo[*]	-69.901	-35.123	38	Puyuhue-Cordon Caulle	-72.112	-40.583
9	Risco Plateado[*]	-69.993	-34.919	39	Antillanca	-72.156	-40.777
10	Planchon-Peteroa	-70.574	-35.240	40	Puntiguido-Cordon Cenizos	-72.267	-40.973
11	Calabozos	-70.500	-35.567	41	Osorno	-72.497	-41.105
12	Descabezado Grande	-70.752	-35.588	42	Cayute-La Viguera	-72.282	-41.250
13	Cerro Azul	-70.764	-35.657	43	Calbuco	-72.609	-41.330
14	Los Hornitos	-70.810	-35.729	44	Yate	-72.399	-41.759
15	San Pedro-Pellado	-70.852	-35.993	45	Hornopiren	-72.433	-41.880
16	Laguna del Maule[*]	-70.492	-36.058	46	Apagado	-72.589	-41.884
17	Nevado de Longavi	-71.165	-36.199	47	Huequi	-72.583	-42.382
18	Loma Blancas	-71.010	-36.290	48	Machinmahuida	-72.446	-42.799
19	Volcan Resago	-70.920	-36.450	49	Chaiten	-72.656	-42.836
20	Nevados de Chillan	-71.378	-36.868	50	Corcovado	-72.792	-43.193
21	Antuco	-71.351	-37.410	51	Yanteles	-72.811	-43.497
22	Copahue	-71.173	-37.863	52	Palena Volcanic Group[*]	-72.488	-43.796
23	Callaqui	-71.449	-37.927	53	Melimoyo	-72.869	-44.074
24	Laguna Marinaqui[*]	-71.162	-38.256	54	Puyuhuapi[*]	-72.544	-44.307
25	Tralihue[*]	-70.900	-38.510	55	Mentolat	-73.078	-44.693
26	Tolhuaca	-71.645	-38.310	56	Cay	-72.985	-45.059
27	Lonquimay	-71.590	-38.379	57	Maca	-73.170	-45.106
28	Sierra Nevada	-71.563	-38.582	58	Meulin	-73.049	-45.205
29	Llaima	-71.730	-38.697	59	Cerro Hudson	-72.947	-45.929
30	Sollipulli	-71.521	-38.975				

(cont.)

No.	Volcano Name	Longitude	Latitude	No.	Volcano Name	Longitude	Latitude
13. Scotia							
1	Protector Shoal	-28.080	-55.921	6	Saunders	-26.464	-57.780
2	Zavodovski	-27.582	-56.297	7	Montagu	-26.361	-58.423
3	Leskov[*]	-28.130	-56.670	8	Bristol	-26.589	-59.062
4	Hodson	-27.177	-56.712	9	Thule Islands	-27.361	-59.442
5	Candlemas	-26.706	-57.084				
14. Kermadec-North Island							
1	Ruapehu	175.564	-39.281	22	Kibblewhite	179.264	-34.577
2	Ngaruhue	175.632	-39.157	23	Sonne	179.579	-34.078
3	Tongariro	175.651	-39.137	24	Ngatoroirangi	179.827	-33.732
4	Taupo	176.000	-38.820	25	Cole	179.954	-33.414
5	Maroa	176.080	-38.420	26	Kuiwai	-179.954	-33.162
6	Reporoa	176.330	-38.420	27	Haungaroa	-179.622	-32.619
7	Tarawera	176.510	-38.225	28	Oliver-Speight	-179.588	-32.388
8	Okataina	176.501	-38.117	29	Wright	-179.180	-31.851
9	White Island	177.183	-37.521	30	Havre Seamount	-179.031	-31.080
10	Clark	177.838	-36.449	31	Curtis Island	-178.556	-30.543
11	Tangaroa	178.028	-36.322	32	Macauley	-178.436	-30.231
12	Rumble IV	178.050	-36.131	33	Giggenbach	-178.714	-30.038
13	Rumble V	178.197	-36.143	34	Raoul Island	-177.920	-29.265
14	Rumble III	178.478	-35.746	35	Hinatapeka	-177.826	-28.832
15	Rumble II East	178.652	-35.420	36	Volcano OP	-177.690	-28.224
16	Rumble II West	178.526	-35.355	37	Putoto	-177.617	-27.861
17	Thompson	178.865	-35.287	38	Volcano Q	-177.504	-27.473
18	Silent II East	178.978	-35.211	39	Gamble	-177.407	-27.206
19	Silent II West	178.902	-35.171	40	Rakahore	-177.398	-26.810
20	Healy	178.973	-35.005	41	Hinepuia	-177.266	-26.391
21	Brothers	179.075	-34.875	42	Monowai	-177.188	-25.887

(cont.)

No.	Volcano Name	Longitude	Latitude	No.	Volcano Name	Longitude	Latitude
15. Tonga							
1	Volcano 19	-177.018	-24.802	23	Tonga Hunga-Hunga Ha'apai	-175.391	-20.546
2	Volcano 18	-176.924	-24.582	24	Fonuafo'ou	-175.420	-20.320
3	Volcano 16	-176.849	-24.177	25	Volcano C	-175.162	-20.126
4	Volcano 15	-176.779	-23.897	26	Tofua	-175.071	-19.732
5	Volcano 2	-176.666	-23.565	27	Kao	-175.014	-19.670
6	Volcano 8S	-176.405	-22.976	28	Volcano D	-174.938	-19.420
7	Volcano 8	-176.416	-22.841	29	Methis Shoal	-174.852	-19.180
8	Volcano 7	-176.388	-22.707	30	Home Reef	-174.775	-18.992
9	Volcano 7B	-176.444	-22.553	31	Late	-174.648	-18.806
10	Volcano 6.5	-176.346	-22.456	32	Volcano F	-174.365	-18.326
11	Volcano 4 SE	-176.187	-22.191	33	Toku	-174.180	-18.162
12	Volcano 4 S	-176.243	-22.146	34	Fonualei	-174.317	-18.023
13	Volcano 4	-176.299	-22.029	35	Volcano H	-174.250	-17.872
14	Volcano 5 SW	-176.094	-22.085	36	Volcano I	-174.153	-17.548
15	Volcano 5a N	-176.032	-22.026	37	Volcano J	-173.970	-17.251
16	Volcano 3	-175.930	-21.831	38	Volcano M	-173.822	-16.841
17	Volcano 2.5	-175.750	-21.378	39	Volcano K	-173.763	-16.550
18	Unnamed	-175.650	-21.338	40	Volcano L	-173.899	-16.221
19	Volcano 1	-175.750	-21.150	41	Tafahi	-173.747	-15.854
20	Volcano A	-175.550	-20.853	42	Curacoa	-173.670	-15.621
21	Volcano B-S	-175.450	-20.700	43	Volcano N	-173.693	-15.572
22	Volcano B-W	-175.531	-20.581				
16. Vanuatu							
1	Eastern Gemini	170.282	-20.987	9	Lopevi	168.341	-16.509
2	Aneityum	169.788	-20.188	10	Ambrym	168.128	-16.249
3	Yasur	169.447	-19.529	11	Ambae	167.830	-15.391
4	Traitor's Head	169.234	-18.755	12	Mere Lava	168.040	-14.460
5	North Vate	168.359	-17.460	13	Gaua	167.518	-14.285
6	NE Shepherd Island	168.592	-16.992	14	Suretamatai	167.470	-13.800
7	Kuwae	168.536	-16.829	15	Motlav	167.670	-13.671
8	Epi	168.370	-16.680	16	Ureparapara	167.338	-13.538

(cont.)

No.	Volcano Name	Longitude	Latitude	No.	Volcano Name	Longitude	Latitude
17. Mariana							
1	Nikko (NI)	142.326	23.078	20	Agrigan (AG)[1]	145.667	18.750
2	Ichiyo (IC)	142.533	22.958	21	Pagan (PA)[1]	145.750	18.120
3	Syoyo (SY)	142.983	22.475	22	Alamagan (AL)[1]	145.850	17.600
4	S Fukuyama (SF)	143.096	22.355	23	Guguan (GU)[1]	145.867	17.300
5	Fukujin (FU)	143.458	21.942	24	Zealandia (ZE)[2]	145.800	16.883
6	Kasuga 1 (K1)	143.708	21.777	25	Sarigan (SA)[1]	145.783	16.700
7	NW Eifuku (NWE)	144.043	21.488	26	S Sarigan (SS)[2]	145.775	16.588
8	Eifuku (EI)	144.145	21.415	27	Anatahan (AN)[1]	145.667	16.333
9	Daikoku (DA)	144.194	21.324	28	E. Diamante (ED)[2]	145.658	15.917
10	SE Daikoku (SED)	144.417	21.208	29	N Ruby 2 (NR)[2]	145.617	15.733
11	S Daikoku (SD)	144.525	21.023	30	Ruby (RU)[1]	145.573	15.604
12	Chamorro (CH)	144.704	20.810	31	W Saipan (WS)[2]	145.450	15.300
13	Farallone de Parajos (FP)[1]	144.883	20.530	32	W Tinian (WT)[2]	145.417	15.083
14	Ahyi (AH)[1]	145.029	20.438	33	Esmeralda (ES)[1]	145.246	14.958
15	Supply Reef (SR)[2]	145.100	20.133	34	NW Rota 3 (NR3)	144.996	14.596
16	Maug (MA)[1]	145.222	20.021	35	W Rota (WR)	144.833	14.325
17	Asuncion (AS)[1]	145.453	19.700	36	NW Guam (NWG)	144.638	14.017
18	Cheref (CE)[2]	145.467	19.408	37	Tracey (TR)	144.411	13.633
19	Poyo (PO)[2]	145.517	19.223				
Explanation for Mariana Arc: [1] Volcanoes included in GVP04 dataset; [1] and [2] Volcanoes included in GVP04+SM dataset							
18. Java and Lesser Sunda							
1	Krakatau (Krk)	105.423	-6.101	24	Sumbing (Smb)	110.074	-7.382
2	Pulosari (Pls)	105.978	-6.342	25	Ungaran[*] (Ugr)	110.344	-7.189
3	Parakasak (Pks)	105.981	-6.248	26	Telomoyo[*] (Tlm)	110.403	-7.360
4	Karang (Krg)	106.047	-6.272	27	Merbabu[*] (Mbb)	110.439	-7.453
5	Endut (End)	106.362	-6.620	28	Merapi (Mrp)	110.447	-7.539
6	Perbakti (PG)	106.693	-6.751	29	Lawu (Lwu)	111.193	-7.626
7	Salak (Slk)	106.732	-6.708	30	Wilis (Wls)	111.760	-7.812
8	Gede (Gde)	106.985	-6.791	31	Kelud (Klt)	112.308	-7.936

(cont.)

No.	Volcano Name	Longitude	Latitude	No.	Volcano Name	Longitude	Latitude
9	Patuha (Pth)	107.406	-7.176	32	Kawi (KB)	112.443	-7.921
10	Tangkuban Perahu (TP)	107.607	-6.759	33	Arjuna-Welirang (AW)	112.589	-7.765
11	Malabar (Mlb)	107.622	-7.136	34	Penanggungan (Png)	112.620	-7.615
12	Wayang-Windu (WW)	107.631	-7.224	35	Semeru (Smr)	112.922	-8.109
13	Kendang (Kdg)	107.720	-7.230	36	Tengger Caldera (Tgg)	112.951	-7.950
14	Papandayan (Ppd)	107.729	-7.321	37	Lamongan (Lmg)	113.340	-7.981
15	Kamojang[*] (Kmj)	107.800	-7.125	38	Argapura (IA)	113.595	-7.976
16	Guntur[*] (Gtr)	107.842	-7.146	39	Raung (Rag)	114.055	-8.120
17	Tampomas (Tmp)	107.962	-6.763	40	Ijen (Ijn)	114.242	-8.057
18	Talagabodas[*] (Tlg)	108.059	-7.225	41	Bratan (Brt)	115.139	-8.262
19	Galunggung[*] (Glg)	108.059	-7.248	42	Batur (Btr)	115.377	-8.238
20	Ciremai (Crm)	108.408	-6.895	43	Agung (Agg)	115.507	-8.343
21	Slamet (Slm)	109.216	-7.242	44	Rinjani (Rjn)	116.413	-8.409
22	Dieng Vol. Complex[*] (Dng)	109.902	-7.224	45	Nangi (Nng)	116.561	-8.413
23	Sundoro[*] (Sdr)	109.996	-7.3				
19. Sumatra							
1	Pulau We (Pwe)	95.284	5.874	21	Kunyit (Kny)	101.483	-2.274
2	Seulawah Agam (Sag)	95.658	5.448	22	Hutapanjang (Htp)	101.600	-2.330
3	Peuet Sague (Psa)	96.329	4.914	23	Sumbing (Smb)	101.728	-2.414
4	Geureudong (Geu)	96.820	4.813	24	Tungkat (Tgk)	102.025	-2.480
5	Bur Ni Telong (Bnt)	96.821	4.769	25	Lumut (Lum)	102.207	-3.214
6	Kembar (Kbr)	97.664	3.850	26	Gedanghululai (Gdh)	102.239	-3.245
7	Sibayak (Sby)	98.501	3.248	27	Daun (Bda)	102.370	-3.380
8	Sinabung (Snb)	98.392	3.170	28	Kaba (Kba)	102.627	-3.515
9	Pusuk Bukit (PB)	98.653	2.602	29	Isauisau[*] (Isa)	103.624	-3.968
10	Toba (Tob)	98.830	2.580	30	Dempo (Dmp)	103.124	-4.016
11	Andiantorping (Adt)	98.968	1.961	31	Lumut-Balai[*] (Blb)	103.621	-4.224
12	Sibualbuali (Sbl)	99.255	1.556	32	Besar 1 (Bs1)	103.365	-4.243
13	Lubuk Raya (Lbr)	99.209	1.478	33	Patah (Pta)	103.300	-4.270
14	Sorik Merapi (Srm)	99.541	0.684	34	Besar 2 (Bs2)	103.679	-4.442
15	Sarik-Gajah (Srg)	100.200	0.080	35	Ranau (Rna)	103.927	-4.855
16	Talamau (Tlm)	99.980	0.079	36	Seminung (Smu)	103.960	-4.912

(cont.)

No.	Volcano Name	Longitude	Latitude	No.	Volcano Name	Longitude	Latitude
17	Marapi (Mrp)	100.473	-0.381	37	Sekincau (Skc)	104.314	-5.088
18	Tandikat-Singgalang (Tds)	100.331	-0.390	38	Suoh (Suo)	104.291	-5.248
19	Talang (Tlg)	100.679	-0.978	39	Krakatau (Krk)	105.423	-6.101
20	Kerinci (Krc)	101.264	-1.697				

[*] off-segment volcanoes as it lies $\geq$ 30 km from the great circle trend
[**] volcanoes not included in geometric fitting due to subduction complexity

Appendix C

Spatial Analysis Methods

C.1 Small Circles

C.1.1 Simulated Annealing

Small circle fitting into arc volcano dataset used optimisation principle by simulated annealing method (Kirkpatrick et al., 1983). Simulated annealing is a probabilistic method for estimating the global optimum of a given function as a solution of unconstrained and bound-constrained optimisation problem. The optimisation focused on three adjustable properties of a small circle which are: radius, centre's longitude, and centre's latitude. Optimisation is constrained by the average root-mean-square distance from small circle to volcano locations (Equation 2.1). Optimisation follows the pesudo-code below.

- Let $s = s_0$
- For $k = 0$ through k_{max} (exclusive):
  - $T \longleftarrow$ variable$(k_{max}/(k+1))$
  - Pick a random neighbour, $s_{new} \longleftarrow$ neighbour(s)
  - If $P(E(s), E(s_{new}), T) \geq$ random$(0, 1)$:
  - $s \longleftarrow s_{new}$
- Output: the final state s

C.1.2 Script

```
function AnnealingSC

%Input
clear;
[num,txt,raw] = xlsread('dataset.xlsx');
vlon = num(:,1);
vlat = num(:,2);
vname = txt;
nvol = numel(vlon);

%Parameters

maxiter = 10000000;
minrad = 5;
maxrad = 10000;

%% Initial Process

%Convert to Radians

sumlon = 0;
```

```
sumlat = 0;
for i=1:nvol
    vlon(i) = vlon(i)*(pi/180);
    vlat(i) = vlat(i)*(pi/180);
    sumlon = sumlon + vlon(i);
    sumlat = sumlat + vlat(i);
end

%Generate Random Parameters for Initial Small Circle

lonSC = sumlon / nvol + (rand - 0.5)*0.1;
latSC = sumlat / nvol + (rand - 0.5)*0.1;
radSC = rand * 50;

%Initial Current Small Circle Parameters

currlonSC = lonSC;
currlatSC = latSC;
currradSC = radSC;

%Initial Best Small Circle Parameters

bestlonSC = lonSC;
bestlatSC = latSC;
bestradSC = radSC;
bestiter = 0;

[currdist,currmisfit] = calcdist(vlon,vlat,lonSC,latSC,radSC,nvol);
[bestdist, bestmisfit] = calcdist(vlon,vlat,lonSC,latSC,radSC,nvol)
    ;

%Write Initial Distance

x00 = ['Initial Small Circle'];
x01 = ['RMS: ', num2str(sqrt(bestdist/nvol))];
x02 = ['Lat: ', num2str(bestlatSC*180.0/pi)];
x03 = ['Lon: ', num2str(bestlonSC*180.0/pi)];
x04 = ['Rad: ', num2str(bestradSC)];

clc; disp(x00); disp(x03); disp(x02); disp(x04); disp(x01);

%% Simulated Annealing Loop

f = waitbar(0,'Processing...','Name','Small Circle Annealing
    Simulation');

for k=1:maxiter

    r = rand;
    if (r <= 0.33333) %randomise radius
        radSC = currradSC + (rand - 0.5) * 5.0;
        radSC = max([radSC minrad]);
        radSC = min([radSC maxrad]);

    elseif (r > 0.33333) && (r <= 0.66667) %randomise longitude
        lonSC = currlonSC + (rand - 0.5) * 0.01;
```

```
76
77          if (lonSC > 180)
78              lonSC = lonSC - 360;
79
80          elseif (lonSC < -180)
81              lonSC = lonSC + 360;
82          end
83
84      else %randomise latitude
85          latSC = currlatSC + (rand - 0.5) * 0.01;
86
87          if (latSC > 90)
88              latSC = 180 - latSC;
89
90          elseif (latSC < -90)
91              latSC = (-180) - latSC;
92
93          end
94
95      end
96
97      [dist,misfit] = calcdist(vlon,vlat,lonSC,latSC,radSC,nvol);
98
99      if (dist < currdist)
100         currradSC = radSC;
101         currlonSC = lonSC;
102         currlatSC = latSC;
103         currdist = dist;
104         currmisfit = misfit;
105
106     else
107         if ((rand * (dist - currdist)) < (1000 / k))
108             currradSC = radSC;
109             currlonSC = lonSC;
110             currlatSC = latSC;
111             currdist = dist;
112             currmisfit = misfit;
113         end
114
115     end
116
117     if dist < bestdist
118         bestlonSC = lonSC;
119         bestlatSC = latSC;
120         bestradSC = radSC;
121         bestdist = dist;
122         bestiter = k;
123         bestmisfit = misfit;
124     end
125
126    waitbar(k/maxiter,f);
127
128 end
129
130 delete(f)
131
```

```
x10 = ['Best Fit Small Circle'];
x11 = ['RMS: ', num2str(sqrt(bestdist/nvol))];
x12 = ['Lat: ', num2str(bestlatSC*180.0/pi)];
x13 = ['Lon: ', num2str(bestlonSC*180.0/pi)];
x14 = ['Rad: ', num2str(bestradSC)];
x15 = ['Iteration: ', num2str(bestiter)];
x16 = ['n Volcanoes: ', num2str(nvol)];

fprintf('\n');
disp(x10); disp(x13); disp(x12); disp(x14); disp(x11); disp(x15);
   disp(x16);

fprintf('\n%-20s %10s\n','Volcano','XTD');
for j = 1 : numel(vlon);
fprintf('%-20s %10.5f\n',char(vname(j)),bestmisfit(j));
end

function [dist,misfit] = calcdist(vlon,vlat,lonSC,latSC,radSC,nvol)
    % Calculate Distance Function

    dist = 0;
    misfit = zeros(size(vlon));

    for j=1:nvol

        vlonTemp = vlon(j);
        vlatTemp = vlat(j);
        s1 = (sin((latSC-vlatTemp)/2))^2;
    s2 = cos(latSC)*cos(vlatTemp)*(sin((lonSC-vlonTemp)/2))^2;
    d1 = 2*asin(sqrt(s1+s2));
    d  = d1*(180.0*60.0/pi)*1.852 - radSC;
    dist = dist + d*d;
        misfit(j) = d;

    end
```

C.2 Great Circles

C.2.1 Hough Transform

A line through a particular point in an image can be quantified using ρ, algebraic distance, and θ, angle, from a point of reference in Cartesian coordinate system (Duda & Hart, 1972). The line is then described by the equation:

$$x\cos\theta + y\sin\theta = \rho \tag{C.1}$$

in which the rotation angle variable (θ) is restricted in [0,π] range, while x and y are the coordinate in the same Cartesian system. Algebraic distance, ρ, is defined to be

perpendicular to the line (**Figure C.1a**).

Each volcano is treated as a point and lines within the permitted range for θ are passed through it, with the results plotted in a plot of θ versus ρ. **Figure C.1a** explains how the latter (panel [3]) identifies potentially aligned points. Thresholds can be set for the minimum number in an alignment, and how far points are separated from one another to be considered a potential alignment of multiple volcanoes.

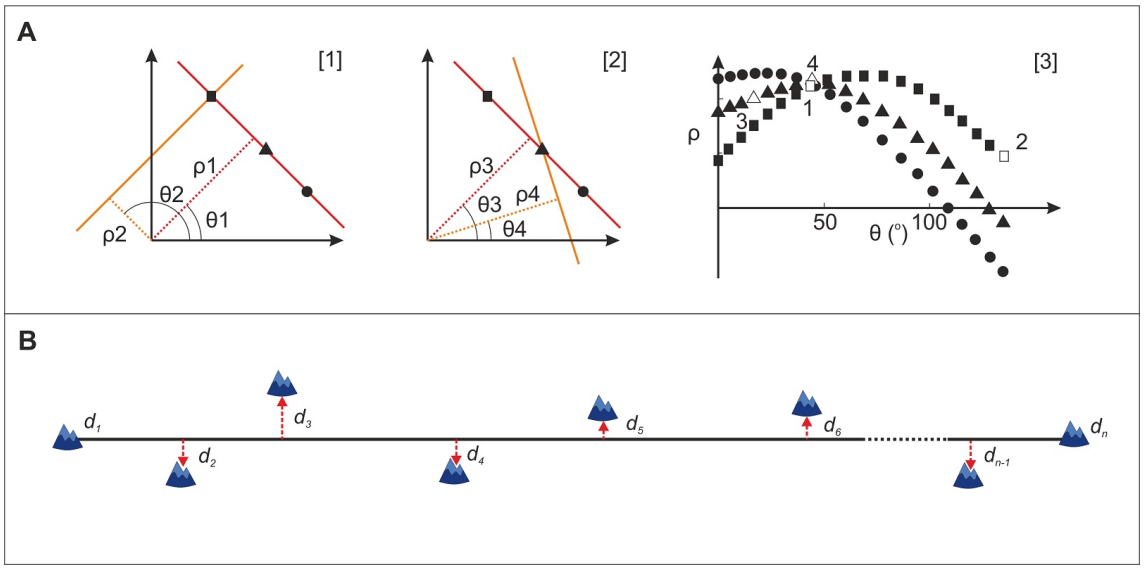

Figure C.1. Great circle fitting procedure based on Hough Transform analysis; (**A**) Simplified illustration of Hough Transform method for recognising alignment (modified after Pacey et al. (2013)). Possible lines are projected through each of three points. Examples of two lines passing through [1] the square point, and [2] the triangular point, are shown. The attributes of every line (θ and ρ) are plotted on a Cartesian diagram [3], which produces a sinusoidal curve for each point. Lines (1 to 4) (illustrated [1] and [2]) are shown as open symbols. Intersections of sinusoidal curves on panel [3] mark the attribute of lines that fit to multiple points and are, thus, aligned; (**B**) Misfit determination of Hough Transform results. The misfit for each volcano is determined from the shortest distance from the volcano to the line segment.

C.2.2 Script

```
function HTPoints
clc;
%input
[num,txt] = xlsread('dataset.xlsx'); %Dataset Name
lon = num(:,1);
lat = num(:,2);

ts = 180; %theta steps DEFAULT = 180
rs = 200; %rho steps DEFAULT = 200
nv = 5; %number of volcanoes in a line DEFAULT = 5
result01 = ['Theta increment: ', num2str(180/ts), ' degree(s)'];
```

```
result02 = ['Minimum volcanoes each line: ', num2str(nv)];
disp(result01); disp(result02); fprintf('\n');

%conversion
lonr = lon .* (pi/180);
latr = lat .* (pi/180);

%% GNOMONIC PROJECTION

lonc = (max(lonr)+min(lonr))/2; latc = (max(latr)+min(latr))/2;   % centre properties
sinxc = sin(lonc); sinyc = sin(latc);
cosxc = cos(lonc); cosyc = cos(latc);

for i = 1:numel(lonr)   %gnomonic calculation

    cosc(i) = sinyc * sin(latr(i)) + cosyc * cos(latr(i)) * cos(lonr(i)-lonc);
    k(i) = 1/cosc(i);
    long(i) = 1 * k(i) * cos(latr(i)) * sin(lonr(i)-lonc);
    latg(i) = 1 * k(i) * (cosyc * sin(latr(i)) - sinyc * cos(latr(i)) * cos(lonr(i)-lonc));

end

figure(1);
hold on;
plot(long,latg,'^r','MarkerFaceColor','red');
pbaspect([1 1 1]); grid on; grid minor; axis equal;
xlim([min(long)-0.02 max(long)+0.02]);
ylim([min(latg)-0.02 max(latg)+0.02]);
title('Hough Transform Line Detection');
xlabel('Longitude'); ylabel('Latitude');

%% HOUGH TRANSFORM

mintheta = 0; maxtheta = 180;

for i = 1:numel(long) % max rho
    maxd(i) = sqrt(long(i)^2+latg(i)^2);
end

maxrho = max(maxd);

thetad = linspace(0,1,ts+1)*maxtheta;
thetar = linspace(0,1,ts+1)*(pi);
rho = linspace(-1,1,rs+1)*maxrho;

hough = zeros(rs+1,ts+1);
houghvol = zeros(rs+1,ts+1,numel(long));

for i = 1:numel(long) %rho and theta calculation
    for j = 1:numel(thetar)

        rho2 = long(i)*cos(thetar(j))+latg(i)*sin(thetar(j));
        rhoel = (rs/2+1)+round((rho2)/(2*maxrho/(rs+1)));
```

```
        hough(rhoel,j) = hough(rhoel,j) + 1; %Hough matrix
        houghvol(rhoel,j,i) = houghvol(rhoel,j,i) + 1;

    end
end

figure(2)  %plot Hough Matrix
imagesc(thetad,rho,hough); c = colorbar;
xlabel('\theta (degree)'); ylabel('\rho');
title('Hough Transform Lines on \rho and \theta system');
c.Label.String = 'Number of Volcanoes';

httop = hough >= nv; %matrix that has more than nv points

n = 1; %theta and rho matrix index

for i = 1 : ts+1  %extracting top theta and rho in real scale
    for j = 1 : rs+1
        if httop(j,i) == 1
            toptheta(n) = i * ((pi)/(ts+1));
            toprho(n) = (j * (maxrho*2/(rs+1))) - maxrho;
            for k = 1 : numel(long)
                topvol(n,k) = houghvol(j,i,k);
            end
            n = n + 1;
        end
    end
end

f = waitbar(0,'Processing...','Name','Small Circle Annealing
    Simulation');

for i = 1 : numel(toptheta)  %plotting and calculating lines with >
    nv points
    m = 1;

    for k = 1 : numel(long)
        if topvol(i,k) == 1
            lonv(m) = long(k);
            latv(m) = latg(k);
            namev(m) = txt(k);
            lonht(m) = lonr(k);
            latht(m) = latr(k);
            m = m+1;
        end
    end

    for j = 1 : numel(lonv)
        if lonv(j) == min(lonv)
            lonp(1) = lonv(j);
            latp(1) = latv(j);
            lonpr(1) = lonht(j);
            latpr(1) = latht(j);
        elseif lonv(j) == max(lonv)
            lonp(2) = lonv(j);
            latp(2) = latv(j);
```

```
            lonpr(2) = lonht(j);
            latpr(2) = latht(j);
        end
    end

    [distradAB,distkmAB] = calcdist(lonpr(1),latpr(1),lonpr(2),
    latpr(2));
    [azradAB,azdegAB] = calcaz(lonpr(1),latpr(1),lonpr(2),latpr(2))
    ;

    sumxtd2 = 0;

    for l = 1 : numel(lonht)
        [distradAD(l),distkmAD(l)] = calcdist(lonpr(1),latpr(1),
    lonht(l),latht(l));
        [azradAD(l),azdegAD(l)] = calcaz(lonpr(1),latpr(1),lonht(l)
    ,latht(l));
        [xtdrad(l),xtdkm(l)] = calcxtd(distradAD(l),azradAB,azradAD
    (l));

        sumxtd2 = sumxtd2 + xtdkm(l)*xtdkm(l);
    end

    sumxtd = sqrt(sumxtd2/numel(xtdkm));

    result1 = ['Line ', num2str(i)];
    result2 = ['phi = ', num2str(toprho(i)), ' ; theta = ', num2str
    (toptheta(i)*(180/pi))];
    result3 = ['Number of volcanoes included: ', num2str(numel(
    lonht))];
    result4 = [namev];
    result5 = ['RMS Misfit = ', num2str(sumxtd), ' km'];

    disp(result1); disp(result2); disp(result3); disp(result4);
    disp(result5); fprintf('\n');

    waitbar(i/numel(toptheta),f);

    figure(1)
    hold on
    plot(lonp,latp,'LineWidth',1);

    clear lonv latv namev lonht latht;
end

delete(f)

function [distrad,distkm] = calcdist(XA,YA,XB,YB) % Calculate
    Distance Function

s1 = (sin((YA-YB)/2))^2;
s2 = cos(YA)*cos(YB)*(sin((XA-XB)/2))^2;
distrad = 2*asin(sqrt(s1+s2));
distkm  = distrad*(180.0*60.0/pi)*1.852;

function [azrad,azdeg] = calcaz(XA,YA,XB,YB) % Calculate Course
```

```
    Function
166
167 azrad = mod(atan2(sin(XA-XB)*cos(YB),cos(YA)*sin(YB)-sin(YA)*cos(YB
    )*cos(YA-YB)),2*pi);
168 azdeg = 360-(azrad*(180/pi));
169
170 function [xtdrad,xtdkm] = calcxtd(distradAD,azradAB,azradAD) %
    Calculate Cross Track Distance Function
171
172 xtdrad = asin(sin(distradAD)*sin(azradAD-azradAB));
173 xtdkm = xtdrad*(180.0*60.0/pi)*1.852;
```

Appendix D

Geometric Fitting Results

D.1 Small Circles

Table D.1. Best-fit small circle parameters at each arc

No.	Arc Name	nV	Longitude (°)	Latitude (°)	Radius (km)	Mrms (km)
1	Kamchatka	65	131.048	57.962	1804	14.4
2	Kuriles	39	126.633	60.397	2208	9.1
3	North Japan	30	133.828	40.627	625	22.4
4	Izu-Bonin	24	-151.289	21.253	6826	5.0
5	Ryukyu	15	117.441	34.817	1284	6.6
6	Aleutians	37	-178.587	62.675	1197	9.8
7	Alaska	43	-169.522	62.678	927	16.0
8	Central America	66	-96.025	-0.475	1761	14.3
9	Lesser Antilles	17	-65.295	14.099	449	3.9
10	Northern Andes	25	-90.084	10.594	1746	16.6
11	Central Andes	57	-77.454	-22.930	981	26.1
12	Southern Andes	49	-25.704	-37.575	3978	10.7
13	Scotia	8	-31.440	-57.943	298	6.2
14	Kermadec-North Island	40	148.156	-14.634	3819	6.9
15	Tonga	43	129.446	7.016	6756	12.3
16	Vanuatu	16	196.011	-6.163	3226	14.8
17	Mariana	37	139.306	17.333	689	8.4
18	Java	36	119.387	33.630	4673	17.5
19	Sumatra	37	175.170	35.481	8649	28.0

Explanation: nV = number of volcanoes, Mrms = root-mean-square misfit

D.2 Segmented Great Circles

Table D.2. Great circle fitting properties I

Arc-segment No.	nV	Initial Great Circle						
		Lon A (°)	**Lat A** (°)	**Lon B** (°)	**Lat B** (°)	**Length** (km)	**Azimuth** (°E)	**Mrms** (km)
01 Kamchatka 1	12	154.016	48.758	156.014	50.686	258	33	8.7
01 Kamchatka 2	26	156.720	51.100	158.520	52.920	237	31	8.8
01 Kamchatka 3	17	158.833	53.256	160.762	55.061	237	31	8.6
01 Kamchatka 4	10	160.527	55.759	161.360	56.652	112	27	11.3
02 Kuriles 1	9	151.786	46.815	153.022	47.756	140	41	3.7
02 Kuriles 2	8	149.672	45.755	150.866	46.522	125	47	2.4
02 Kuriles 3	11	146.928	44.479	148.852	45.506	189	53	8.0
02 Kuriles 4	4	145.505	43.844	146.139	44.454	85	37	7.5
02 Kuriles 5	7	144.006	43.385	145.163	44.130	124	48	6.6
03 North Japan 1	13	137.478	35.895	139.777	36.900	234	61	17.7
03 North Japan 2	7	139.963	37.125	140.779	38.967	217	19	5.0
03 North Japan 3	10	140.792	39.752	141.377	42.691	330	8	7.3
04 Izu-Bonin 1	9	140.305	30.482	139.527	34.086	407	350	4.4
04 Izu-Bonin 2	15	141.480	24.286	140.357	29.808	624	350	4.8
05 Ryukyu 1	6	128.228	27.869	129.926	29.968	286	35	3.4
05 Ryukyu 2	9	130.216	30.446	131.392	33.282	334	19	6.9
06 Aleutians 1	5	-166.928	53.887	-165.660	54.252	92	64	1.0
06 Aleutians 2	13	-171.255	52.495	-168.130	53.429	233	63	8.2
06 Aleutians 3	13	-178.795	51.789	-172.513	52.313	433	82	9.7
06 Aleutians 4	6	175.908	52.346	179.586	51.936	255	100	7.9
07 Alaska 1	5	-153.432	59.361	-152.411	61.641	259	12	8.8
07 Alaska 2	16	-156.379	57.747	-153.542	58.854	206	53	8.4
07 Alaska 3	11	-160.098	55.869	-156.745	57.202	253	54	7.8
07 Alaska 4	11	-164.650	54.517	-161.213	55.629	251	60	4.8
08 Central America 1	15	-92.109	15.132	-90.271	14.339	216	114	10.7
08 Central America 2	25	-90.4	14.153	-87.639	13.273	314	108	9.7

(cont.)

Arc-segment No.	**nV**	**Initial Great Circle**						
		Lon A (°)	**Lat A** (°)	**Lon B** (°)	**Lat B** (°)	**Length** (km)	**Azimuth** (°E)	**Mrms** (km)
08 Central America 3	8	-87.567	12.982	-86.539	12.424	127	119	1.2
08 Central America 4	8	-86.341	12.244	-85.512	11.445	127	134	4.3
08 Central America 5	10	-85.472	10.979	-83.763	10.020	215	120	6.3
09 Lesser Antilles 1	4	-61.675	12.162	-61.047	13.838	198	20	2.7
09 Lesser Antilles 2	7	-61.167	14.810	-61.664	16.043	147	339	4.7
09 Lesser Antilles 3	6	-62.176	16.711	-63.239	17.634	153	312	6.1
10 Northern Andes 1	7	-75.390	4.487	-75.365	5.212	81	2	4.6
10 Northern Andes 2	4	-76.936	1.500	-76.026	2.932	188	32	2.1
10 Northern Andes 3	4	-77.934	0.819	-77.360	1.221	78	55	7.1
10 Northern Andes 4	10	-78.904	-0.860	-78.290	0.469	163	25	9.4
11 Central Andes 1	11	-70.854	-16.614	-72.640	-15.237	245	309	23.8
11 Central Andes 2	11	-68.835	-19.156	-70.604	-16.766	325	324	22.2
11 Central Andes 3	20	-67.739	-23.949	-68.558	-20.734	367	346	20.2
11 Central Andes 4	15	-68.560	-27.195	-68.250	-24.180	336	5	18.0
12 Southern Andes 1	17	-71.378	-36.868	-69.797	-33.425	409	21	12.3
12 Southern Andes 2	19	-72.609	-41.33	-71.351	-37.410	449	15	15.2
12 Southern Andes 3	13	-73.049	-45.205	-72.399	-41.759	386	8	7.9
13 Scotia 1	4	-26.706	-57.084	-28.080	-55.921	154	326	1.7
13 Scotia 2	4	-27.361	-59.442	-26.464	-57.78	192	16	19.6
14 Kermadec-North Island 1	15	175.564	-39.281	178.652	-35.420	508	34	6.1
14 Kermadec-North Island 2	16	178.865	-35.287	181.564	-30.231	616	25	5.2
14 Kermadec-North Island 3	9	-177.920	-29.265	-177.188	-25.887	382	11	2.3
15 Tonga 1	10	-177.018	-24.802	-176.346	-22.456	269	15	4.0
15 Tonga 2	15	-176.187	-22.191	-175.162	-20.126	253	25	8.6
15 Tonga 3	6	-175.071	-19.732	-174.648	-18.806	112	23	2.4
15 Tonga 4	8	-174.365	-18.326	-173.763	-16.551	207	18	5.8
15 Tonga 5	4	-173.899	-16.221	-173.693	-15.572	75	17	2.7
16 Vanuatu 1	5	170.282	-20.987	168.359	-17.460	441	332	8.0
16 Vanuatu 2	6	168.592	-16.992	167.830	-15.391	196	335	5.2
16 Vanuatu 3	5	168.040	-14.460	167.338	-13.538	127	323	17.7

(cont.)

Arc-segment No.	nV	Initial Great Circle						
		Lon A (°)	Lat A (°)	Lon B (°)	Lat B (°)	Length (km)	Azimuth (°E)	Mrms (km)
17 Mariana 1	6	145.450	15.300	144.411	13.633	216	211	0.8
17 Mariana 2	8	145.800	16.883	145.417	15.083	204	192	4.2
17 Mariana 3	6	145.467	19.408	145.867	17.300	238	170	3.9
17 Mariana 4	7	144.417	21.208	145.453	19.700	199	147	3.3
17 Mariana 5	10	142.326	23.078	144.525	21.023	322	135	3.0
18 Java 1	13	105.423	-6.101	107.729	-7.321	288	118	8.9
18 Java 2	11	107.607	-6.759	112.922	-8.109	605	104	5.4
18 Java 3	12	112.590	-7.765	116.561	-8.414	443	99	9.1
19 Sumatra 1	9	98.830	2.580	95.285	5.874	537	313	17.9
19 Sumatra 2	5	99.541	0.684	98.653	2.603	235	335	5.6
19 Sumatra 3	11	102.207	-3.214	100.200	0.080	429	329	12.7
19 Sumatra 4	12	105.423	-6.101	102.240	-3.245	474	312	6.3

Explanation: nV = number of volcanoes, Lon = longitude, Lat = latitude Mrms = root-mean-square misfit

Table D.3. Great circle fitting properties II

Arc-segment No.	**nV**	**Optimised Great Circles**		**Arc Mrms** (km)	**Arc Opt. Mrms** (km)
		Opt. Az. (°E)	**Opt. Mrms** (km)		
01 Kamchatka 1	12	33	8.3	9.2	7.8
01 Kamchatka 2	26	30	8.3		
01 Kamchatka 3	17	34	6.9		
01 Kamchatka 4	10	26	6.8		
02 Kuriles 1	9	43	2.7	6.0	4.3
02 Kuriles 2	8	47	2.4		
02 Kuriles 3	11	57	5.6		
02 Kuriles 4	4	40	5.2		
02 Kuriles 5	7	47	4.6		
03 North Japan 1	13	63	15.0	12.6	10.8
03 North Japan 2	7	19	4.6		
03 North Japan 3	10	7	6.6		
04 Izu-Bonin 1	9	351	3.9	4.7	4.3
04 Izu-Bonin 2	15	350	4.5		
05 Ryukyu 1	6	35	2.2	5.7	4.7
05 Ryukyu 2	9	18	5.8		
06 Aleutians 1	5	64	0.9	8.2	6.0
06 Aleutians 2	13	65	7.0		
06 Aleutians 3	13	80	6.5		
06 Aleutians 4	6	101	4.6		
07 Alaska 1	5	13	6.0	7.6	6.5
07 Alaska 2	16	55	7.7		
07 Alaska 3	11	54	6.5		
07 Alaska 4	11	60	4.6		
08 Central America 1	15	114	5.4	8.4	6.6
08 Central America 2	25	110	9.4		
08 Central America 3	8	119	1.1		
08 Central America 4	8	132	3.2		
08 Central America 5	10	120	2.9		

(cont.)

Arc-segment No.	**nV**	**Optimised Great Circles**		**Arc Mrms** (km)	**Arc Opt. Mrms** (km)
		Opt. Az. (°E)	**Opt. Mrms** (km)		
09 Lesser Antilles 1	4	21	2.2	4.9	3.1
09 Lesser Antilles 2	7	339	3.2		
09 Lesser Antilles 3	6	313	3.5		
10 Northern Andes 1	7	5	3.4	7.1	5.6
10 Northern Andes 2	4	33	2.0		
10 Northern Andes 3	4	57	4.9		
10 Northern Andes 4	10	26	7.7		
11 Central Andes 1	11	301	16.9	20.8	14.5
11 Central Andes 2	11	321	11.9		
11 Central Andes 3	20	344	12.2		
11 Central Andes 4	15	5	16.9		
12 Southern Andes 1	17	22	9.6	12.6	8.9
12 Southern Andes 2	19	13	9.6		
12 Southern Andes 3	13	8	6.6		
13 Scotia 1	4	327	1.6	13.9	9.9
13 Scotia 2	4	15	13.9		
14 Kermadec-North Island 1	15	34	5.8	5.1	4.9
14 Kermadec-North Island 2	16	25	5.2		
14 Kermadec-North Island 3	9	11	2.1		
15 Tonga 1	10	15	4.0	6.1	5.8
15 Tonga 2	15	24	8.0		
15 Tonga 3	6	22	1.9		
15 Tonga 4	8	18	5.8		
15 Tonga 5	4	18	1.8		
16 Vanuatu 1	5	333	7.3	11.3	10.4
16 Vanuatu 2	6	335	4.4		
16 Vanuatu 3	5	331	16.4		

(cont.)

Arc-segment No.	**nV**	**Optimised Great Circles**		**Arc Mrms** (km)	**Arc Opt. Mrms** (km)
		Opt. Az. (°E)	**Opt. Mrms** (km)		
17 Mariana 1	6	211	0.7	3.3	2.7
17 Mariana 2	8	191	2.9		
17 Mariana 3	6	170	2.7		
17 Mariana 4	7	147	3.2		
17 Mariana 5	10	135	2.9		
18 Java 1	13	118	6.2	8.0	6.6
18 Java 2	11	104	5.1		
18 Java 3	12	100	7.9		
19 Sumatra 1	9	312	12.4	11.9	9.1
19 Sumatra 2	5	335	4.4		
19 Sumatra 3	11	326	10.5		
19 Sumatra 4	12	313	5.8		

Explanation: nV = number of volcanoes, Opt. Az. = optimised azimuth,
Mrms = root-mean-square misfit, Opt. Mrms = optimised root-mean-square misfit

D.3 Segmented Small Circles

Table D.4. Parameters of best-fit small circles at each arc-segment

Arc-segment No.	**nV**	**Longitude** (°E)	**Latitude** (°N)	**Radius** (km)	**Mrms** (km)	**Arc Mrms** (km)
01 Kamchatka 1	12	142.176	53.947	997	8.9	8.1
01 Kamchatka 2	26	168.074	47.446	911	8.7	
01 Kamchatka 3	17	168.818	49.792	794	6.9	
01 Kamchatka 4	10	146.318	59.032	914	7.3	
02 Kuriles 1	9	148.342	49.658	404	2.3	4.2
02 Kuriles 2	8	154.568	42.666	517	2.6	
02 Kuriles 3	11	141.422	51.050	824	6.4	
02 Kuriles 4	4	145.056	44.633	93	4.4	
02 Kuriles 5	7	142.874	45.098	211	2.7	
03 North Japan 1	13	142.038	30.467	744	15.0	11.0
03 North Japan 2	7	132.632	39.991	707	4.8	
03 North Japan 3	10	153.565	39.296	1088	7.4	
04 Izu-Bonin 1	9	123.795	28.998	1586	7.2	8.4
04 Izu-Bonin 2	15	162.488	28.732	2134	9.1	
05 Ryukyu 1	6	121.031	33.517	927	3.0	5.6
05 Ryukyu 2	9	142.254	28.001	1192	6.7	
06 Aleutians 1	5	-163.883	50.908	389	1.6	6.4
06 Aleutians 2	13	-164.624	44.792	979	7.6	
06 Aleutians 3	13	-184.638	69.968	2038	7.5	
06 Aleutians 4	6	179.940	58.168	694	2.4	
07 Alaska 1	5	-168.096	61.479	833	5.0	6.1
07 Alaska 2	16	-145.963	49.387	1151	8.4	
07 Alaska 3	11	-153.934	52.647	535	3.8	
07 Alaska 4	11	-169.066	60.299	690	3.8	

(cont.)

Arc-segment No.	**nV**	**Longitude** (°E)	**Latitude** (°N)	**Radius** (km)	**Mrms** (km)	**Arc Mrms** (km)
08 Central America 1	15	-89.598	18.030	417	2.8	6.8
08 Central America 2	25	-92.014	4.958	1031	10.2	
08 Central America 3	8	-88.674	9.921	360	1.3	
08 Central America 4	8	-88.848	8.681	474	3.8	
08 Central America 5	10	-88.311	4.086	819	4.9	
09 Lesser Antilles 1	4	-55.521	10.717	688	4.5	2.7
09 Lesser Antilles 2	7	-65.151	14.006	437	2.3	
09 Lesser Antilles 3	6	-64.720	15.058	328	0.8	
10 Northern Andes 1	7	-71.940	4.595	379	3.8	6.1
10 Northern Andes 2	4	-82.568	6.081	802	3.6	
10 Northern Andes 3	4	-80.257	5.086	533	5.5	
10 Northern Andes 4	10	-73.872	-2.458	580	8.1	
11 Central Andes 1	11	-75.207	-20.808	651	16.1	13.6
11 Central Andes 2	11	-75.914	-22.583	848	10.8	
11 Central Andes 3	20	-76.484	-24.316	898	11.2	
11 Central Andes 4	15	-58.986	-25.640	956	16.0	
12 Southern Andes 1	17	-54.114	-38.999	1514	11.2	10.1
12 Southern Andes 2	19	-87.697	-35.485	1470	10.1	
12 Southern Andes 3	13	-89.715	-40.442	1444	8.3	
13 Scotia 1	4	-37.815	-59.484	699	2.0	2.6
13 Scotia 2	4	-29.067	-58.298	162	3.1	
14 Kermadec-North Island 1	15	163.618	-28.963	1575	7.8	8.2
14 Kermadec-North Island 2	16	204.988	-39.022	2332	9.8	
14 Kermadec-North Island 3	9	-190.795	-24.632	1367	4.8	
15 Tonga 1	10	-167.843	-25.435	920	5.5	6.0
15 Tonga 2	15	-181.678	-18.669	688	7.9	
15 Tonga 3	6	-171.921	-20.361	334	1.5	
15 Tonga 4	8	-168.387	-19.114	630	5.8	
15 Tonga 5	4	-175.416	-15.377	187	1.2	

(cont.)

Arc-segment No.	**nV**	**Longitude** (°E)	**Latitude** (°N)	**Radius** (km)	**Mrms** (km)	**Arc Mrms** (km)
16 Vanuatu 1	5	155.506	-24.851	1562	8.1	8.2
16 Vanuatu 2	6	172.202	-14.327	484	2.9	
16 Vanuatu 3	5	167.872	-13.981	54	11.9	
17 Mariana 1	6	138.052	18.339	853	3.2	3.3
17 Mariana 2	8	140.011	16.989	613	2.7	
17 Mariana 3	6	139.612	17.221	662	2.1	
17 Mariana 4	7	139.222	16.916	721	3.9	
17 Mariana 5	10	151.154	28.569	1066	3.8	
18 Java 1	13	111.102	1.403	1030	7.6	7.6
18 Java 2	11	114.468	8.918	1886	8.1	
18 Java 3	12	116.401	2.858	1247	7.2	
19 Sumatra 1	9	89.683	-4.215	1270	9.6	9.4
19 Sumatra 2	5	93.239	-1.120	727	3.5	
19 Sumatra 3	11	110.416	4.777	1255	11.5	
19 Sumatra 4	12	92.358	-16.193	1793	8.8	

Explanation: nV = number of volcanoes, Mrms = root-mean-square misfit

D.4 Comparing Small and Great Circles

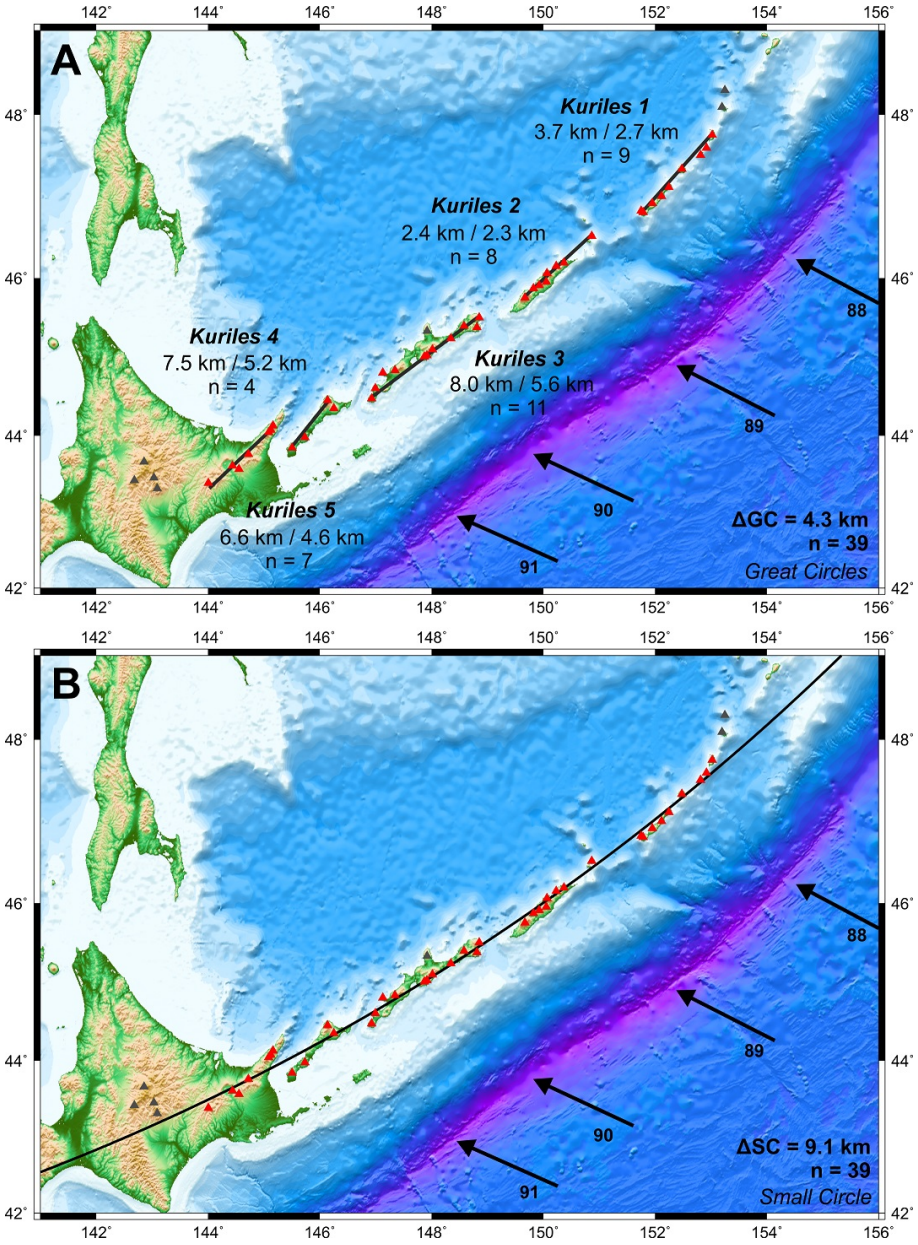

Figure D.1. Geometric fitting of arc volcanoes in Kuriles. Full explanation in **Chapter 5**.

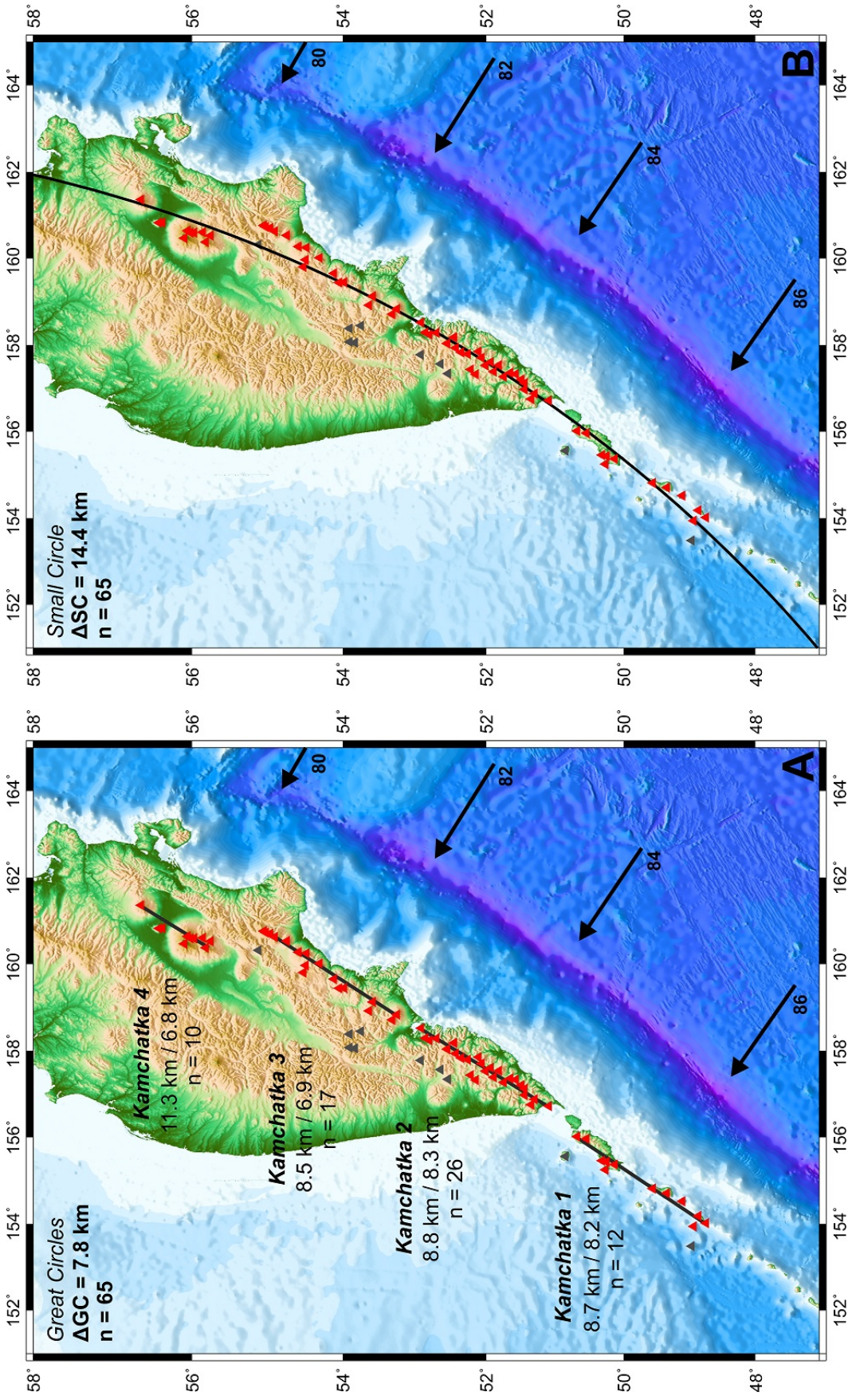

Figure D.2. Geometric fitting of arc volcanoes in Kamchatka.

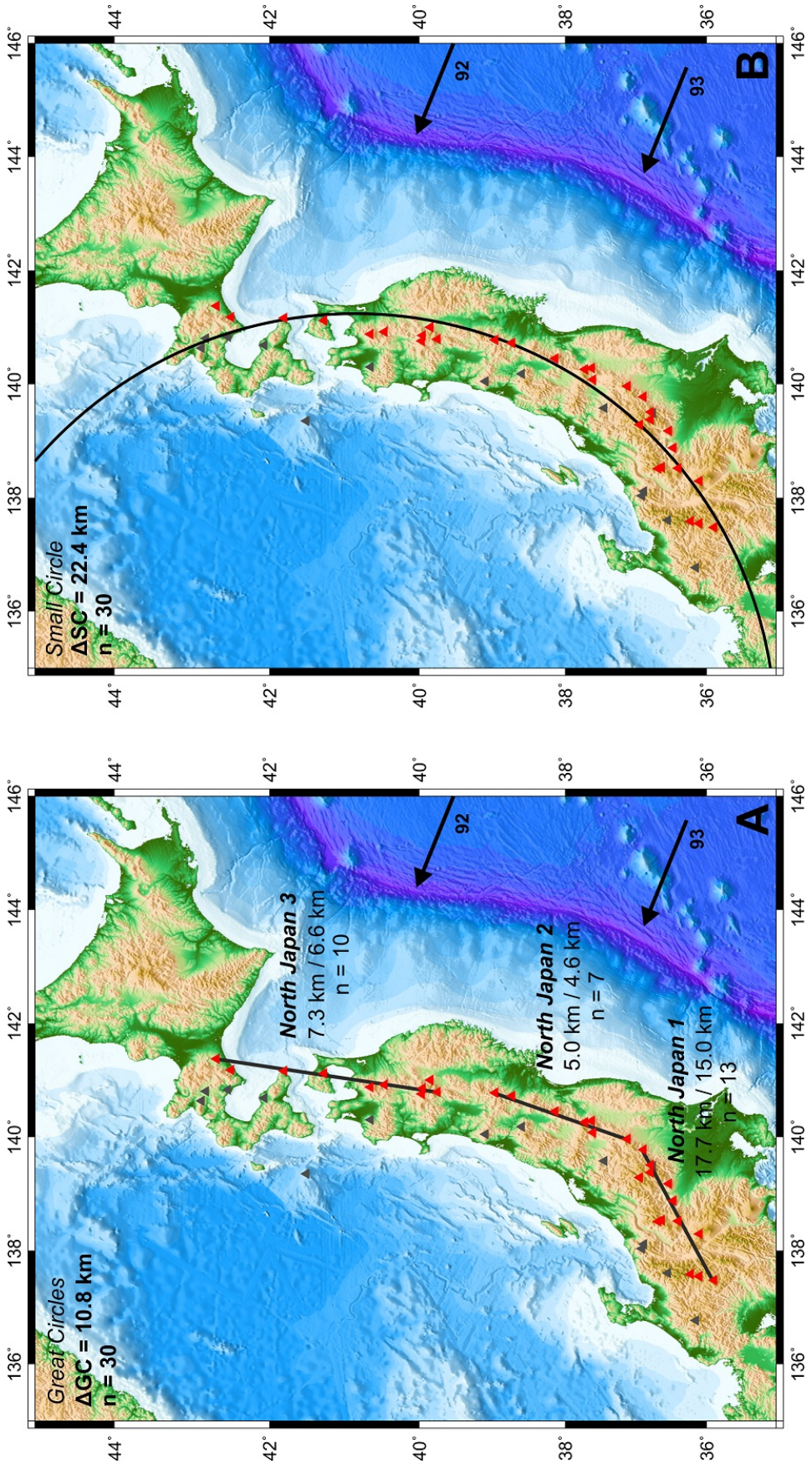

Figure D.3. Geometric fitting of arc volcanoes in North Japan.

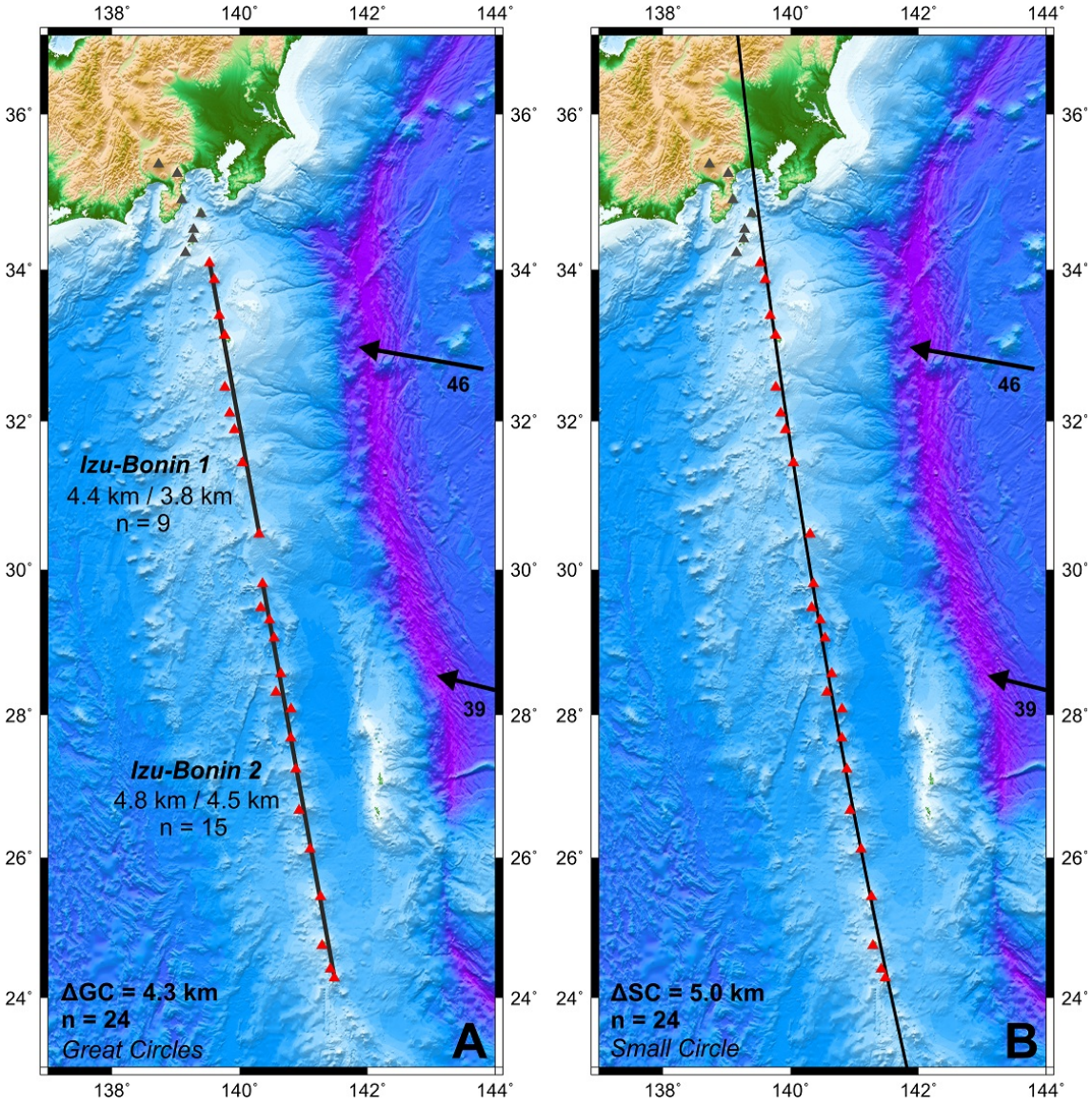

Figure D.4. Geometric fitting of arc volcanoes in Izu-Bonin.

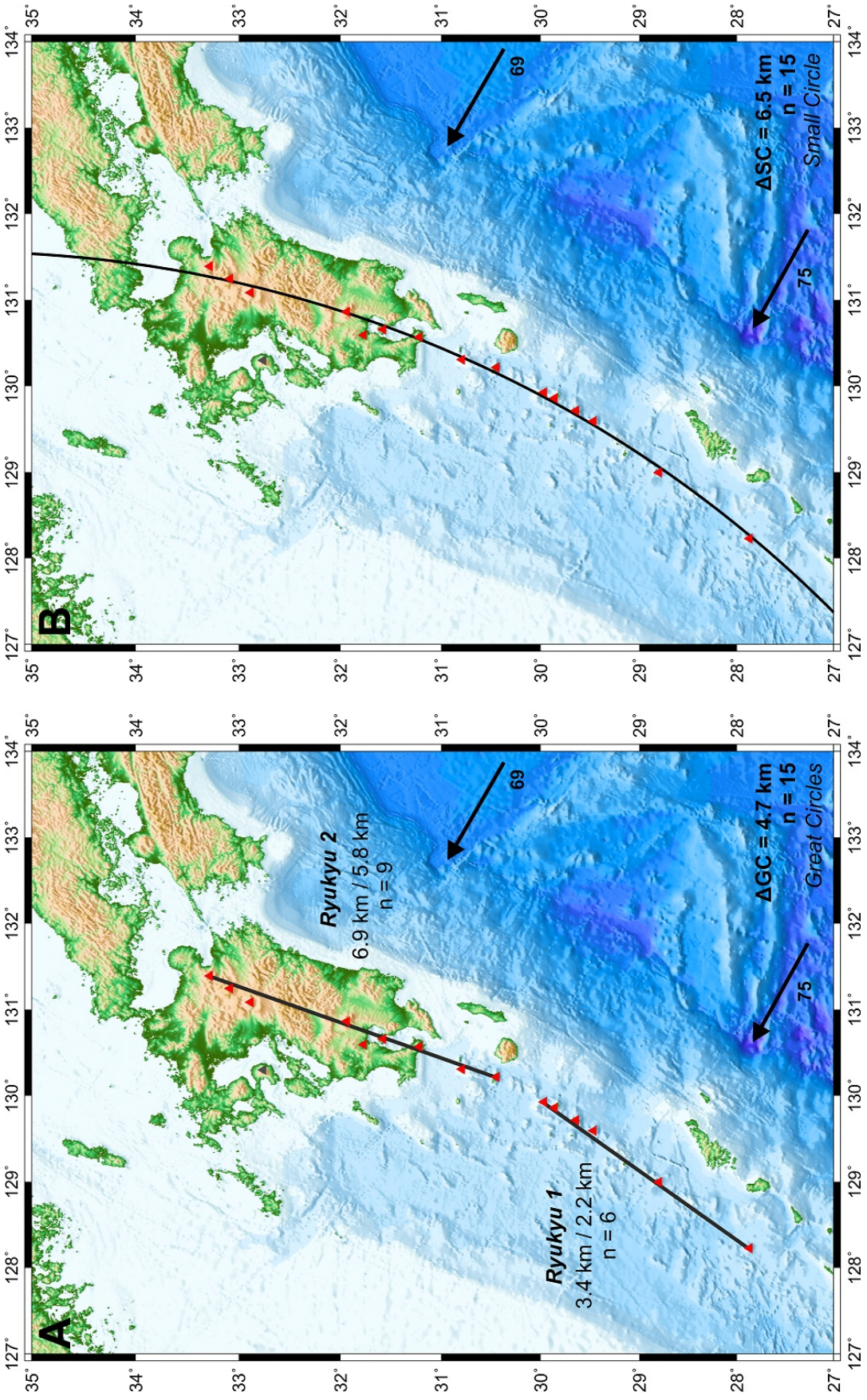

Figure D.5. Geometric fitting of arc volcanoes in Ryukyu.

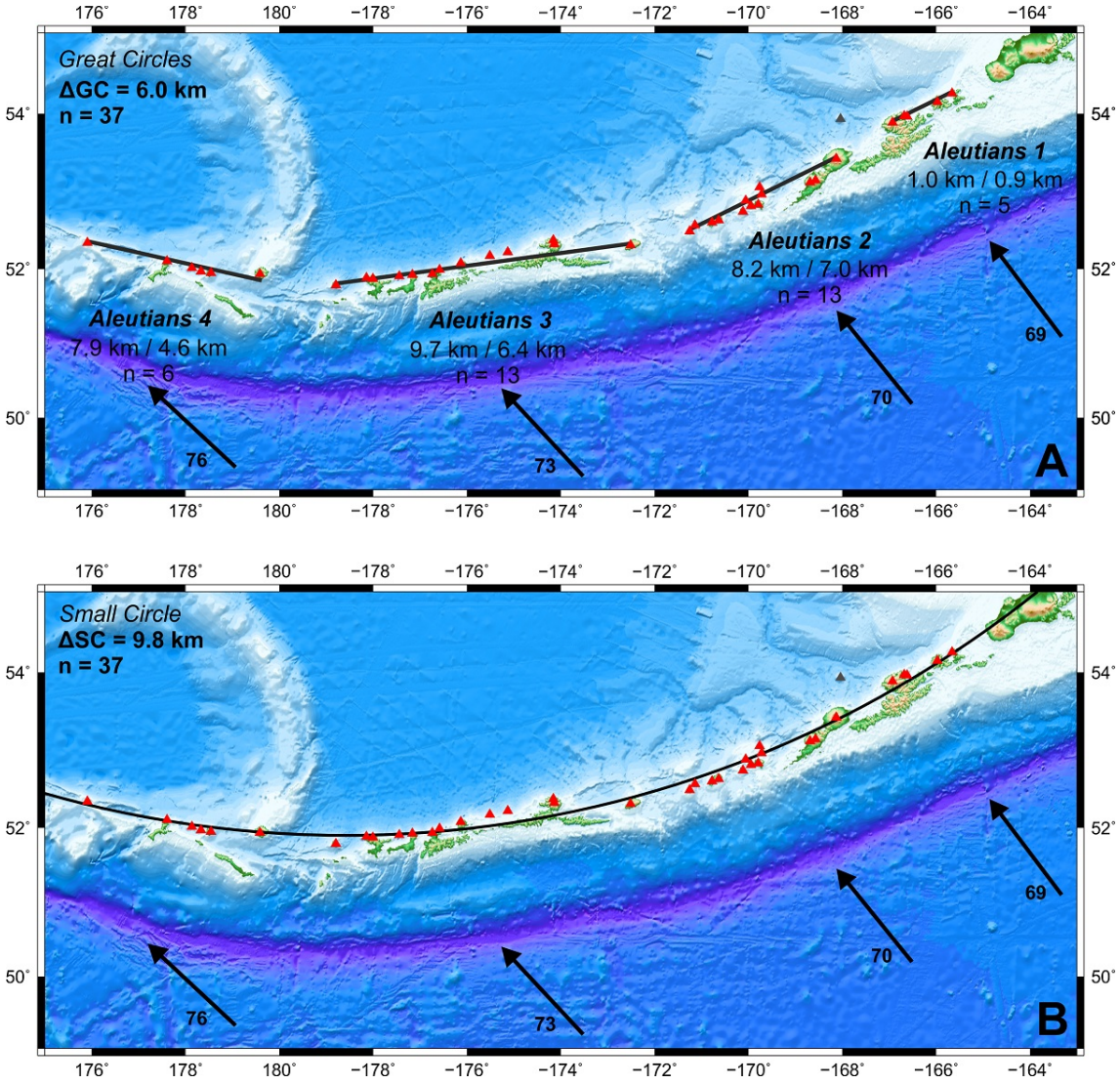

Figure D.6. Geometric fitting of arc volcanoes in Aleutians.

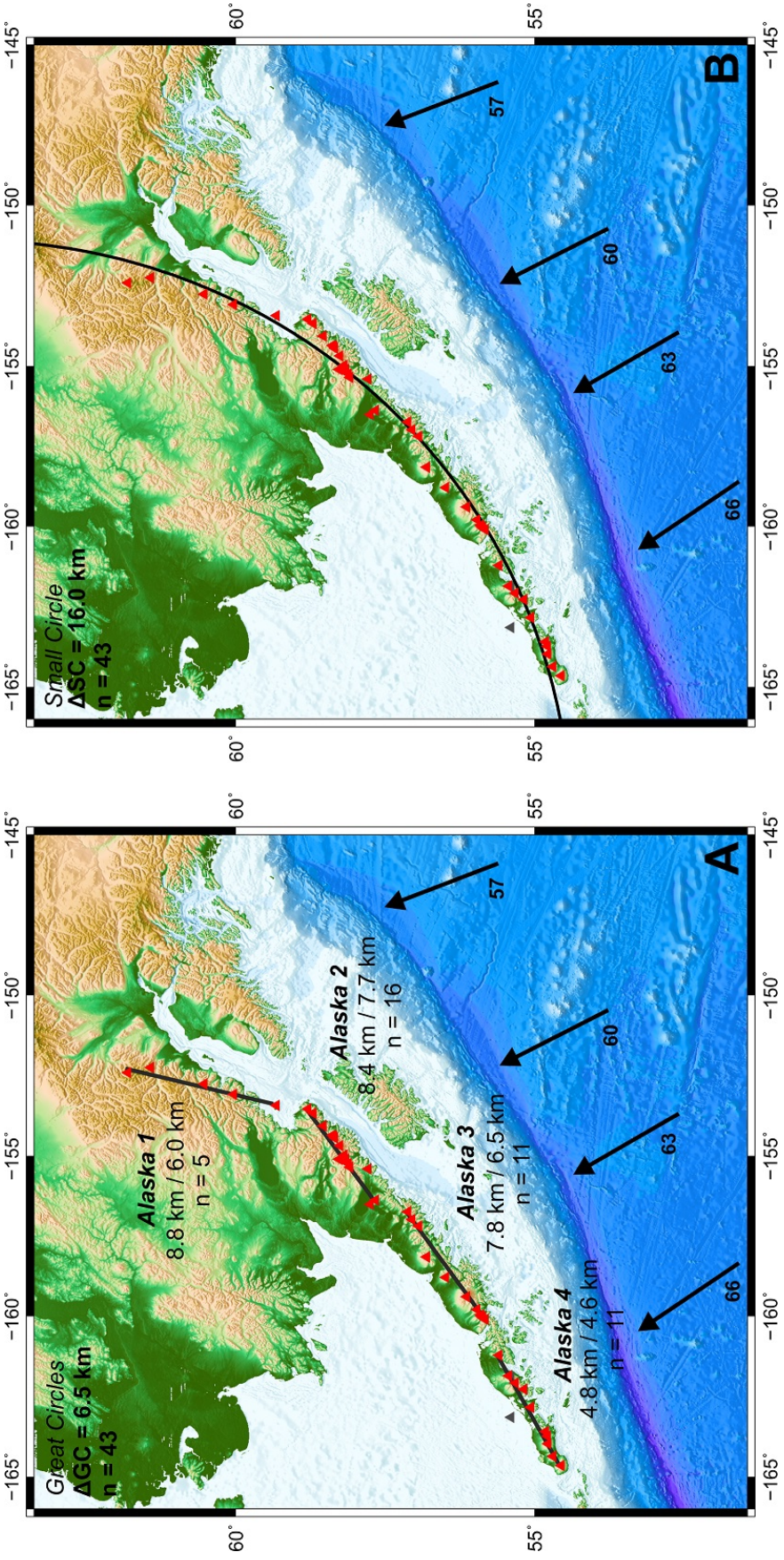

Figure D.7. Geometric fitting of arc volcanoes in Alaska.

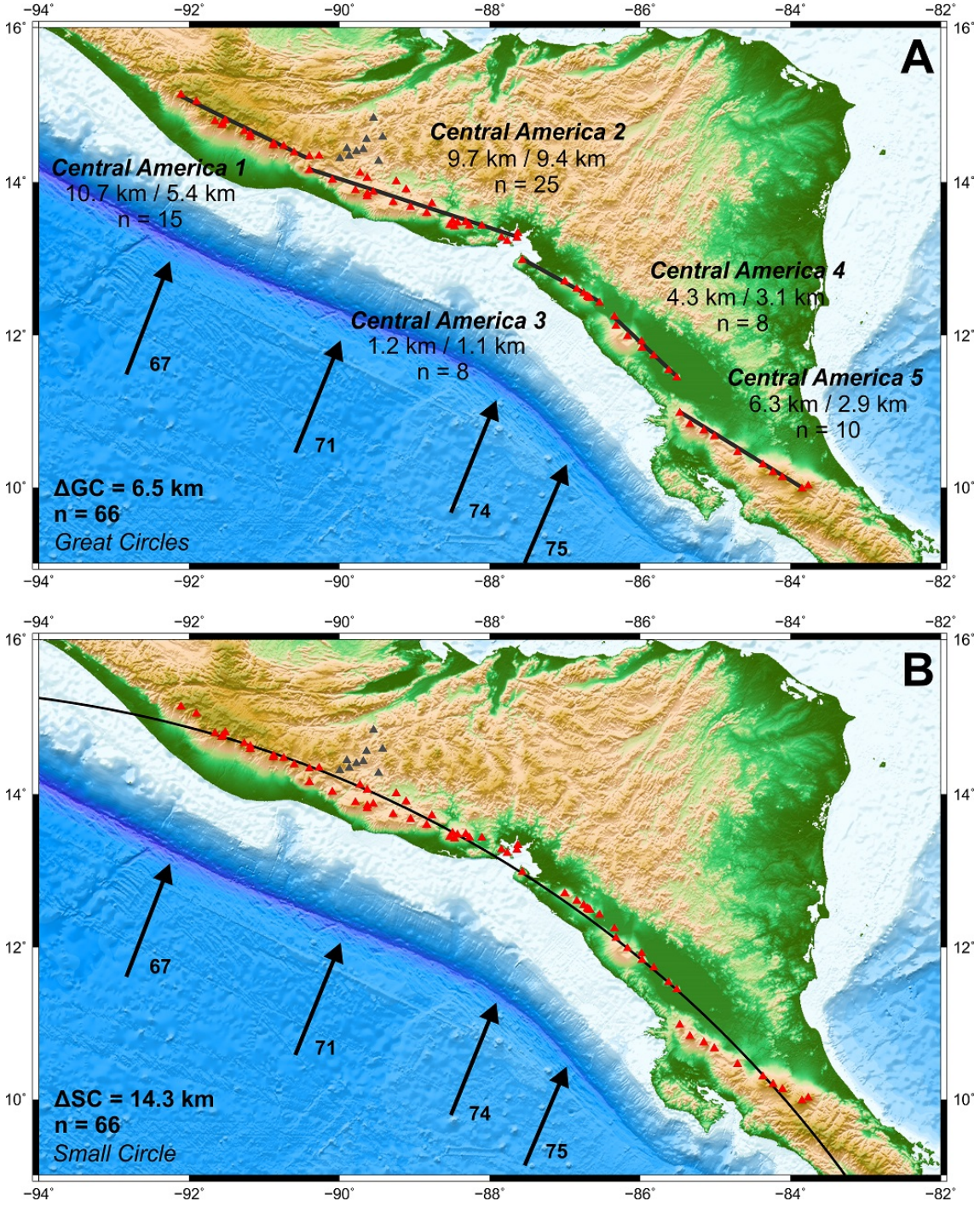

Figure D.8. Geometric fitting of arc volcanoes in Central America.

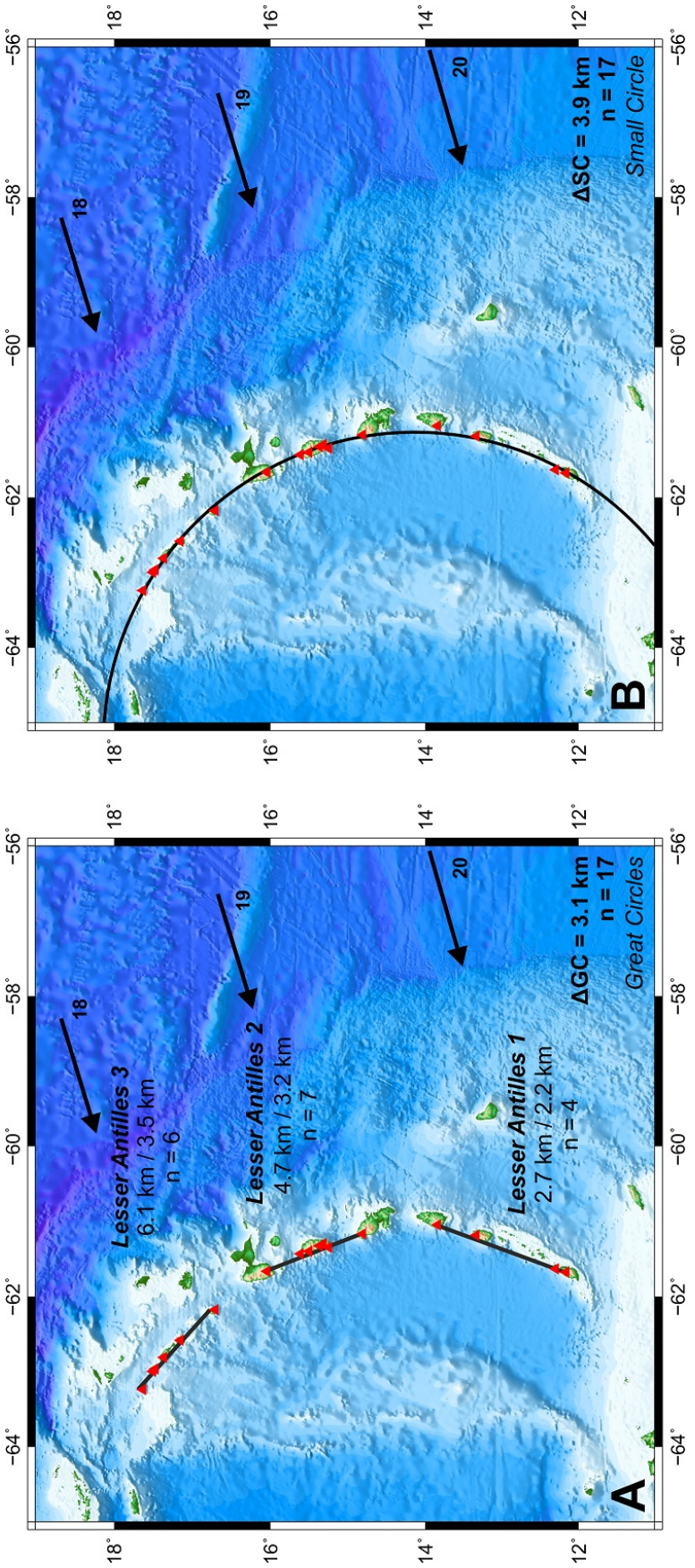

Figure D.9. Geometric fitting of arc volcanoes in Lesser Antilles.

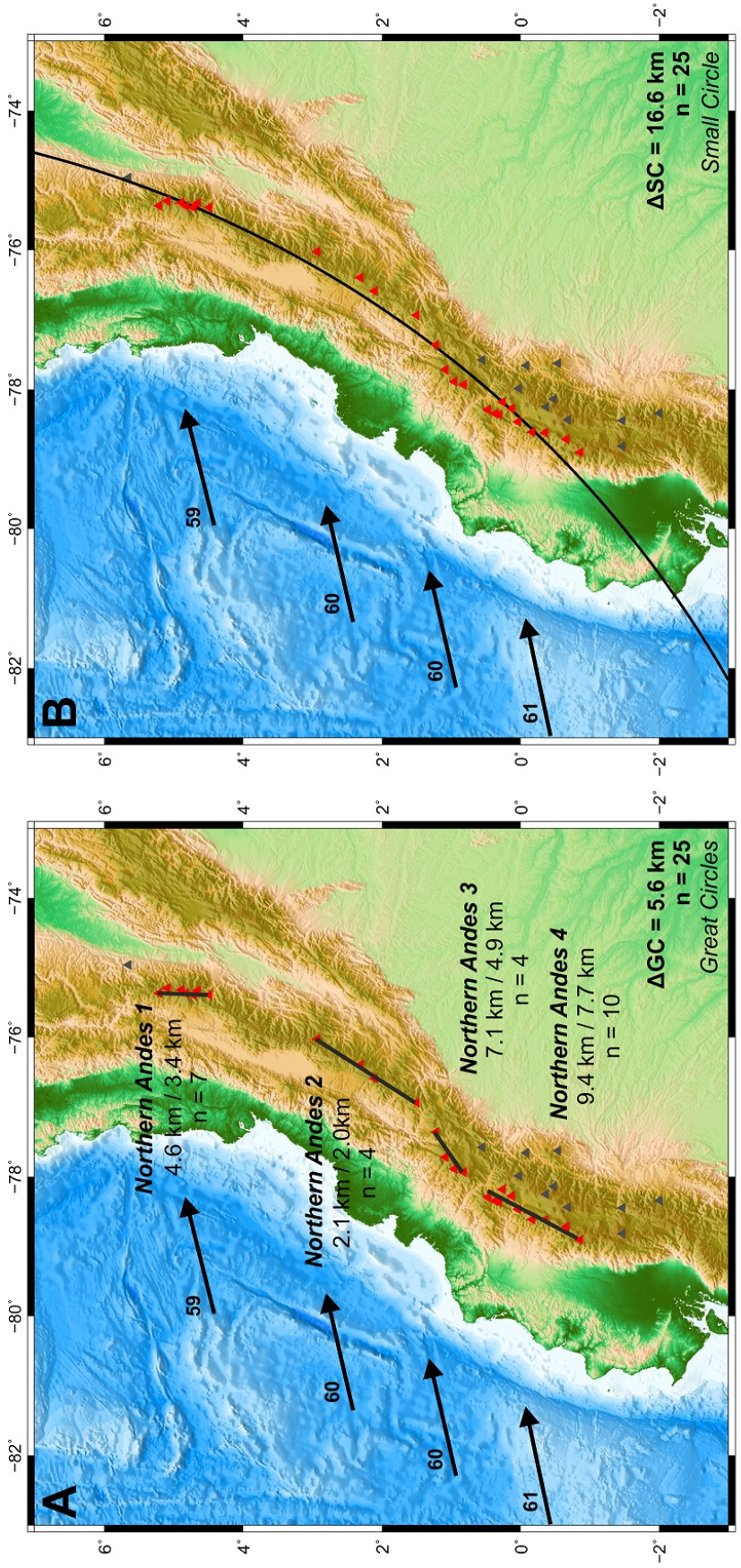

Figure D.10. Geometric fitting of arc volcanoes in Northern Andes.

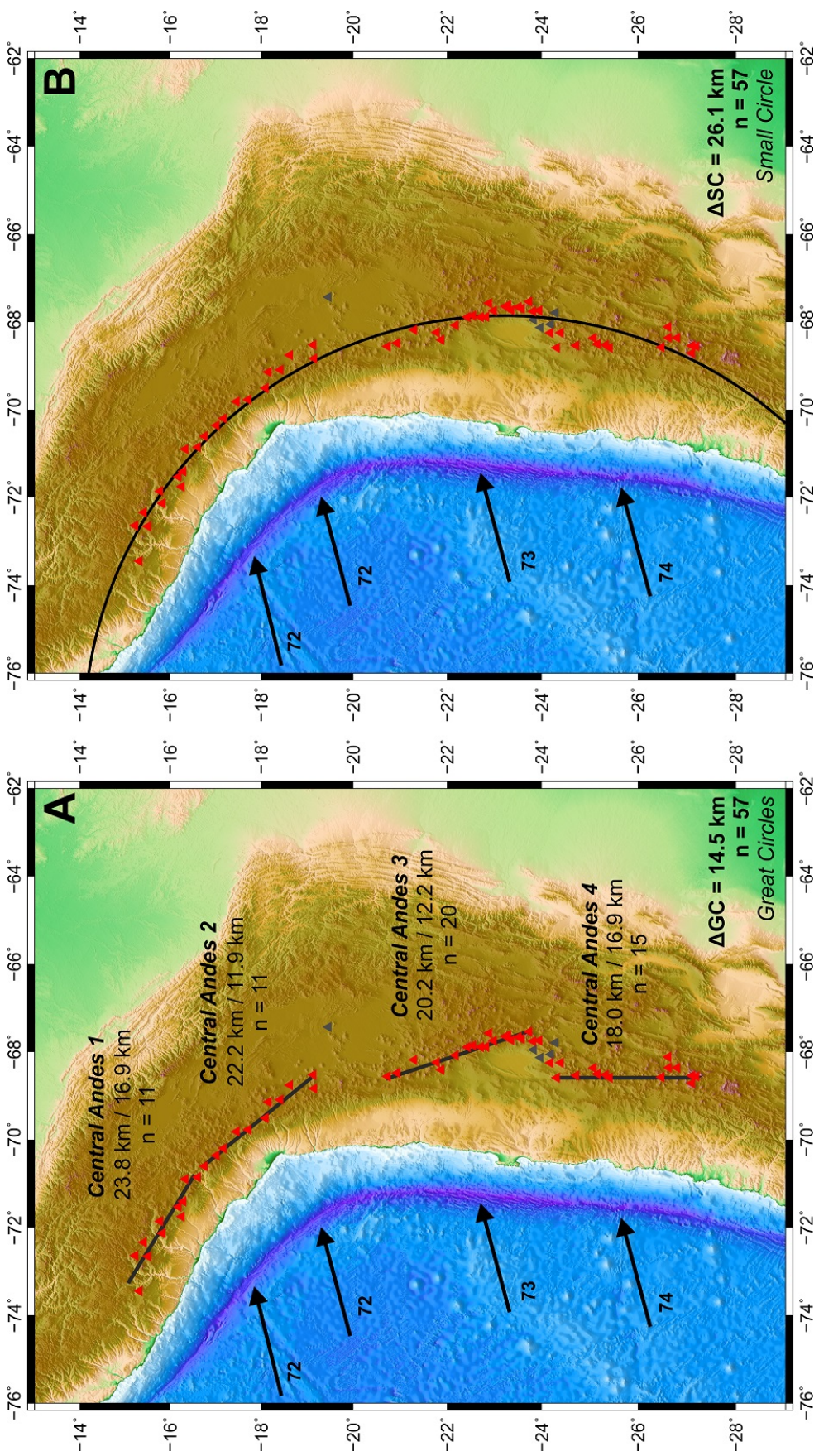

Figure D.11. Geometric fitting of arc volcanoes in Central Andes.

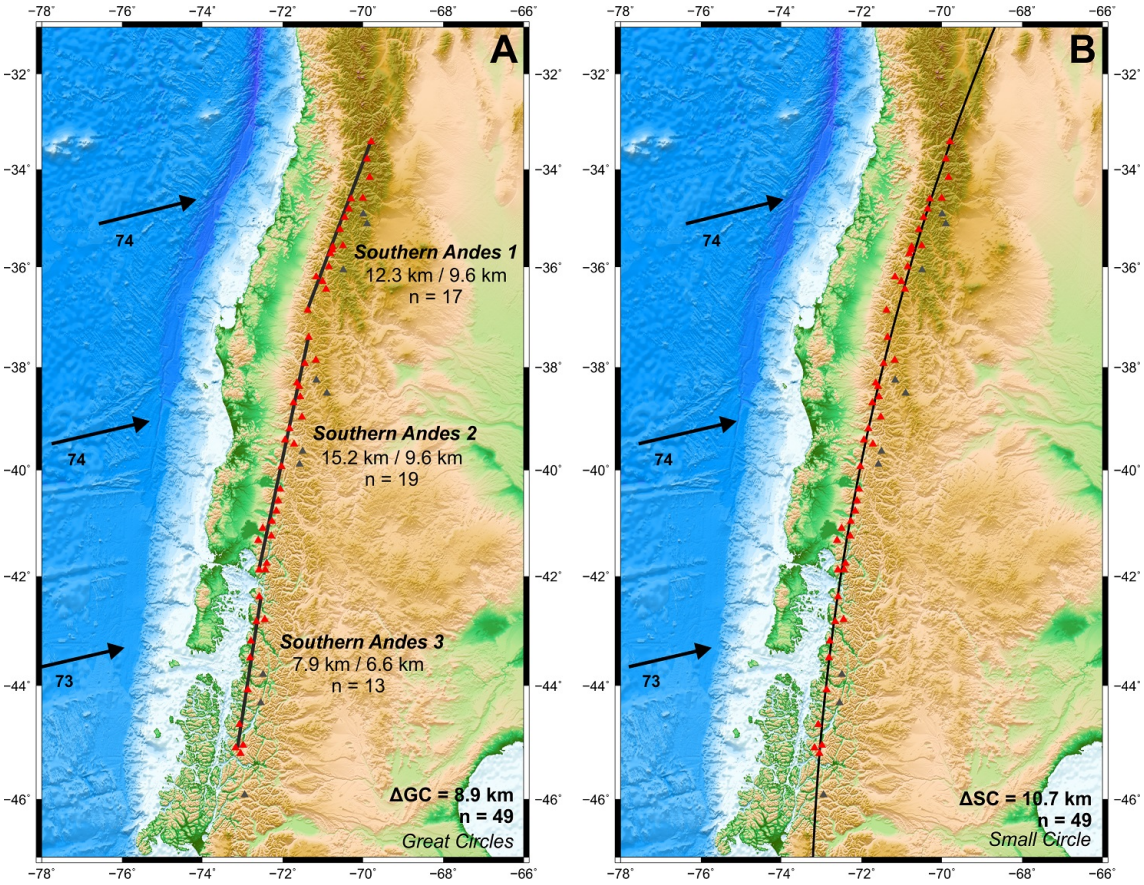

Figure D.12. Geometric fitting of arc volcanoes in Southern Andes.

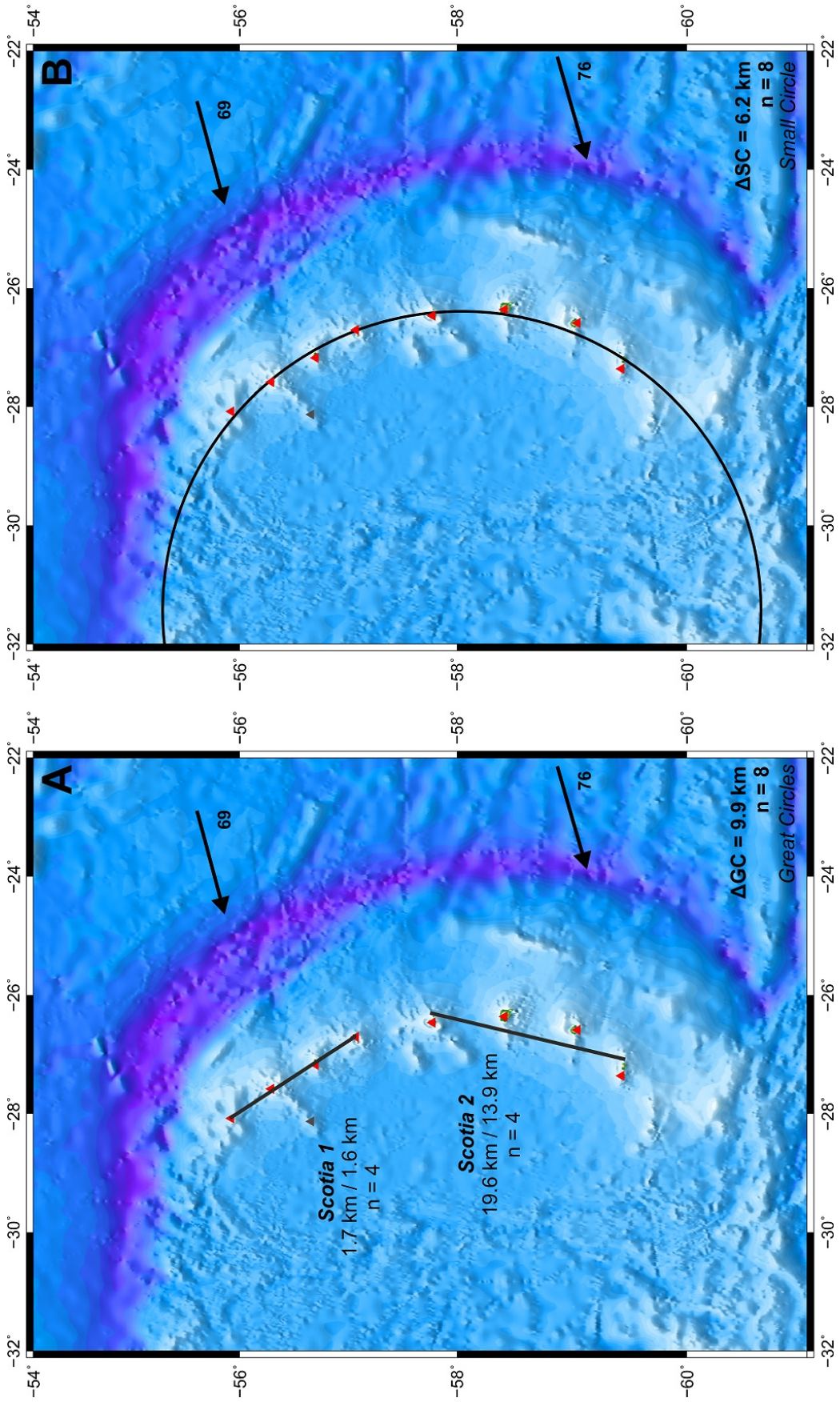

Figure D.13. Geometric fitting of arc volcanoes in Scotia.

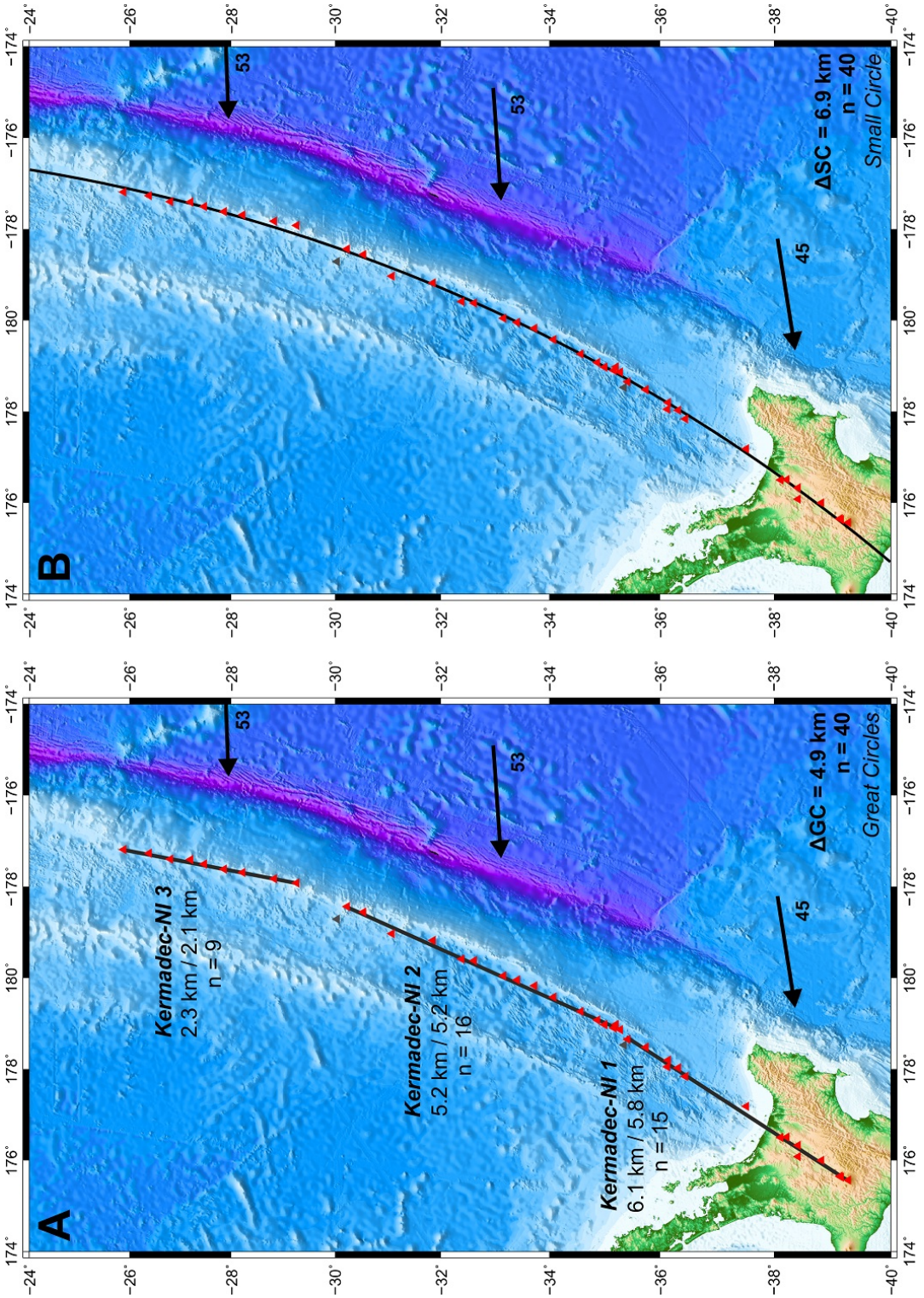

Figure D.14. Geometric fitting of arc volcanoes in Kermadec-North Island.

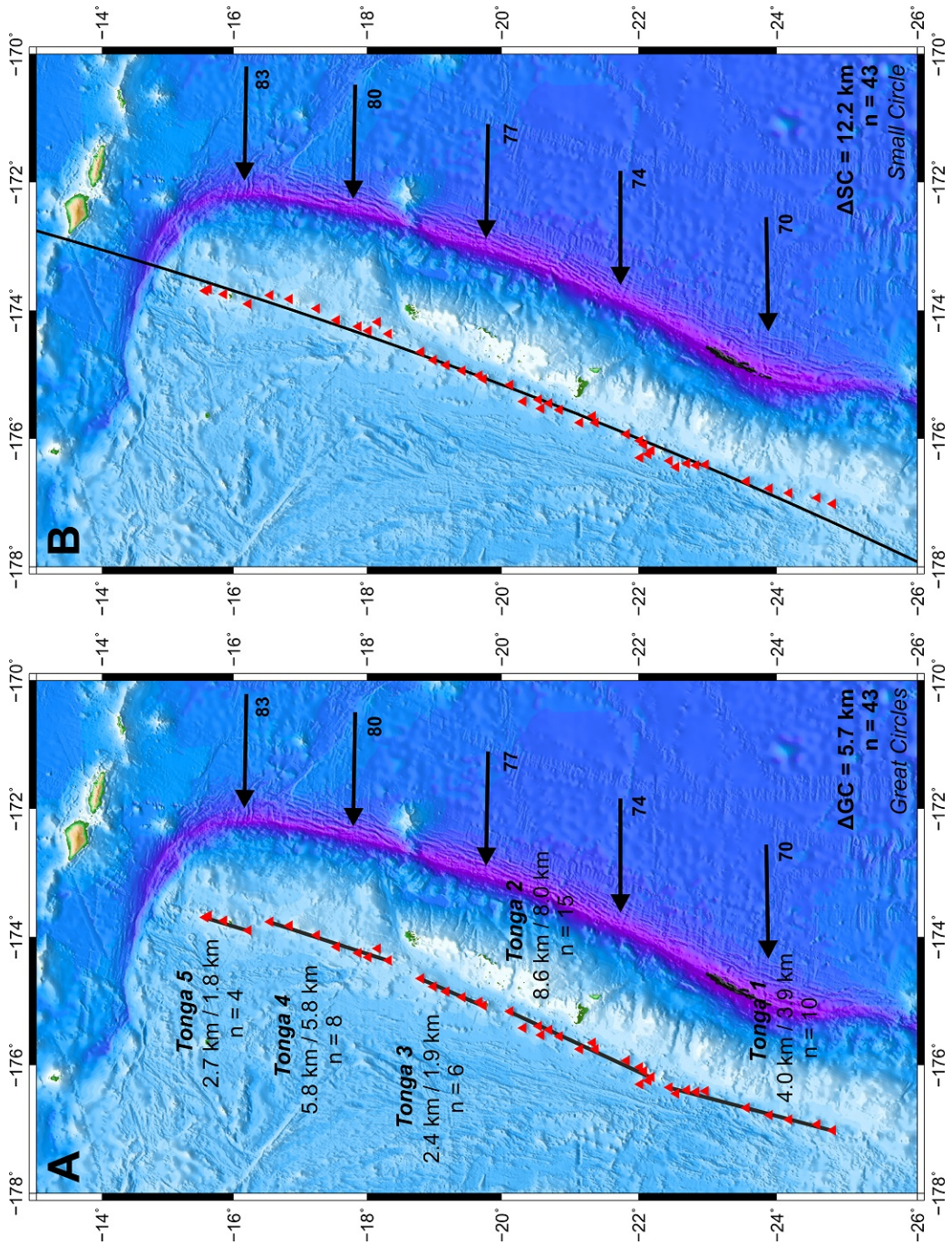

Figure D.15. Geometric fitting of arc volcanoes in Tonga.

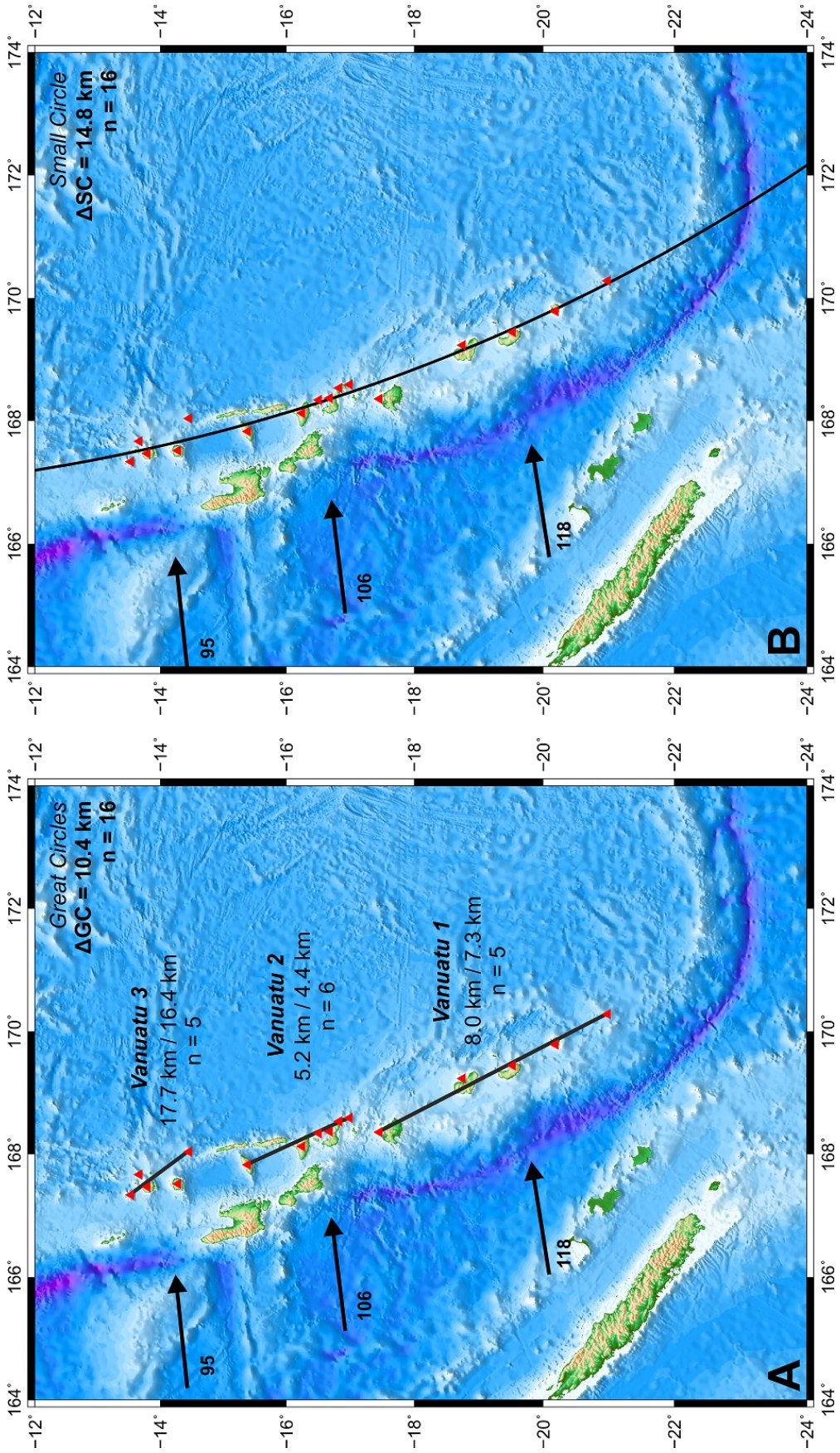

Figure D.16. Geometric fitting of arc volcanoes in Vanuatu.

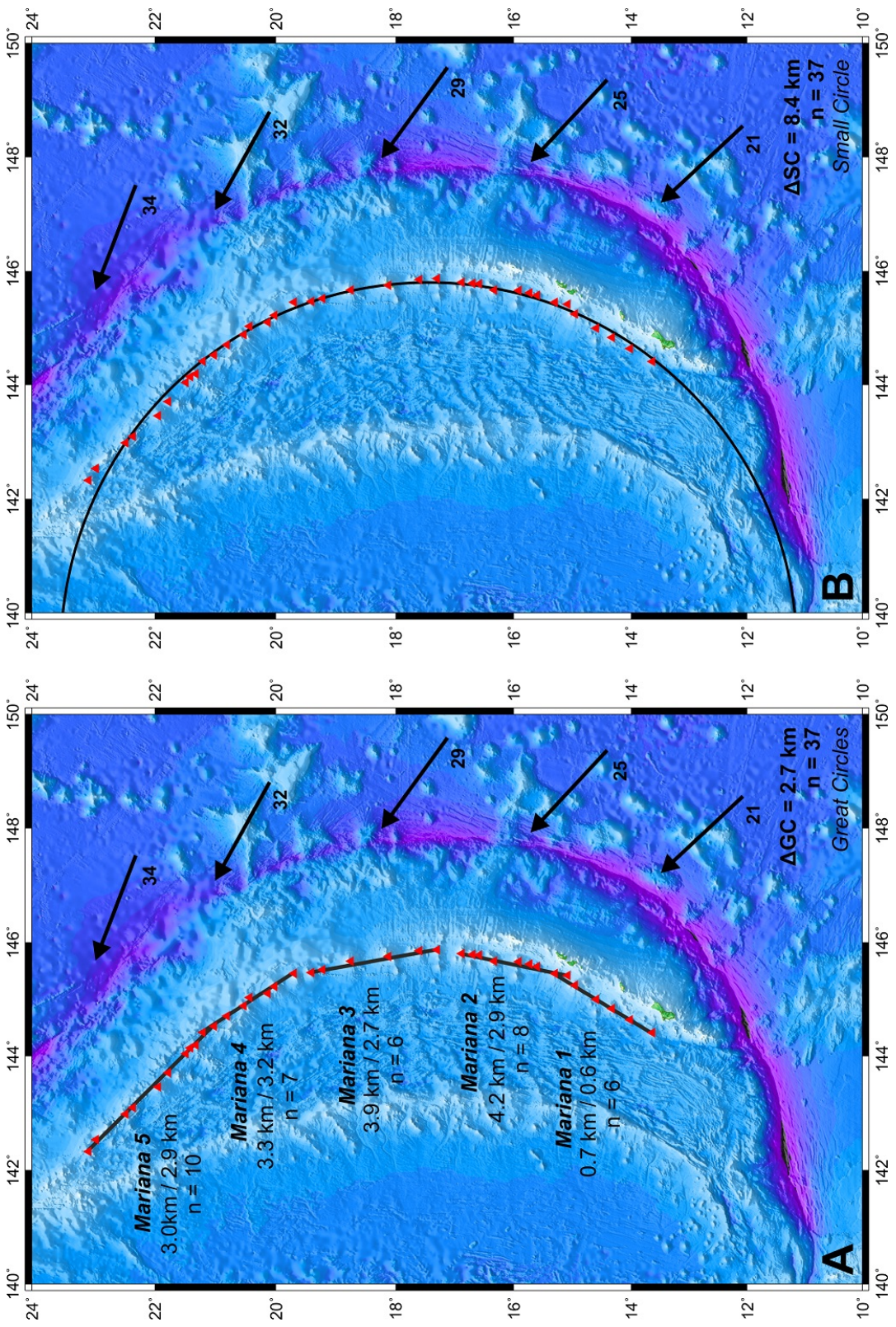

Figure D.17. Geometric fitting of arc volcanoes in Mariana.

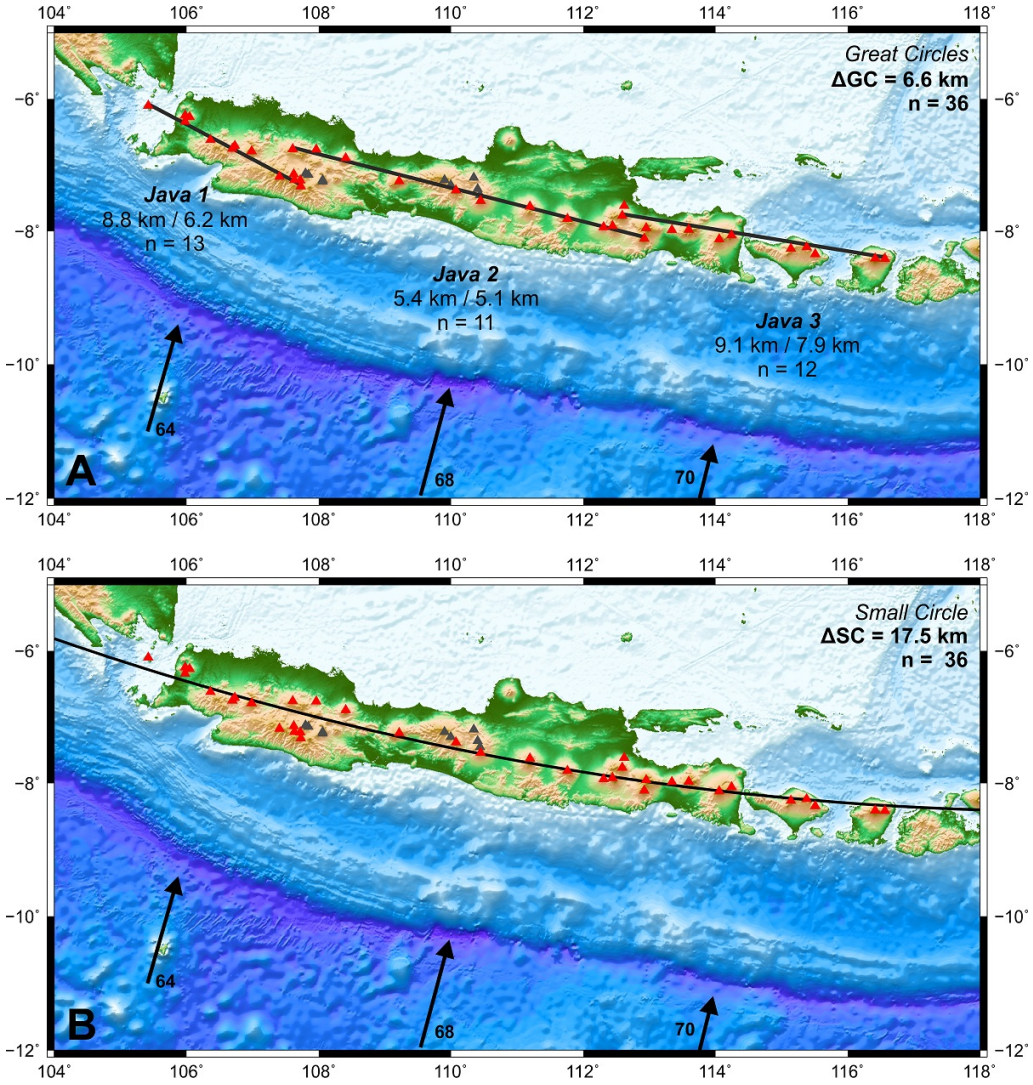

Figure D.18. Geometric fitting of arc volcanoes in Java and the Lesser Sunda Islands.

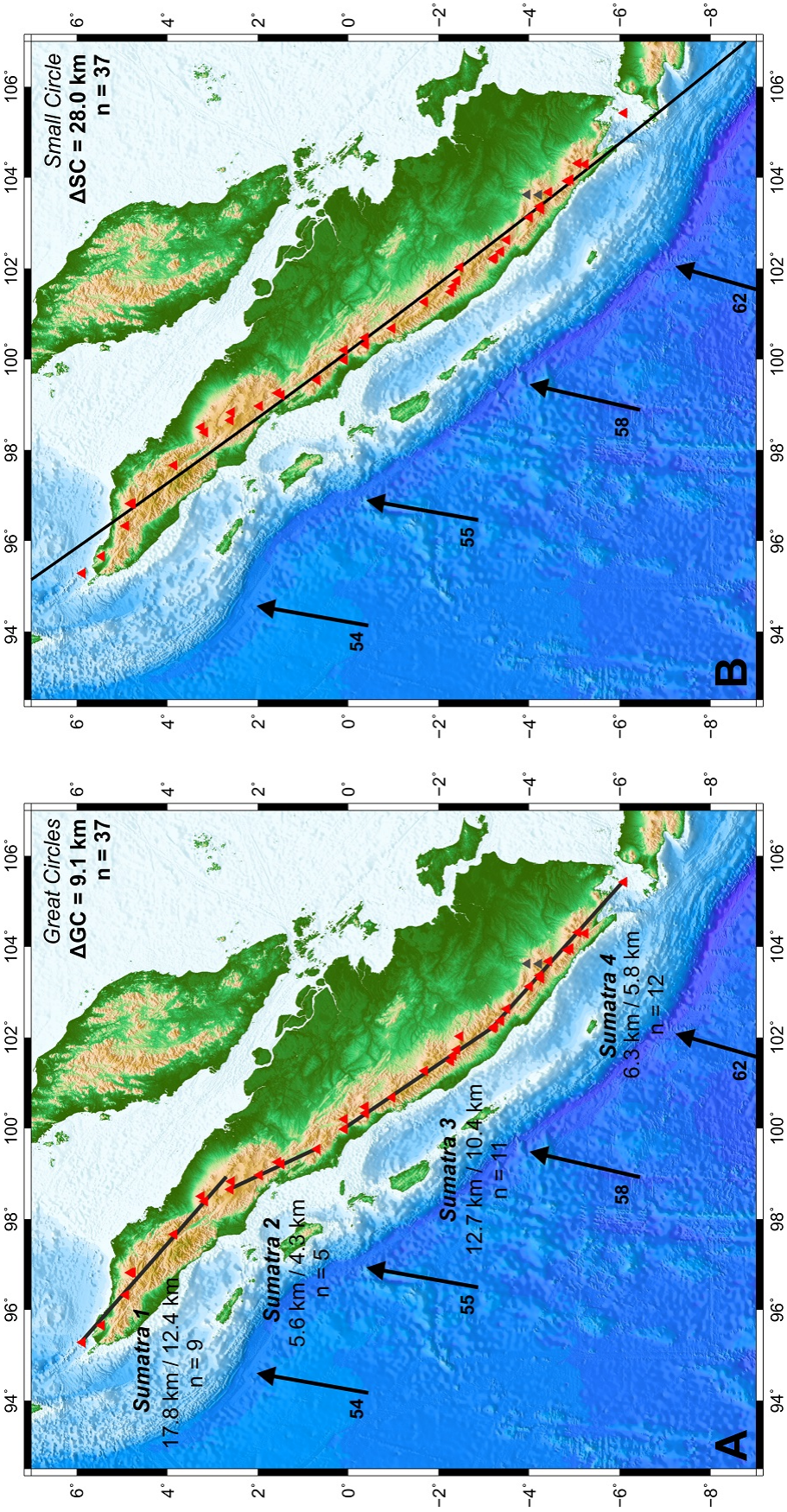

Figure D.19. Geometric fitting of arc volcanoes in Sumatra.

D.5 Residual Analyses

D.5.1 Mariana Arc

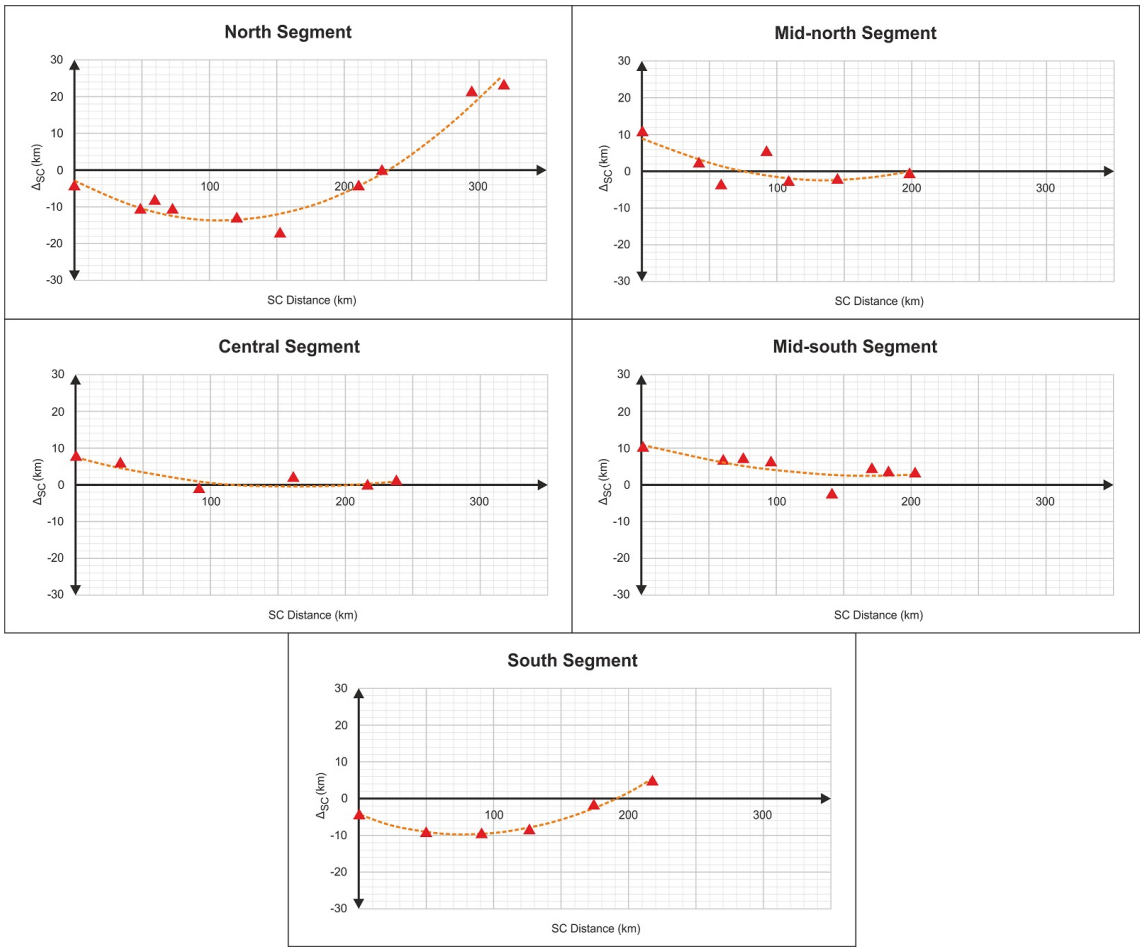

Figure D.20. Plots between arc volcano misfits against the distance of a single small circle in the Mariana.

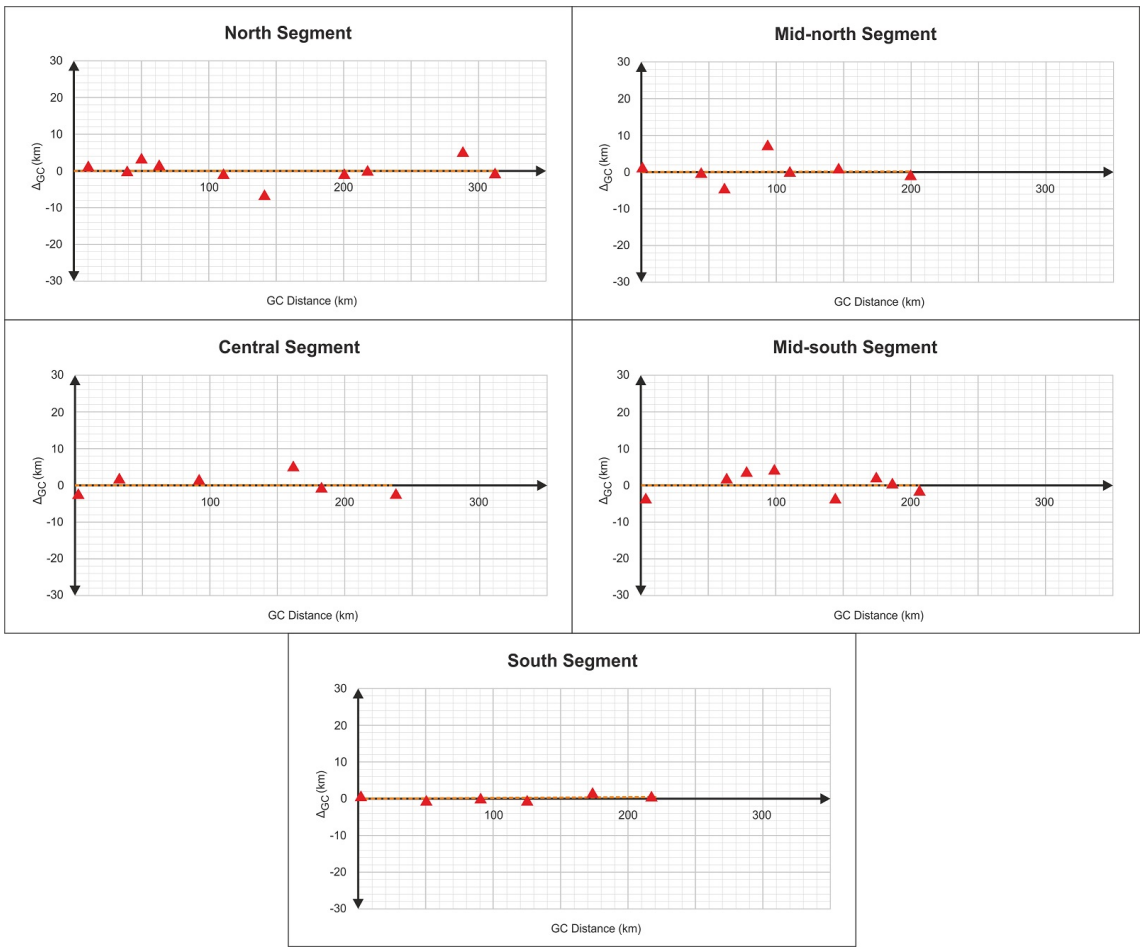

Figure D.21. Plots between arc volcano misfits against the distance of segmented great circles in the Mariana.

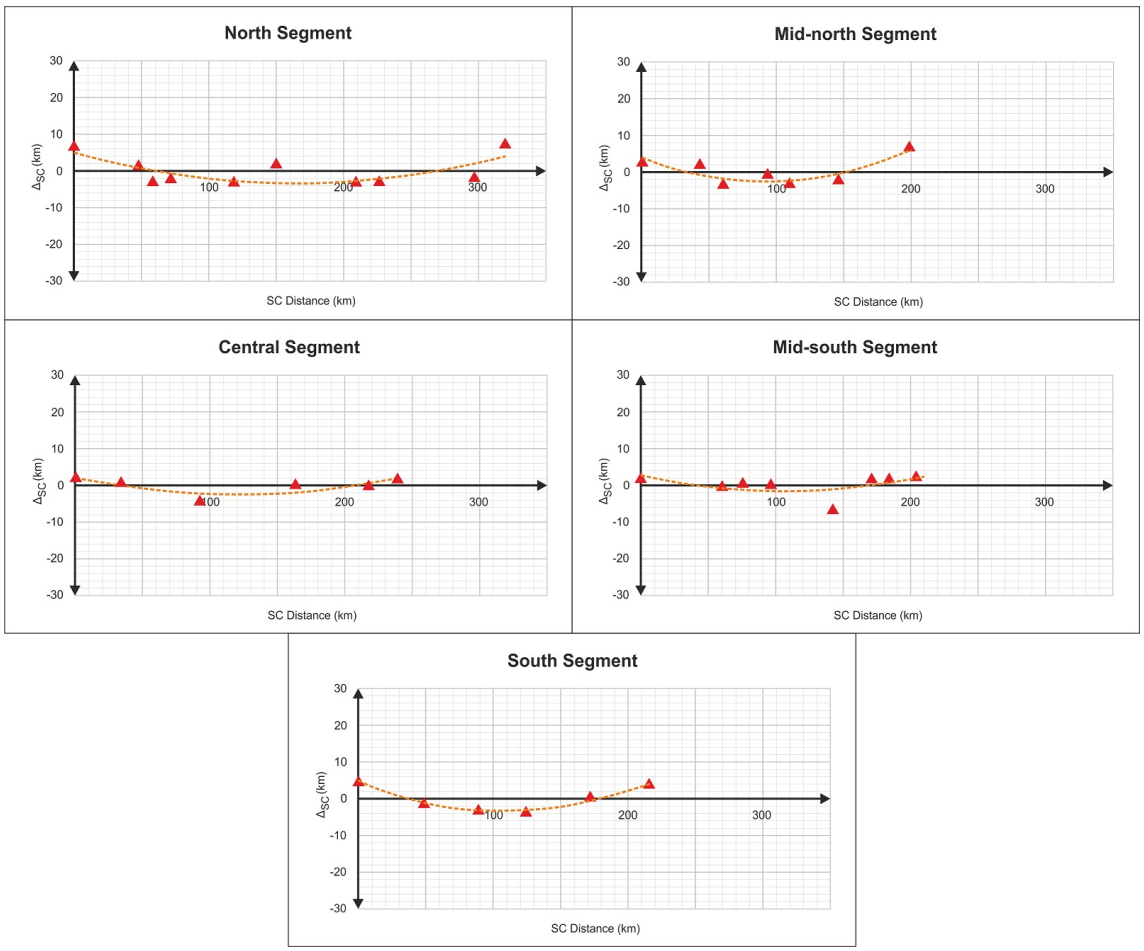

Figure D.22. Plots between arc volcano misfits against the distance of segmented small circles in the Mariana.

D.5.2 Java and the Lesser Sunda

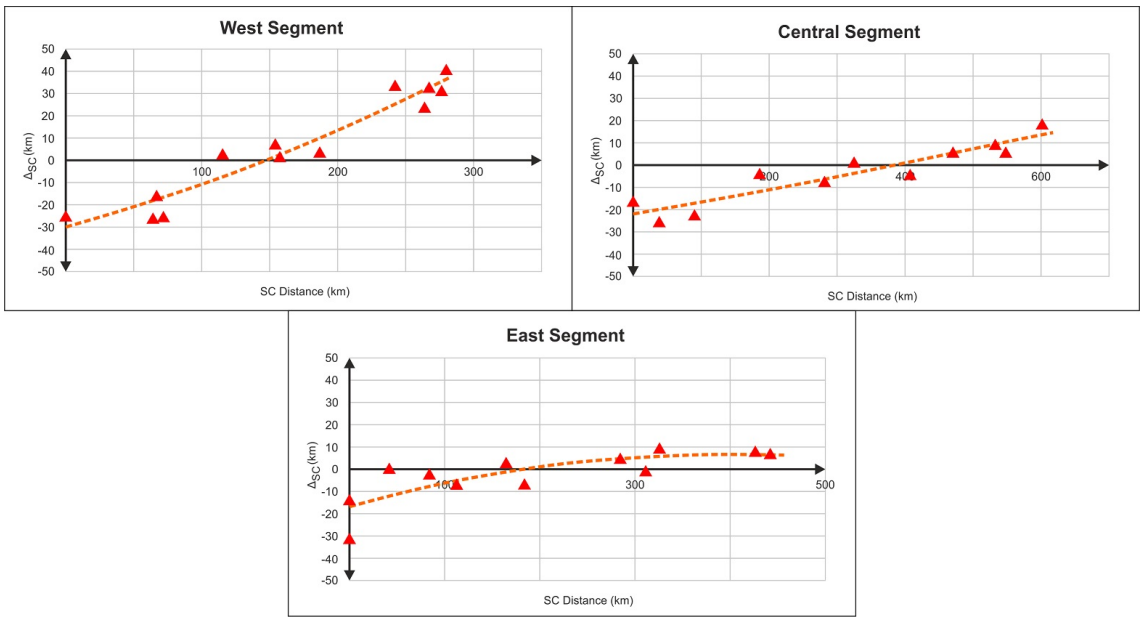

Figure D.23. Plots between arc volcano misfits against the distance of a single small circle in Java and the Lesser Sunda.

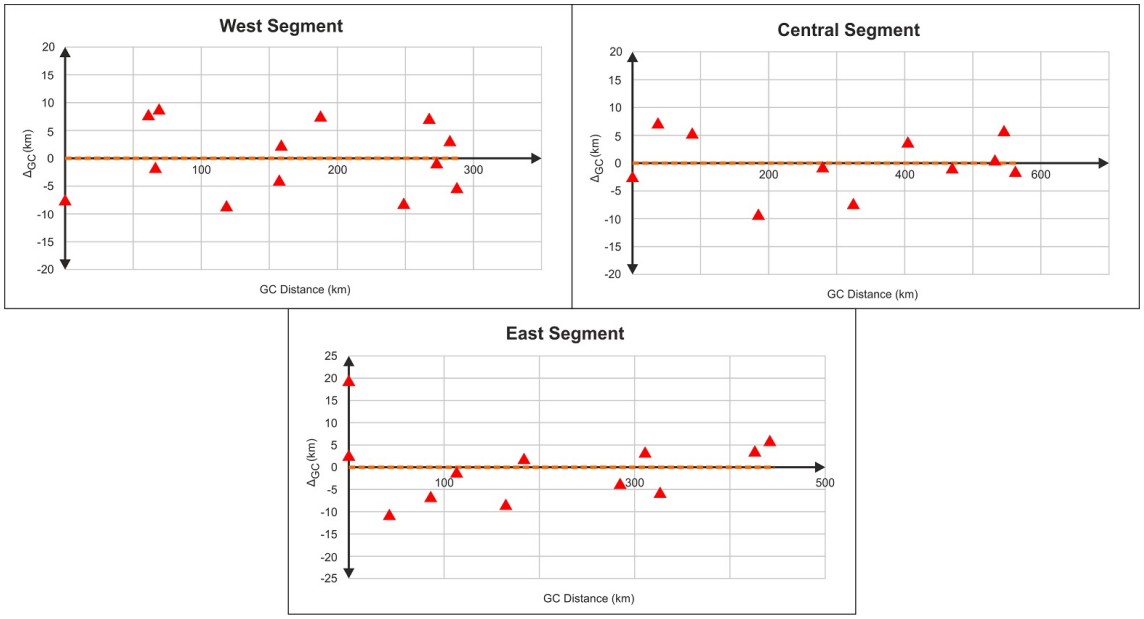

Figure D.24. Plots between arc volcano misfits against the distance of segmented great circles in Java and the Lesser Sunda.

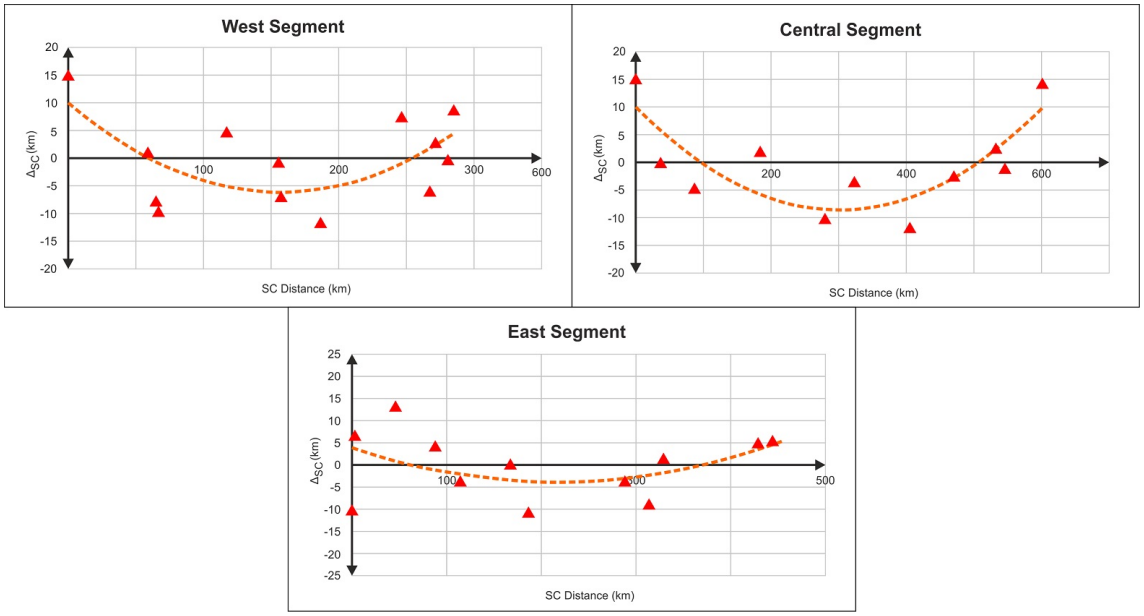

Figure D.25. Plots between arc volcano misfits against the distance of segmented small circles in Java and the Lesser Sunda.

D.5.3 Sumatra

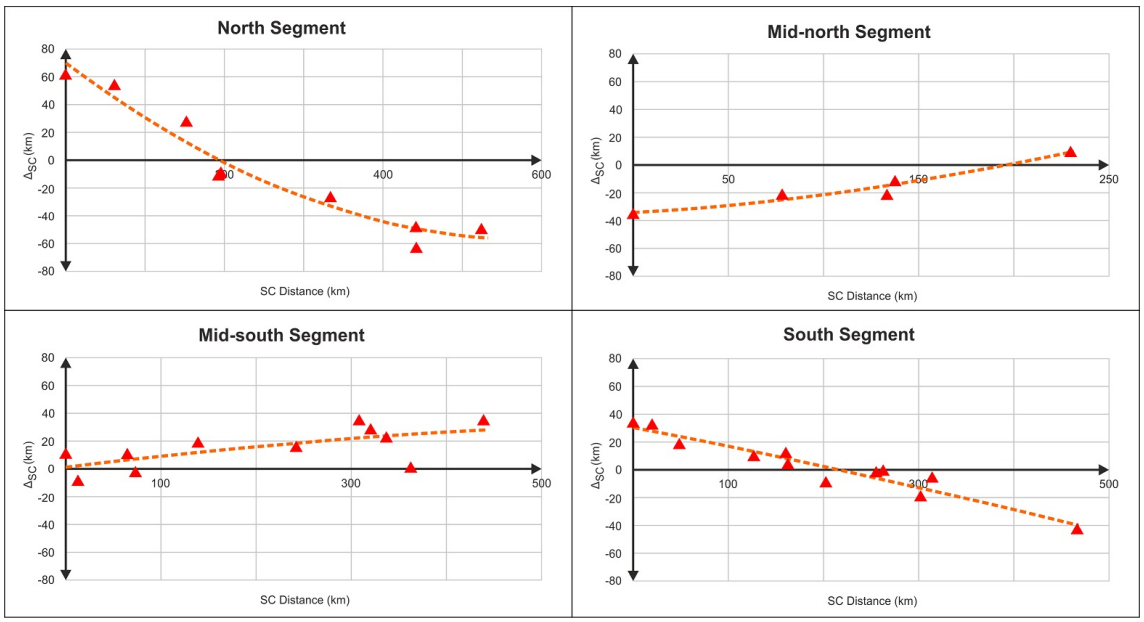

Figure D.26. Plots between arc volcano misfits against the distance of a small circle in Sumatra.

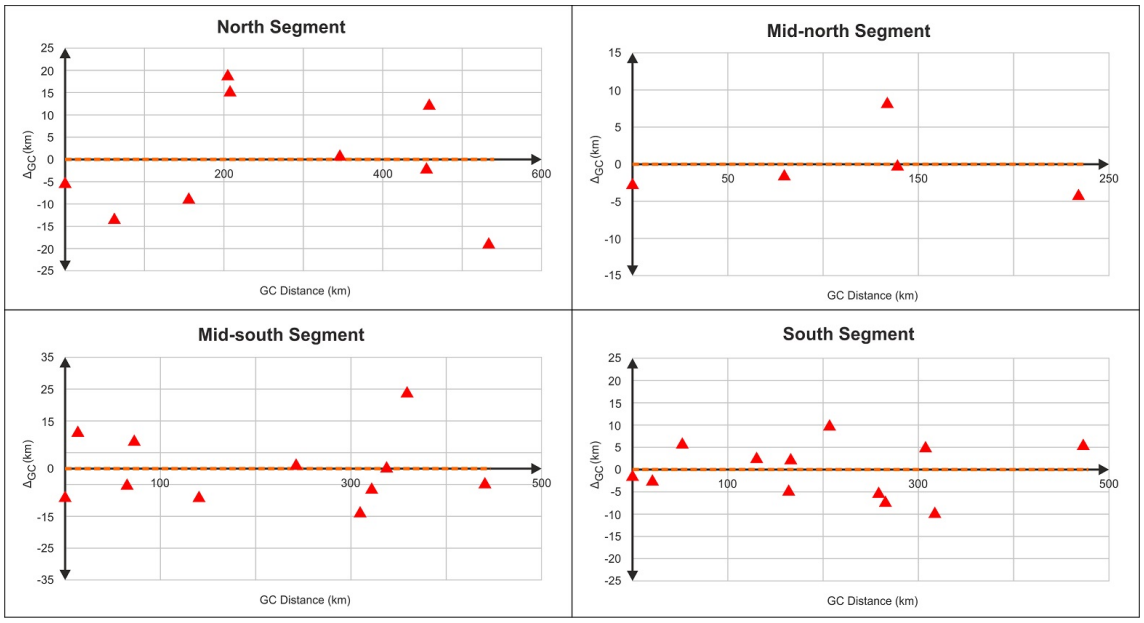

Figure D.27. Plots between arc volcano misfits against the distance of segmented great circles in Sumatra.

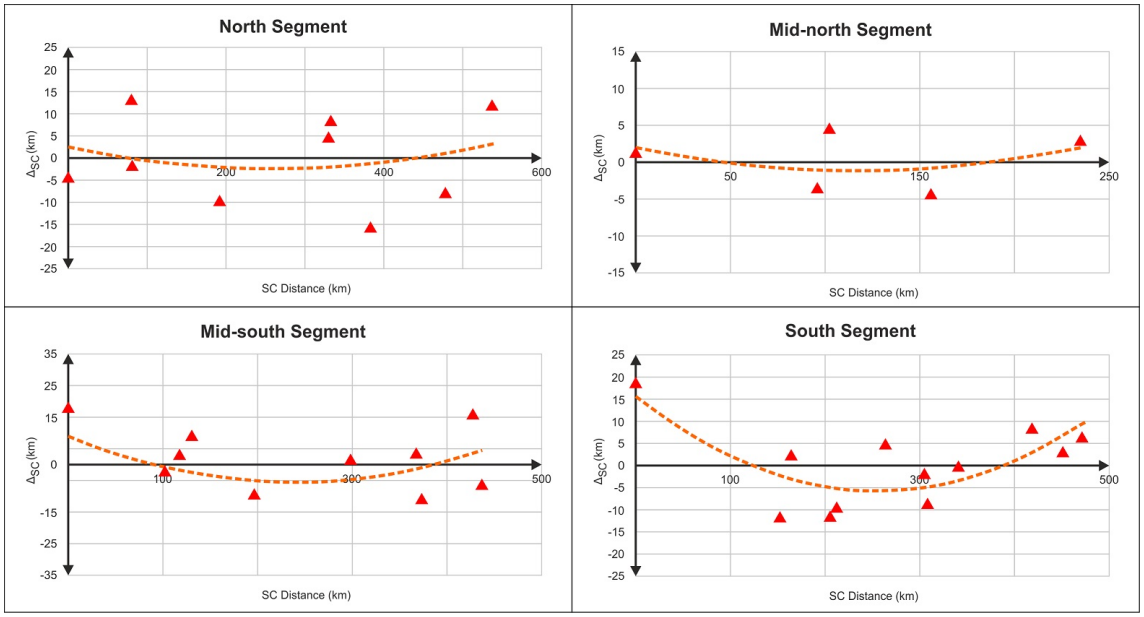

Figure D.28. Plots between arc volcano misfits against the distance of segmented small circles in Sumatra.

Appendix E

Surface Strain Observations

E.1 Ellipticity of Mariana Arc volcanoes

Loading from the volcanic edifice would cause vertical stress (σ_v) to be the intermediate principal stress (σ_2) in the shallow crust (Nakamura & Uyeda, 1980). A uniform stress field would produce a radially symmetrical edifice, crater, and radial dyke swarm. A non-uniform stress regime would generate dyke intrusion and an associated central conduit with preferred orientation. The maximum and minimum horizontal (σ_{Hmax} and σ_{Hmin}) stresses are the maximum and minimum principal stresses (σ_1 and σ_3), respectively. These maximum and minimum principal stress (σ_{Hmax} and σ_{Hmin}) directions may be approximated by the shortest and longest axes of volcano ellipticity (**Figure E.1**). Marliyani (2016) applied this ellipticity method in Java to develop a stress model of this near-orthogonal subduction zone. However, vertical stress increases with crustal depth (McGarr & Gay, 1978) and will, at some point, change the principal stresses geometry. Thus, such stress indicators should only be employed to estimate the shallow crustal stress regime surrounding volcanic edifices.

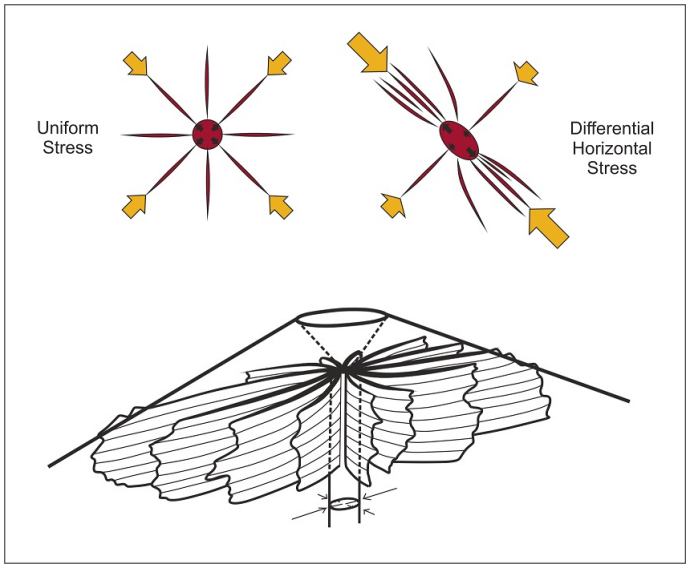

Figure E.1. Horizontal stress configuration that influences volcano morphology, also incorporating the geometry of the radial dyke system (Nakamura, 1977). Uniform horizontal stress would create a volcano with less-elliptic geometry. In contrast, variation in horizontal stress causes elongation of the radial dykes normal to minimum horizontal stress (Nakamura & Uyeda, 1980).

Volcano craters were prioritised for use in determining elongation (Marliyani, 2016) but, if this was absent or unclear, then the base of the volcano was used (Tibaldi, 1995). Ellipticity could not be determined for every volcano in the Mariana Arc due to the prox-

imity of other volcanoes, which results in uncertainty mapping their bases. **Figure E.2** illustrates examples of this approach for specific Mariana Arc volcanoes.

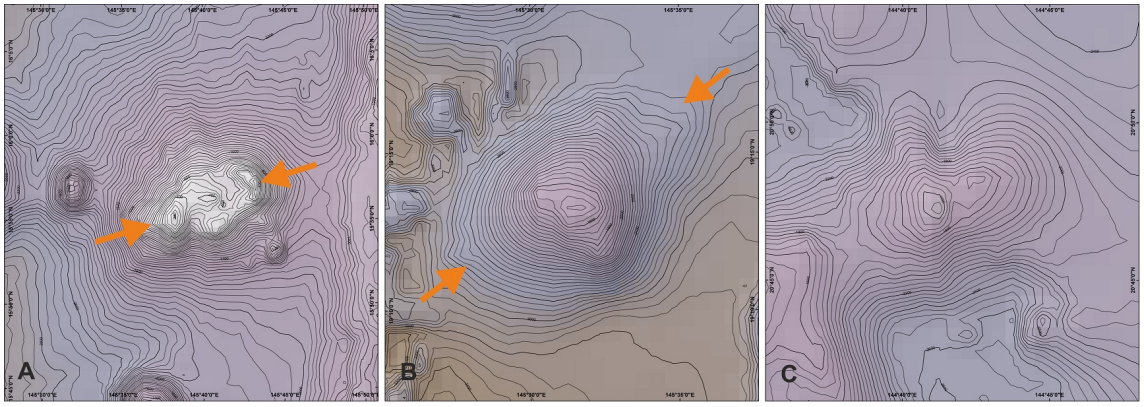

Figure E.2. Examples of the longest axis orientation of volcano ellipticity in Mariana Arc. (**A**) Longest axis determined from crater shape in East Diamante. (**B**) Longest axis determined from the base boundary of isolated volcano, Poyo. (**C**) Volcanoes such as Chamorro, which has no crater and no clear base was not included in the ellipticity analysis.

The result of volcano ellipticity observation is shown on **Table E.1** below and illustrated on **Figure 2.6** on the main manuscript.

Table E.1. Mariana arc volcano ellipticity observation result

Volcano Name	Code	Observation Type	Azimuth (N ... °E)	
			Shorter Axis	Longer Axis
Nikko	NI	Crater	156	66
Ichiyo	IC	Edifices Shape	89	179
Syoyo	SY	Crater	144	54
S Fukuyama	SF	Edifices Shape	132	42
Fukujin	FU	N/A	-	-
Kasuga #1	K1	Edifices Shape	112	22
NW Eifuku	NWE	N/A	-	-
Eifuku	EI	N/A	-	-
Daikoku	DA	N/A	-	-
SE Daikoku	SED	Edifices Shape	154	64
S Daikoku	SD	Edifices Shape	164	74
Chamorro	CH	N/A	-	-
Farallone de Parajos	FP	Crater	133	43
Ahyi	AH	Edifices Shape	0	90
Supply Reef	SR	N/A	-	-
Maug	MA	N/A	-	-
Asuncion	AS	Edifices Shape	155	65
Cheref	CE	N/A	-	-
Poyo	PO	Edifices Shape	144	54
Agrigan	AG	Crater	96	6
Pagan	PA	Crater	116	26
Alamagan	AL	Crater	75	165
Guguan	GU	Crater	105	15
Zealandia	ZE	N/A	-	-
Sarigan	SA	Crater	60	150
S Sarigan	SS	N/A	-	-
Anatahan	AN	Crater	1	91
E. Diamante	ED	Crater	167	77
N Ruby 2	NR	N/A	-	-
Ruby	RU	N/A	-	-
W Saipan	WS	Crater	13	103
W Tinian	WT	Edifices Shape	136	46
Esmeralda	ES	Crater	89	179
NW Rota #3	NR3	N/A	-	-
W Rota	WR	Crater	174	84
NW Guam	NWG	Edifices Shape	111	21
Tracey	TR	Crater	86	176

E.2 Structural Lineaments of Java LS

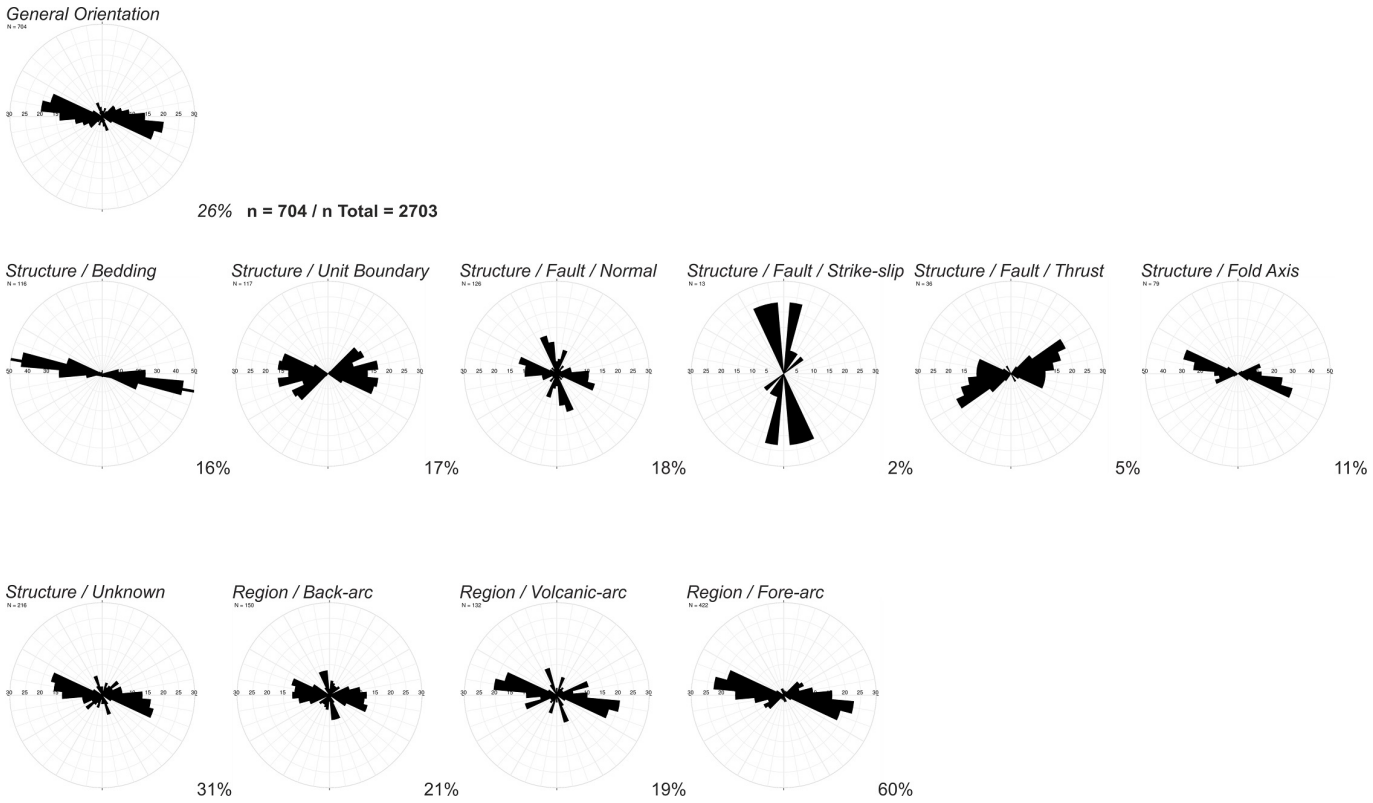

Figure E.3. Structural lineament orientations in the west segment of Java LS

Figure E.4. Structural lineament orientations in the central segment of Java LS

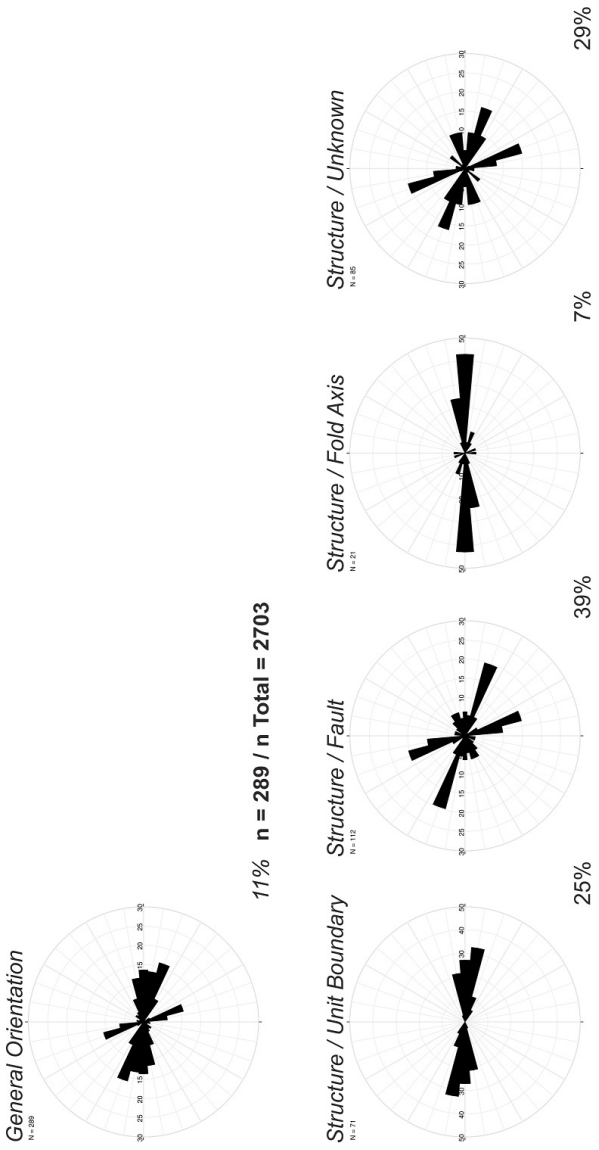

Figure E.5. Structural lineament orientations in the east segment of Java LS

E.3 Structural Lineaments of Sumatra

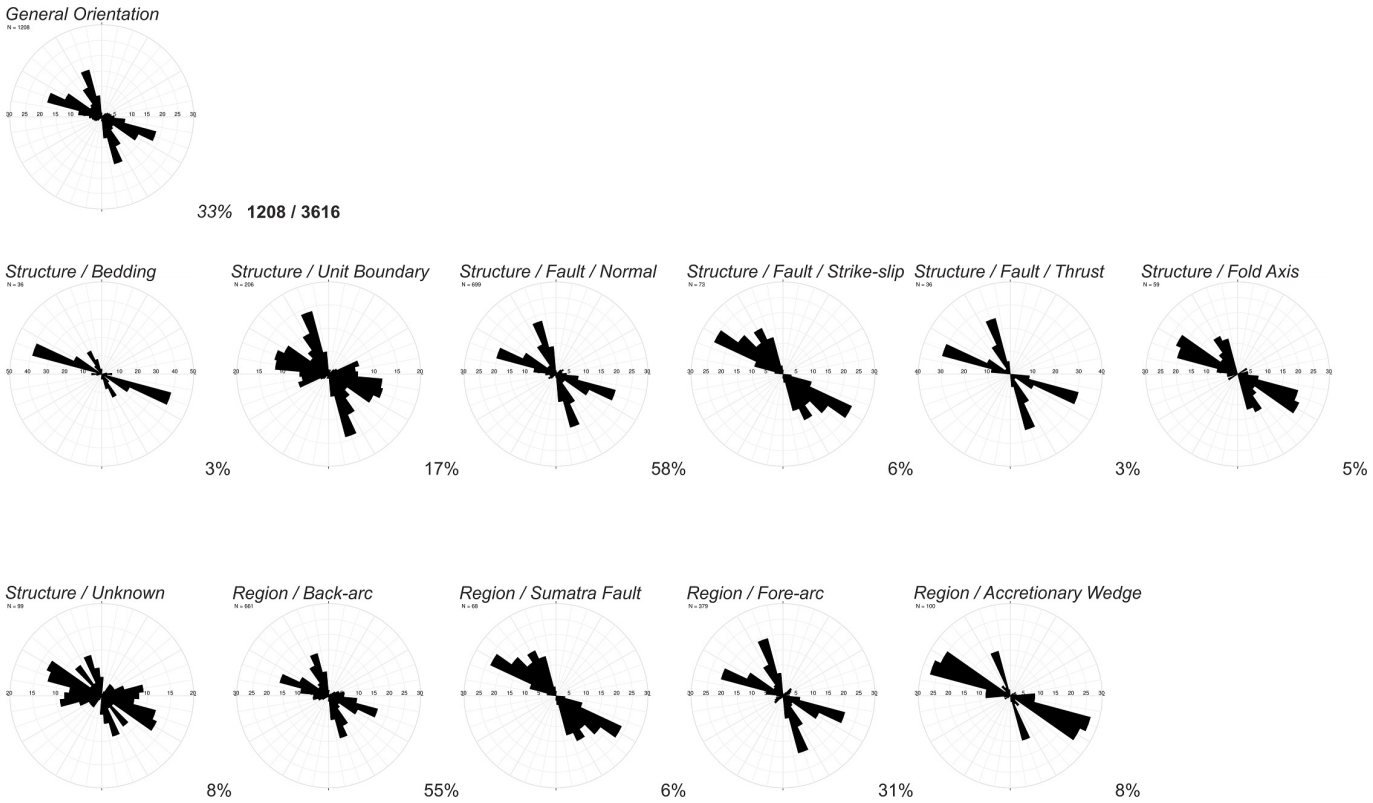

Figure E.6. Structural lineament orientations in the north segment of Sumatra

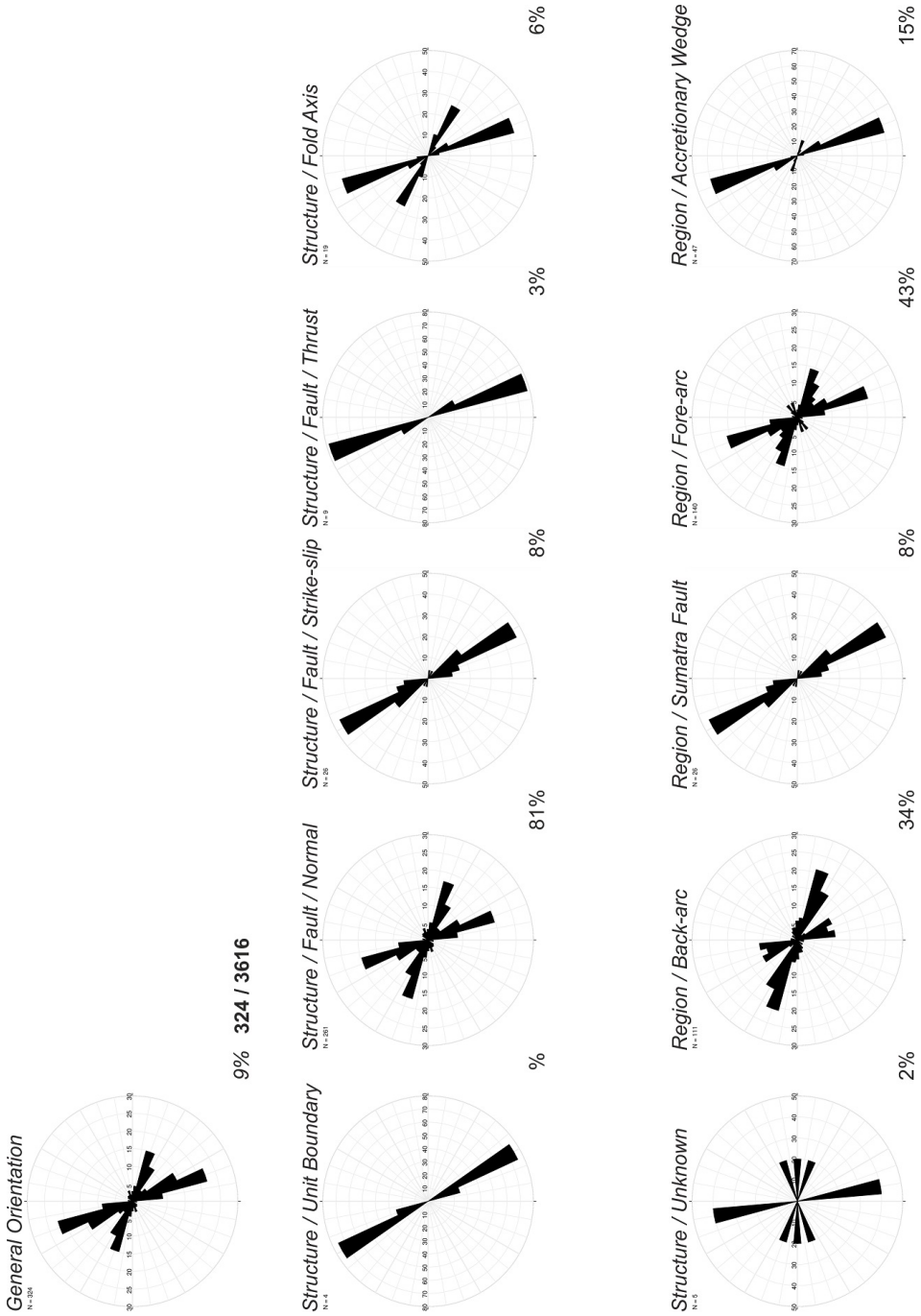

Figure E.7. Structural lineament orientations in the mid-north segment of Sumatra

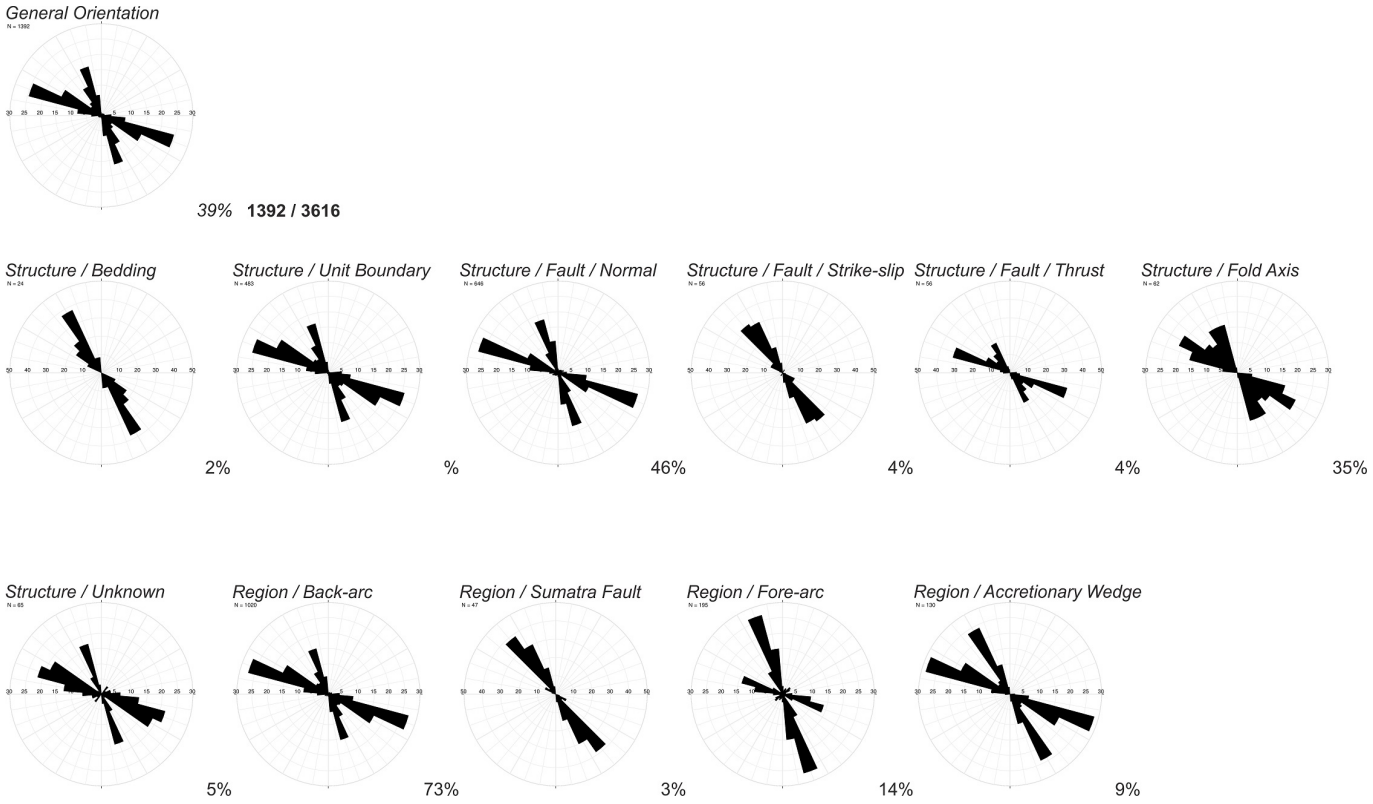

Figure E.8. Structural lineament orientations in the mid-south segment of Sumatra

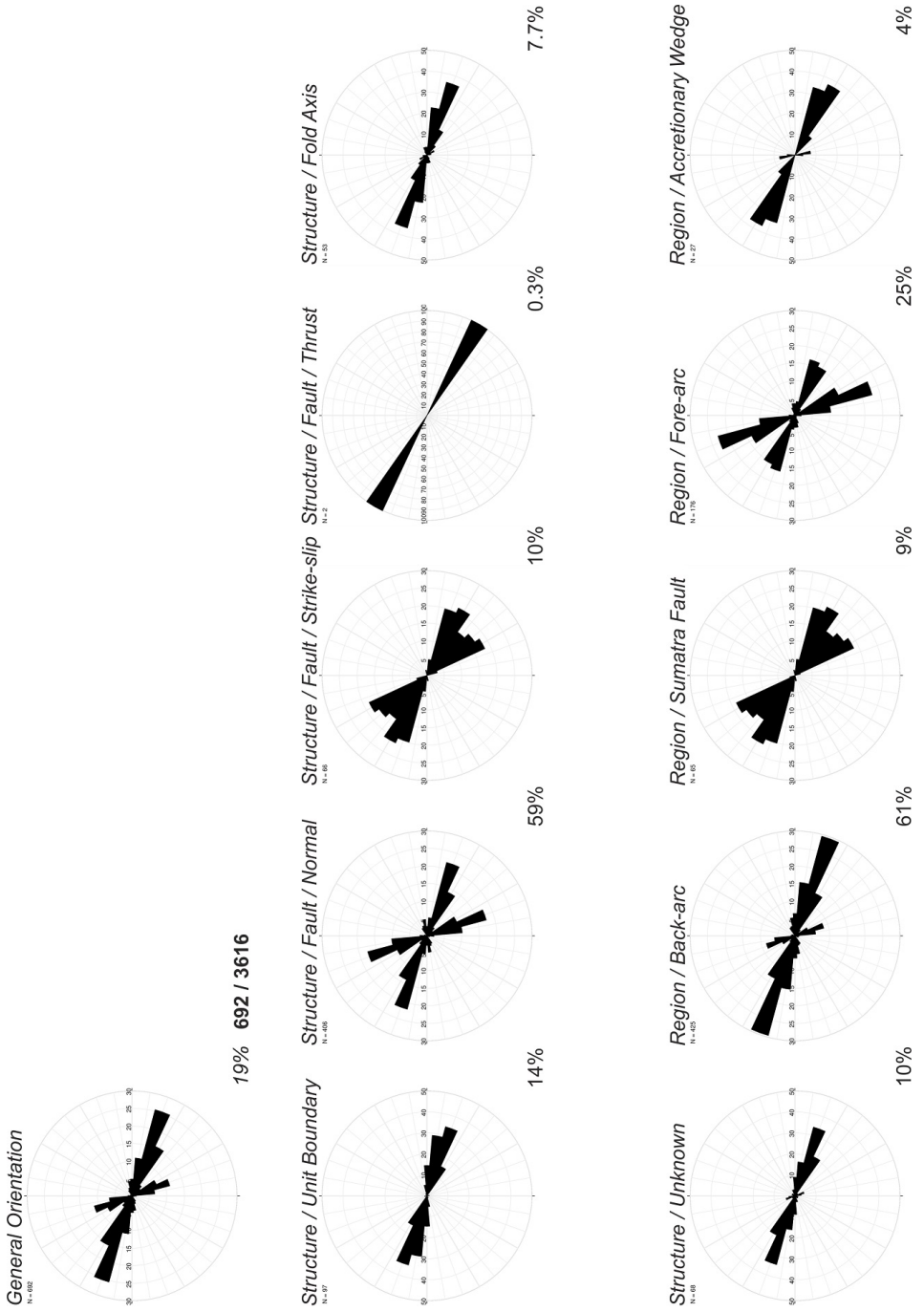

Figure E.9. Structural lineament orientations in the south segment of Sumatra

Appendix F

Subduction Dynamic Variables

Table F.1. Subduction dynamic variables I

Arc-segment	**nV**	**Lseg** (km)	**S.Az.** (deg)	**Mrms** (km)	**Dt** (km)	± (km)	**T.Az.** (deg)	**At** (deg)	**Ts** (km)	**Ht** (m)	**Htrel** (m)
01 Kamchatka 1	12	258	33	8.3	198	23	46	13	0.65	7743	7761
01 Kamchatka 2	26	237	30	8.3	215	7	35	5	0.63	7451	7874
01 Kamchatka 3	17	237	34	6.9	211	10	28	6	0.60	6861	7640
01 Kamchatka 4	10	112	26	6.8	211	17	10	15	0.60	5770	6598
02 Kuriles 1	9	140	43	2.7	181	2	42	2	0.40	8179	8051
02 Kuriles 2	8	125	47	2.4	200	10	56	8	0.45	9134	9259
02 Kuriles 3	11	189	57	5.6	196	3	54	3	0.50	8667	8848
02 Kuriles 4	4	85	40	5.2	238	7	49	9	0.50	8337	8592
02 Kuriles 5	7	124	47	4.6	260	8	58	11	0.50	7192	7581
03 North Japan 2	7	217	19	4.6	294	13	27	8	0.90	7672	8461
03 North Japan 3	10	330	7	6.6	298	11	15	8	0.77	7495	7715
04 Izu-Bonin 1	9	407	171	3.9	202	13	174	3	0.40	9415	8485
04 Izu-Bonin 2	15	624	170	4.5	219	27	173	3	0.40	9333	7326
05 Ryukyu 1	6	286	35	2.2	201	13	34	1	0.35	5598	4981
05 Ryukyu 2	9	334	18	5.8	228	43	35	17	2.00	4727	5031
06 Aleutians 1	5	92	64	0.9	185	2	68	4	2.00	6859	7043
06 Aleutians 2	13	233	65	7.0	163	9	69	3	2.00	6900	6691
06 Aleutians 3	13	433	80	6.5	160	8	81	1	1.60	7240	6922
06 Aleutians 4	6	255	101	4.6	156	12	106	5	2.00	7293	6496
07 Alaska 1	5	259	13	6.0	431	43	53	39	2.65	4657	5636
07 Alaska 2	16	206	55	7.7	315	3	56	1	2.75	5357	6086
07 Alaska 3	11	253	54	6.5	278	17	60	6	0.80	5632	6148
07 Alaska 4	11	251	60	4.6	216	27	74	13	0.80	6449	6775
08 Central America 1	15	216	114	5.4	196	5	116	2	0.30	5830	7964
08 Central America 2	25	314	110	9.4	182	12	112	2	0.20	5456	5968
08 Central America 3	8	127	119	1.1	174	7	125	6	0.50	5103	5330
08 Central America 4	8	127	132	3.2	179	3	137	5	0.60	4899	5064
08 Central America 5	10	215	120	2.9	173	12	117	4	0.70	3667	4386
09 Lesser Antilles 1*	4	198	21	2.2	444	26	4	17	6.25	4283	3333
09 Lesser Antilles 2*	7	147	159	3.2	288	8	159	0	1.00	5740	5382

(cont.)

Arc-segment	**nV**	**Lseg** (km)	**S.Az.** (deg)	**Mrms** (km)	**Dt** (km)	± (km)	**T.Az.** (deg)	**At** (deg)	**Ts** (km)	**Ht** (m)	**Htrel** (m)
09 Lesser Antilles 3*	6	153	133	3.5	253	13	122	11	0.80	6677	6315
10 Northern Andes 1	7	81	5	3.4	306	7	11	6	2.00	3793	7461
10 Northern Andes 2	4	188	33	2.0	297	7	35	2	2.00	3856	7107
10 Northern Andes 3	4	78	57	4.9	283	20	26	31	3.00	3278	6283
10 Northern Andes 4	10	163	26	7.7	243	7	29	3	0.35	3797	6898
11 Central Andes 1	11	245	121	16.9	248	6	129	9	0.55	6730	10987
11 Central Andes 2	11	325	141	11.9	260	26	152	11	0.35	6947	11078
11 Central Andes 3	20	367	164	12.2	325	53	5	21	0.13	7631	11589
11 Central Andes 4	15	336	5	16.9	313	5	5	1	0.23	6874	11420
12 Southern Andes 1	17	409	22	9.6	261	19	20	3	2.02	5348	7955
12 Southern Andes 2	19	449	13	9.6	249	29	8	6	1.66	4535	5476
12 Southern Andes 3	13	386	8	6.6	232	13	6	2	2.08	3698	4174
13 Scotia 1*	4	154	147	1.6	145	6	146	0	0.50	7491	6389
13 Scotia 2*	4	192	15	13.9	152	2	1	14	0.30	7136	5834
14 Kermadec-North Island 1	15	508	34	5.8	226	31	27	7	1.10	4008	4952
14 Kermadec-North Island 2	16	616	25	5.2	191	25	20	6	0.40	8307	6076
14 Kermadec-North Island 3	9	382	11	2.1	175	11	13	2	0.40	8796	7529
15 Tonga 1	10	269	15	4.0	178	15	18	3	0.40	9506	7984
15 Tonga 2	15	253	24	8.0	195	3	25	1	0.40	9278	7879
15 Tonga 3	6	112	22	1.9	199	6	17	5	0.40	9492	8679
15 Tonga 4	8	207	18	5.8	174	8	13	5	0.40	8748	7915
15 Tonga 5	4	75	18	1.8	178	9	3	15	0.40	8596	8042
16 Vanuatu 1*	5	441	153	7.3	138	18	157	4	0.30	6318	5618
16 Vanuatu 2*	6	196	155	4.4	133	12	150	5	0.60	5003	4286
16 Vanuatu 3*	5	127	151	16.4	178	37	176	25	1.20	4540	3645
17 Mariana 1	6	216	31	0.7	216	21	42	11	0.40	9441	7326
17 Mariana 2	8	204	11	2.9	222	6	12	1	0.40	7486	5779
17 Mariana 3	6	238	170	2.7	210	11	170	0	0.40	7451	5502
17 Mariana 4	7	199	147	3.2	201	14	153	6	0.40	6978	5123
17 Mariana 5	10	322	135	2.9	189	9	135	0	0.40	7645	5327
18 Java 1	13	288	118	6.2	252	11	124	5	1.20	6626	7320

(cont.)

Arc-segment	**nV**	**Lseg** (km)	**S.Az.** (deg)	**Mrms** (km)	**Dt** (km)	± (km)	**T.Az.** (deg)	**At** (deg)	**Ts** (km)	**Ht** (m)	**Htrel** (m)
18 Java 2	11	605	104	5.1	311	22	100	4	0.80	6787	7497
18 Java 3	12	443	100	7.9	320	11	101	1	0.47	6374	6857
19 Sumatra 1	9	537	132	12.4	308	29	127	4	5.00	5379	6309
19 Sumatra 2	5	235	155	4.4	277	12	152	3	4.00	5299	6334
19 Sumatra 3	11	429	146	10.5	284	20	143	4	1.85	5740	6845
19 Sumatra 4	12	474	133	5.8	286	17	134	1	0.97	6272	7106

Explanation: nV = number of volcanoes, $Lseg$ = arc-segment length, $S.Az.$ = arc-segment orientation (clockwise from North), Dt = arc-segment distance from trench, $T.Az.$ = general trench orientation, At = angle between arc-segment and trench, Ts = trench sediment thickness, Ht = trench depth, $Htrel$ = relative trench depth from He

* = Segments are not included in the multivariate statistics (see main text)

Table F.2. Subduction dynamic variables II

Arc-segment	δ (deg)	δ_s (deg)	δ_d (deg)	**H** (km)	**Fix.Pl.**	**Mov.Pl.**	**Vtot** (mm/yr)	$\pm$ (mm/yr)	**Sub.Dir.** (deg)	$\pm$ (deg)	**Ao** (deg)
01 Kamchatka 1	50	36	50	81	OK	PA	86	3	300	2	16
01 Kamchatka 2	51	37	51	83	OK	PA	84	3	302	2	3
01 Kamchatka 3	50	38	56	83	OK	PA	82	3	304	2	5
01 Kamchatka 4	-	40	64	121	OK	PA	80	3	305	2	24
02 Kuriles 1	46	34	48	66	OK	PA	88	3	298	2	14
02 Kuriles 2	47	32	46	89	OK	PA	89	3	297	2	29
02 Kuriles 3	45	30	40	96	OK	PA	90	3	295	2	29
02 Kuriles 4	41	27	33	99	OK	PA	91	3	294	2	25
02 Kuriles 5	36	24	32	103	OK	PA	91	3	294	2	35
03 North Japan 2	33	24	30	87	OK	PA	93	3	292	2	6
03 North Japan 3	29	21	27	96	OK	PA	92	3	292	2	8
04 Izu-Bonin 1	49	30	56	100	PS	PA	46	1	280	1	15
04 Izu-Bonin 2	63	34	73	143	PS	PA	39	1	284	1	21
05 Ryukyu 1	48	35	61	73	YZ	PS	75	1	299	1	5
05 Ryukyu 2	57	26	64	116	YZ	PS	69	1	300	1	5
06 Aleutians 1	46	32	-	83	NA	PA	69	1	323	1	15
06 Aleutians 2	52	34	60	75	NA	PA	70	1	321	1	18
06 Aleutians 3	58	37	59	85	NA	PA	73	1	317	1	34
06 Aleutians 4	53	40	57	91	NA	PA	76	1	313	1	64
07 Alaska 1	36	17	38	90	NA	PA	57	1	339	2	16
07 Alaska 2	43	22	44	75	NA	PA	60	1	333	2	8
07 Alaska 3	45	25	-	88	NA	PA	63	1	330	1	0
07 Alaska 4	45	30	53	90	NA	PA	66	1	326	1	18
08 Central America 1	54	28	54	88	CA	CO	67	3	21	1	5
08 Central America 2	60	30	64	104	CA	CO	71	3	22	1	0
08 Central America 3	61	32	66	127	CA	CO	74	3	22	1	13
08 Central America 4	64	31	62	134	CA	CO	75	3	23	1	25
08 Central America 5	57	29	57	94	CA	CO	78	3	24	1	3
09 Lesser Antilles 1*	41	34	55	79	CA	SA	20	0	253	1	20
09 Lesser Antilles 2*	49	39	-	96	CA	SA	19	0	253	2	3

(cont.)

Arc-segment	δ (deg)	δ_s (deg)	δ_d (deg)	**H** (km)	**Fix.Pl.**	**Mov.Pl.**	**Vtot** (mm/yr)	$\pm$ (mm/yr)	**Sub.Dir.** (deg)	$\pm$ (deg)	**Ao** (deg)
09 Lesser Antilles 3*	50	36	-	85	CA	SA	18	0	254	2	42
10 Northern Andes 1	31	28	50	123	SA	NZ	59	2	76	1	25
10 Northern Andes 2	37	26	45	147	SA	NZ	60	2	77	1	48
10 Northern Andes 3	34	21	45	118	SA	NZ	60	2	77	1	39
10 Northern Andes 4	25	-	-	107	SA	NZ	61	2	78	1	41
11 Central Andes 1	25	17	50	100	SA	NZ	72	2	76	1	36
11 Central Andes 2	33	25	41	111	SA	NZ	72	2	75	1	13
11 Central Andes 3	28	18	45	108	SA	NZ	73	2	75	1	20
11 Central Andes 4	22	16	48	92	SA	NZ	74	2	75	1	20
12 Southern Andes 1	28	22	35	106	SA	NZ	74	2	76	1	33
12 Southern Andes 2	34	25	-	102	SA	NZ	74	2	77	1	21
12 Southern Andes 3	39	-	-	91	SA	NZ	73	2	77	1	19
13 Scotia 1*	67	56	85	90	SW	SR	69	3	255	3	19
13 Scotia 2*	61	51	78	114	SW	SR	76	3	254	2	17
14 Kermadec-North Island 1	52	-	-	87	AU	PA	45	1	261	1	36
14 Kermadec-North Island 2	62	43	67	102	AU	PA	53	1	266	1	24
14 Kermadec-North Island 3	56	39	57	83	AU	PA	63	1	268	1	15
15 Tonga 1	54	39	57	76	AU	PA	70	1	269	4	19
15 Tonga 2	51	39	56	80	AU	PA	74	1	270	2	25
15 Tonga 3	54	37	53	82	AU	PA	77	1	271	2	16
15 Tonga 4	52	36	52	64	AU	PA	80	1	271	2	12
15 Tonga 5	54	35	53	47	AU	PA	83	1	271	1	2
16 Vanuatu 1*	68	50	66	104	NH	AU	118	3	81	1	14
16 Vanuatu 2*	71	48	71	104	NH	AU	106	3	83	1	23
16 Vanuatu 3*	69	52	82	162	NH	AU	95	3	84	2	2
17 Mariana 1	49	40	74	159	PS	PA	21	0	317	2	5
17 Mariana 2	56	35	84	141	PS	PA	25	0	313	3	32
17 Mariana 3	59	35	86	137	PS	PA	29	0	306	3	46
17 Mariana 4	61	36	84	122	PS	PA	32	0	299	3	56
17 Mariana 5	64	36	72	134	PS	PA	34	0	291	4	66
18 Java 1	49	27	70	81	SU	AU	64	0	16	1	18

(cont.)

Arc-segment	δ (deg)	δ_s (deg)	δ_d (deg)	**H** (km)	**Fix.Pl.**	**Mov.Pl.**	**Vtot** (mm/yr)	$\pm$ (mm/yr)	**Sub.Dir.** (deg)	$\pm$ (deg)	**Ao** (deg)
18 Java 2	47	29	69	128	SU	AU	68	1	15	1	5
18 Java 3	45	30	68	128	SU	AU	70	1	14	1	3
19 Sumatra 1	49	31	48	124	SU	AU	54	0	10	1	28
19 Sumatra 2	46	28	40	109	SU	AU	55	0	10	1	52
19 Sumatra 3	48	28	49	106	SU	AU	58	0	13	1	39
19 Sumatra 4	50	28	62	82	SU	AU	62	0	16	1	28

Explanation: δ = average slab dip, δ_s = shallow slab dip (less than 125 km), δ_d = deep slab dip (deeper than 125 km),
H = depth to the slab beneath the arc, $Fix.Pl.$ = fixed plate, $Mov.Pl.$ = relatively moving plate, $Vtot$ = convergence rate,
$Sub.Dir.$ = subduction direction, Ao = convergence obliquity
Tectonic plate abbreviation: AU = Australia, CA = Caribbean, CO = Cocos, NA = North America, NH = New Hebrides,
NZ = Nazca, OK = Okhostk, PA = Pacific, PS = Philippine Sea, SA = South America,
SR = Sur, SU = Sundaland, SW = Sandwich, YZ = Yangtze.
* = Segments are not included in the multivariate statistics (see main text)

Table F.3. Subduction dynamic variables III

Arc-segment	**Vort** (mm/yr)	**Vdes** (mm/yr)	**Vlat** (mm/yr)	ϕ (km)	**Fsp** (10^{12} N/m)	**Age** (Ma)	**Vhs** (mm/yr)	**L** (km)	**Tc** (km)	**UPN** (o/c)	**UPS** (E3-C3)	**He** (m)
01 Kamchatka 1	83	63	67	6869	31.68	108	59	924	26	c	C1	18
01 Kamchatka 2	84	66	67	6952	30.83	106	70	909	32	c	C1	423
01 Kamchatka 3	82	63	64	6423	28.62	102	61	860	36	c	E1	779
01 Kamchatka 4	73	-	56	-	16.42	100	61	500	33	c	E1	828
02 Kuriles 1	85	61	71	7130	34.14	116	56	963	21	c	C1/C2	-128
02 Kuriles 2	78	57	66	6621	35.67	117	56	1001	22	c	C2	125
02 Kuriles 3	79	56	68	6678	39.37	119	75	1098	18	c	C2	181
02 Kuriles 4	82	53	73	6530	46.42	122	51	1276	26	c	C2	255
02 Kuriles 5	75	44	68	5538	49.45	126	131	1336	29	c	C2	389
03 North Japan 2	92	51	84	6837	53.41	135	59	1397	29	c	C3	789
03 North Japan 3	91	44	85	5746	58.74	131	102	1559	31	c	C3	220
04 Izu-Bonin 1	45	34	39	4575	35.28	136	65	918	16	o	E2	-930
04 Izu-Bonin 2	37	33	31	4649	31.15	141	40	796	7	o	E2	-2007
05 Ryukyu 1	75	56	61	-	-	-	-	447	26	c	E2	-617
05 Ryukyu 2	69	57	62	1974	9.59	34	42	497	33	c	-	304
06 Aleutians 1	66	47	56	2646	14.54	56	27	590	28	c	E1	184
06 Aleutians 2	67	52	55	3137	15.75	60	27	618	24	c	0/E1	-209
06 Aleutians 3	60	51	48	2895	16.46	56	26	667	18	c	0	-318
06 Aleutians 4	34	27	26	1397	11.31	52	49	476	18	c	C1	-797
07 Alaska 1	54	32	52	1250	14.97	39	37	730	36	c	C1	979
07 Alaska 2	60	41	55	1805	12.79	44	39	586	33	c	0/C1	729
07 Alaska 3	63	45	57	2275	15.65	51	79	665	32	c	0	516
07 Alaska 4	63	45	55	2465	16.53	55	37	675	30	c	0	326
08 Central America 1	67	54	59	1248	9.61	23	57	606	25	c	0	2134
08 Central America 2	71	61	61	1493	9.02	24	57	556	30	c	0	512
08 Central America 3	72	63	61	1509	8.67	24	49	537	28	c	0	227
08 Central America 4	68	61	59	1476	9.11	24	49	562	33	c	0/C1	165
08 Central America 5	78	65	68	1159	8.15	18	59	586	37	c	C1	719
09 Lesser Antilles 1*	19	13	16	1152	28.52	92	42	904	20	p	E1	-950
09 Lesser Antilles 2*	19	14	15	1130	26.47	80	21	900	25	p	E1	-358

(cont.)

Arc-segment	**Vort** (mm/yr)	**Vdes** (mm/yr)	**Vlat** (mm/yr)	ϕ (km)	**Fsp** (10^{12} N/m)	**Age** (Ma)	**Vhs** (mm/yr)	**L** (km)	**Tc** (km)	**UPN** (o/c)	**UPS** (E3-C3)	**He** (m)
09 Lesser Antilles 3*	13	10	11	842	23.07	84	27	765	20	p	E1	-362
10 Northern Andes 1	53	27	47	291	10.53	11	127	978	47	c	C3	3668
10 Northern Andes 2	40	24	36	287	12.04	12	118	1056	44	c	C3	3251
10 Northern Andes 3	47	26	44	344	13.39	13	118	1120	46	c	C3	3005
10 Northern Andes 4	46	20	-	291	-	15	31	-	53	-	-	3101
11 Central Andes 1	58	24	55	1233	26.75	51	50	1139	54	c	C3	4257
11 Central Andes 2	71	38	64	2004	26.82	52	46	1126	57	c	C3	4131
11 Central Andes 3	69	32	65	1604	27.42	50	41	1175	62	c	C3	3958
11 Central Andes 4	69	26	67	1207	27.16	47	104	1206	61	c	C3	4546
12 Southern Andes 1	62	29	57	1006	25.37	35	55	1299	49	c	C1	2607
12 Southern Andes 2	69	38	63	1099	-	29	57	-	40	c	C1	941
12 Southern Andes 3	69	43	-	506	-	12	52	-	36	-	-	476
13 Scotia 1*	65	60	36	3618	17.84	60	18	698	7	o	E3	-1102
13 Scotia 2*	73	64	46	2047	13.51	32	69	723	7	o	E3	-1302
14 Kermadec-North Island 1	36	28	-	3437	-	121	39	-	24	-	-	944
14 Kermadec-North Island 2	49	43	35	4625	26.61	108	48	778	10	o	E2	-2231
14 Kermadec-North Island 3	61	50	48	4618	26.87	92	46	853	11	o	E2	-1267
15 Tonga 1	66	54	52	4776	26.32	89	55	848	10	o	E3	-1522
15 Tonga 2	67	52	52	4971	27.74	95	54	863	10	o	E3	-1399
15 Tonga 3	74	59	59	5913	29.41	99	69	896	11	o	E3	-813
15 Tonga 4	78	62	64	6331	30.29	103	69	907	11	o	E3	-833
15 Tonga 5	83	67	68	7081	30.50	106	68	900	10	o	E3	-554
16 Vanuatu 1*	114	105	73	3297	14.00	31	29	760	13	o	E3	-700
16 Vanuatu 2*	97	91	65	3817	15.85	42	27	745	11	o	E3	-717
16 Vanuatu 3*	95	88	58	-	-	-	-	709	10	o	E3	-895
17 Mariana 1	21	16	16	2424	31.05	154	40	761	7	o	E3	-2115
17 Mariana 2	21	17	17	2621	31.07	152	40	766	7	o	E3	-1707
17 Mariana 3	20	17	17	2568	30.70	148	82	767	7	o	E3	-1949
17 Mariana 4	18	16	14	2245	30.12	145	79	761	7	o	E3	-1855
17 Mariana 5	14	12	11	1747	29.95	140	76	768	7	o	E3	-2318
18 Java 1	61	46	55	4713	28.65	102	66	863	31	c	0	694

(cont.)

Arc-segment	**Vort** (mm/yr)	**Vdes** (mm/yr)	**Vlat** (mm/yr)	ϕ (km)	**Fsp** (10^{12} N/m)	**Age** (Ma)	**Vhs** (mm/yr)	**L** (km)	**Tc** (km)	**UPN** (o/c)	**UPS** (E3-C3)	**He** (m)
18 Java 2	68	49	59	5850	30.42	119	25	848	32	c	0	710
18 Java 3	70	49	61	6395	31.52	129	56	842	31	c	0	483
19 Sumatra 1	48	36	41	1793	22.16	50	47	954	33	c	0	930
19 Sumatra 2	34	24	30	1082	24.43	44	62	1114	33	c	0	1035
19 Sumatra 3	45	33	39	2117	25.99	64	48	988	33	c	0	1105
19 Sumatra 4	55	42	48	3722	27.69	90	54	888	32	c	0	834

Explanation: $Vort$ = orthogonal speed, $Vdes$ = descend speed of the slab, $Vlat$ = lateral speed, ϕ = thermal parameter,
Fsp = slab-pull force, Age = slab age, Vhs = half-spreading rate, L = slab length,
Tc = crustal thickness, UPN = upper plate nature, UPS = upper plate strain, He = average elevation
* = Segments are not included in the multivariate statistics (see main text)

Appendix G

Multivariate Statistics

this page is intentionally left blank

G.1 Coefficient of Correlation

Table G.1. Coefficient of correlation among subduction dynamic variables

nV	**1.00**																								
Lseg	0.46	**1.00**																							
S.Az.	0.04	0.26	**1.00**																						
Mrms	**0.55**	0.35	0.09	**1.00**																					
Dt	-0.02	0.20	-0.02	0.40	**1.00**																				
T.Az.	-0.07	0.22	**0.91**	0.00	-0.07	**1.00**																			
At	-0.22	-0.22	-0.16	0.06	0.41	-0.22	**1.00**																		
Ts	-0.18	0.10	0.03	0.12	0.40	0.07	0.18	**1.00**																	
Ht	-0.03	0.03	0.00	-0.16	-0.37	-0.01	-0.18	**-0.51**	**1.00**																
Htrel	0.12	-0.07	0.00	0.45	0.16	-0.13	0.07	-0.31	**0.51**	**1.00**															
δ	0.01	0.12	0.30	**-0.52**	**-0.64**	0.38	-0.29	-0.17	0.27	**-0.51**	**1.00**														
δ_s	-0.04	-0.01	-0.08	**-0.50**	**-0.74**	-0.02	-0.36	-0.26	0.48	-0.3	**0.77**	**1.00**													
δ_d	0.05	0.22	0.32	-0.29	-0.39	0.34	-0.30	-0.29	0.10	-0.47	0.70	**0.54**	**1.00**												
H	-0.15	0.15	0.34	-0.08	0.22	0.33	0.00	0.07	-0.20	-0.20	0.06	-0.04	0.39	**1.00**											
Vtot	0.12	-0.28	-0.34	0.19	-0.07	-0.36	0.09	-0.12	0.06	0.36	-0.32	-0.17	**-0.66**	**-0.58**	**1.00**										
Vort	0.21	-0.21	-0.38	0.17	-0.04	-0.40	0.10	-0.21	0.09	0.34	-0.25	-0.17	**-0.55**	**-0.59**	0.92	**1.00**									
Vdes	0.19	-0.17	-0.22	-0.14	-0.38	-0.19	-0.05	-0.24	0.19	0.04	0.30	0.24	-0.19	**-0.58**	**0.73**	**0.84**	**1.00**								
Vlat	0.22	-0.18	-0.37	0.26	0.11	-0.40	0.16	-0.19	-0.04	0.38	-0.41	-0.36	**-0.63**	**-0.55**	**0.90**	**0.98**	**0.74**	**1.00**							
ϕ	0.02	-0.02	-0.23	-0.20	-0.23	-0.19	-0.09	-0.43	0.7	0.32	0.20	0.37	-0.12	-0.42	0.44	**0.51**	**0.57**	0.43	**1.00**						
Fsp	-0.08	0.09	-0.14	0.02	0.11	-0.14	-0.09	-0.35	**0.64**	0.43	-0.26	-0.02	-0.28	-0.10	0.21	0.21	-0.01	0.23	**0.71**	**1.00**					
Age	-0.11	0.12	0.02	-0.28	-0.18	0.06	-0.15	-0.47	**0.73**	0.14	0.3	0.43	0.29	0.05	-0.18	-0.12	-0.03	-0.17	**0.73**	**0.79**	**1.00**				
Vhs	-0.21	-0.34	-0.16	-0.06	0.20	-0.15	0.07	-0.02	-0.12	0.11	-0.29	-0.24	-0.27	0.12	0.11	0.02	-0.16	0.04	-0.01	0.2	0.01	**1.00**			
Ao	-0.29	-0.03	0.27	-0.02	-0.04	0.26	-0.09	0.25	-0.10	-0.12	0.00	0.07	0.10	0.33	-0.37	**-0.67**	**-0.67**	**-0.64**	-0.36	-0.01	0.01	0.20	**1.00**		
L	-0.05	0.01	-0.14	0.32	0.43	-0.22	0.11	0.02	0.20	**0.63**	**-0.71**	-0.48	**-0.67**	-0.01	0.29	0.22	-0.19	0.31	0.28	**0.73**	0.22	0.46	0.13	**1.00**	
Tc	0.22	-0.02	0.00	**0.63**	**0.57**	-0.12	0.27	0.25	**-0.61**	0.31	**-0.77**	**-0.76**	**-0.5**	0.06	0.31	0.26	-0.13	0.42	-0.46	-0.23	**-0.66**	0.14	-0.06	0.33	**1.00**
He	0.15	-0.10	-0.01	**0.60**	**0.54**	-0.12	0.25	0.22	**-0.55**	0.45	**-0.77**	**-0.75**	**-0.53**	0.02	0.29	0.23	-0.16	0.39	-0.42	-0.22	**-0.63**	0.22	-0.01	0.40	0.94
	nV	***Lseg***	***S.Az.***	***Mrms***	***Dt***	***T.Az.***	***At***	***Ts***	***Ht***	***Htrel***	δ	δ_s	δ_d	***H***	***Vtot***	***Vort***	***Vdes***	***Vlat***	ϕ	***Fsp***	***Age***	***Vhs***	***Ao***	***L***	***Tc***	***He***

Table G.2. P-value of subduction dynamic variables correlations

nV	-																										
Lseg	0.00	-																									
S.Az.	0.75	0.05	-																								
Mrms	0.00	0.01	0.50	-																							
Dt	0.88	0.13	0.86	0.00	-																						
T.Az.	0.60	0.10	0.00	0.99	0.60	-																					
At	0.10	0.10	0.22	0.65	0.00	0.08	-																				
Ts	0.17	0.46	0.80	0.35	0.00	0.59	0.17	-																			
Ht	0.84	0.85	0.97	0.24	0.00	0.95	0.19	0.00	-																		
Htrel	0.35	0.58	1.00	0.00	0.22	0.32	0.59	0.02	0.00	-																	
δ	1.00	0.39	0.02	0.00	0.00	0.00	0.03	0.19	0.04	0.00	-																
δ_s	0.74	0.97	0.56	0.00	0.00	0.91	0.01	0.05	0.00	0.02	0.00	-															
δ_d	0.70	0.12	0.02	0.03	0.00	0.01	0.03	0.03	0.46	0.00	0.00	0.00	-														
H	0.26	0.27	0.01	0.52	0.10	0.01	0.98	0.62	0.13	0.13	0.63	0.77	0.00	-													
Vtot	0.39	0.03	0.01	0.15	0.59	0.01	0.49	0.38	0.69	0.01	0.02	0.20	0.00	0.00	-												
Vort	0.11	0.12	0.00	0.20	0.77	0.00	0.44	0.11	0.49	0.01	0.06	0.21	0.00	0.00	0.00	-											
Vdes	0.16	0.21	0.09	0.30	0.00	0.15	0.72	0.07	0.16	0.77	0.03	0.08	0.18	0.00	0.00	0.00	-										
Vlat	0.11	0.17	0.01	0.06	0.45	0.00	0.24	0.18	0.78	0.00	0.00	0.01	0.00	0.00	0.00	0.00	0.00	-									
ϕ	0.91	0.89	0.09	0.14	0.09	0.16	0.51	0.00	0.00	0.02	0.14	0.01	0.40	0.00	0.00	0.00	0.00	0.00	-								
Fsp	0.60	0.50	0.30	0.85	0.44	0.31	0.53	0.01	0.00	0.00	0.07	0.87	0.05	0.45	0.14	0.13	0.95	0.10	0.00	-							
Age	0.41	0.38	0.87	0.03	0.18	0.66	0.25	0.00	0.00	0.30	0.02	0.00	0.04	0.70	0.17	0.37	0.80	0.20	0.00	0.00	-						
Vhs	0.11	0.01	0.24	0.65	0.14	0.26	0.64	0.88	0.38	0.43	0.03	0.07	0.06	0.38	0.39	0.86	0.26	0.77	0.95	0.16	0.97	-					
Ao	0.03	0.84	0.04	0.86	0.78	0.05	0.51	0.06	0.45	0.37	0.99	0.65	0.49	0.01	0.01	0.00	0.00	0.00	0.01	0.93	0.91	0.14	-				
L	0.72	0.92	0.31	0.02	0.00	0.11	0.40	0.92	0.15	0.00	0.00	0.00	0.00	0.91	0.03	0.11	0.16	0.02	0.04	0.00	0.11	0.00	0.32	-			
Tc	0.09	0.89	0.98	0.00	0.00	0.38	0.04	0.05	0.00	0.02	0.00	0.00	0.00	0.69	0.02	0.04	0.33	0.00	0.00	0.10	0.00	0.28	0.63	0.01	-		
He	0.26	0.46	0.97	0.00	0.00	0.37	0.06	0.09	0.00	0.00	0.00	0.00	0.00	0.91	0.03	0.08	0.24	0.00	0.00	0.11	0.00	0.09	0.92	0.00	0.00	-	
	nV	***Lseg***	***S.Az.***	***Mrms***	***Dt***	***T.Az.***	***At***	***Ts***	***Ht***	***Htrel***	δ	δ_s	δ_d	***H***	***Vtot***	***Vort***	***Vdes***	***Vlat***	ϕ	***Fsp***	***Age***	***Vhs***	***Ao***	***L***	***Tc***	***He***

G.2 Scatter Plots

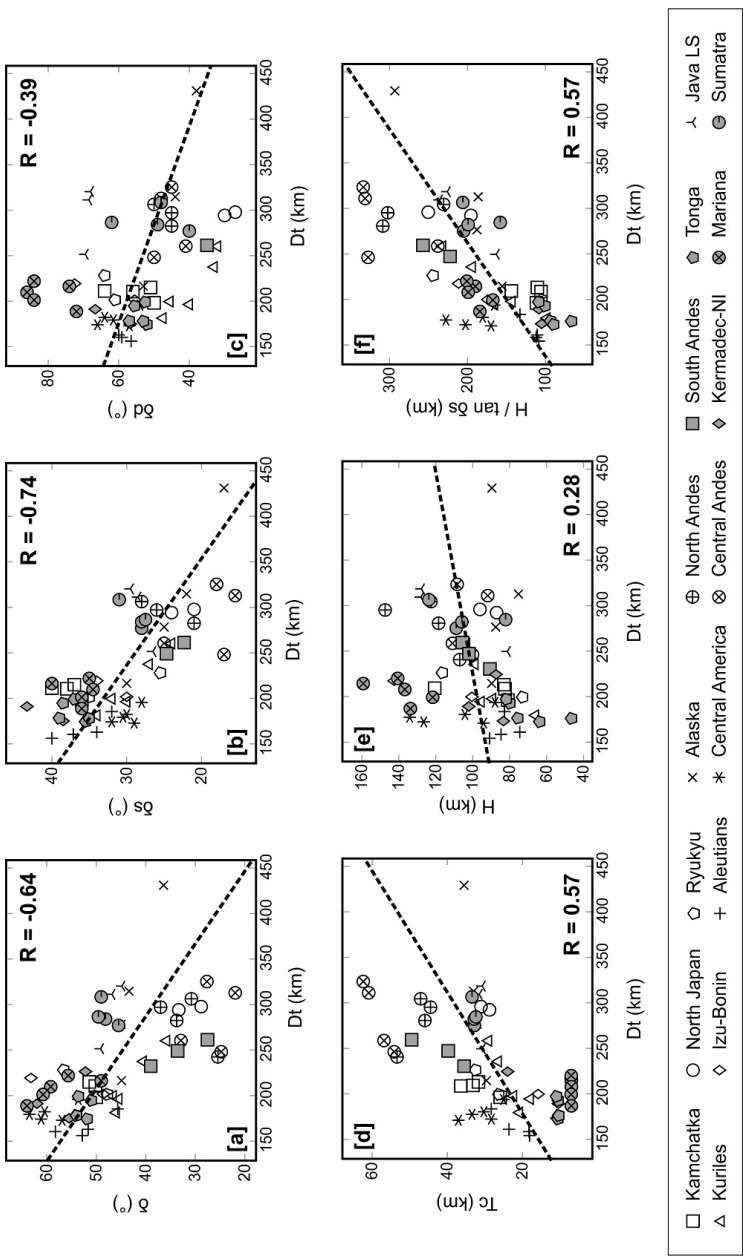

Figure G.1. Scatter plot of the arc-segment distance from trench (Dt) and (**A**) Slab dip, (**B**) shallow slab dip; (**C**) deep slab dip, (**D**) crustal thickness, (**E**) depth to slab under the arc, and (**F**) horizontal component of H ($H/\tan\delta_s$).

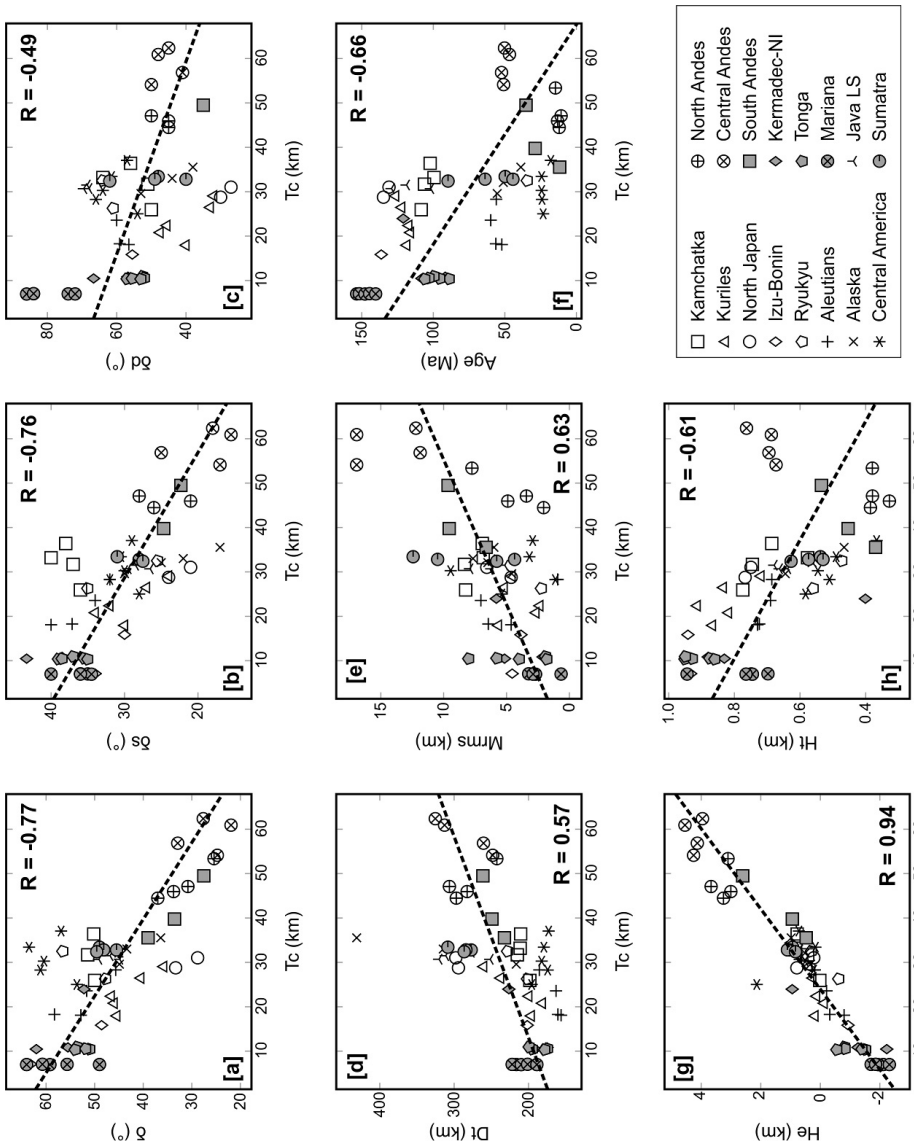

Figure G.2. Scatter plot of the crustal thickness (Tc) and (**A**) Slab dip, (**B**) shallow slab dip, (**C**) deep slab dip, (**D**) arc-segment distance from trench, (**E**) arc-segment rms-misfits, (**F**) slab age, (**G**) average elevation, and (**H**) trench depth.

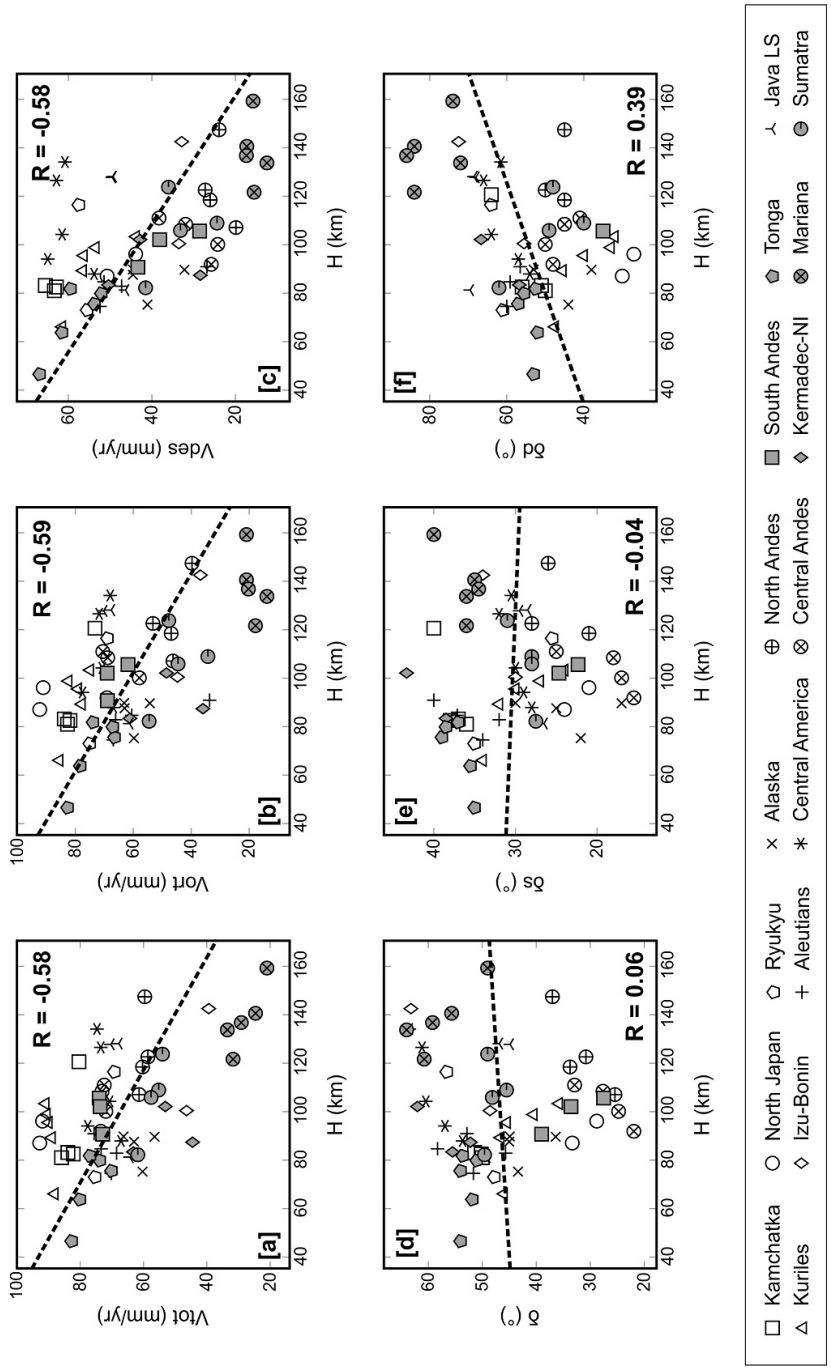

Figure G.3. Scatter plot of the depth to the slab beneath the arc (H) and (**A**) convergence rate, (**B**) orthogonal speed of the slab, (**C**) descent speed of the slab, (**D**) slab dip, (**E**) shallow slab dip, and (**F**) deep slab dip.

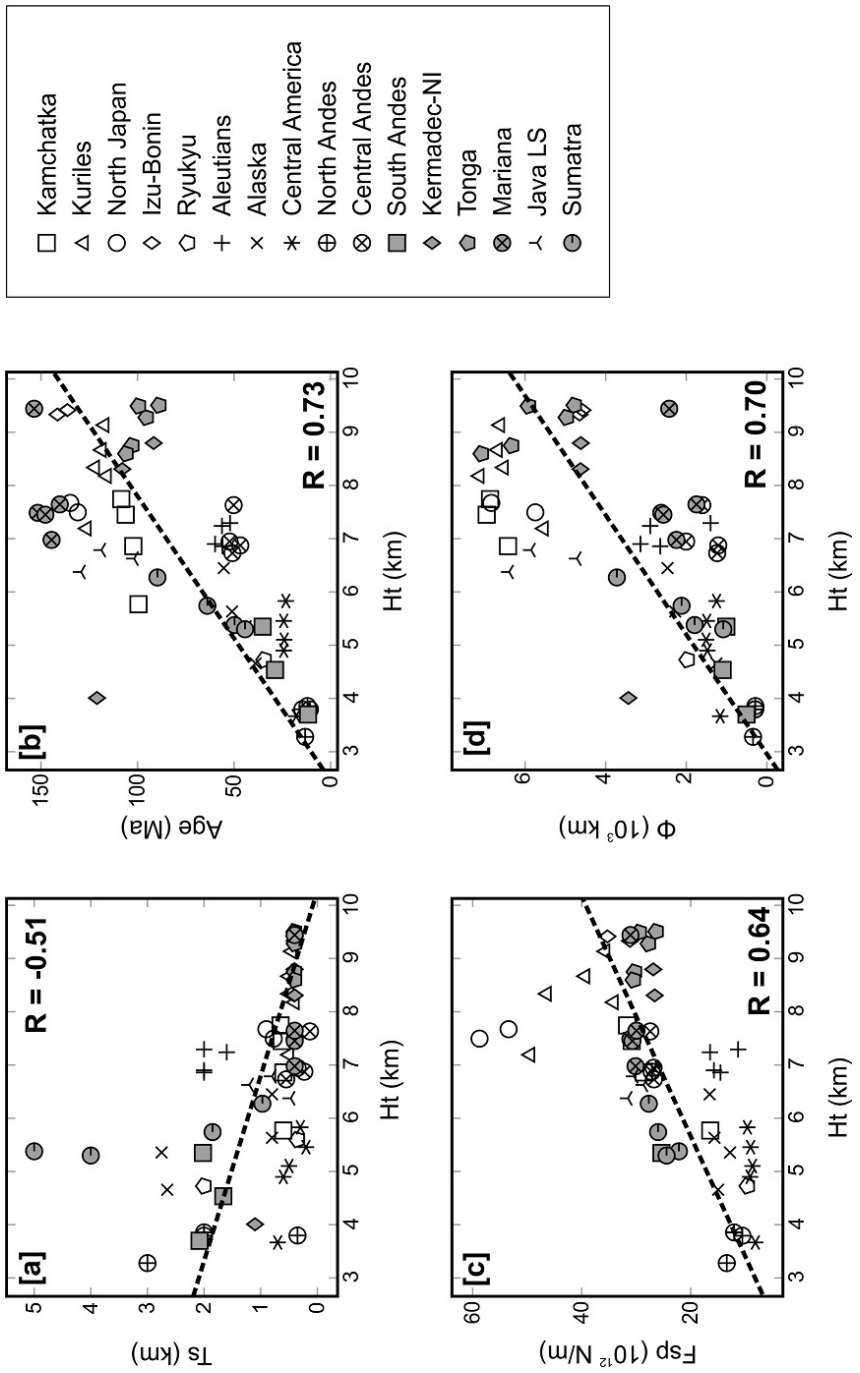

Figure G.4. Scatter plot of the trench depth (*Ht*) and (**A**) sediment thickness, (**B**) slab age, (**C**) slab pull force, and (**D**) thermal parameter.

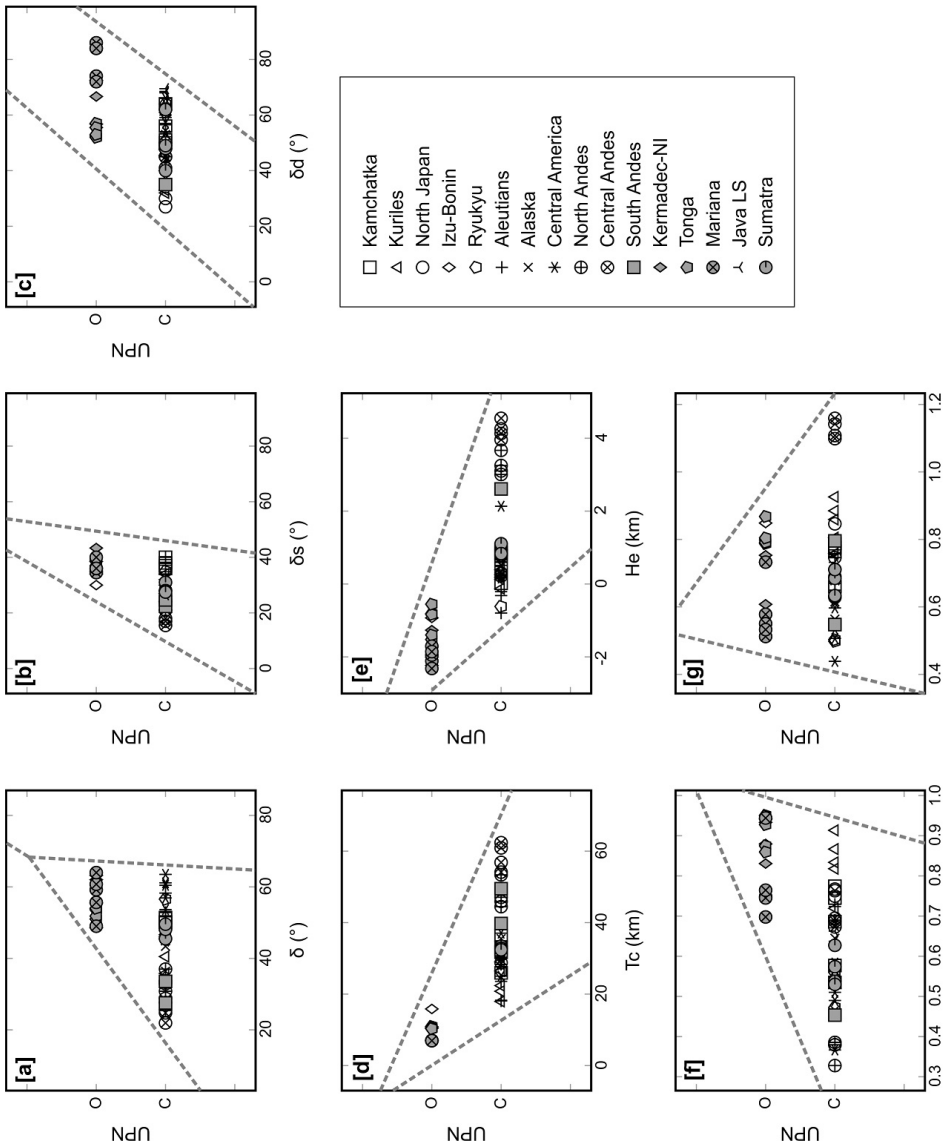

Figure G.5. Plot of the Upper Plate Nature (UPN) against (**A**) Slab dip, (**B**) shallow slab dip, (**C**) deep slab dip, (**D**) crustal thickness, (**E**) average elevation, (**F**) trench depth, and (**G**) relative trench depth.

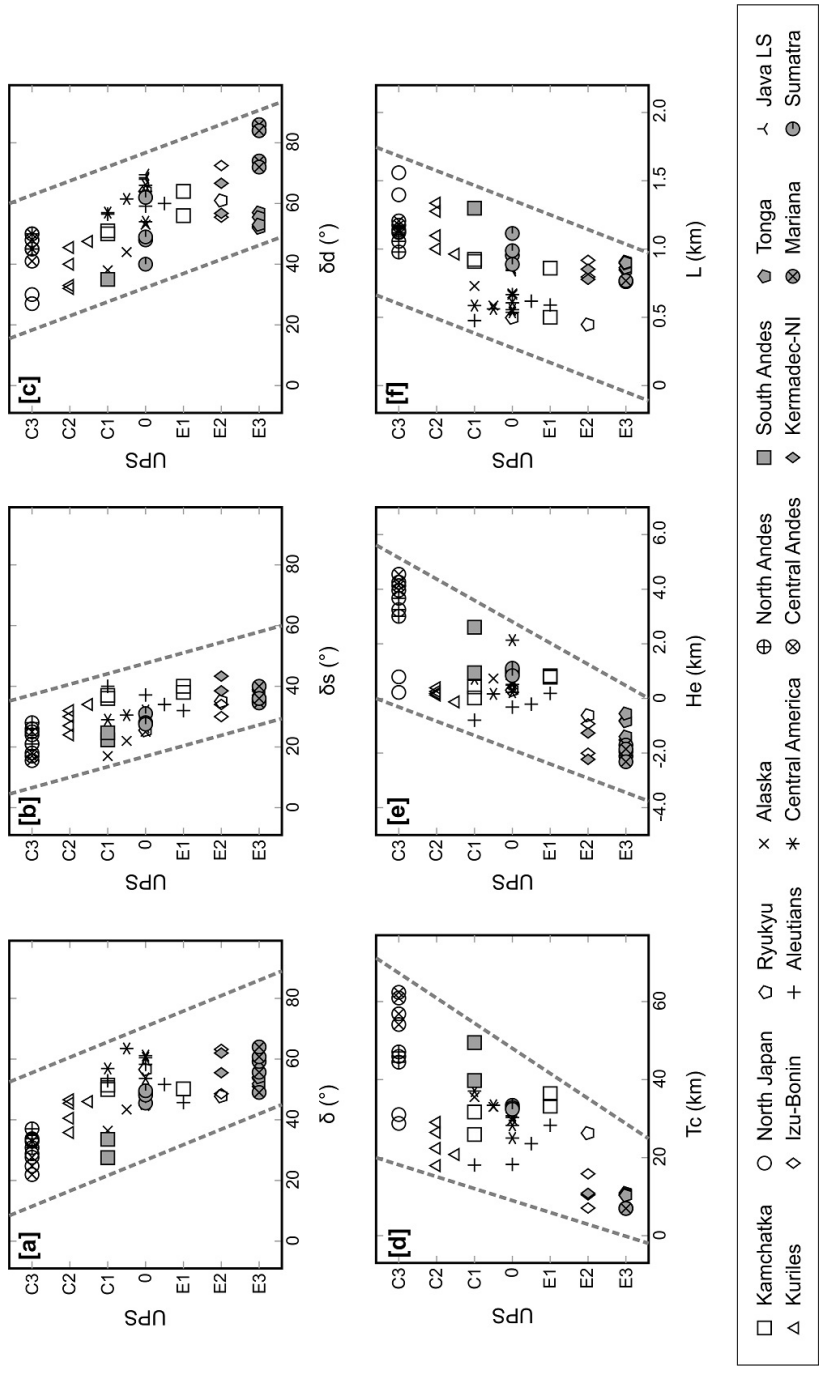

Figure G.6. Plot of the Upper Plate Strain (*UPS*) against (**A**) slab dip, (**B**) shallow slab dip, (**C**) deep slab dip, (**D**) crustal thickness, (**E**) average elevation, and (**F**) slab length.

References

Abidin, H. Z., Andreas, H., Kato, T., Ito, T., Meilano, I., Kimata, F., ... Harjono, H. (2009). Crustal deformation studies in Java (Indonesia) using GPS. *Journal of Earthquake and Tsunami*, *3*(2), 77-88.

Acocella, V., Bellier, O., Sandri, L., Sébrier, M., & Pramumijoyo, S. (2018). Weak tectono-magmatic relationships along an obliquely convergent plate boundary: Sumatra, Indonesia. *Frontiers in Earth Science*, *6*(3), 1-20.

Acocella, V., & Funiciello, F. (2010). Kinematic setting and structural control of arc volcanism. *Earth and Planetary Science Letters*, *289*, 43-53.

Afnimar, Yulianto, E., & Rasmid. (2015). Geological and tectonic implications obtained from first seismic activity investigation around Lembang fault. *Geoscience Letters*, *2*(4), 1-11.

Akaike, H. (1974). A new look at the statistical model identification. *IEEE Transactions on Automatic Control*, *19*(6), 716-723.

Akpa, O. M., & Unuabonah, E. I. (2011). Small-sample corrected akaike information criterion: an appropriate statistical tool for ranking of adsorption isotherm models. *Desalination*, *272*, 20-26.

Aldiss, D. T., & Ghazali, S. A. (1984). The regional geology and evolution of the Toba volcano-tectonic depression, Indonesia. *Journal of the Geological Society*, *141*, 487-500.

Andikagumi, H., Macpherson, C. G., & McCaffrey, K. J. W. (2020). Upper plate stress controls the distribution of Mariana arc volcanoes. *Journal of Geophysical Research: Solid Earth*. doi: 10.1029/2019JB017391

Annen, C., Blundy, J. D., & Sparks, R. S. (2006). The genesis of intermediate and silicic magmas in deep crustal hot zones. *Journal of Petrology*, *47*(3), 505-539.

Apperson, K. D. (1991). Stress fields of the overriding plate at convergent margins and beneath active volcanic arcs. *Science*, *254*(532), 670-678.

Argus, D. F., Gordon, R. G., & DeMets, C. (2011). Geologically current motion of 56 plates relative to the no-net-rotation reference frame. *Geochemistry, Geophysics, Geosystems*, *12*(11), Q11001.

Artyushkov, E. V. (1973). Stresses in the lithosphere caused by crustal thickness inhomogeneities. *Journal of Geophysical Research*, *78*(32), 7675-7708.

Bada, G., Horváth, F., Cloetingh, S., Coblentz, D. D., & Tóth, T. (2001). Role of topography-induced gravitational stresses in basin inversion: the case study of the Pannonian basin. *Tectonics*, *20*(3), 343-363.

Baker, E. T., Embley, R. W., Walker, S. L., Resing, J. A., Lupton, J. E., Nakamura, K., ... Massoth, G. J. (2008). Hydrothermal activity and volcano distribution along the Mariana arc. *Journal of Geophysical Research*, *113*, B08S09.

Banks, H. T., & Joyner, M. L. (2017). AIC under the framework of least squares estimation. *Applied Mathematics Letters*, *74*, 33-45.

Barber, A. J., Crow, M. J., & De Smet, M. E. M. (2005). Sumatra: Geology, resources and tectonic evolution. In R. J. Pankhurst et al. (Eds.), (Vol. 31, p. 234-259). London: Geological Society Special Publications.

Becker, J. J., Sandwell, D. T., Smith, W. H. F., Braud, J., Binder, B., Depner, J., ... Weatherall, P. (2009). Global bathymetry and elevation data at 30 arc seconds resolution: Srtm30 plus. *Marine Geodesy*, *32*, 355-371.

Becker, T. W., Schaeffer, A. J., Lebedev, S., & Conrad, C. P. (2015). Toward a generalized plate motion reference frame. *Geophysical Research Letters*, *42*, 3188-3196.

Bellier, O., & Sébrier, M. (1994). Relationship between tectonism and volcanism along the Great Sumatran Fault Zone deduced by spot image analyses. *Tectonophysics*, *233*, 215-231.

Billen, M. I., & Gurnis, M. (2001). A low viscosity wedge in subduction zones. *Earth and Planetary Science Letters*, *193*, 227-236.

Bird, P. (1991). Lateral extrusion of lower crust from under high topography, in the isostatic limit. *Journal of Geophysical Research*, *96*(B6), 10275-10286.

Bird, P. (2003). An updated digital model of plate boundaries. *Geochemistry, Geophysics, Geosystems*, *4*(3), 1027-1078.

Bird, R. T., & Pockalny, R. A. (1994). Late Cretaceous and Cenozoic seafloor and oceanic basement roughness: Spreading rate, crustal age and sediment thickness correlations. *Earth and Planetary Science Letters*, *123*, 239-254.

Bleacher, J. E., Glaze, L. S., Greeley, R., Hauber, E., Baloga, S. M., Sakimoto, S. E., ... Glotch, T. D. (2009). Spatial and alignment analyses for a field of small volcanic vents south of Pavonis Mons and implications for the Tharsis province, Mars. *Journal of Volcanology and Geothermal Research*, *185*, 96-102.

Blong, R. J. (1984). *Volcanic hazards: sourcebook on the effects of eruptions*. North Ryde, N. S. W.: Academic Press Australia.

Bloomer, S. H., Stern, R. J., & Smoot, N. C. (1989). Physical volcanology of the submarine mariana and volcano arcs. *Bulletin of Volcanology*, *51*, 210-224.

Bodine, J. H., & Watts, A. B. (1979). On lithospheric flexure seaward of the Bonin and Mariana trenches. *Earth and Planetary Science Letters*, *43*, 132-148.

Bolge, L. L., Carr, M. J., Milidakis, K. I., Lindsay, F. N., & Feigenson, M. D. (2009). Correlating geochemistry, tectonics, and volcanic volume along the central american volcanic front. *Geochemistry, Geophysics, Geosystems*, *10*(12), Q12S18.

Bonini, M. (2012). Mud volcanoes: Indicators of stress orientation and tectonic controls. *Earth-Science Reviews*, *115*, 121-152.

Bonnardot, M.-A., Hassani, R., & Tric, E. (2008). Numerical modelling of lithosphere–asthenosphere interaction in a subduction zone. *Earth and Planetary Science Letters*, *272*, 698-708.

Boutelier, D., & Cruden, A. (2013). Slab rollback rate and trench curvature controlled by arc deformation. *Geology*, *41*(8), 911-914.

Brace, W. F., & Kohlstedt, D. L. (1980). Limits on lithospheric stress imposed by laboratory experiment. *Journal of Geophysical Research*, *85*(B11), 6248-6252.

Bradley, K. E., Feng, L., Hill, E. M., Natawidjaja, D. H., & Sieh, K. (2017). Implications of the diffuse deformation of the Indian Ocean lithosphere for slip partitioning of oblique plate convergence in Sumatra. *Journal of Geophysical Research: Solid Earth*, *122*, 572-591.

Brounce, M., Kelley, K. A., Stern, R., Martinez, F., & Cottrell, E. (2016). The Fina Nagu volcanic complex: Unusual submarine arc volcanism in the rapidly deforming southern mariana margin. *Geochemistry, Geophysics, Geosystems*, *17*, 4078-4091.

Budd, D. A., Troll, V. R., Deegan, F. M., Jolis, E. M., Smith, V. C., Whitehouse, M. J., ... Bindeman, I. N. (2017). Magma reservoir dynamics at Toba caldera, Indonesia, recorded by oxygen isotope zoning in quartz. *Scientific Reports*, *7*(40624), 1-11.

Burkart, B., & Self, S. (1985). Extension and rotation of crustal blocks in northern Central America and effect on the volcanic arc. *Geology*, *13*, 22-26.

Burnham, K. P., & Anderson, D. R. (2004). Multimodel inference: Understanding aic and bic in model selection. *Sociological Methods & Research*, *33*(2), 261-304.

Burov, E. B. (2011). Rheology and strength of the lithosphere. *Marine and Petroleum Geology*, *28*, 1402-1443.

Capitanio, F. A., & Morra, G. (2012). The bending mechanics in a dynamic subduction system: Constraints from numerical modelling and global compilation analysis. *Tectonophysics*, *522-523*, 224-234.

Carlile, J. C., & Mitchell, A. H. G. (1994). Magmatic arcs and associated gold and copper mineralization in Indonesia. *Journal of Geochemical Exploration*, *50*, 91-142.

Carlson, R. L., Hilde, T. W. C., & Uyeda, S. (1983). The driving mechanisms of plate tectonics: Relation to age of the lithosphere at trenches. *Geophysical Research Letters*, *10*(4), 297-300.

Carr, M. J., Stoiber, R. E., & Drake, C. L. (1973). Discontinuities in the deep seismic zones under the japanese arcs. *Geological Society of America Bulletin*, *84*, 2917-2930.

Cebriá, J. M., Martín-Escorza, C., López-Ruiz, J., Morán-Zenteno, D. J., & Martiny, B. M. (2011). Numerical recognition of alignments in monogenetic volcanic areas: Examples from the Michoacán-Guanajuato Volcanic Field in Mexico and Calatrava in Spain. *Journal of Volcanology and Geothermal Research*, *201*, 73-82.

Chesner, C. A. (2012). The Toba Caldera complex. *Quaternary International*, *258*, 5-18.

Chesner, C. A., & Rose, W. I. (1991). Stratigraphy of the Toba Tuffs and the evolution of the Toba Caldera Complex, Sumatra, Indonesia. *Bulletin of Volcanology*, *53*, 343-356.

Christie-Blick, N., & Biddle, K. T. (1985). Strike-slip deformation, basin formation and sedimentation. In K. T. Biddle & N. Christie-Blick (Eds.), (Vol. 37, p. 1-34). The Society of Economic Paleontologists and Mineralogists Special Publication.

Christova, C., & Scholz, C. H. (2003). Stresses in the Vanuatu subducting slab: A test of two hypotheses. *Geophysical Research Letters*, *30*(15), 1790-1793.

Clements, B., Hall, R., Smyth, H. R., & Cottam, M. A. (2009). Thrusting of a volcanic arc: A new structural model for Java. *Petroleum Geoscience*, *15*, 159-174.

Cloetingh, S., & Wortel, R. (1986). Stress in the Indo-Australian plate. *Tectonophysics*, *132*, 49-67.

Cole, J. W., Milner, D. M., & Spinks, K. D. (2005). Calderas and caldera structures: A review. *Earth-Science Reviews*, *69*, 1-26.

Conrad, C. P., Bilek, S., & Lithgow-Bertelloni, C. (2004). Great earthquakes and slab pull: Interaction between seismic coupling and plate-slab coupling. *Earth and Planetary Science Letters*, *218*, 109-122.

Conrad, C. P., & Lithgow-Bertelloni, C. (2006). Influence of continental roots and asthenosphere on plate-mantle coupling. *Geophysical Research Letters*, *33*(L05312), 1-4.

Corbi, F., Funiciello, F., Faccenna, C., Ranalli, G., & Heuret, A. (2011). Seismic variability of subduction thrust faults: Insights from laboratory models. *Journal of Geophysical Research*, *116*(B06304), 1-14.

Cowie, P. A., Gupta, S., & Dawers, N. H. (2000). Implications of fault array evolution for synrift depocentre development: Insights from a numerical fault growth model. *Basin Research*, *12*, 241-261.

Crameri, F., Lithgow-Bertelloni, C. R., & Tackley, P. J. (2017). The dynamical control of subduction parameters on surface topography. *Geochemistry, Geophysics, Geosystems*, *18*, 1661-1687.

Crane, K., & Ballard, R. D. (1981). Volcanics and structure of the famous narrowgate rift: Evidence for cyclic evolution: AMAR 1. *Journal of Geophysical Research*, *86*(B6), 5112-5124.

Cunningham, W. D., & Mann, P. (2007). *Tectonics of strike-slip restraining and releasing bends* (Vol. 290). London: Geological Society Special Publication. (eds.)

Dardji, N., Villemin, T., & Rampnoux, J. P. (1994). Paleostresses and strike-slip movement: the Cimandiri Fault Zone, West Java, Indonesia. *Journal of Southeast Asian Earth Sciences*, *9*(1-2), 3-11.

Daryono, M. R., Natawidjaja, D. H., Sapiie, B., & Cummins, P. (2019). Earthquake geology of the Lembang Fault, West Java, Indonesia. *Tectonophysics*, *751*, 180-191.

de Bremond d'Ars, J., Jaupart, C., & Sparks, R. S. J. (1995). Distribution of volcanoes in active margins. *Journal of Geophysical Research*, *100*(B10), 20421-20432.

Delescluse, M., & Chamot-Rooke, N. (2007). Instantaneous deformation and kinematics of the India-Australia plate. *Geophysical Journal International*, *168*, 818-842.

DeMets, C., Gordon, R. G., & Argus, D. F. (2010). Geologically current plate motions. *Geophysical Journal International*, *181*, 1-80.

Deschamps, A., & Fujiwara, T. (2003). Asymmetric accretion along the slow-spreading mariana ridge. *Geochemistry, Geophysics, Geosystems*, *4*(10), 8622.

de Silva, S. (2008). Arc magmatism, calderas, and supervolcanoes. *Geology*, *36*(8), 671-672.

de Silva, S., & Gosnold, W. D. (2007). Episodic construction of batholiths: Insights from the spatiotemporal development of an ignimbrite flare-up. *Journal of Volcanology and Geothermal Research*, *167*, 320-335.

Dixon, T. H., & Stern, R. J. (1983). Petrology, chemistry, and isotopic composition of submarine volcanoes in the southern Mariana arc. *Geological Society of America Bulletin*, *94*, 1159-1172.

Duarte, J. C., Schellart, W. P., & Cruden, A. R. (2015). How weak is the subduction zone interface? *Geophysical Research Letters*, *42*, 2664-2673.

Duda, R. O., & Hart, P. E. (1972). Use of the Hough Transformation to detect lines and curves in pictures. *Communications of the ACM*, *15*(1), 11-15.

Dziewonski, A. M., Chou, T.-A., & Woodhouse, J. H. (1981). Determination of earthquake source parameters from waveform data for studies of global and regional seismicity. *Journal of Geophysical Research*, *86*(B4), 2825-2852.

Edwards, C., Menzies, M., & Thirlwall, M. (1991). Evidence from Muriah, Indonesia, for the interplay of supra-subduction zone and intraplate processes in the genesis of potassic alkaline magmas. *Journal of Petrology*, *32*(3), 555-592.

Edwards, C., Menzies, M., Thirlwall, M., Morris, J. D., Leeman, W. P., & Harmon, R. S. (1994). The transition to potassic alkaline volcanism in island arcs: The Ringgit-Beser complex, East Java, Indonesia. *Journal of Petrology*, *35*(6), 1557-1595.

Edwards, M. H., Fornari, D. J., Melinverno, A., & Ryan, W. B. F. (1991). The regional tectonic fabric of the east pacific rise from 12°50′n to 15°10′n. *Journal of Geophysical Research*, *96*(B5), 7995-8017.

Ekström, G., Nettles, M., & Dziewoński, A. M. (2012). The global CMT project 2004-2010: Centroid-moment tensors for 13,017 earthquakes. *Physics of the Earth and Planetary Interiors*, *200-201*, 1-9.

England, P. C., Engdahl, R., & Thatcher, W. (2004). Systematic variation in the depths of slabs beneath arc volcanoes. *Geophysical Journal International*, *156*, 377-408.

England, P. C., & Katz, R. F. (2010). Melting above the anhydrous solidus controls the location of volcanic arcs. *Nature*, *467*, 700-704.

Faccenna, C., Di Giuseppe, E., Funiciello, F., Lallemand, S., & van Hunen, J. (2009). Control of seafloor aging on the migration of the Izu-Bonin-Mariana trench. *Earth and Planetary Science Letters*, *288*, 386-398.

Farr, T. G., Rosen, P. A., Caro, E., Crippen, R., Duren, R., Hensley, S., ... Alsdorf, D. (2007). The Shuttle Radar Topography Mission. *Reviews of Geophysics*, *45*, 1-33.

Fernández-Álvarez, J.-P., González-Quirós, A., & Rubio-Melendi, D. (2016). Assessment of the value of microgravity to estimate the principal directions of the anisotropic transmissivity of aquifers from pumping tests: A study using a Hough transform based automatic algorithm. *Journal of Applied Geophysics*, *134*, 172-182.

Feuillet, N., Leclerc, F., Tapponnier, P., Beauducel, F., Boudon, G., Le Friant, A., ... Clément, V. (2010). Active faulting induced by slip partitioning in Montserrat and link with volcanic activity: New insights from the 2009 GWADASEIS marine cruise data. *Geophysical Research Letters*, *37*, L00E15.

Feuillet, N., Manighetti, I., & Tapponnier, P. (2002). Arc parallel extension and localization of volcanic complexes in Guadeloupe, Lesser Antilles. *Journal of Geophysical Research*, *107*(B12), 2331.

Fornari, D. J., Haymon, R. M., Perfit, M. R., Gregg, T. K. P., & Edwa, M. H. (1998). Axial summit trough of the east pacific rise 9°-10°N: Geological characteristics and evolution of the axial zone on fast spreading mid-ocean ridges. *Journal of Geophysical Research*, *103*(B5), 9827-9855.

Forte, A. M., Moucha, R., Simmons, N. A., Grand, S. P., & Mitrovica, J. X. (2010). Deep-mantle contributions to the surface dynamics of the North American continent. *Tectonophysics*, *481*(1-4), 3-15.

Fryer, P. (1995). Backarc basins. In B. Taylor (Ed.), (p. 237-297). Boston, MA: Springer.

Fryer, P. (1996). Evolution of the Mariana convergent plate margin system. *Reviews of Geophysics*, *34*(1), 89-125.

Fukao, Y., Widiyantoro, S., & Obayashi, M. (2001). Stagnant slabs in the upper and lower mantle transition region. *Reviews of Geophysics*, *39*(3), 291-323.

Gelman, S. E., Gutiérrez, F. J., & Bachmann, O. (2013). On the longevity of large upper crustal silicic magma reservoirs. *Geology*, *41*(7), 759-762.

Ghosh, A., Holt, W. E., & Wen, L. (2013). Predicting the lithospheric stress field and plate motions by joint modeling of lithosphere and mantle dynamics. *Journal of Geophysical Research: Solid Earth*, *118*(1), 346-368.

Gill, J. B. (2012). *Orogenic andesites and plate tectonics* (Vol. 16). Berlin: Springer Science & Business Media.

Global Volcanism Program. (2013). *Smithsonian institution. Volcanoes of the World, v. 4.8.0. Venzke, E. (ed.).* Retrieved from https://volcano.si.edu/ (Retrieved on 1 November 2015)

Grandin, R., Jacques, E., Nercessian, A., Ayele, A., Doubre, C., Socquet, A., ... King, G. C. P. (2011). Seismicity during lateral dike propagation: Insights from new data in the recent Manda Hararo-Dabbahu rifting episode (Afar, Ethiopia). *Geochemistry, Geophysics, Geosystems*, *12*(4), Q0AB08.

Gregg, P. M., de Silva, S., Grosfils, E. B., & Parmigiani, J. P. (2012). Catastrophic caldera-forming eruptions: Thermomechanics and implications for eruption triggering and maximum caldera dimensions on Earth. *Journal of Volcanology and Geothermal Research*, *241-242*, 1-12.

Griffin, J., Nguyen, N., Cummins, P., & Cipta, A. (2019). Historical earthquakes of the eastern Sunda Arc: Source mechanisms and intensity-based testing of Indonesia's national seismic hazard assessment. *Bulletin of the Seismological Society of America*, *109*(1), 46-65.

Grosfils, E. B., & Head, J. W. (1994). The global distribution of giant radiating dike swarms on Venus: Implications for the global stress state. *Geophysical Research Letters*, *21*(8), 701-704.

Grove, T. L., Till, C. B., Lev, E., Chatterjee, N., & Médard, E. (2009). Kinematic variables and water transport control the formation and location of arc volcanoes. *Nature*, *459*, 694-697.

Gurnis, M., Eloy, C., & Zhong, S. (719-727). Free-surface formulation of mantle convection - II. Implication for subduction-zone observables. *Geophysical Journal International*, *127*, 1996.

Gvirtzman, Z., & Stern, R. J. (2004). Bathymetry of Mariana trench-arc system and formation of the Challenger Deep as a consequence of weak plate coupling. *Tectonics*, *23*, TC2011.

Hall, R. (2000, October). Neogene history of collision in the Halmahera region, Indonesia. In *Proceedings of the indonesian petroleum association 27th annual convention* (p. 487-493).

Hall, R. (2002). Cenozoic geological and plate tectonic evolution of SE Asia and the SW Pacific: Computer-based reconstructions, model and animations. *Journal of Asian Earth Sciences*, *20*, 353-431.

Hall, R. (2012). Late Jurassic-Cenozoic reconstructions of the Indonesian region and the Indian Ocean. *Tectonophysics*, *570-571*, 1-41.

Hall, R., & Smyth, H. R. (2008). Formation and applications of the sedimentary record in arc collision zones. In A. Draut, P. Clift, & D. Scholl (Eds.), (Vol. 436, p. 27-54). Geological Society of America Special Paper.

Hall, R., van Hattum, M. W., & Spakman, W. (2008). Impact of India-Asia collision on SE Asia: The record in Borneo. *Tectonophysics*, *451*, 366-389.

Hamilton, W. B. (1979). *Tectonics of the Indonesian region* (No. 1078). US Govt. Print. Off.

Hamilton, W. B. (1988). Plate tectonics and island arcs. *Geological Society of America Bulletin*, *100*, 1503-1527.

Harding, T. P. (1974). Petroleum traps associated with wrench faults. *The American Association of Petroleum Geologists Bulletin*, *58*(7), 1290-1304.

Hasegawa, H. S., Adams, J., & Yamazaki, K. (1985). Upper crustal stresses and vertical stress migration in eastern Canada. *Journal of Geophysical Research: Solid Earth*, *90*(B5), 3637-3648.

Hassani, R., Jongmans, D., & Chèry, J. (1997). Study of plate deformation and stress in subduction processes using two-dimensional numerical models. *Journal of Geophysical Research*, *102*(B8), 17951-17965.

Hayes, G. P., Moore, G. L., Portner, D. E., Hearne, M., Flamme, H., Furtney, M., & Smoczyk, G. M. (2018). Slab2, a comprehensive subduction zone geometry model. *Science*, *362*, 58-61.

Head, J. W., Crumpler, L. S., Aubele, J. C., & Saunders, R. S. (1992). Venus volcanism: Classification of volcanic features and structures, associations, and global distribution from Magellan data. *Journal of Geophysical Research*, *97*(E8), 13153-13197.

Heuret, A., Conrad, C. P., Funiciello, F., Lallemand, S., & Sandri, L. (2012). Relation between subduction megathrust earthquakes , trench sediment thickness and upper plate strain. *Geophysical Research Letters*, *39*(L05304), 1-6.

Heuret, A., & Lallemand, S. (2005). Plate motions, slab dynamics and back-arc deformation. *Physics of the Earth and Planetary Interiors*, *149*, 31-51.

Hickman, R. G., Dobson, P. F., van Gerven, M., Sagala, B. D., & Gunderson, R. P. (2004). Tectonic and stratigraphic evolution of the Sarulla graben geothermal area, North Sumatra, Indonesia. *Journal of Asian Earth Sciences*, *23*, 435-448.

Hieronymus, C. F., & Bercovici, D. (1999). Discrete alternating hotspot islands formed by interaction of magma transport and lithospheric flexure. *Nature*, *397*, 604-607.

Hieronymus, C. F., & Bercovici, D. (2000). Non-hotspot formation of volcanic chains: control of tectonic and flexural stresses on magma transport. *Earth and Planetary Science Letters*, *181*, 539-554.

Hieronymus, C. F., & Bercovici, D. (2001). A theoretical model of hotspot volcanism: Control on volcanic spacing and patterns via magma dynamics and lithospheric stresses. *Journal of Geophysical Research*, *106*(B1), 683-702.

Hilde, T. W. C., & Uyeda, S. (1983). Geodynamics of the western pacific-indonesian region. In (Vol. 11, p. 75-89).

Holm, R. J., Rosenbaum, G., & Richards, S. W. (2016). Post 8 Ma reconstruction of Papua New Guinea and Solomon Islands: Microplate tectonics in a convergent plate boundary setting. *Earth-Science Reviews*, *156*, 66-81.

Holt, A. F., Becker, T. W., & Buffett, B. A. (2015). Trench migration and overriding plate stress in dynamic subduction models. *Geophysical Journal International*, *201*, 172-192.

Huchon, P., & Le Pichon, X. (1984). Sunda Strait and Central Sumatra fault. *Geology*, *12*, 668-672.

Hughes, G. R., & Mahood, G. A. (2011). Silicic calderas in arc settings: Characteristics, distribution, and tectonic controls. *Bulletin of the Geological Society of America*, *123*(7-8), 1577-1595.

Hughes, J. M., Stoiber, R. E., & Carr, M. J. (1980). Segmentation of the Cascade volcanic chain. *Geology*, *8*(1), 15-17.

Hurvich, C.-L., Clifford M. amd Tsai. (1989). Regression and time series model selection in small samples. *Biometrika*, *76*(2), 297-307.

Husson, L. (2006). Dynamic topography above retreating subduction zones. *Geology*, *34*(9), 741-744.

Hussong, D. M., & Uyeda, S. (1981). Tectonic processes and the history of the Mariana Arc: A synthesis of the results of Deep Sea Drilling Project Leg 60. *Initial Reports of Deep-Sea Drilling Project*, *60*, 909-929.

Isacks, B., Oliver, J., & Sykes, L. R. (1968). Seismology and new global tectonics. *Journal of Geophysical Research*, *73*(18), 5855-5899.

Ishihara, T., Stern, R. J., Fryer, P., Bloomer, S., & Becker, N. C. (2001, December). Seafloor spreading in the southern mariana trough inferred from 3-component magnetometer data. In *AGU Fall Meeting Abstracts* (p. T41C-0895).

Ivanov, M. A., & Head, J. W. (2006). Alba Patera, Mars: Topography, structure, and evolution of a unique late Hesperian-early Amazonian shield volcano. *Journal of Geophysical Research*, *111*(E09003), 1-31.

Jacob, J., Dyment, J., & Yatheesh, V. (2014). Revisiting the structure, age, and evolution of the Wharton Basin to better understand subduction under Indonesia. *Journal of Geophysical Research: Solid Earth*, *119*, 169-190.

Jarrard, R. D. (1986). Relations among subduction parameters. *Reviews of Geophysics*, *24*(2), 217-284.

Jaxybulatov, K., Shapiro, N. M., Koulakov, I., Mordret, A., Landès, M., & Sens-Schönfelder, C. (2014). A large magmatic sill complex beneath the Toba caldera. *Science*, *346*(6209), 617-619.

Kagan, Y. Y., & Knopoff, L. (1980). Spatial distribution of earthquakes: the two-point correlation function. *Geophysical Journal of the Royal Astronomical Society*, *62*, 303-320.

Karig, D. E. (1971). Origin and development of marginal basins in the western Pacific. *Journal of Geophysical Research*, *76*(11), 2542-2561.

Karig, D. E., Anderson, R. N., & Bibee, L. D. (1978). Characteristics of back arc spreading in the Mariana Trough. *Journal of Geophysical Research*, *83*(B3), 1213-1226.

Kato, T., Beavan, J., Matsushima, T., Kotake, Y., Camacho, J. T., & Nakao, S. (2003). Geodetic evidence of back-arc spreading in the Mariana Trough. *Geophysical Research Letters*, *30*(12), 1625-1628.

Kirby, S. H., Stein, S., Okal, E. A., & Rubie, D. C. (1996). Metastable mantle phase transformations and deep earthquakes in subducting oceanic lithosphere. *Reviews of Geophysics*, *34*(2), 261-306.

Kirkpatrick, S., Gelatt, C. D., & Vecchi, M. P. (1983). Optimization by simulated annealing. *Science*, *220*(4598), 671-680.

Kohlstedt, D. L., Evans, B., & Mackwell, S. J. (1995). Strength of the lithosphere: Constraints imposed by laboratory experiments. *Journal of Geophysical Research*, *100*(B9), 17587-17602.

Koulakov, I., Kasatkina, E., Shapiro, N. M., Jaupart, C., Vasilevsky, A., El Khrepy, S., ... Smirnov, S. (2016). The feeder system of the Toba supervolcano from the slab to the shallow reservoir. *Nature Communications*, *7*, 1-12.

Koulali, A., McClusky, S., Susilo, S., Leonard, Y., Cummins, P., Tregoning, P., ... Wijanarto, A. (2017). The kinematics of crustal deformation in Java from GPS observations: Implications for fault slip partitioning. *Earth and Planetary Science Letters*, *458*, 69-79.

Kusznir, N., & Karner, G. (1985). Dependence of the flexural rigidity of the continental lithosphere on rheology and temperature. *Nature*, *316*, 138-142.

Lallemand, S., Heuret, A., & Boutelier, D. (2005). On the relationships between slab dip, back-arc stress, upper plate absolute motion, and crustal nature in subduction zones. *Geochemistry, Geophysics, Geosystems*, *6*(9), Q09006.

Lamb, S. (2006). Shear stresses on megathrusts: Implications for mountain building behind subduction zones. *Journal of Geophysical Research*, *111*, B07401.

Laske, G., Masters, G., Ma, Z., & Pasyanos, M. E. (2013). Update on CRUST1.0: A 1-degree global model of Earth's crust. In *EGU General Assembly* (p. 3743).

Latin, D., & White, N. (1990). Generating melt during lithospheric extension: Pure shear vs. simple shear. *Geology*, *18*, 327-331.

Leeman, W. P., Annen, C., & Dufek, J. (2008). Dynamics of crustal magma transfer, storage and differentiation. In C. Annen & G. F. Zellmer (Eds.), (Vol. 304, p. 235-259). London: Geological Society Special Publications.

Leterrier, J., Yuwono, Y. S., Soeria-Atmadja, R., & Maury, R. C. (1990). Potassic volcanism in Central Java and South Sulawesi, Indonesia. *Journal of Southeast Asian Earth Sciences*, *4*(3), 171-187.

Lim, E., Sutherland, M. G., Friday, D. Z., Eakins, B. W., & McLean, S. J. (2013, February). *Bathymetric digital elevation model of the Mariana Trench* (Tech. Rep.). Boulder, CO: NOAA National Geophysical Data Center (NGDC).

Macedo, J., & Marshak, S. (1999). Controls on the geometry of fold-thrust belt salients. *Bulletin of the Geological Society of America*, *111*(12), 1808-1822.

Macpherson, C. G., & Hall, R. (1999). Tectonic controls of geochemical evolution in arc magmatism of SE Asia. In *Proceedings of the 4th PACRIM Congress* (p. 359-368).

Macpherson, C. G., & Hall, R. (2002). The timing and location of major ore deposits in an evolving orogen. In D. J. Blundell, F. Neubauer, & A. von Quadt (Eds.), (Vol. 204, p. 49-67). London: Geological Society Special Publications.

Maggi, A., Jackson, J. A., McKenzie, D., & Priestley, K. (2000). Earthquake focal depths, effective elastic thickness, and the strength of the continental lithosphere. *Geology*, *28*(6), 495-498.

Magistrale, H., & Sanders, C. (1996). Evidence from precise earthquake hypocenters for segmentation of the San Andreas Fault in San Gorgonio Pass. *Journal of Geophysical Research*, *101*(B2), 3031-3044.

Magni, V., Faccenna, C., van Hunen, J., & Funiciello, F. (2014). How collision triggers backarc extension: Insight into Mediterranean style of extension from 3-D numerical models. *Geology*, *42*(6), 511-514.

Magni, V., van Hunen, J., Funiciello, F., & Faccenna, C. (2012). Numerical models of slab migration in continental collision zones. *Solid Earth*, *3*, 293-306.

Malod, J. A., Karta, K., Beslier, M. O., & Zen, M. T. (1995). From normal to oblique subduction: Tectonic relationships between Java and Sumatra. *Journal of Southeast Asian Earth Sciences*, *12*(1-2), 85-93.

Manea, V. C., Marta, P. G., & Manea, M. (2012). Chilean flat slab subduction controlled by overriding plate thickness and trench rollback. *Geology*, *40*(1), 35-38.

Marliyani, G. I. (2016). *Neotectonics of Java, Indonesia: Crustal deformation in the overriding plate of an orthogonal subduction system* (Unpublished doctoral dissertation). School of Earth and Space Exploration, Arizona State University, Tempe, AZ.

Marliyani, G. I., Arrowsmith, J. R., & Helmi, H. (2019). Evidence for multiple ground-rupturing earthquakes in the past 4,000 years along the Pasuruan Fault, East Java, Indonesia: Documentation of active normal faulting in the Javan backarc. *Tectonics*, *38*, 1489-1506.

Marliyani, G. I., Arrowsmith, J. R., & Whipple, K. X. (2016). Characterization of slow slip rate faults in humid areas: Cimandiri Fault zone, Indonesia. *Journal of Geophysical Research: Earth Surface*, *121*, 2287-2308.

Marsh, B. D. (1979). Island arc development: Some observations, experiments, and speculations. *The Journal of Geology*, *87*(6), 687-713.

Marshak, S. (2004). Thrust tectonics and hydrocarbon systems. In K. R. McClay (Ed.), (Vol. 82, p. 131-156). Association of American Petroleum Geologists Memoir.

Martìnez, F., Fryer, P., Baker, N. A., & Yamazaki, T. (1995). Evolution of backarc rifting: Mariana Trough, 20°–24°N. *Journal of Geophysical Research*, *100*(B3), 3807-3827.

Martìnez, F., Fryer, P., & Becker, N. (2000). Geophysical characteristics of the southern Mariana Trough, 11°50′N–13°40′N. *Journal of Geophysical Research*, *105*(B7), 16591-16607.

Martinez, F., Stern, R. J., Kelley, K. A., Ohara, Y., Sleeper, J. D., Ribeiro, J. M., & Brounce, M. (2018). Diffuse extension of the southern Mariana margin. *Journal of Geophysical Research: Solid Earth*, *123*, 892-916.

Martinez, F., & Taylor, B. (2003). Intra-oceanic subduction systems: Tectonic and magmatic processes. In R. D. Larter & P. T. Leat (Eds.), (Vol. 219, p. 19-54). London: Geological Society Special Publications.

Mazzarini, F. (2007). Vent distribution and crustal thickness in stretched continental crust: The case of the Afar Depression (Ethiopia). *Geosphere*, *3*(3), 152-162.

McCaffrey, K. J. W. (1992). Igneous emplacement in a transpressive shear zone: Ox Mountains igneous complex. *Journal of the Geological Society*, *149*, 221-235.

McCaffrey, R. (1992). Oblique plate convergence, slip vectors, and forearc deformation. *Journal of Geophysical Research*, *97*(B6), 8905-8915.

McCaffrey, R. (1996a). Estimates of modern arc-parallel strain rates in fore arcs. *Geology*, *24*(1), 27-30.

McCaffrey, R. (1996b). Tectonic evolution of Southeast Asia. In R. Hall & D. Blundell (Eds.), (Vol. 106, p. 3-18). London: Geological Society Special Publications.

McCaffrey, R., & Nabelek, J. (1987). Earthquakes, gravity, and the origin of the Bali Basin: An example of a nascent continental fold-and-thrust belt. *Journal of Geophysical Research*, *92*(B1), 441-460.

McCaffrey, R., Zwick, P. C., Bock, Y., Prawirodirdjo, L., Genrich, J. F., Stevens, C. W., ... Subarya, C. (2000). Strain partitioning during oblique plate convergence in northern Sumatra: Geodetic and seismologic constratints and numerical modeling. *Journal of Geophysical Research*, *105*(B12), 28363-28376.

McGarr, A., & Gay, N. C. (1978). State of stress in the Earth's crust. *Annual Review of Earth and Planetary Sciences*(6), 405-436.

McNulty, B. A., Farber, D. L., Wallace, G. S., Lopez, R., & Palacios, O. (1998). Role of plate kinematics and plate-slip-vector partitioning in continental magmatic arcs: Evidence from the Cordillera Blanca, Peru. *Geology*, *26*(9), 827-830.

Meilano, I., Abidin, H. Z., Andreas, H., Gumilar, I., Sarsito, D., Hanifa, R., ... Fukuda, Y. (2012). Slip rate estimation of the Lembang Fault West Java from geodetic observation. *Journal of Disaster Research*, *7*(1), 12-18.

Meissner, R., & Strehlau, J. (1982). Limits of stresses in continental crusts and their relation to the depth-frequency distribution of shallow earthquakes. *Tectonics*, *1*(1), 73-89.

Meyer, C., & Schellart, W. P. (2013). Three-dimensional dynamic models of subducting plate-overriding plate-upper mantle interaction. *Journal of Geophysical Research: Solid Earth*, *118*, 775-790.

Michaut, C., & Jaupart, C. (2006). Ultra-rapid formation of large volumes of evolved magma. *Earth and Planetary Science Letters*, *250*, 38-52.

Miller, M. S., Gorbatov, A., & Kennett, B. L. N. (2006). Three-dimensional visualization of a near-vertical slab tear beneath the southern Mariana arc. *Geochemistry, Geophysics, Geosystems*, *7*(6), Q06012.

Miller, M. S., Kennett, B. L. N., & Toy, V. G. (2006). Spatial and temporal evolution of the subducting Pacific plate structure along the western Pacific margin. *Journal of Geophysical Research*, *111*, B02401.

Mitchell, A. H., & Bell, J. D. (1973). Island-arc evolution and related mineral deposits. *The Journal of Geology*, *81*(4), 381-405.

Mooney, W. D., Laske, G., & Masters, T. G. (1998). CRUST 5.1: A global crustal model at $5^\circ \times 5^\circ$. *Journal of Geophysical Research*, *103*(B1), 727-747.

Morgan, J. P., Ranero, C. R., & Vannucchi, P. (2008). Intra-arc extension in Central America: Links between plate motions, tectonics, volcanism, and geochemistry. *Earth and Planetary Science Letters*, *272*, 365-371.

Muksin, U., Bauer, K., & Haberland, C. (2013). Seismic Vp and Vp/Vs structure of the geothermal area around Tarutung (North Sumatra, Indonesia) derived from local earthquake tomography. *Journal of Volcanology and Geothermal Research*, *260*, 27-42.

Muller, O. H., & Pollard, D. D. (1977). The stress state near Spanish Peaks, Colorado determined from a dike pattern. *Pure and Applied Geophysics PAGEOPH*, *115*, 69-86.

Müller, R. D., Sdrolias, M., Gaina, C., & Roest, W. R. (2008). Age, spreading rates, and spreading asymmetry of the world's ocean crust. *Geochemistry, Geophysics, Geosystems*, *9*(4), 1-19.

Muraoka, H., Takahashi, M., Sundhoro, H., Sjafra, D., Soeda, Y., Momita, M., & Shimada, K. (2010). Geothermal systems constrained by the Sumatran Fault and its pull-apart basins in Sumatra, western Indonesia. In *Proceedings world geothermal congress 2010.*

Nakakuki, T., & Mura, E. (2013). Dynamics of slab rollback and induced back-arc basin formation. *Earth and Planetary Science Letters*, *361*, 287-297.

Nakamura, K. (1977). Volcanoes as possible indicators of tectonic stress orientation - principle and proposal. *Journal of Volcanology and Geothermal Research*, *2*, 1-16.

Nakamura, K., & Uyeda, S. (1980). Stress gradient in arc-back arc regions and plate subduction stress. *Journal of Geophysical Research*, *85*(B11), 6419-6428.

Nakao, A., Iwamori, H., & Nakakuki, T. (2016). Effects of water transportation on subduction dynamics: Roles of viscosity and density reduction. *Earth and Planetary Science Letters*, *454*, 178-191.

Naliboff, J. B., Conrad, C. P., & Lithgow-Bertelloni, C. (2009). Modification of the lithospheric stress field by lateral variations in plate-mantle coupling. *Geophysical Research Letters*, *36*(22), 1-5.

Naylor, M. A., Mandl, G., & Supesteijn, C. H. K. (1986). Fault geometries in basement-induced wrench faulting under different initial stress states. *Journal of Structural Geology*, *8*(7), 737-752.

Ninkovich, D. (1976). Late Cenozoic clockwise rotation of Sumatra. *Earth and Planetary Science Letters*, *29*, 269-275.

Oakley, A. J., Taylor, B., Moore, G. F., & Goodliffe, A. (2009). Sedimentary, volcanic, and tectonic processes of the central Mariana Arc: Mariana Trough back-arc basin formation and the West Mariana Ridge. *Geochemistry, Geophysics, Geosystems*, *10*(8), Q08X07.

O'Driscoll, L. J., Richards, M. A., & Humphreys, E. D. (2012). Nazca-South America interactions and the late Eocene-late Oligocene flat-slab episode in the central Andes. *Tectonics*, *31*(TC2013), 1-16.

Oppenheimer, C. (2003). Climatic, environmental and human consequences of the largest known historic eruption: Tambora volcano (Indonesia) 1815. *Progress in Physical Geography*, *27*(2), 230-259.

Oppenheimer, C. (2011). *Eruptions that shook the world.* Cambridge: Cambridge University Press.

Pacey, A., Macpherson, C. G., & McCaffrey, K. J. W. (2013). Linear volcanic segments in the central Sunda Arc, Indonesia, identified using Hough Transform analysis: Implications for arc lithosphere control upon volcano distribution. *Earth and Planetary Science Letters*, *369-370*, 24-33.

Pasyanos, M. E. (2010). Lithospheric thickness modeled from long-period surface wave dispersion. *Tectonophysics*, *481*, 38-50.

Pasyanos, M. E., Masters, T. G., Laske, G., & Ma, Z. (2014). LITHO1.0: An updated crust and lithospheric model of the Earth. *Journal of Geophysical Research: Solid Earth*, *119*, 2153-2173.

Pearce, J. A., Stern, R. J., Bloomer, S. H., & Fryer, P. (2005). Geochemical mapping of the Mariana arc-basin system: Implications for the nature and distribution of subduction components. *Geochemistry, Geophysics, Geosystems*, *6*(7), Q07006.

Perrin, A., Goes, S., Prytulak, J., Rondenay, S., & Davies, D. R. (2018). Mantle wedge temperatures and their potential relation to volcanic arc location. *Earth and Planetary Science Letters*, *501*, 67-77.

Petrini, K., & Podladchikov, Y. (2000). Lithospheric pressure-depth relationship in compressive regions of thickened crust. *Journal of Metamorphic Geology*, *18*, 67-77.

Pubellier, M., & Morley, C. K. (2014). The basins of Sundaland (SE Asia): Evolution and boundary conditions. *Marine and Petroleum Geology*, *58*, 555-578.

Ranalli, G., & Murphy, D. C. (1987). Rheological stratification of the lithosphere. *Tectonophysics*, *132*, 281-295.

Ranneft, T. S. M. (1979). Segmentation of island arcs and application to petroleum geology. *Journal of Petroleum Geology*, *1*(3), 35-53.

Rapp, R. P., & Watson, E. B. (1995). Dehydration melting of metabasalt at 8-32 kbar: Implications for continental growth and crust-mantle recycling. *Journal of Petrology*, *36*(4), 891-931.

Richard, P. D., Naylor, M. A., & Koopman, A. (1995). Experimental models of strike-slip tectonics. *Petroleum Geoscience*, *1*, 71-80.

Richards, S., Holm, R., & Barber, G. (2011). When slabs collide: A tectonic assessment of deep earthquakes in the Tonga-Vanuatu region. *Geology*, *39*(8), 787-790.

Richardson, J. A., Bleacher, J. E., & Glaze, L. S. (2013). The volcanic history of Syria Planum, Mars. *Journal of Volcanology and Geothermal Research*, *252*, 1-13.

Roda, M., Marotta, A. M., & Spalla, M. I. (2011). The effects of the overriding plate thermal state on the slab dip in an ocean-continent subduction system. *Comptes Rendus Geoscience*, *343*(2011), 323-330.

Rodríguez-González, J., Negredo, A. M., & Billen, M. I. (2012). The role of the overriding plate thermal state on slab dip variability and on the occurrence of flat subduction. *Geochemistry, Geophysics, Geosystems*, *13*(1), 1-21.

Rooney, T. O., Bastow, I. D., & Keir, D. (2011). Insights into extensional processes during magma assisted rifting: Evidence from aligned scoria cones. *Journal of Volcanology and Geothermal Research*, *201*, 83-96.

Royden, L. H. (1993). The tectonic expression of slab pull at continental convergent boundaries. *Tectonics*, *12*(2), 303-325.

Safitri, A. A., Meilano, I., Gunawan, E., Abidin, H. Z., Efendi, J., & Kriswati, E. (2018). Strain variation along Cimandiri Fault, West Java based on continuous and campaign GPS observation from 2006-2016. In 41^{st} *HAGI Annual Convention and Exhibition 2016* (Vol. 132, p. 012027). IOP Conference Series: Earth and Environmental Science.

Saita, H., Nakajima, J., Shiina, T., & Kimura, J.-I. (2015). Slab-derived fluids, fore-arc hydration, and sub-arc magmatism beneath Kyushu, Japan. *Geophysical Research Letters*, *42*, 1685–1693.

Schaber, G., Strom, R., Moore, H., Soderblom, L. A., Kirk, R. L., Chadwick, D., ... Russell, J. (1992). Geology and distribution of impact craters on Venus: What are they telling us? *Journal of Geophysical Research*, *97*(E8), 13257-13301.

Schepers, G., Van Hinsbergen, D. J., Spakman, W., Kosters, M. E., Boschman, L. M., & McQuarrie, N. (2017). South-American plate advance and forced Andean trench retreat as drivers for transient flat subduction episodes. *Nature Communications*, *8*(15249), 1-9.

Schlüter, H. U., Gaedicke, C., Roeser, H. A., Schreckenberger, B., Meyer, H., Reichert, C., ... Prexl, A. (2008). Tectonic features of the southern Sumatra-western Java forearc of Indonesia. *Tectonics*, *21*(5), 1047-1062.

Schmidt, M. W., & Poli, S. (1998). Experimentally based water budgets for dehydrating slabs and consequences for arc magma generation. *Earth and Planetary Science Letters*, *163*, 361-379.

Scott, E. M. (2019). *Geochemical evolution of andean arc volcanism and the uplift of the Andes* (Unpublished doctoral dissertation). Department of Earth Sciences, Durham University, Durham, UK.

Scott, E. M., Allen, M. B., Macpherson, C. G., McCaffrey, K. J., Davidson, J. P., Saville, C., & Ducea, M. N. (2018). Andean surface uplift constrained by radiogenic isotopes of arc lavas. *Nature Communications*, *9*(1), 1-8.

Searle, R. C. (1992). Ophiolites and their modern oceanic analogues. In L. M. Parson, B. J. Murton, & P. Browning (Eds.), (Vol. 60, p. 65-79). London: Geological Society Special Publication.

Sharples, W., Jadamec, M. A., Moresi, L. N., & Capitanio, F. A. (2014). Overriding plate controls on subduction evolution. *Journal of Geophysical Research: Solid Earth*, *119*, 6684-6704.

Sieh, K., & Natawidjaja, D. (2000). Neotectonics of the Sumatran fault, Indonesia. *Journal of Geophysical Research*, *105*(B12), 28295-28326.

Simandjuntak, T. O., & Barber, A. J. (1996). Tectonic evolution of southeast asia. In R. Hall & D. Blundell (Eds.), (Vol. 106, p. 185-201). London: Geological Society Special Publications.

Simons, W. J. F., Socquet, A., Vigny, C., Ambrosius, B. A. C., Abu, S. H., Promthong, C., ... Spakman, W. (2007). A decade of GPS in Southeast Asia: Resolving Sundaland motion and boundaries. *Journal of Geophysical Research*, *112*, B06420.

Simpson, G. D. H. (2010). Formation of accretionary prisms influenced by sediment subduction and supplied by sediments from adjacent continents. *Geology*, *38*(2), 131-134.

Sisson, T. W., Ratajeski, K., Hankins, W. B., & Glazner, A. F. (2005). Voluminous granitic magmas from common basaltic sources. *Contributions to Mineralogy and Petrology*, *148*, 635-661.

Smellie, J. L. (1995). *Volcanism associated with extension at consuming plate margins* (Vol. 81). London: Geological Society Special Publication. (eds.)

Soeria-Atmadja, R., Maury, R. C., Bellon, H., Pringgoprawiro, H., Polve, M., & Priadi, B. (1994). Tertiary magmatic belts in Java. *Journal of Southeast Asian Earth Sciences*, *9*(1-2), 13-27.

Spakman, W., & Hall, R. (2010). Surface deformation and slab-mantle interaction during Banda arc subduction rollback. *Nature Geoscience*, *3*, 562-566.

Stankiewicz, J., Ryberg, T., Haberland, C., Fauzi, & Natawidjaja, D. (2010). Lake Toba volcano magma chamber imaged by ambient seismic noise tomography. *Geophysical Research Letters*, *37*(L17306), 1-5.

Stern, R. J. (2002). Subduction zones. *Reviews of Geophysics*, *40*(4), 1-38.

Stern, R. J., & Smoot, N. C. (1998). A bathymetric overview of the Mariana forearc. *The Island Arc*, *7*, 525-540.

Stern, R. J., Tamura, Y., Masuda, H., Fryer, P., Martinez, F., Ishizuka, O., & Bloomer, S. H. (2013). How the Mariana volcanic arc ends in the south. *Island Arc*, *22*, 133-148.

Stoiber, R. E., & Carr, M. J. (1973). Quaternary volcanic and tectonic segmentation of Central America. *Bulletin of Volcanology*, *37*(3), 304-325.

Susilohadi, S., Gaedicke, C., & Djajadihardja, Y. (2009). Structures and sedimentary deposition in the Sunda Strait, Indonesia. *Tectonophysics*, *467*, 55-71.

Susilohadi, S., Gaedicke, C., & Ehrhardt, A. (2005). Neogene structures and sedimentation history along the Sunda forearc basins off southwest Sumatra and southwest Java. *Marine Geology*, *219*, 133-154.

Syracuse, E. M., & Abers, G. A. (2006). Global compilation of variations in slab depth beneath arc volcanoes and implications. *Geochemistry, Geophysics, Geosystems*, *7*(5), 1-18.

Syracuse, E. M., van Keken, P. E., & Abers, G. A. (2010). The global range of subduction zone thermal models. *Physics of the Earth and Planetary Interiors*, *2010*, 73-90.

Takahashi, N., Kodaira, S., Klemperer, S. L., Tatsumi, Y., Kaneda, Y., & Suyehiro, K. (2007). Crustal structure and evolution of the Mariana intra-oceanic island arc. *Geology*, *35*(3), 203-206.

Tan, E., Lavier, L. L., van Avendonk, H. J., & Heuret, A. (2012). The role of frictional strength on plate coupling at the subduction interface. *Geochemistry, Geophysics, Geosystems*, *13*(10), 1-19.

Tatsumi, Y. (1986). Formation of the volcanic front in subduction zones. *Geophysical Research Letters*, *13*(8), 717-720.

Tatsumi, Y. (2005). The subduction factory: How it operates in the evolving Earth. *GSA Today*, *15*(7), 4-10.

Tibaldi, A. (1995). Morphology of pyroclastic cones and tectonics. *Journal of Geophysical Research*, *100*(B12), 24521-24535.

Tikoff, B., & Teyssier, C. (1992). Crustal-scale, *en echelon* 'p-shear' tensional bridges: A possible solution to the batholithic room problem. *Geology*, *20*, 927-930.

Tovish, A., & Schubert, G. (1978). Island arc curvature, velocity of convergence and angle of subduction. *Geophysical Research Letters*, *5*(5), 329-332.

Tovish, A., Schubert, G., & Luyendyk, B. P. (1978). Mantle flow pressure and the angle of subduction: Non-Newtonian corner flows. *Journal of Geophysical Research*, *83*(B12), 5892-5898.

Tsuji, T., Yamamoto, K., Matsuoka, T., Yamada, Y., Onishi, K., Bahar, A., ... Abidin, H. Z. (2009). Earthquake fault of the 26 may 2006 Yogyakarta earthquake observed by SAR interferometry. *Earth, Planets and Space*, *61*, 29-32.

Turcotte, D. L., McAdoo, D. C., & Caldwell, J. G. (1978). An elastic-perfectly plastic analysis of the bending of the lithosphere at a trench. *Tectonophysics*, *47*, 193-205.

Turner, S. J., Langmuir, C. H., Katz, R. F., Dungan, M. A., & Escrig, S. (2016). Parental arc magma compositions dominantly controlled by mantle-wedge thermal structure. *Nature Geoscience*, *9*(10), 772-776.

Vlaar, N. J., & Wortel, M. J. R. (1976). Lithospheric aging, instability and subduction. *Tectonophysics*, *32*, 331-351.

von Veh, M. W., & Németh, K. (2009). An assessment of the alignments of vents on geostatistical analysis in the Auckland Volcanic Field, New Zealand. *Géomorphologie – Relief, Processus, Environment*, *15*(3), 175-186.

Wadge, G., & Cross, A. (1988). Quantitative methods for detecting aligned points: an application to the volcanic vents of the Michoacan-Guanajuato volcanic field, Mexico. *Geology*, *16*, 815-818.

Walcott, R. I. (1970). Flexural rigidity, thickness, and viscosity of the lithosphere. *Journal of Geophysical Research*, *75*(20), 3941-3954.

Waldron, J. W. F. (2005). Extensional fault arrays in strike-slip and transtension. *Journal of Structural Geology*, *27*, 23-34.

Walker, R. J. (2016). Controls on transgressive sill growth. *Geology*, *44*(2), 99-102.

Walker, R. J., Healy, D., Kawanzaruwa, T. M., Wright, K. A., England, R. W., McCaffrey, K. J. W., ... Blenkinsop, T. G. (2017). Igneous sills as a record of horizontal shortening: The San Rafael subvolcanic field: Utah. *Geological Society of America Bulletin*, *129*(9-10), 1052-1070.

Waltham, D., Hall, R., Smyth, H. R., & Ebinger, C. J. (2008). Formation and applications of the sedimentary record in arc collision zones. In A. Draut, P. Clift, & D. Scholl (Eds.), (Vol. 436, p. 11-26). Geological Society of America Special Paper.

Weinberg, R. F. (1992). Neotectonics development of western Nicaragua. *Tectonics*, *11*(5), 1010-1017.

Wessel, P., & Smith, W. H. F. (1998). New, improved version of generic mapping tools released. *Eos, Transactions American Geophysical Union*, *79*(47), 579.

White, L. T., Rawlinson, N., Lister, G. S., Waldhauser, F., Hejrani, B., Thompson, D. A., ... Morgan, J. P. (2019). Earth's deepest earthquake swarms track fluid ascent beneath nascent arc volcanoes. *Earth and Planetary Science Letters*, *521*, 25-36.

White, R. S., McKenzie, D., & O'Nions, R. K. (1992). Oceanic crustal thickness from seismic measurements and rare earth element inversions. *Journal of Geophysical Research*, *97*(B13), 19683-19715.

Whitford, D. J. (1975). Strontium isotopic studies of the volcanic rocks of the Sunda arc, Indonesia, and their petrogenetic implications. *Geochimica et Cosmochimica Acta*, *39*, 1287-1302.

Widiyantoro, S., & Fauzi. (2005). Note on seismicity of the Bali convergent region in the eastern Sunda Arc, Indonesia. *Australian Journal of Earth Sciences*, *52*(3), 379-383.

Widiyantoro, S., & van der Hilst, R. (1996). Structure and evolution of lithospheric slab beneath the Sunda Arc, Indonesia. *Science*, *271*(5255), 1566-1570.

Williams, M. (2012). The 73 ka Toba super-eruption and its impact: History of a debate. *Quaternary International*, *258*, 19-29.

Wilson, C. R., Spiegelman, M., van Keken, P. E., & Hacker, B. R. (2014). Fluid flow in subduction zones: The role of solid rheology and compaction pressure. *Earth and Planetary Science Letters*, *401*, 261-274.

Woodcock, N. H., & Fischer, M. (1986). Strike-slip duplexes. *Journal of Structural Geology*, *8*(7), 725-735.

Wortel, R. (1982). Seismicity and rheology of subducted slabs. *Nature*, *296*, 553-556.

Xiao, Y., Wu, G., Lei, Y., & Chen, T. (2017). Analogue modeling of through-going process and development pattern of strike-slip fault zone. *Petroleum Exploration and Development*, *44*(3), 368-376.

Yamasaki, T., & Gernigon, L. (2009). Styles of lithospheric extension controlled by underplated mafic bodies. *Tectonophysics*, *468*, 169-184.

Yamazaki, T., Seama, N., Okino, K., Kitada, K., Joshima, M., Oda, H., & Naka, J. (2003). Spreading process of the northern Mariana Trough: Rifting-spreading transition at 22°N. *Geochemistry, Geophysics, Geosystems*, *4*(9), 1075.

Yang, T. F., Lee, T., Chen, C. H., Cheng, S. N., Knittel, U., Punongbayan, R. S., & Rasdas, A. R. (1996). A double island arc between Taiwan and Luzon: Consequence of ridge subduction. *Tectonophysics*, *258*, 85-101.

Yue, H., Lay, T., & Koper, K. D. (2012). *En échelon* and orthogonal fault ruptures of the 11 april 2012 great intraplate earthquakes. *Nature*, *490*, 245-249.

Zandt, G., & Ammon, C. J. (1995). Continental crust composition constrained by measurements of crustal Poisson's ratio. *Nature*, *374*, 152-154.

Zellmer, G. F. (2008). Dynamics of crustal magma transfer, storage and differentiation. In C. Annen & G. F. Zellmer (Eds.), (Vol. 304, p. 15-31). London: Geological Society Special Publications.

Zhong, S., & Gurnis, M. (1992). Viscous flow model of a subduction zone with a faulted lithosphere: Long and short wavelength topography, gravity and geoid. *Geophysical Research Letters*, *19*(18), 1891-1894.